Università degli Studi di Padova

Sede Amministrativa: Università degli Studi di Padova

Dipartimento di Geoscienze

CORSO DI DOTTORATO DI RICERCA IN GEOSCIENCES

CICLO XXXV

STRUCTURE, EVOLUTION AND DEFORMATION MECHANISMS OF CRUSTAL-SCALE SEISMOGENIC FAULTS (BOLFIN FAULT ZONE, NORTHERN CHILE)

Tesi redatta con il contributo finanziario della Fondazione Cariparo

Coordinatrice: Ch.ma Prof.ssa Claudia Agnini

Supervisore: Ch.mo Prof. Giulio Di Toro

Co-Supervisori: Ch.mo Prof. José Cembrano

Ch.mo Prof. Giorgio Pennacchioni

Dottorando: Simone Masoch

2023

Abstract

Earthquakes are among the deadliest natural disasters causing, causalities for >50000 people for year and tens of billions of euros of damage in the XXI century. Among the many factors controlling earthquake mechanics, the three-dimensional architecture (i.e., geometry, topology and spatial distribution of fault networks and fault-related damage) of fault systems and fluids contribute to the seismic vs. aseismic behavior of faults. However, crustal faults (i.e., capable to generate >6.0 M_W earthquakes) are hardly well exposed at the Earth's surface. In turn, little is known about their architecture and spatio-temporal evolution. In this thesis, I studied the Bolfin Fault Zone (BFZ), a crustal-scale Early Cretaceous strike-slip fault exceptionally exposed over more than 40 km in the Atacama Desert (Northern Chile). Specifically, I focused on the (i) structural evolution and along-strike architectural variability of the fault, and (ii) the deformation and ambient conditions (including fluid-rock interaction) during fault activity.

The BFZ is arranged into three main segments and has a sinuous crustal-scale geometry cutting through Jurassic to Early Cretaceous diorite and tonalite-granodiorite plutons. Ancient (125-118 Ma) seismic faulting, documented by pseudotachylytes, occurred at 5-7 km depth and ≤ 300 °C in a fluid-rich environment as recorded by extensive propylitic alteration and epidote-chlorite(-quartz-calcite) veining. The sinuous crustal-scale geometry of the BFZ resulted from (i) exploitation of precursory geometrical anisotropies (i.e., magmatic foliation of plutons and dyke swarms) during fault nucleation and (ii) hard linkage of these anisotropy-pinned fault segments, through splay faults, during fault growth. Overall, the BFZ architecture consists of hydrothermally altered multiple fault core strands, presenting pseudotachylytes, enveloped within a hydrothermally altered damage zone, which includes clusters of epidote-rich fault-vein networks and dilational breccias occurring at fault intersections and linkages. By comparison with active crustal fault zones, the pseudotachylyte-bearing fault network and extensive epidote-rich fault-vein networks were associated with mainshock-aftershocks and swarm-like earthquake sequences, respectively. Hydrogen isotope geochemistry indicates that pseudotachylytes formed in a rock-buffered environment, characterized by limited and local fluid circulation. Instead, the later fluid-driven seismicity attested by the hydrothermal fault-vein network was controlled by the ingression of surficial fluids in a more mature, hydraulically connected, upper-crustal hydrothermal system. In conclusion, the BFZ represents an exhumed analogue of crustal seismogenic volume, capable to have generated mainshock-aftershocks and later swarm-like earthquake sequences. The transition in the type of seismic activity was controlled by the fault architecture and the geochemical environment.

Riassunto

I terremoti sono tra i più letali disastri naturali causando più di 50000 vittime all'anno e decine di miliardi di euro di danni nel XXI secolo. Tra i molti fattori che controllano la meccanica dei terremoti, l'architettura tridimensionale (cioè la geometria, topologia e distribuzione spaziale del network di faglie e il danneggiamento associato alle faglie) dei sistemi di faglia e i fluidi contribuiscono a controllare il comportamento sismico vs. asismico delle faglie. Tuttavia, le faglie crostali (cioè in grado di generare terremoti >6.0 M_W) sono difficilmente ben esposte sulla superficie terrestre. Per questo motivo, conosciamo poco la loro architettura e la loro evoluzione spazio-temporale. In questa tesi, ho studiato la Faglia Bolfin (o Bolfin Fault Zone, BFZ). E' una faglia trascorrente a scala crostale del Cretaceo Inferiore eccezionalmente esposta per oltre 40 km nel deserto di Atacama (Cile settentrionale). Nello specifico, ho studiato (i) l'evoluzione strutturale, e (ii) la variabilità architetturale della faglia lungo strike, e (ii) le condizioni deformative e ambientali (compresa l'interazione fluido-roccia) durante l'attività della faglia.

La BFZ è composta di tre segmenti principali, ha una geometria sinuosa a scala crostale che taglia plutoni dioritici e tonalitici-granodioritici del Giurassico-Cretaceo Inferiore. La antica sismicità (125-118 Ma), documentata da pseudotachiliti, è avvenuta a 5-7 km di profondità e ≤ 300 °C in un ambiente ricco di fluidi come documentato da un'estesa alterazione propillitica e vene di epidoto-clorite(-quarzo-calcite). La geometria sinuosa a scala crostale della BFZ è il risultato di (i) sfruttamento di anisotropie geometriche (cioè foliazione magmatica di plutoni e sciami di dicchi) durante la nucleazione della faglia e (ii) connessione di questi segmenti di faglia vincolati dalle anisotrope, attraverso faglie di tipo splay, durante la crescita della faglia. Nel complesso, l'architettura della BFZ è costituita da nuclei di faglia multipli e alterati idrotermalmente, che presentano pseudotachiliti, inclusi all'interno di una zona di danneggiamento alterata idrotermalmente, che include network di vene-faglie mineralizzate a epidoto e brecce dilatanti che si trovano in corrispondenza di intersezioni e connessioni di faglia. Comparando la BFZ con faglie crostali sismicamente attive, il network di faglie a pseudotachiliti e l'esteso network di vene-faglie mineralizzate a epidoti sono associate rispettivamente a terremoti mainshock-aftershock (i) e sciami sismici. La geochimica degli isotopi dell'idrogeno indica che le pseudotachiliti si sono formate in un ambiente tamponato dalle rocce incassanti, caratterizzato da una circolazione limitata e locale di fluido. Invece, la successiva sismicità guidata da a fluidi attestata dal network di vene-faglie idrotermali è stata controllata dall'ingresso di fluidi superficiali in un sistema idrotermale più maturo e collegato idraulicamente. In conclusione, la BFZ rappresenta un analogo esumato del volume sismogenico crostale, in grado di aver generato terremoti mainshock-aftershock, e

successivi sciami sismici. La transizione del tipo di attività sismica era controllata dall'architettura della faglia e dall'ambiente geochimico.

Table of contents

Introduction

Fault zones are geological structures controlling the deformation of the Earth's crust, with a strong impact on human social and economic activities by, in most cases, producing earthquakes. Fault zones control the redistribution of water (e.g., Keegan-Treloar et al., 2022; Perrin and Luetscher, 2008) and other natural resources, such as hydrocarbons (e.g., Aydin, 2000; Grauls et al., 2002; Moretti, 1998) and ore-rich fluids (orgenic gold deposits: e.g., Goldfarb et al., 2005; Robert and Poulsen, 2001; Sibson and Scott, 1998; Iron-Oxide-Cupper-Gold deposits: e.g., Duncan et al., 2014; Williams et al., 2005; ephitermal deposits: e.g., Berger and Henley, 2011; Sanchez-Alfaro et al., 2016; Simmons et al., 2005; giant porhyry deposits: e.g., Piquer et al., 2021; Richards, 2013; Sillitoe, 2010), in the crust, which are essential for life and strategic for technological and economic progress. Fault zones also affect landscape evolution by creating geomorphological and topographic features favorable to human settlements and land use (e.g., valleys, bays: Bailey et al., 2011; King and Bailey, 2006). As a consequence, human settlements and economic activities are often located nearby seismically active fault zones. In turn, this means that human life and infrastructures are often developed in regions exposed to seismic hazard. The risk associated with seismic hazard is particularly high in densely populated regions with complex infrastructures. Despite progress in earthquake engineering, and fault and earthquake mechanics in the last decades, earthquakes are still among the deadliest natural disasters, causing causalities for >50000 people per year (statistics based on the 2000-2015 period; US Geological Survey, 2016) and tens of billions of euros of damage (just to remain in Italy, 6 billion Euro per year since 1980). For instance, the recent 2023 Kahramanmaraş Earthquake Sequence (Turkey and Syria), characterized by two large-in-magnitude doublet events (magnitude moment M_W 7.8 and M_W 7.6 earthquakes) caused an official death toll of over 57300 people (data at the end of March, 2023: Wikipedia). As a result, improving our understanding regarding faults and their underlying processes, and consequently regarding earthquake mechanics, is a scientific challenge pivotal for a safer development of human settlements and economic activities.

Earthquake mechanics is controlled by many factors over a wide range of scales (i.e., from nm to tens of km), including three-dimensional (3-D) architecture of fault systems, composition and frictional properties of wall and fault zone rocks, stiffness of the wall rocks, mechanical and chemical effects of fluids, deformation rates and regional and local stress fields, etc. (Scholz, 2019). At the scale of seismic rupture propagation (i.e., over tens of kilometers), the 3-D architecture (i.e., geometry, topology and spatial distribution of fault networks and fault-related damage; Fig. 1) of fault systems plays a first-order role in

controlling earthquake rupture nucleation, propagation and arrest, spatiotemporal evolution of seismic sequence and ground motion (e.g., Ben-Zion and Sammis, 2003; Chu et al., 2021; Cirella et al., 2012; Dal Zilio et al., 2020; Howarth et al., 2021; Perrin et al., 2016; Pischiutta et al., 2017; Ross et al., 2020; Sibson, 1985; Sylvester, 1988; Wesnousky, 2006, 1988; Wollherr et al., 2019). Fault systems are composed by multiple fault segments, possibly linked each other by branching faults, horsetail and splay faults, relay ramps, contractional and dilational jogs and a combination of these structure, resulting in complex fault networks/arrays which evolve through space and time (e.g., Cembrano et al., 2005; Crider and Peacock, 2004; d'Alessio and Martel, 2004; Kim et al., 2004, 2003; Martel, 1990; Segall and Pollard, 1983; Shipton and Cowie, 2001; Vermilye and Scholz, 1998). Specifically, fault segmentation contributes to the propagation and arrest of seismic ruptures (e.g., Wesnousky, 2006) and the relation between the fault systems and the regional stress field influences the distribution of foreshocks and aftershocks during seismic sequences and the slip distribution accommodated across the fault network (e.g., Kaven and Pollard, 2013). For instance, the 1992 M_W 7.3 Landers Earthquake (South California) ruptured five overlapping distinct fault segments and the seismic rupture migration across the main fault segments was controlled by branching linkage faults within overstepping step-overs (e.g., Abercrombie and Mori, 1994; Wollherr et al., 2019). In particular, only the two segments of the dextral strike-slip fault system optimally oriented with the regional stress field slipped over their relative total length, while only parts of the other involved segments ruptured (Wollherr et al., 2019). Furthermore, fault systems consist of multiple fault zones interacting to each other in space and time, producing complex along-strike and down-dip fault architecture (or fault system architecture). Consequently, the structural evolution and architecture of brittle fault zones contribute to the seismic vs. aseismic behavior of faults.

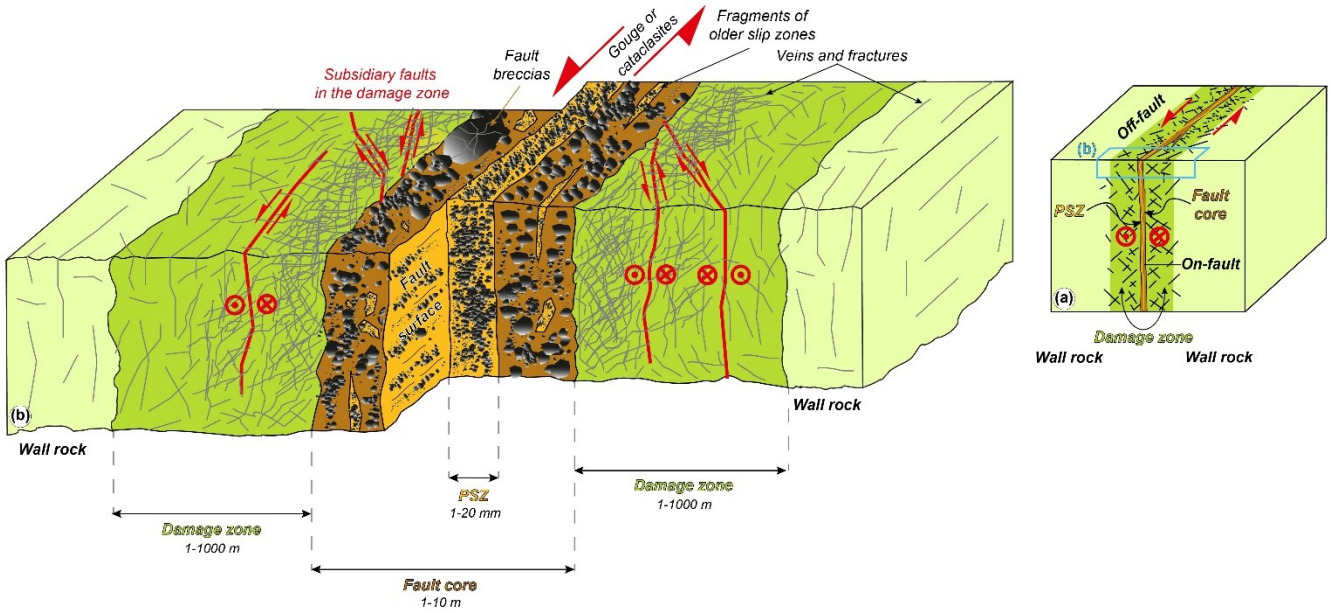

Fig. 1. Model of the architecture of a seismogenic fault zone. Modified from Cocco et al. (2023) (a) Conceptual model of fault zone architecture composed of a fault core enveloped with a damage zone. (b) A fault zone consists of a (zoned) damage zone containing a fault core(s) where strain is localized within a principal slip zone (PSZ), where available energy is released by co-seismic slip during earthquakes. The scale changes from the PSZ (thickness of 1–20 mm) to the damage zone (thickness of 1–1000 m).

Despite progress in imaging (i) fault zone architecture through modern geophysical and seismological techniques (Fig. 2) (double-difference tomography, trapped waves, earthquakes relocation: e.g., Allam and Ben-Zion, 2012; Ben-Zion, 1998; Chiaraluce et al., 2011; Hale, 2013; Lewis and Ben-Zion, 2010; Li et al., 2004; Ross et al., 2020; Unsworth et al., 1997; Valoroso et al., 2014, 2013; Zigone et al., 2015), and (ii) spatiotemporal evolution of seismic sequences in active fault zones thanks to earthquake relocation method (e.g., Chiaraluce et al., 2011; Ross et al., 2020; Sánchez-Reyes et al., 2021; Shelly et al., 2022; Valoroso et al., 2013), these techniques hardly achieve high spatial resolution (i.e., of the order of hundreds of meters) at seismogenic depths (i.e., 5-15 km depth, depending on geological setting, geothermal gradient, lithology, etc.; Scholz, 2019), where most of earthquakes nucleate in the continental crust, except for rare cases (Collettini et al., 2022; Liu et al., 2022; Ross et al., 2022, 2019). Fault-drilling projects allow direct characterization depths of "fresh" fault zone rocks (e.g., Chelungpu Fault, Tohoku-Oki megathrust, Wenchuan Fault, Alpine Fault, San Andreas Fault: Boullier et al., 2009; Chester et al., 2013; Li et al., 2013; Sutherland et al., 2012; Zoback et al., 2011), but the investigated rock volumes is too small to furnish a 3-D characterization of the fault zone architecture and the drilling depth is limited to 3-4 km at most. Consequently, the best tools to image and to quantify fault zone architecture remain the field-based studies of exhumed fault zones. The study of exhumed fault zones provides also information on fault evolution, fault kinematics and fault zone assemblages at high

resolution to constrain fault mechanical and hydraulic behavior and deformation processes active during the seismic cycle (e.g., Bistacchi et al., 2010; Cembrano et al., 2005, 2002; Coppola et al., 2021; Cox and Munroe, 2016; Demurtas et al., 2016; Di Toro and Pennacchioni, 2005; Fondriest et al., 2020a, 2015; Gomila et al., 2016; Grocott, 1981; Jensen et al., 2019; Kirkpatrick et al., 2008; Kirkpatrick and Shipton, 2009; Lucca et al., 2019; Marchesini et al., 2022; Masoch et al., 2019; Melosh et al., 2014; Mitchell and Faulkner, 2009; Mittempergher et al., 2014; Rowe et al., 2005; Rowe and Griffith, 2015; Smith et al., 2013; Snoke et al., 1998; Tesei et al., 2013; Wibberley and Shimamoto, 2003).

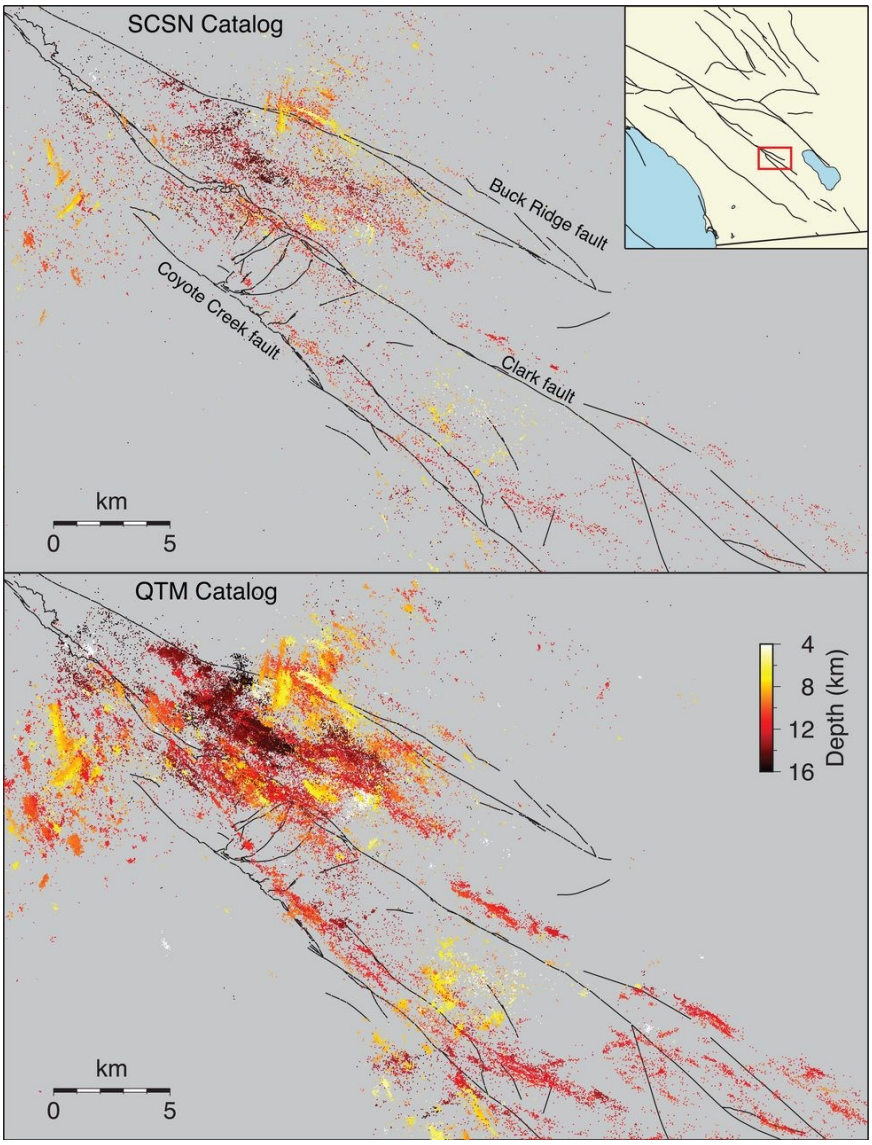

Fig. 2 Seismicity map of the San Jacinto Fault Zone (Southern California); modified from Ross et al., (2019). Black lines represent Quaternary faults. Colored dots are hypocenters (classified by depth) relocated from the South California Seismic Network catalog (upper panel), including 180000 earthquakes, and from the catalog implemented by using quake template matching (lower panel), including 1.81 million of earthquakes. Note the increase in spatial resolution at seismogenic depths in imaging architecture of faults by this new method.

Many continental crustal earthquakes nucleate in crystalline basement rocks (Scholz, 2019). Geological and geophysical studies have highlighted that the nucleation and growth of brittle fault zones cutting through these rocks are associated with either (i) formation of new fractures whose orientation is controlled by the regional or local stress field based on the rock failure criteria ("Anderson theory"; e.g., Anderson, 1951; Mandl, 1988; Naylor et al., 1986; Pennacchioni and Mancktelow, 2013; Swanson, 2006a;

Woodcock, 1986) and (ii) exploitation of either pre-existing (i.e., inherited from earlier deformation history; related to stratigraphic and paleogeographic boundaries) or precursory (i.e., related to the same deformation history and regional stress field) structures within the crystalline basements (e.g., fractures, dykes, ductile shear zones, weak mylonitic horizons, etc.: Bistacchi et al., 2012, 2010; Butler et al., 2008; Crider, 2015; Crider and Peacock, 2004; d'Alessio and Martel, 2005; Kirkpatrick et al., 2008; Mandl, 1988; Martel, 1990; Massironi et al., 2011; Mittempergher et al., 2021; Pachell and Evans, 2002; Pennacchioni et al., 2006; Phillips et al., 2019; Segall and Pollard, 1983; Smith et al., 2013; Storti et al., 2003; Swanson, 2006b, 1988; Sylvester, 1988; Wedmore et al., 2020; Whipp et al., 2014). Nevertheless, how major crustal-scale fault zone nucleate and evolve in crystalline basements and how their architecture varies along strike represent long-standing, but poorly investigated, issues in structural and earthquake geology, which only a few contributions have attempted to constrain (e.g., Bistacchi et al., 2010; Butler et al., 2008; Cembrano et al., 1996; Kirkpatrick et al., 2013; Perrin et al., 2016; Shigematsu et al., 2017; Wedmore et al., 2020). Even more rare in the literature are the cases of major, *seismogenic* fault zones whose structural evolution and architecture have been quantitatively documented over segments of a few kilometers (Bistacchi et al., 2010; Cembrano et al., 1996; Faulkner et al., 2008; Wibberley and Shimamoto, 2003) Indeed, moderate to large in magnitude (M_W >6) earthquakes rupture faults extending for >15 km in length, but these faults are rarely well-exposed along their whole length at the Earth's surface due to weathering and vegetation or Quaternary cover. Moreover, mature fault zones record a long, polyphase deformation history, which might obliterate the incipient stages of their formation and growth. Thus, the field geologists' challenge in studying ancient, crustal-scale seismogenic fault systems is to find large outcrops which meet the following criteria:

- excellent preservation over kilometer-scale exposures of the spatial arrangement of structures (e.g., fractures, dykes and faults) related to multiple deformation stages;
- faults exhumed from depths (i.e., 5-15 km depending on tectonic regime, rock composition, temperature gradient, etc.; Scholz, 2019), where moderate to large in magnitude earthquakes nucleate in the continental crust;
- excellent preservation of the fault and fracture networks over extensive exposures coupled with the presence of tectonic pseudotachylytes (i.e., solidified frictional melts), unambiguous evidence of seismic slip in the rock record (Cowan, 1999; Rowe and Griffith, 2015; Sibson, 1975).

The sinistral strike-slip Atacama Fault System in the exhumed magmatic arc of the Coastal Cordillera (Northern Chile) (Arabasz, 1971; Brown et al., 1993; Cembrano et al., 2005; Grocott and Taylor, 2002; Scheuber and González, 1999; Seymour et al., 2021), associated with the ancient subduction of the Aluk

(Phoenix) plate beneath the South America plate (Jaillard et al., 1990), is well exposed along strike over more than 1000 km. The exceptional outcrop conditions result from the hyper-arid climate since 25-22 Ma (Dunai et al., 2005) and the slow erosion rates in the Atacama Desert. This makes the Atacama Fault System an outstanding setting for studying the structural evolution and architectural variability of major faults hosted in the continental crust. In this thesis, we selected the Bolfin Fault Zone (BFZ), a major fault of the crustal-scale dilational jog of the Caleta Coloso Duplex (Cembrano et al., 2005), because of (i) widespread occurrence of pseudotachylytes along the fault zone and (ii) exceptional preservation of magmatic-related structures, and of fault and fracture networks over more than 40 km along strike (Fig. 3).

In the first part of the thesis (Chapters 1-2), I addressed the spatio-temporal evolution of the BFZ (Chapter 1) and characterized and quantified the along-strike architectural variability of the BFZ (Chapter 2), by using high-resolution geological surveys, analysis of satellite and drone images, construction of digital outcrop models and detailed microstructural and mineralogical investigations of the fault zone rocks. The BFZ is arranged into three main segments, has a sinuous crustal-scale geometry cutting through Jurassic to Early Cretaceous diorite and tonalite-granodiorite plutons. Ancient (125-118 Ma) seismic faulting, documented by pseudotachylytes, occurred at 5-7 km depth and ≤ 300 °C in a fluid-rich environment as recorded by extensive propylitic alteration and epidote-chlorite(-quartz-calcite) veining. In Chapter 1, I show that the sinuous crustal-scale geometry of the BFZ resulted from (i) exploitation of precursory geometrical anisotropies (i.e., magmatic foliation of plutons and dyke swarms) during fault nucleation and (ii) hard linkage of these anisotropy-pinned fault segments, through splay faults, during fault growth. In Chapter 2, I show that the BFZ architecture consists of hydrothermally altered multiple fault core strands, presenting pseudotachylytes, enveloped within a hydrothermally altered damage zone, which includes clusters of epidote-rich fault-vein networks and dilational breccias occurring at fault intersections and linkages. After describing the BFZ architecture, I compare it with presently active crustal fault zones and I discuss how the geodynamic setting played a first-order role in controlling (i) the pervasive fluid-rock interaction affecting the fault zone and (ii) the fluid-driven distributed seismicity occurring within the fault damage zone. The extensive hydrothermal fault-vein networks found in the fault damage zone motivated the following sections of the thesis, aiming at constraining the mechanics (Chapter 3) and the geochemical environment (Chapter 4) associated with the ancient fluid-driven seismicity.

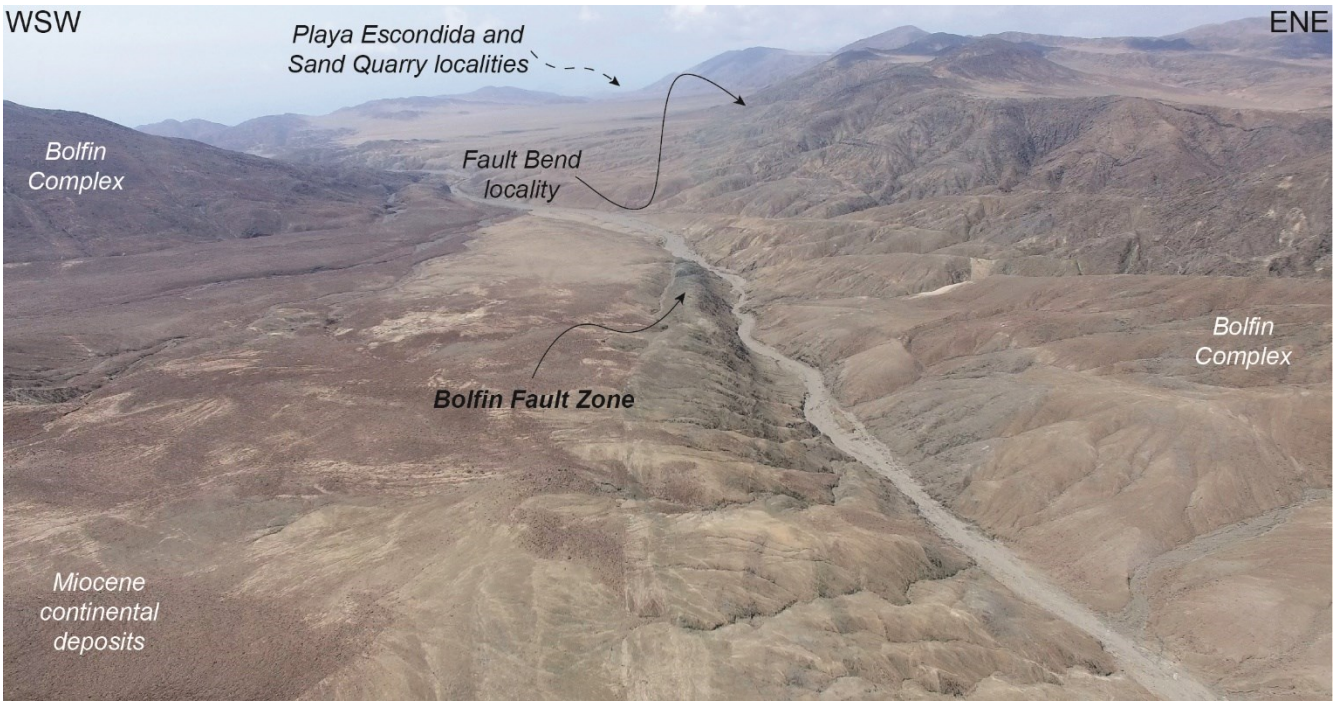

Fig. 3. The exceptional exposure of Bolfin Fault Zone in the Atacama Desert (Northern Chile). In this image collected with a drone (unmanned aerial vehicle imagery has been used systematically in the thesis), the fault zone is exposed over more than 10 km along strike.

Besides earthquake nucleation, propagation and arrest, fault zone architecture and its variability influence hydraulic behavior of faults. Indeed, fault zones can act as either barriers or conduits for migration of fluids in the Earth's crust, such as magma (e.g., active magmatism and volcanism along the Liquiñe-Ofqui Fault System and the Andean Transverse Faults, Southern Andean Volcanic Zone: Cembrano and Lara, 2009; Late Oligocene plutonism along the Periadriatic Fault System, Alps: Rosenberg, 2004), hydrothermal fluids (e.g., Mittempergher et al., 2014; Richards, 2013; Smeraglia et al., 2021; Tardani et al., 2016; Williams et al., 2005), hydrocarbons (e.g., Aydin, 2000; Grauls et al., 2002) and groundwater (e.g., Keegan-Treloar et al., 2022; Perrin and Luetscher, 2008). Fluids control fault mechanics by affecting mechanical and chemical processes during the seismic cycle (Scholz, 2019). Seismic ruptures propagating along faults allow transient increase of fault permeability promoting fluid flow (e.g., Cox, 2016; Micklethwaite et al., 2010; Sibson, 1985); on the other hand, interseismic fault sealing due to hydrothermal precipitation can promote regain of strength of ruptured fault segments and inhibit fluid flow (e.g., Cox and Munroe, 2016; Di Toro and Pennacchioni, 2005; Masoch et al., 2019). Transient increases of pore fluid pressure can however lead to seismicity by lowering the effective stress active on a fault and triggering earthquake nucleation ("Terzaghi effect": e.g., Cocco and Rice, 2002; Cox, 2010; Miller et al., 2004; Sibson, 1992). Moreover, fluid-rock interaction can facilitate mass transfer processes and mineral reaction, gradually modifying the composition and fabric of

fault rocks which in turn affect their mechanical and frictional properties (e.g., Gratier et al., 2011; Wintsch et al., 1995). As a result, the mechanical and hydraulic behavior of fault zones varies substantially through space and time are intrinsically coupled with each other (Caine et al., 1996; Chester and Logan, 1986; Faulkner et al., 2010).

Seismic faulting coupled with sustained fluid flow is often observed in active hydrothermal-magmatic systems (e.g., Yellowstone caldera, Wyoming: Shelly et al., 2013a; Long Valley Caldera, California: Shelly et al., 2016, 2015; Mount Rainer, Washington: Shelly et al., 2013b; Mineral Mountains, Utah: Mesimeri et al., 2021; West-Bohemia/Vogtland, Central and Western Europe: Fischer et al., 2014; Vavryčuk, 2002; Hakone caldera, Japan: Yukutake et al., 2011; Patagonian batholith, Southern Andes, Chile: Legrand et al., 2011), where the enhanced seismicity is mostly associated with swarm-like earthquake sequences (e.g., Fischer et al., 2014; Legrand et al., 2011; Shapiro, 2015; Shelly et al., 2022). Earthquake swarm-like sequences are characterized by clusters of low-in-magnitude seismic events without a characteristic mainshock that do not follow Omori's law of aftershocks (Mogi, 1963). Earthquake swarms have been thought to be triggered by pore fluid pressure transients in dense km-scale mesh-like dilatant fault-fracture networks (Fig. 4) (Hill, 1977; Sibson, 1996) and the associated seismic activity lasts from few days to months (e.g., Fischer et al., 2014; Legrand et al., 2011; Shelly et al., 2022). Similar human-induced sequences are associated with industrial fluid injection in boreholes (Ellsworth, 2013; Healy et al., 1968; Shapiro, 2015) and geothermal activities (e.g., Basel geothermal field; Deichmann et al., 2014). Despite progress in (i) monitoring and imaging evolution in space and time of swarm-like earthquake sequences (e.g., Fischer et al., 2014; Shelly et al., 2022) and (ii) scaling injected fluid volumes with seismic energy release through fluid-injection experiments (e.g., Dorbath et al., 2009; Guglielmi et al., 2015), to date, our knowledge from the geological record about the early evolution of a hydraulically mature, upper-crustal hydrothermal system (i.e., fluid-buffered environment with high fluid/rock ratio), capable to have generated earthquake swarms remains limited (Cox and Munroe, 2016; Dempsey et al., 2014; Sibson, 1996). Moreover, the source (e.g., magmatic, meteoric) of the hydrothermal fluids triggering seismicity in these high-flux fluid settings is still poorly constrained.

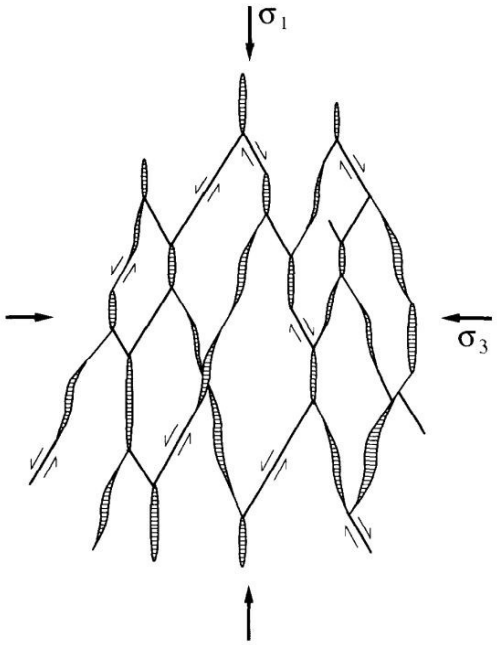

Fig. 4. Mesh-like fault-fracture model for earthquake swarms proposed by Hill (1977). The model includes interconnected shear, extensional and hybrid fractures. Modified from Hill (1977) and Sibson (1996).

In Chapter 3, I investigated selected samples of epidote-rich veins from the extensive epidote-rich fault-vein networks from the BFZ damage zone with the aim of unravelling how rocks may deform in an upper-crustal hydrothermal system. Thanks to high-resolution backscattered electron and cathodoluminescence imaging couple with electron backscattered diffraction analysis, I document that the proximal wall rock of small-displacements (< 1.5 m) sheared veins initially experienced a high-stress pulse, attested by deformation lamellae in magmatic quartz (e.g., Derez et al., 2015; Drury, 1993; Trepmann and Stöckhert, 2013) and instantaneous micro-fracturing healing in a rock-buffered (i.e., relatively low fluid/rock ratio) environment. Instead, the sheared veins associated with the conspicuous epidote deposition show mutually overprinting events of extensional veining and cataclasis in a fluid-buffered (i.e., relatively high fluid/rock ratio) environment. I discuss the complex deformation history recorded in the microstructures of the veins and the associated damaged wall rocks, proposing that they are possible evidences of ancient seismicity.

In Chapter 4, I investigated the origin of the fluids which interacted with the BFZ by using hydrogen isotope geochemistry, a tool sensitive to meteoric water (e.g., Sharp, 2007). Geological data support the hypothesis that the pseudotachylyte-bearing fault network was associated with mainshock-aftershocks earthquake sequences; instead, the extensive hydrothermal fault-vein networks was associated with swarm-

like earthquake sequences. I document that pseudotachylytes production occurred in a rock-buffered environment, characterized by limited, local fluid circulation (i.e., fluids with the same isotopic compositions of those of the magmatic wall rocks) similar to that found in other upper-crustal pseudotachylytes (Gole Larghe Fault Zone, Adamello batholith: Mittempergher et al., 2014; Homestake Shear Zone; Sawatch Range: Moecher and Sharp, 2004). Instead, the later fluid-driven seismicity attested by the extensive hydrothermal fault-vein systems was controlled by the ingression of surficial (i.e., near-surface-derived) fluids in a more mature, hydraulically connected, upper-crustal hydrothermal system. I discuss how the evolution of both the fault-fracture architecture and the geochemical environment (also evidenced by the fault zone rock assemblage), controls the transition from mainshock-aftershocks to swarm-like earthquake sequences.

Methods

1. Structural analysis

Field structural surveys along with remote sensing were performed to characterize the regional-scale pattern of tectonic lineaments (i.e., faults and shear zones) and dykes in the study area (analyzed area: 20 km wide, 50 km long). Remote sensing analysis was performed using satellite images (i.e., Sentinel-2, Google Earth and Bing) as reference maps coupled with published geological and structural maps (Cembrano et al., 2005; Domagala et al., 2016; González and Niemeyer, 2005). Six representative localities along the Bolfin Fault Zone and two along the Cerro Cristales Shear Zone were selected for detailed analysis. At each locality, we used a DJI Phantom 4 Pro drone to take nadir-directed aereophotographs. The images were processed in Agisoft Metashape Professional software to generate high-resolution georeferenced orthomosaics (spatial resolution of ~10 cm/pixel) used as base maps for the surveys at 1:300, 1:500 or 1:1000 scale. To describe the fault zone rocks, we make reference to the classification of Sibson (1977) and Woodcock and Mort (2008). The orientation and kinematics of the different structural elements (magmatic foliations, dykes, joints, faults, ductile shear zones and veins) were systematically measured. Structural maps and data were digitalized using ArcGIS© 10.6 and MOVE© software. Structural measurements were plotted onto stereonets (equal area, low hemisphere) using Stereonet 10 (Allmendinger et al., 2011; Cardozo and Allmendinger, 2013) and FaultKin 7 (Allmendinger et al., 2011; Marrett and Allmendinger, 1990). Further details regarding the definition of the different structural units forming the Bolfin Fault Zone and the quantification of veins and fault abundance are reported in the methodology section of each chapter.

2. Microstructural and mineralogical analysis

Oriented samples were collected for microanalytical investigations. Microstructural observations were conducted on polished thin sections oriented parallel to fault lineation and orthogonal to the fault surface and vein boundary. Transmitted-light optical microscopy was used to determine microstructural features at thin section scale and to identify areas suitable for microanalytical investigations.

Scanning electron microscopy (SEM) was performed with three instruments:

(i) a CamScan MX3000 equipped with backscattered electron (BSE) and semiquantitative energy dispersion spectroscopy (EDS) detectors, installed at Department of Geosciences of Università degli Studi di Padova (Uni. Padova);

(ii) a JOEL JSM-6500F (Field Emission Gun-SEM; FEG-SEM) equipped with high-resolution BSE and semiquantitative EDS detectors, installed at HP-HT laboratories of Istituto Nazionale di Geofisica e Vulcanologia (INGV) in Rome;

(iii) a Tescan Solaris (FEG-SEM) equipped with high-resolution BSE, cathodoluminescence (CL), electron backscattered diffraction (EBSD), and quantitative EDS and wavelength-dispersive spectroscopy (WDS) detectors, installed at Department of Geosciences (Uni. Padova).

Operating conditions of images and data acquisition, and details on EBSD data elaboration are reported at the methodology section of each chapter.

Optical microscopy CL (OM-CL) was applied to obtain information on chemical variations within hydrothermal veins and breccia. The OM-CL was employed using a Nikon microscope equipped with a Nikon camera working at 16-18 kV and 180-240 μA in a vacuum of 0.07-0.09 Torr, installed at Department of Geosciences (Uni. Padova).

Bulk mineralogy of rock samples was retrieved though X-ray powder diffraction (XRPD), and semiquantitative mineralogical composition were retrieved through Reference Intensity Ratio (XRPD-RIR) method. XRPD analyses were performed with a PANalytical X'Pert Pro diffractometer equipped with a Co radiation source, operating at 40 mA and 40 kV in the angular range of $3° < 2\theta < 85°$, installed at Department of Geosciences (Uni. Padova).

The composition of main mineral phases was obtained by electron wavelength-dispersive microprobe analysis (EMPA) and WDS-FEG analysis. EMPA investigations were performed with a JOEL-JXA8200 microprobe equipped with EDS-WDS (five spectrometers with twelve crystals), installed at INGV-Rome, and a Cameca SX50 microprobe, installed at Department of Geosciences (Uni. Padova). WDS-FEG investigations were performed with the Tescan Solaris, installed at Uni. Padova. Operating conditions of data acquisition are reported in the methodology section of each chapter.

3. Geothermobarometry

P-T conditions of high-temperature tectonites forming the Cerro Cristales Shear Zone were estimated using amphibole-plagioclase geothermobarometry. Pairs of amphibole and plagioclase grains in contact with each other to estimate the temperature and pressure of fabric development using the amphibole-plagiocalse NASi-CaAl exchange thermometer by Holland and Blundy (1994) and the empirical amphibole-plagioclase Si-Al partitioning barometer by Molina et al. (2015)

4. Hydrogen isotope analysis

Samples representative of the different structural elements pertaining of the Bolfin Fault Zone were selected for hydrogen isotopic analysis from the six localities along the fault. Hydrogen isotope ratios were measured on (i) hydrogen-bearing mineral phases separated from 700-μm-thick double polished thin sections through hand picking under the binocular microscope and (ii) powders of bulk chlorite-rich cataclasites, bulk pseudotachylytes, and bulk epidote-quartz-prehnite breccias. Manually separated hydrogen-bearing mineral phases are biotite from unaltered tonalites-granodiorites, amphibole from unaltered diorites, chloritized biotite from alteration halos associated with veins, epidote from epidote-rich veins and breccias, epidote from earlier vein fragments within epidote-prehnite-quartz breccias and epidote-prehnite-chlorite cement sealing the breccias. The samples were analyzed using a Flash 2000 Organic Elemental Analyzer in line with a Delta V Advantage Isotope Ratio Mass Spectroscopy (IRMS), installed at Dipartimento di Geochimica (Università degli Studi di Roma La Sapienza), following the method described by Sharp et al. (2001). Between 2 and 4 replicates of 1.0-1.5 mg of biotite and powders of cataclasites and pseudotachylytes, and 2.0-2.5 of amphibole, epidote and powders of hydrothermal breccias were analyzed per each sample, until a reproducibility of ±5‰ was obtained. The results the analyses are presented in the standard *delta* notation:

$$\delta = \left(\frac{R_x - R_{std}}{R_{std}}\right) * 1000$$

where *R* is the ratio of the abundance of the heavy to the light isotope, *x* denotes the sample and *std* the reference standard VSMOW (Vienna Standard Mean Ocean Water). The standards Bonsall biotite, LR151 biotite and LR8 amphibole were analyzed every series of 8-10 analyses, to correct for the apparatus drift, based on standard δD values of -59‰, -115‰ and -178‰, respectively.

Chapter 1

Structural evolution of a crustal-scale seismogenic fault in a magmatic arc: The Bolfin Fault Zone (Atacama Fault System)

This study was performed with the collaboration of Rodrigo Gomila, Michele Fondriest, Erik Jensen, Thomas Mitchell, Giorgio Pennacchioni, José Cembrano and Giulio Di Toro. I was assisted (but not continuously) in the field by Rodrigo Gomila, Michele Fondriest, Erik Jensen, Giorgio Pennacchioni, José Cembrano and Giulio Di Toro. I was assisted (but not continuously) during the remote sensing analysis by Rodrigo Gomila. I was assisted (but not continuously) during the microstructural analysis by Rodrigo Gomila, Michele Fondriest, Giorgio Pennacchioni and Giulio Di Toro. This chapter was published as the following paper: Masoch, S., Gomila, R., Fondriest, M., Jensen, E., Mitchell, T., Pennacchioni, G., Cembrano, J., Di Toro, G., 2021. Structural evolution of a crustal-scale seismogenic fault in a magmatic arc: The Bolfin Fault Zone (Atacama Fault System). Tectonics 40. https://doi.org/10.1029/2021TC006818 . All the authors discussed the data and agreed on their interpretation. I wrote the first version of the manuscript and all the co-authors contributed to its final version.

Abstract

How major crustal-scale seismogenic faults nucleate and evolve in crystalline basements represents a long-standing, but poorly understood, issue in structural geology and fault mechanics. Here, we address the spatio-temporal evolution of the Bolfin Fault Zone (BFZ), a >40-km-long exhumed seismogenic splay fault of the 1000-km-long strike-slip Atacama Fault System. The BFZ has a sinuous fault trace across the Mesozoic magmatic arc of the Coastal Cordillera (Northern Chile) and formed during the oblique subduction of the Aluk plate beneath the South American plate. Seismic faulting occurred at 5-7 km depth and ≤ 300 °C in a fluid-rich environment as recorded by extensive propylitic alteration and epidote-chlorite veining. Ancient (125-118 Ma) seismicity is attested by the widespread occurrence of pseudotachylytes. Field geological surveys indicate nucleation of the BFZ on precursory geometrical anisotropies represented by magmatic foliation of plutons (northern and central segments) and andesitic dyke swarms (southern segment) within the heterogeneous crystalline basement. Seismic faulting exploited the segments of precursory anisotropies that were optimally to favorably oriented with respect to the long-term far-stress field associated with the oblique ancient subduction. The large-scale sinuous geometry of the BFZ resulted from hard linkage of these anisotropy-pinned segments during fault growth.

1. Introduction

Most continental crustal deformation is localized into ductile shear zones and brittle, commonly seismogenic, faults (e.g., Snoke et al., 1998). The nucleation and evolution of brittle faults in the upper continental crust is associated with (i) formation of new fractures whose orientation is controlled by the regional or local stress field based on rock failure criteria (e.g., Anderson, 1951; Chemenda et al., 2016; Jaeger et al., 2009; Mandl, 1988; Naylor et al., 1986; Pennacchioni and Mancktelow, 2013; Swanson, 2006a, 1999a, 1999b; Woodcock, 1986), or (ii) exploitation of pre-existing structures (e.g., fractures, bedding, stratigraphic contacts, fold hinges and limbs, dykes, ductile shear zones, etc.: Crider, 2015; Crider and Peacock, 2004; d'Alessio and Martel, 2005; Davatzes and Aydin, 2003; Fondriest et al., 2020a, 2012; Mandl, 1988; Martel, 1990; Mittempergher et al., 2021; Nasseri et al., 1997, 2003; Pachell and Evans, 2002; Peacock and Sanderson, 1995; Pennacchioni et al., 2006; Segall and Pollard, 1983; Sibson, 1990; Smith et al., 2013; Swanson, 2006b, 1988; Sylvester, 1988). Geological and geophysical studies, rock analogue experiments and numerical models have highlighted that crustal-scale (i.e., tens of km-long) brittle faults commonly exploit exhumed mylonitic horizons in the crystalline basement (e.g., Balázs et al., 2018; Bellahsen and Daniel, 2005; Bistacchi et al., 2012, 2010; Butler et al., 2008; Collanega et al., 2019; Hodge et al., 2018; Holdsworth et al., 2011; Massironi et al., 2011; Naliboff et al., 2020; Phillips et al., 2019; Stewart et al., 2000; Storti et al., 2003; Sylvester, 1988; Wedmore et al., 2020; Whipp et al., 2014). Nevertheless, only a few contributions have attempted to evaluate the influence of precursory structures over crustal-scale faults (e.g., Bistacchi et al., 2010; Hodge et al., 2018; Wedmore et al., 2020). In particular, the influence of magmatic-related structures, such as magmatic foliation of ellipse-shaped plutons and dyke swarms, on fault nucleation and segmentation is poorly investigated. Moreover, the evolution in space and time of crustal-scale, *seismogenic* faults remains poorly known (e.g., Kirkpatrick et al., 2013; Perrin et al., 2016; Shigematsu et al., 2017; Williams et al., 2017). Indeed, moderate to large in magnitude (M >6) earthquakes rupture faults extending for >15 km in length, but such large faults are rarely well-exposed along their whole length at the surface due to weathering and vegetation or Quaternary cover. Major mature faults typically record a long, polyphase deformation history, which might obliterate the incipient stages of nucleation and growth (e.g., Rizza et al., 2019). Thus, the field geologists' challenge in studying ancient, crustal-scale seismogenic fault systems is to find large areas which meet the following criteria:

- excellent preservation over kilometer-scale exposures of the spatial arrangement of structures (e.g., joints, dykes and faults) related to multiple deformation stages;

- faults exhumed from depths (i.e., 5-15 km depending on tectonic regime, rock composition, temperature gradient, etc.; Scholz, 2019), where moderate to large in magnitude earthquakes nucleate in the continental crust;
- presence of tectonic pseudotachylytes (i.e., solidified frictional melts), unambiguous evidence of seismic slip in the rock record (Cowan, 1999; Rowe and Griffith, 2015; Sibson, 1975).

The sinistral strike-slip Atacama Fault System (AFS) in the Coastal Cordillera (Northern Chile; Fig. 1) (Arabasz, 1971; Cembrano et al., 2005; Scheuber and González, 1999), associated with the ancient subduction of the Aluk (Phoenix) plate beneath the South America plate, is well exposed along strike over more than 1000 km. The exceptional outcrop conditions result from the hyper-arid climate since 25-22 Ma (Dunai et al., 2005) and the slow erosion rates in the Atacama Desert. This makes the AFS an outstanding setting for studying the structural evolution of major faults hosted in the continental crust. Here we consider the Middle-Late Jurassic-Early Cretaceous sequence of magmatic, solid-state and brittle deformation that developed along the Northern Paposo segment of the AFS. Specifically, we consider the evolution of the >40-km-long seismogenic Bolfin Fault Zone (BFZ) and the large-scale syn- to post-magmatic Cerro Cristales Shear Zone (CCSZ) (Figs. 1-2). The study integrates (i) geological field mapping, (ii) analysis of satellite and drone images, and (iii) microstructural investigations of fault zone rocks and host rocks. We show that the large-scale sinuous geometry of the seismogenic BFZ is imposed by the local pinning of fault orientation on magmatic structures related to the precursory history of the magmatic arc. The BFZ was seismogenic, as attested by widespread occurrence of pseudotachylytes, and active at ambient temperatures of ≤ 300 °C and depths of 5-7 km in a fluid-rich environment. We conclude that magmatic-related structures, such as foliated plutons and dyke swarms, may partly control the nucleation, evolution and geometry of crustal-scale seismogenic faults.

Fig. 1. Tectonic setting of the Atacama Fault System (AFS) in the Coastal Cordillera (Atacama Desert, Northern Chile). (a) Crustal-scale geometry of the AFS with its three concave-shaped main segments. Shaded-relief image modified from Cembrano et al. (2005) and Veloso et al. (2015). Red box indicates the area shown in (b). The inset map shows the approximate plate configuration coeval with the Mesozoic sinistral strike-slip deformation along the AFS. Redrawn from Jaillard et al. (1990). (b) Simplified geological map of the Coastal Cordillera along the Paposo segment. Igneous lithologies are mapped with color coding by age. Unmapped areas represent metamorphic units and sedimentary covers. Data compiled and simplified from Cembrano et al. (2005), Domagala et al. (2016), González and Niemeyer (2005) and SERNAGEOMIN (2003). DTM base layer elaborated from USGS Aster GDEM database (https://earthexplorer.usgs.gov/) as base map. Red box indicates the studied area (Figs. 2-3).

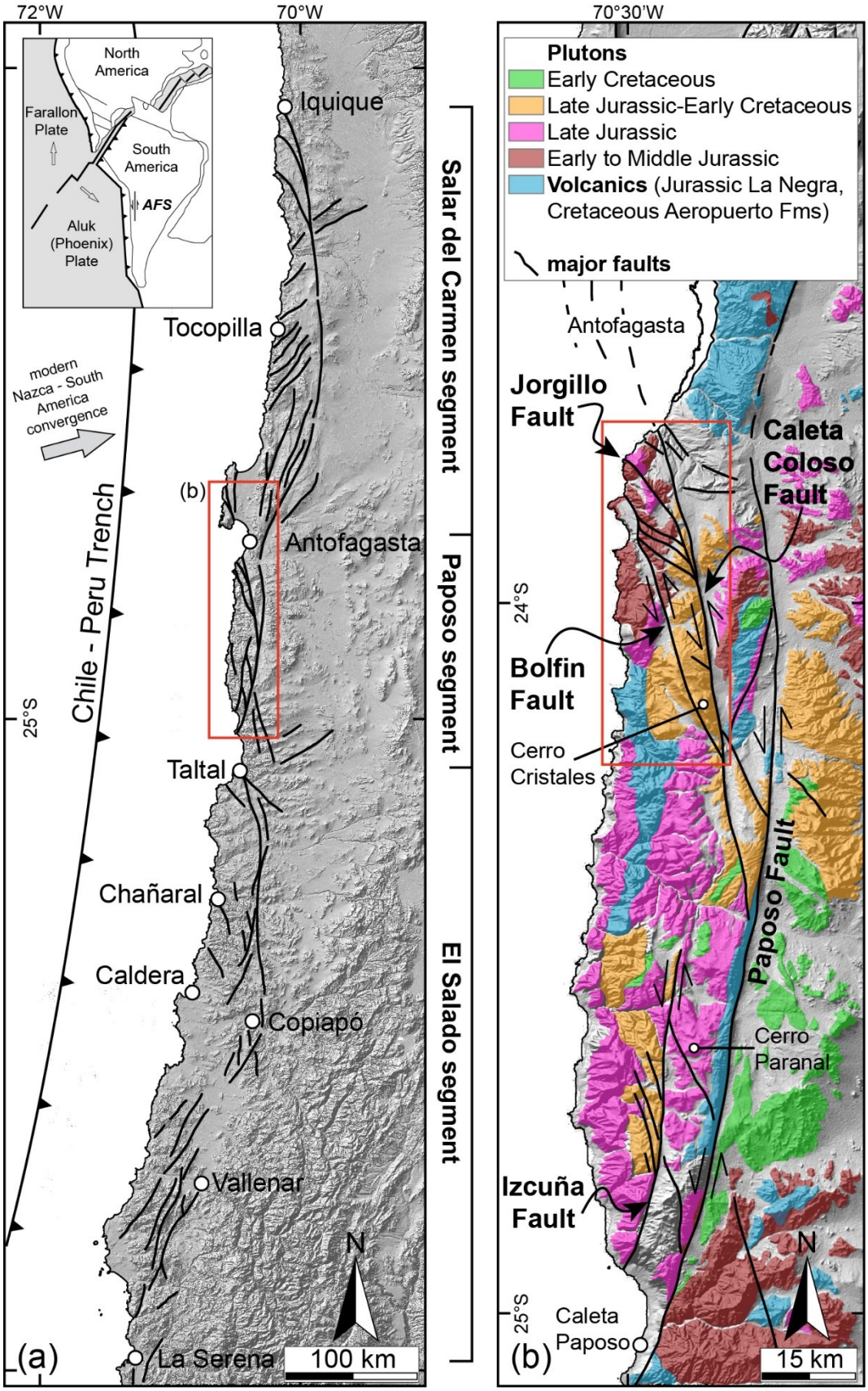

Fig. 1. Caption on previous page.

2. Geological setting

2.1. Coastal Cordillera

The Coastal Cordillera represents the Jurassic-Early Cretaceous continental magmatic arc, formed during oblique subduction of the Aluk (Phoenix) oceanic plate underneath the South America plate (inset in Fig. 1a) (Parada et al., 2007 and references therein). The magmatic arc is mainly composed of gabbro to granodiorite plutons and basaltic to andesitic volcanic rocks (La Negra Formation) (Fig. 1b). Mesozoic plutons are large, elongated (N-S) bodies intruded at middle to upper crustal levels within a Paleozoic metamorphic basement (Mejillones Metamorphic Complex and Chañaral Mélange) (Hervé et al., 2007 and references therein).

Since Middle-Late Jurassic, growth of the magmatic arc was associated with nearly arc-perpendicular crustal extension, under a Mariana-type subduction. This promoted the emplacement of large intrusions at shallow depth (Brown et al., 1993; Grocott et al., 1994; Grocott and Taylor, 2002; Scheuber and González, 1999). This stage is recorded by N-S trending extensional brittle faults and ductile shear zones, and homoclinal tilting of Jurassic La Negra Formation (Brown et al., 1993; Scheuber and González, 1999). During Late Jurassic-Early Cretaceous, intra-arc dextral transtension induced the emplacement of NE-striking andesitic dykes (Scheuber and González, 1999). Since Early Cretaceous, the Coastal Cordillera underwent intra-arc sinistral and sinistral transtensional deformation due to the SE-directed oblique subduction (Scheuber and González, 1999). This deformation stage is recorded by the emplacement of NW-striking andesitic dykes and the formation of the trench-parallel AFS (Scheuber and Andriessen, 1990; Scheuber and González, 1999).

2.2. Atacama Fault System (AFS)

The 1000-km-long AFS is the major crustal-scale, strike-slip fault system within the present-day forearc of the Central Andes (Fig. 1) (Arabasz, 1971; Brown et al., 1993; Cembrano et al., 2005; Scheuber and González, 1999). The AFS includes three main, curved segments (from north to south): (i) Salar del Carmen, (ii) Paposo and (iii) El Salado (Fig. 1a).

The AFS developed in Early Cretaceous accommodating intra-arc sinistral and sinistral transtensional deformation, once the axis of arc magmatism migrated eastwards (Scheuber et al., 1995; Scheuber and González, 1999). Brittle faults overprinted mylonites of similar kinematics and the age of ductile and brittle deformation varies along strike (Brown et al., 1993; Scheuber et al., 1995; Scheuber and González, 1999; Seymour et al., 2021, 2020). Along the Paposo segment, in the outer shell of the Cerro Paranal Pluton, syn-mylonitic hornblende and biotite yield $^{40}Ar/^{39}Ar$ and Rb-Sr ages in the range between 138 and 125 Ma

(Scheuber et al., 1995). Similar zircon U-Pb ages, referred to the onset of ductile deformation, were reported in the southern Paposo segment (~139 Ma; Ruthven et al., 2020). Brittle faulting was constrained between 125 and 118 Ma (Olivares et al., 2010; Scheuber and Andriessen, 1990). Extensional faulting along the AFS was reported during Miocene to post-Miocene in response to large magnitude subduction earthquakes (e.g., González et al., 2006, 2003).

2.3. Geology of the Bolfin area (23°45'S - 24°15'S)

The crystalline basement of the Bolfin area consists of (i) Early-Middle Jurassic meta-igneous Bolfin Complex, (ii) Late Jurassic plutons and (iii) Late Jurassic to Early Cretaceous Cerro Cristales Pluton, and (iv) volcanoclastic rocks of the La Negra Formation (Figs. 1b, 2, 3). The Bolfin Complex consists of diorites and gabbros, partially to completely recrystallized at amphibolite-granulite facies, metamorphic conditions (González and Niemeyer, 2005; Lucassen and Franz, 1994; Lucassen and Thirlwall, 1998).

The Cerro Cristales Pluton, formed by tonalite-granodiorite and diorite-quartz-diorite units (Domagala et al., 2016; González, 1999; González and Niemeyer, 2005), is a NNE-elongated body showing an outer shell of strongly foliated rocks (Figs. 2-3). The eastern and southern contact between the pluton and host rocks is marked by the large-scale CCSZ (González, 1999) (Fig. 2). According to González (1999), the CCSZ is a sinistral strike-slip ductile shear zone active at amphibolite-facies conditions, favoring and controlling the emplacement of the pluton. NW-striking syn-kinematic diorite and andesite dykes cut both the plutonic and volcanic rocks. These dykes represent the last magmatic event coeval with the formation of the AFS (Olivares et al., 2010; Scheuber and González, 1999).

Large-scale, sinistral strike-slip faults of the AFS cut through the crystalline rocks (Figs. 1-3). Some of the N-striking major faults and NW- to NNW-striking splay faults are hierarchically organized into strike-slip duplexes over a wide range of scales (Cembrano et al., 2005; Jensen et al., 2011; Veloso et al., 2015). Most of the splay faults accommodated displacements up to a few kilometers (Cembrano et al., 2005; Gomila et al., 2016; Mitchell and Faulkner, 2009). Brittle faulting occurred at 5-7 km depth at greenschist- to sub-greenschist-facies conditions (280-350 °C: Arancibia et al., 2014; Cembrano et al., 2005). Faulting developed chlorite-rich cataclasites, associated with pervasive syn-kinematic hydrothermal activity attested by the widespread occurrence of epidote- and chlorite-rich faults and veins (Arancibia et al., 2014; Cembrano et al., 2005; Herrera et al., 2005; Olivares et al., 2010). In our study, we focus on the chlorite-rich cataclastic rocks.

The BFZ is a third-order fault of the AFS bounding the kilometer-scale Caleta Coloso Duplex (Figs. 1b, 2, 3) (Cembrano et al., 2005; Herrera et al., 2005; Olivares et al., 2010). The Early Cretaceous strike-slip

structure of the BFZ was overprinted by Late Cenozoic extensional faulting. During this later stage, Miocene-to-Pliocene continental deposits were juxtaposed with chlorite-rich cataclasites of the BFZ fault core.

Fig. 2. Geological map of the Bolfin area and structural data from the two localities along the Cerro Cristales Shear Zone (CCSZ). Stereoplots (lower hemisphere, equal area) display (i) poles-to-planes (bold circles) of high-temperature foliation, magmatic foliation and aplite/pegmatite dykes and (ii) mineral stretching lineations (open circles) within high-temperature and magmatic foliations. In the stereoplots, the dashed line indicates the mean attitude of the CCSZ at each locality. The structural data of deformation stage 2, associated with the ductile reworking of dykes, are presented in Fig. 5c. Dashed black boxes indicate the locations of geological maps in Figs. 6-7.

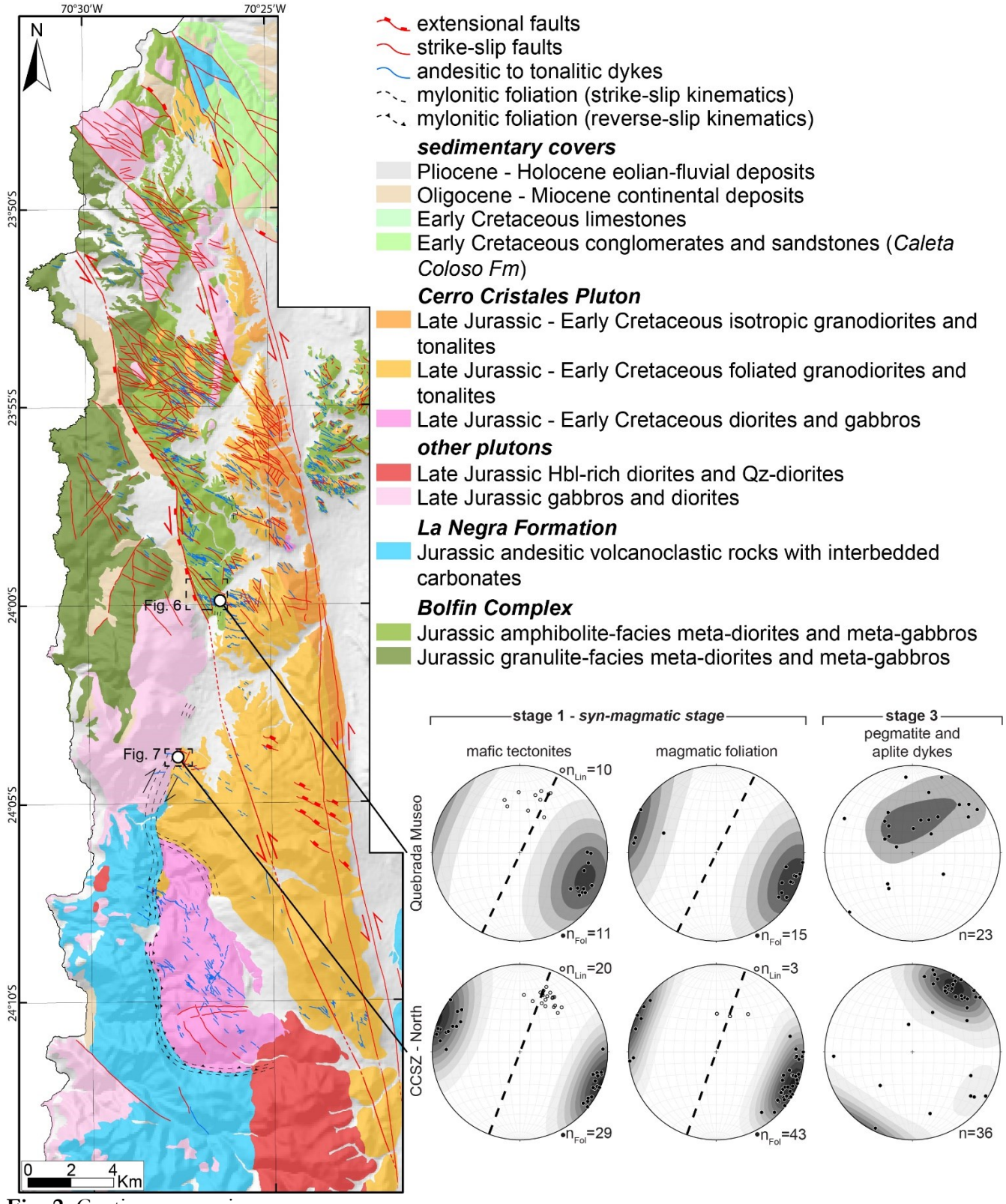

Fig. 2. Caption on previous page.

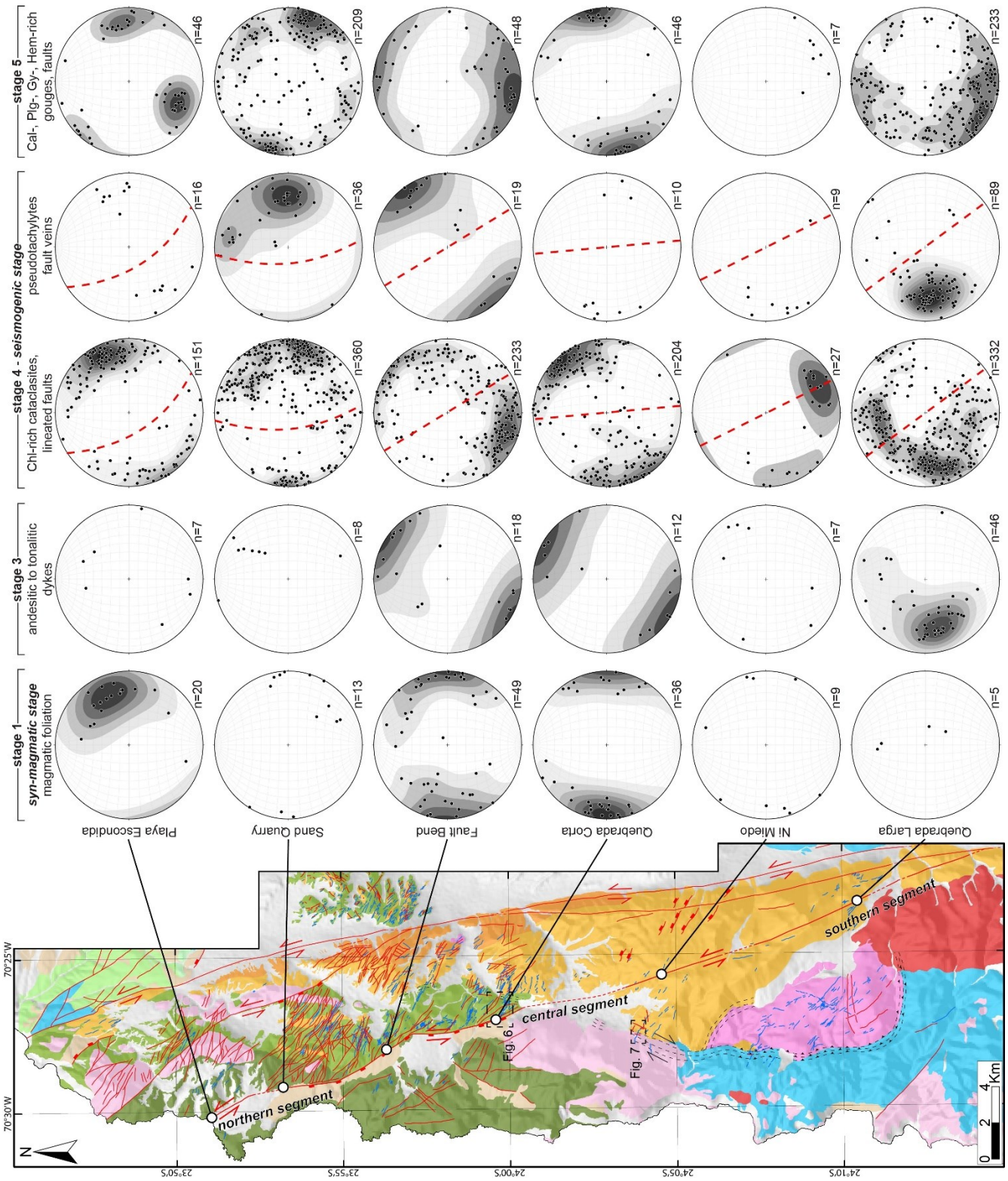

Fig. 3. Geological map of the Bolfin area and structural data from the six localities along the Bolfin Fault Zone (BFZ) divided by deformation stages (see Fig. 2 for the map legend). In the stereoplots (lower hemisphere, equal area), the dashed red line indicates the mean attitude of the fault core of the BFZ. Structural data of deformation stage 2, associated with the ductile reworking of dykes, are presented in Fig. 5c. Dashed black boxes indicate the locations of geological maps in Figs. 6-7.

3. Methods

Original field structural surveys along with remote sensing analysis were performed to characterize the regional-scale pattern of tectonic lineaments (i.e., faults and shear zones) and dykes in the study area (20 km wide, 50 km long). Remote sensing analysis was performed using satellite images (i.e., Sentinel-2, Google Earth and Bing) as reference maps coupled with published geological and structural maps (Cembrano et al., 2005; Domagala et al., 2016; González and Niemeyer, 2005). Six representative localities along the BFZ and two along the CCSZ were selected for a detailed analysis (Figs. 2-3). At each locality, we used a DJI Phantom 4 Pro drone to take nadir-directed aereophotographs. The images were processed in Agisoft Metashape Professional software to generate high-resolution georeferenced orthomosaics (spatial resolution of ~10 cm/pixel) used as base maps for the surveys at 1:300, 1:500 or 1:1000 scale. The orientation and kinematics of the different structural elements (magmatic foliations, dykes, joints, faults and ductile shear zones) were systematically measured and digitalized using ArcGIS 10.6 software. Structural measurements (n=2716) were plotted onto stereonets (equal area, low hemisphere) using Stereonet 10 (Allmendinger et al., 2011; Cardozo and Allmendinger, 2013).

Oriented rock samples (n=178) were collected for microanalytical investigations. Microstructural observations were conducted on polished thin sections (n=60) oriented parallel to the X kinematic direction (stretching lineation and slickenline in shear zones and faults, respectively) and orthogonal to the X-Y plane (shear zone boundary and fault plane). Transmitted-light optical microscopy (OM) was used to determine microstructural features at thin section scale and to identify areas suitable for microanalytical investigations. Scanning electron microscopy (SEM) was used to acquire high-resolution backscattered electron (BSE) images coupled with semiquantitative energy dispersion spectroscopy (EDS) elemental analysis. SEM and Field-emission SEM investigations were performed with a CamScan MX3000 operating at 25 kV at Department of Geosciences at Università degli Studi di Padova and a JOEL JSM-6500F operating at 15 kV at HP-HT laboratories of Istituto Nazionale di Geofisica e Vulcanologia (INGV) in Rome, respectively. Bulk mineralogy of rock samples was retrieved through X-ray powder diffraction (XRPD), and semiquantitative mineralogical composition were retrieved through Reference Intensity Ratio (XRPD-RIR) method. XRPD analyses were performed with a PANalytical X'Pert Pro diffractometer equipped with a Co radiation source, operating at 40 mA and 40 kV in the angular range $3° < 2\theta < 85°$, installed at Department of Geosciences (Padova). Mineral composition of main mineral phases was obtained by electron wavelength-dispersive microprobe analysis (EMPA). EMPA investigations were performed with a Joel-JXA8200 microprobe equipped with EDS-WDS (five spectrometers with twelve crystals), installed at INGV-Rome, and a Cameca SX50 microprobe, installed at Department of Geosciences (Padova). Data were collected using 15 kV as

accelerating voltage and 7.5 nA as beam current. A slightly defocused electron beam with a size of 5 μm was used, with a counting time of 5 s on background and 10 s on peak. Albite (Si, Al and Na), forsterite (Mg), pyrite (Fe), rutile (Ti), orthoclase (K) and apatite (Ca and P) were used as standards. Sodium and potassium were analyzed first to prevent alkali migration effects. The precision of the microprobes was measured through the analysis of well-characterized synthetic oxide and mineral secondary standards. Based on counting statistics, analytical uncertainties relative to their reported concentrations indicate that precision was better than 5% for all cations.

4. Field observations

We describe the spatial distribution and attitude data for magmatic, solid-state and brittle deformation structures for eight localities. Two localities are along the CCSZ, at the contact between the Cerro Cristales Pluton and either the meta-diorite of the Bolfin Complex (Quebrada Museo) or the Late Jurassic gabbro of the Cerro Mulato (CCSZ-North) (see locations in Fig. 2). Six localities are along the BFZ and are referred to as Playa Escondida, Sand Quarry, Fault Bend, Quebrada Corta (within the Bolfin Complex), Ni Miedo and Quebrada Larga (within the Cerro Cristales tonalite-granodiorite) (see locations in Fig. 3).

4.1. Dyke generations

Four generations of dykes were recognized based on their composition and crosscutting relationships (Fig. 4). From the oldest to the youngest they include:

(i) Amphibolitic dykes are composed of amphibole and minor plagioclase with grain size of up to 5 mm. The dykes, up to 50-cm-thick, have wavy boundaries or magma-mingling structures with the host rocks (Fig. 4a) and are commonly foliated. They strike preferentially NE-SW to NW-SE with moderate to sub-vertical dip angles (>45°) (Fig. 5a) and intrude both the plutonic rocks of the Bolfin Complex and of the Cerro Cristales Pluton, and the fault rocks of the CCSZ.

(ii) Leucocratic dykes are composed of plagioclase with minor amphibole with grain size up to 15 mm. The dykes, up to 50-cm-thick, exhibit sharp boundaries with the host rocks and commonly localized ductile (solid-state) shearing along their boundaries (Fig. 4b). The dykes are steeply dipping (>80°) and strike preferentially E-W; instead, a minor set strikes N-S (Fig. 5b).

(iii) Pegmatite and aplite dykes are widespread along both the CCSZ and the BFZ. These dykes are zoned (with K-feldspar margins and quartz-plagioclase-muscovite cores), have sharp boundaries with the host rocks, and do not show an internal ductile fabric (Fig. 4c-d). Pegmatites, up to ~50-cm-thick (Fig. 4c), are

arranged into two sets striking to NE and NW (the latter set is more pervasive) (Fig. 5d). Steeply dipping (>70°) pegmatites cut the CCSZ (Figs. 4c, 7). Aplites, up to 5-cm-thick (Fig. 4d), are arranged into three main sets, moderately to shallowly dipping towards NE, SW and SE (Figs. 4d, 5d). Pegmatites and aplites cut each other and cut the amphibolitic and leucocratic dykes (Figs. 4a, 4c-d).

(iv) Andesitic and tonalitic dykes have sharp contacts with the host rocks and do not show ductile internal deformation. The dyke contacts are locally exploited by brittle faults. The andesitic dykes, the most common dykes in the Bolfin area, have lengths up to several kilometers and widths up to ~3 meters (Figs. 6-8). The few tonalitic dykes have lengths up to hundreds of meters and widths up to 4 meters (Figs. 6-7). The andesitic dykes cut the CCSZ and are cut by the BFZ (Figs. 6-7). There are several sets of andesitic and tonalitic dykes (Fig. 5e). The steeply (>70°) and gently (< 60°) dipping NW-striking andesitic dykes cut: (i) the CCSZ, (ii) the pegmatite and aplite dykes, (iii) the NE-striking andesitic to tonalitic dykes, and (iv) the gently dipping (< 60°) NW-striking tonalitic dykes (at CCSZ-North, Fig. 7). Along the BFZ (in the Ni Miedo area, Fig. 3), the NW-striking tonalitic dykes cut the NE-striking andesitic to tonalitic dykes. In conclusion, the andesitic and tonalitic dyke cut each other and cut all the other generations of dykes.

Fig. 4. Dykes and syn-magmatic to post-magmatic high–temperature structures related to the tectono-magmatic evolution of the studied area (**deformation stages 1-3** or pre-Bolfin Fault Zone s.s.). (a) Dismembered amphibolitic dyke **(deformation stage 1**) within the foliated meta-diorites of the Bolfin Complex. The black amphibolitic dyke is cut by leucocratic (dashed black lines; **deformation stage 2**) and pegmatite dykes (solid lines; **deformation stage 3**). Lens cover for scale; cover width: 5.2 cm. WGS84 GPS location: 24.000489°S, 70.442743°W. (b) Paired ductile shear zone at the boundary of a leucocratic dyke within the meta-diorites of the Bolfin Complex (**deformation stage 2**). Dextral sense of shear. WGS84 GPS location: 23.999886°S, 70.444403°W. (c) Pink pegmatite dykes cutting the Cerro Cristales Shear Zone at CCSZ-North locality **(deformation stage 3**). WGS84 GPS location: 24.063805°S, 70.457332°W. (d) Shallow dipping aplite dykes (pink; **deformation stage 3**) cutting a dark grey amphibolitic dyke **(deformation stage 1**). Hammer for scale; height 33 cm. WGS84 GPS location: 24.000409°S, 70.443231°W. (e) Foliated meta-diorite of the Bolfin Complex close to the contact with the CCSZ at Quebrada Museo locality (**deformation stage 1**). Mafic enclaves define the magmatic foliation. Lens cover for scale. WGS84 GPS location: 23.9983694°S, 70.4409305°W. (f) Mafic tectonite of the CCSZ (**deformation stage 1**, Quebrada Museo locality). Sigmoidal amphiboles and sigma-type plagioclase porphyroclasts (white lines) indicate dextral sense of shear. XZ section. 1-euro coin for scale. WGS84 GPS location: 23.9967600°S, 70.4396600°W. (g) Foliated tonalite of the Cerro Cristales Pluton (**deformation stage 1**, CCSZ-North locality). The magmatic foliation is defined by asymmetric mafic microgranular enclaves (white lines) indicating dextral kinematics. Hammer for scale; head width: 18 cm. WGS84 GPS location: 24.062278°S, 70.456497°W. (h) Mafic tectonite along the CCSZ at CCSZ-North (**deformation stage 1**). Sigmoidal amphibole lenses and shear band boudins indicate dextral sense of shear. Nearly XZ section. 100-pesos coin for scale. WGS84 GPS location: 24.062922°S, 70.460754°W.

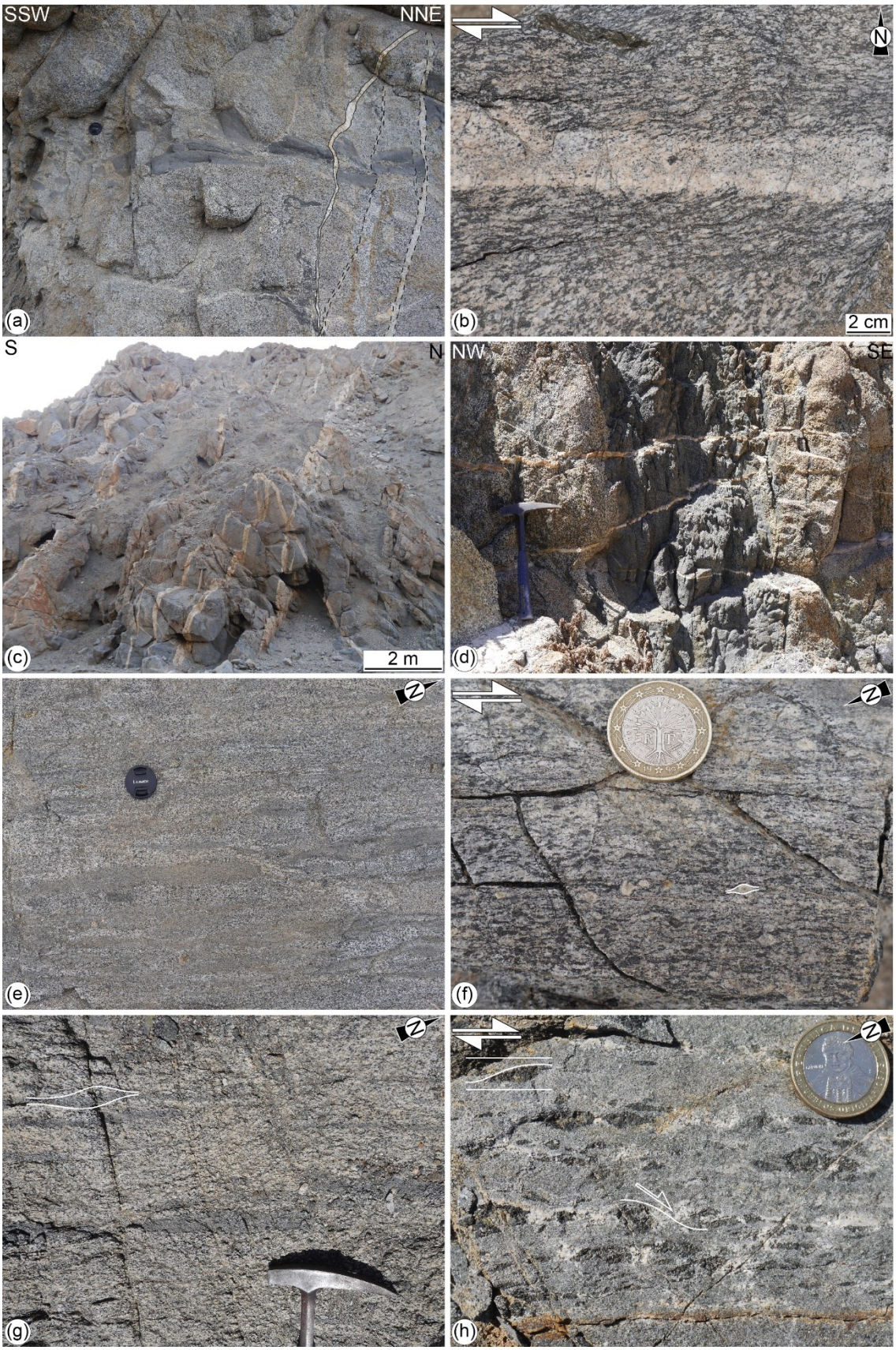

Fig. 4. Caption on previous page.

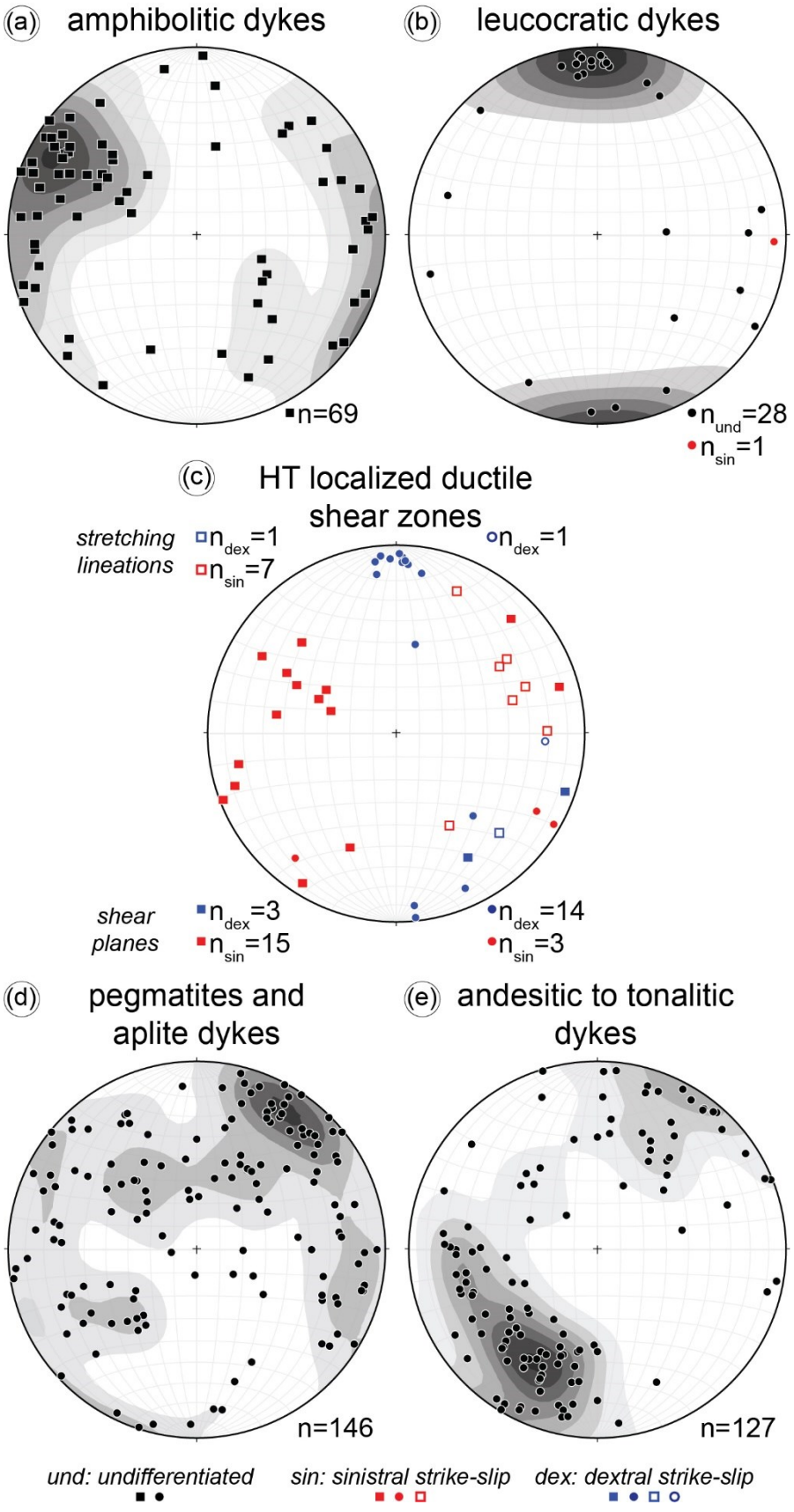

Fig. 5. Caption on next page.

Fig. 5. Lower hemisphere, equal area stereonets of poles to (a) amphibolitc dykes, (b) leucocratic dykes, (c) small-scale high-temperature ductile shear zones (associated with the **deformation stage 2**) exploiting the amphibolitic dykes (squares) and nucleating at the external boundaries of the leucocratic dykes (circles), (d) pegmatite and aplite dykes (cumulative stereographic plot) and (e) andesitic to tonalitic dykes (cumulative stereographic plot). The structural data are from all the eight studied localities along the Cerro Cristales Shear Zone (Fig. 2) and the Bolfin Fault zone (Fig. 3). Solid symbols indicate planes and shear planes, whereas open ones indicate mineral stretching lineations.

4.2. Magmatic and solid-state deformation

4.2.1. Cerro Cristales Shear Zone (CCSZ)

The CCSZ is a 30-km-long and up to ~600-m-thick shear zone bounding the eastern and southern sides of the ellipse-shaped Cerro Cristales Pluton (Fig. 2). The CCSZ mainly strikes NNE-SSW, bending towards E-W in its southern end (Fig. 2). At Quebrada Museo locality (Figs. 2, 6), the meta-diorite shows a steep (>75°) NNE-striking magmatic foliation defined by alignment of feldspar and amphibole crystals. The contact between the CCSZ and the Bolfin Complex is transitional and highlighted by a swarm of elongate mafic microgranular enclaves sub-parallel to the magmatic foliation (Fig. 4e). The CCSZ consists of strongly foliated and lineated high-grade rocks (hereafter referred to as mafic tectonites). The foliation of the mafic tectonites is steeply dipping (>80°) and parallel to the magmatic foliation with a prominent stretching lineation, marked by amphibole, plunging shallowly (< 30°) to NNE (Fig. 2). Kinematic indicators indicate dextral sense of shear (Fig. 4f).

At CCSZ-North locality (Figs. 2, 7), the Cerro Cristales tonalite is strongly foliated (Fig. 4g). The sub-vertical magmatic foliation, marked by alignment of euhedral plagioclase and amphibole crystals, strikes sub-vertically (>80°) NNE-SSW and is associated with a mineral lineation, marked by quartz aggregates, plunging shallowly toward NNE (Fig. 2). Close to the contact with the CCSZ, the presence of asymmetric mafic microgranular enclaves within the Cerro Cristales tonalite indicate a dextral sense of shear (Fig. 4g). The contact between the Cerro Cristales tonalite and the mafic tectonites of the CCSZ is sharp (Fig. 7). The mafic tectonites show the same structural features as observed at Quebrada Museo locality (Figs. 2, 4h).

4.2.2. Magmatic foliation along the Bolfin Fault Zone (BFZ)

The rocks of the Bolfin Complex and Cerro Cristales Pluton are foliated along most of the BFZ. The magmatic foliation is defined by the preferred alignment of plagioclase and amphibole crystals (Fig. 8), and by elongated mafic enclaves. From north to south (localities, geological maps and structural data in Fig. 3), the magmatic foliation:

- strikes N-S and dips steeply to the E (Bolfin Complex, Playa Escondida and Sand Quarry localities);

- strikes N-S and is sub-vertical (Bolfin Complex, Fault Bend locality);
- strikes N-S, is sub-vertical and ~4-km-long and ~300-m-wide (Bolfin Complex, Quebrada Corta area. Figs. 6, 8);
- strikes NW-SE to NNW-SSE and is sub-vertical (Cerro Cristales Pluton, Ni Miedo locality);
- is weak and scattered (the plutonic rocks are mainly isotropic), and strikes ENE-WSW with moderate to shallow dip angles (< 40°) towards S or NNW (Cerro Cristales Pluton, Quebrada Larga locality).

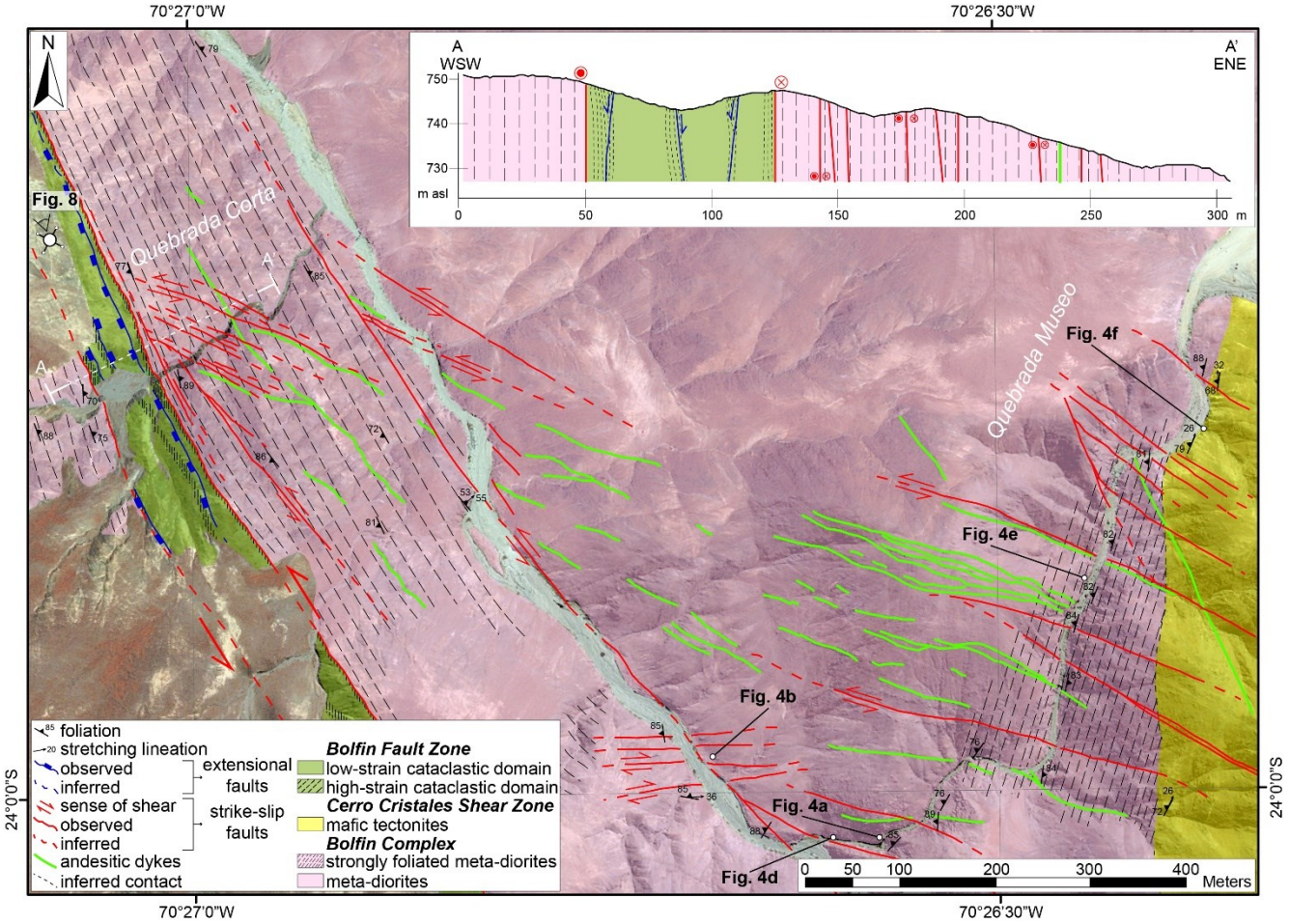

Fig. 6. Detailed geological map of Quebrada Corta and Quebrada Museo localities along the Bolfin Fault Zone and the Cerro Cristales Shear Zone, respectively, and geological cross-section across the Bolfin Fault Zone. The cross section is oriented N64°E (i.e., perpendicular to the fault core strike). The ~75-m-wide cataclastic fault core (i.e., low- and high-strain domains) of the BFZ overprints the well-developed sub-vertical magmatic foliation of the Jurassic meta-diorites belonging to the Bolfin Complex. The axes are in scale X:Y = 1:2 (i.e., vertical exaggeration of 2×). Google Earth imagery is used as base reference map. Coordinate reference system and projection are WGS84 UTM Zone 19S and Transverse Mercator, respectively. Unmapped areas represent Miocene to Quaternary continental deposits.

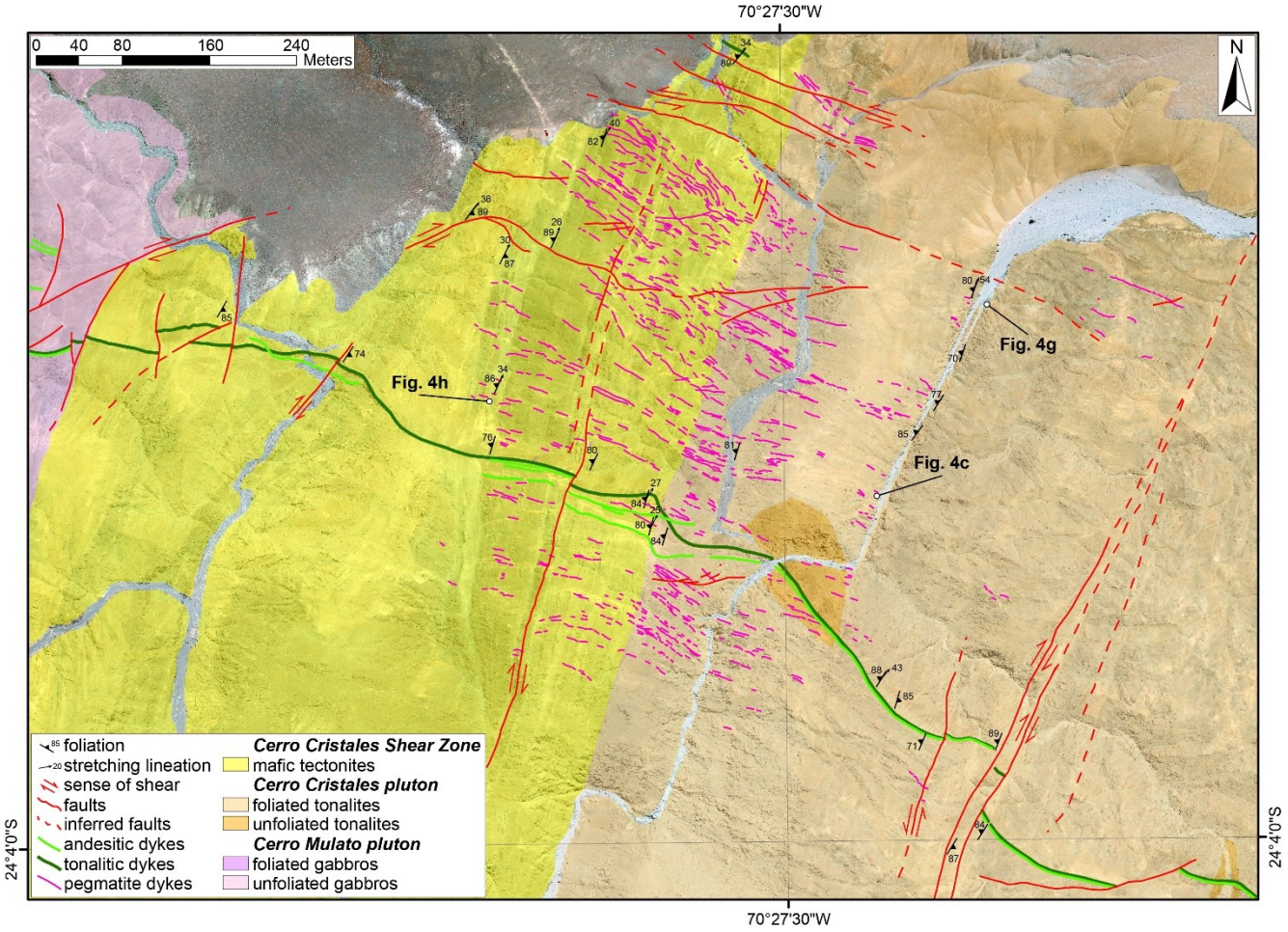

Fig. 7. Detailed geological map of CCSZ-North locality along the Cerro Cristales Shear Zone. Google Earth imagery as base reference map. Coordinate reference system and projection are WGS84 UTM Zone 19S and Transverse Mercator, respectively. Unmapped areas represent Miocene to Quaternary continental deposits.

4.2.3. Small-scale ductile shear zones

Small-scale (cm-dm thick) ductile shear zones are common in the studied area. Paired shear zones (*sensu* Pennacchioni and Mancktelow, 2018) flank sub-vertical leucocratic dykes in the Bolfin Complex (Fig. 4b). These strike-slip shear zones accommodated either dextral (E-striking set) or sinistral (N- to NW-striking set) displacement (Fig. 5c) of as much as 1 m. Some of the N- to NW-striking amphibolitic dykes localized sinistral, strike-slip ductile shearing (Fig. 5c) with development of internal S-C foliation and sigmoidal amphiboles.

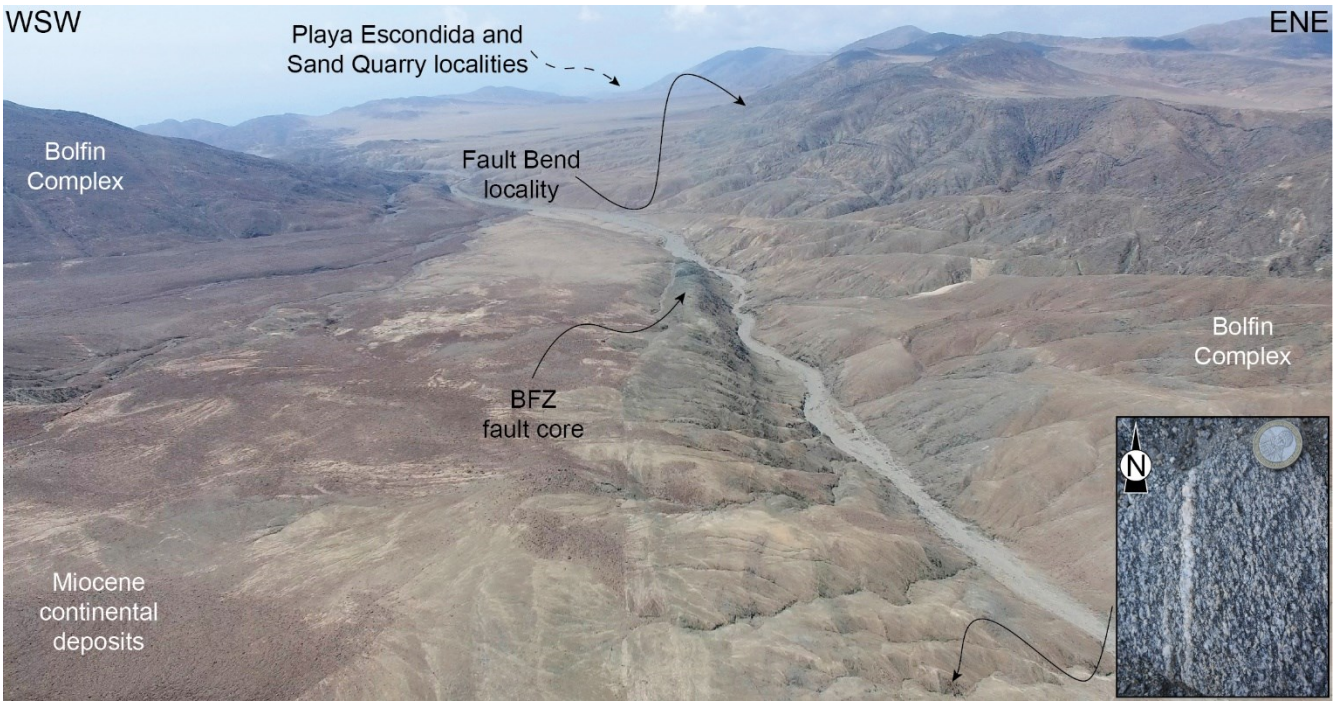

Fig. 8. The exceptional exposure of the Bolfin Fault Zone in the Atacama Desert. The BFZ fault core overprints the well-developed magmatic foliation of the meta-diorites of the Bolfin Complex along the central fault segment (see detail in the bottom right, for location see the black arrow) (drone photo taken to the north of Quebrada Corta locality, see Fig. 6).

4.3. Brittle deformation

4.3.1. Brittle overprint of the Cerro Cristales Shear Zone

At CCZS-North locality (Figs. 2, 7), brittle faults occur in two sets striking NNE and W-to-NW, respectively. The NNE-striking faults overprint the foliation of both the Cerro Cristales Pluton and the mafic tectonites of the CCSZ, and crosscut the NW-striking dykes (Fig. 7). The fault rocks consist of dark green, massive cataclasites bounding light green fault gouges, up to tens of centimeters thick. The few measured chlorite-bearing slickenlines in cataclasites are shallowly plunging to NNE. The presence of dykes offset by cataclasites indicate dextral strike-slip kinematics.

The W-to-NW-striking fault set dips gently (>45°) towards N to NE. This set consists of (i) dark green cataclasites and (ii) lineated fault surfaces. The cataclasites are commonly associated with brownish-colored pseudotachylytes, similar to those found along the BFZ s.s. (section 4.3.2). Riedel-type structures indicate dextral strike-slip kinematics. In contrast, the lineated fault surfaces show well-developed epidote-bearing slickenfibers indicating mainly normal dip-slip kinematics, with measured displacement of as much as 1 m. Locally, red-colored fault gouges exploit the W- to NW-striking faults. The fault gouges consist of

palygorskite, calcite, gypsum and hematite in variable modal proportions (XRPD-RIR analysis, section 5.3) and are associated with the Late Cenozoic extensional reactivation (section 4.3.3).

4.3.2. Bolfin Fault Zone sensu-strictu (BFZ s.s.)

The BFZ includes multiple fault core strands, up to 5-m-thick each, over a zone as wide as 75 m (Figs. 6, 8). The fault core strands (high-strain cataclastic domains) consist of dark green to black cataclasites and ultracataclasites (Figs. 6, 9a-c), transitionally or sharply bounding low-strain cataclastic domains of dark green protobreccias to protocataclasites, where the original magmatic fabric of the host rocks is still recognizable. Thin anastomosing bands of cataclasites are commonly observed within the low-strain domains. The cataclastic rocks are cemented by chlorite and minor epidote (section 5.2). The cataclasites and ultracataclasites are either massive or foliated with an S-C fabric indicating sinistral strike-slip kinematics (Fig. 9a-c). Exposed slickenlines are rare and plunge shallowly towards NNW to N. From north to south (localities, geological map and structural data in Fig. 3), the sinuous fault core of the BFZ:

- strikes ~NW-SE and dips towards SW sub-parallel to the magmatic foliation (Bolfin Complex, Playa Escondida locality);
- strikes N-S and dips towards W sub-parallel to the magmatic foliation (Bolfin Complex, Sand Quarry locality);
- bends from NNW-SSE to N-S, is sub-vertical (>80°) and partially overprints the magmatic foliation (Bolfin Complex, Fault Bend locality);
- strikes N-S, is sub-vertical and exploits the ~4-km-long magmatic foliation (Bolfin Complex, Quebrada Corta locality, Figs. 6, 8);
- strikes N-S, is sub-vertical and exploits the magmatic foliation (Cerro Cristales Pluton, Ni Miedo locality);
- is poorly exposed towards the fault linkage with the Caleta Coloso Fault (Cerro Cristales Pluton, Quebrada Larga locality).

Brittle deformation within the damage zone is accommodated by dark green cataclasites and sharp chlorite-bearing lineated slip surfaces. These structures are either oriented sub-parallel to the fault core or strike NW-SE. The latter correspond to Riedel-type and splay faults of the BFZ related to the large-scale Caleta Coloso Duplex (Cembrano et al., 2005). Steeply-dipping brittle-ductile shear zones with a composite S-C and S-C' foliation, indicating sinistral strike-slip kinematics, are discontinuously present within the BFZ

fault core (Fig. 9e). These foliated fault rocks are up to 1 m thick and make transition to both the green cataclasites of the fault core strands and the foliated damaged host rocks.

Pseudotachylyte veins (brownish to black in color and up to 2 cm in thickness) occur along the BFZ (Fig. 9b-d), especially in the fault core. The pseudotachylytes are polyphase and dismembered (Fig. 9d). In the Quebrada Larga locality, pseudotachylytes are common in subsidiary faults across the damage zone and decorate the contact between green cataclasites and NE- to E-dipping andesitic dykes (Fig. 9d). Here, pseudotachylyte reactivation is rare.

4.3.3. Cenozoic shallow extensional faulting

Fault gouges, discrete faults and calcite-bearing veins either exploit or cut the cataclasites both in the fault core and in the damage zone of the BFZ (Figs. 3, 9a, 9f) (see also Olivares et al., 2010). The fault gouges consist of palygorskite, calcite, halite, gypsum and hematite in variable modal proportions (Table 1), and show S-C composite foliations consistent with an extensional kinematics (Fig. 9f). The discrete faults have calcite- and hematite-bearing slickenlines and slickenfibers on the fault surface and occur in two sets: (i) a NW- to NNE-striking extensional to dextral-transtensional set, and (ii) an E- to ESE-striking, extensional to sinistral-transtensional set (Fig. 3).

Fig. 9. Brittle structures along the Bolfin Fault Zone (**deformation stages 4 and 5**). (a) Fault core section nearly orthogonal to fault strike. The fault core (~17-meter-wide) includes green chlorite-rich protocataclasites to ultracataclasites (**deformation stage 4**). To the left, the reddish, foliated fault gouge (**deformation stage 5**) overprints the chlorite-rich cataclasites (Sand Quarry locality) and puts in contact the Miocene continental deposits with the crystalline rocks. WGS84 GPS location: 23.8831611°S, 70.4880389°W. (b) Pseudotachylyte fault vein (fv) with cm in size injection vein (iv) intruding protobreccias and cataclasites of the fault core (**deformation stage 4**, Playa Escondida locality). 100-pesos coin for scale. WGS84 GPS location: 23.8498611°S, 70.5032555°W. (c) Massive green cataclasites at the fault core of the BFZ. Multiple generations of brown to black, dismembered and altered pseudotachylytes are found in the fault core (**deformation stage 4**, Ni Miedo locality). Hammer for scale; head width: 12 cm. WGS84 GPS location: 24.0796167°S, 70.4270750°W. (d) Brownish pseudotachylyte fault vein at the contact between an andesitic dyke and green cataclasite, and sketch (**deformation stage 4**, sample 19-98 from the damage zone at Quebrada Larga locality). WGS84 GPS location: 24.1732900°S, 70.3903500°W. (e) S-C and S-C' brittle-ductile shear zones spatially and kinematically (same sinistral strike-slip shear sense) associated with the BFZ fault core (**deformation stage 4**, Fault Bend locality). WGS84 GPS location: 23.9430930°S, 70.462819°W. (f) Red foliated fault gouge associated with the late Cenozoic extension exploiting and overprinting the chlorite-rich cataclasites within the BFZ core (**deformation stage 5**, Ni Miedo locality). 100-pesos coin for scale. WGS84 GPS location: 24.0744450°S, 70.4306630°W.

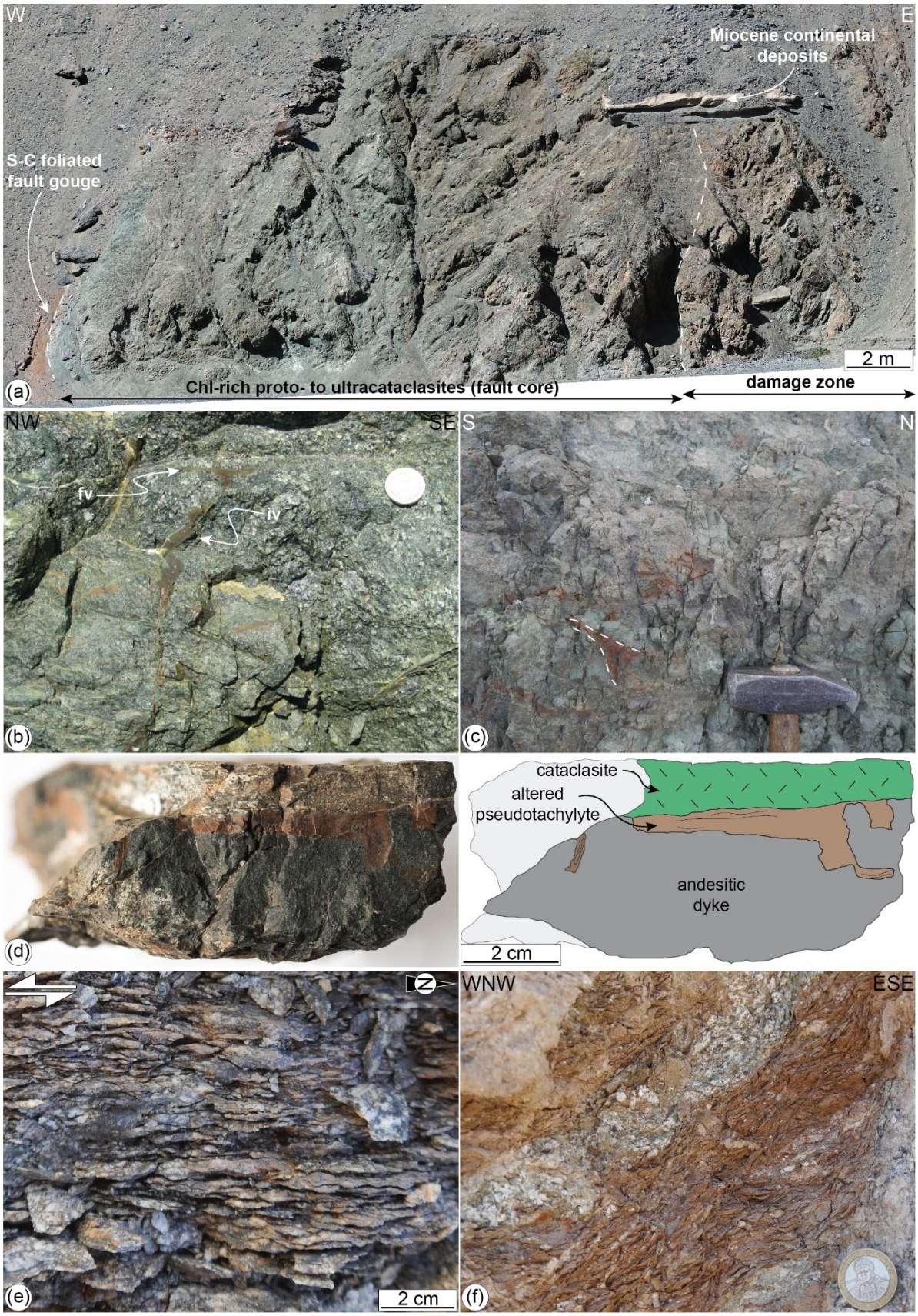

Fig. 9. Caption on previous page.

5. Microstructural observations

We describe the microstructures of the ductile and brittle features pertaining to the CCSZ and BFZ s.s.. The XRPD-RIR and EMPA analyses of the fault zone rocks and the mineral phases are reported in Tables 1 and 2, respectively.

5.1. Magmatic and solid-state deformation (T >700 °C)

Mafic tectonites forming the CCSZ consist of equigranular, polygonal aggregates of plagioclase and amphibole of ~150-250 μm grain size (Fig. 10a). Plagioclase ranges in composition between $Ab_{50}An_{50}Or_0$ and, more commonly, $Ab_{43}An_{56}Or_1$ (Table 2). Ilmenite is commonly present in the plagioclase aggregates at triple grain junctions and along grain boundaries (Fig. 10a). Plagioclase is locally replaced by oligoclase + calcite + sericite. Amphibole, mostly hornblende and minor edenite (Table 2), is locally replaced by chlorite. Plagioclase-amphibole geothermometry (Holland and Blundy, 1994b; Molina et al., 2015) yields T = 788±50 °C and P = 185±150 MPa for recrystallization.

Localized ductile shear zones bounding leucocratic dykes (Fig. 4b) have a homogeneous recrystallized polygonal matrix (~50 μm grain size) of plagioclase ($Ab_{67}An_{32}Or_1$), amphibole and magnetite wrapping around mm-sized amphibole and plagioclase ($Ab_{52}An_{47}Or_1$) porphyroclasts (Fig. 10b and Table 2).

5.2. Brittle seismogenic deformation (T ≤ 300 °C)

Damaged host rocks contain pervasive microfractures and veins whose spatial density increases towards to the fault core (seeGomila et al., 2016; Jensen et al., 2011; Mitchell and Faulkner, 2009 for description of nearby faults). Magmatic minerals present intense fluid-induced alteration. Plagioclase is either altered to fine-grained sericite + calcite ± epidote or replaced by albite (Table 2). Amphibole is replaced by either (Fe-)actinolite or chlorite and opaques. Biotite is replaced by chlorite and opaques. Quartz shows undulose extinction and K-feldspar is fractured and micro-faulted. Micro-stylolite seams are common in the damaged host rocks and are sub-parallel to the cataclasites.

Brittle-ductile shear zones consist of (i) microlithons of plagioclase (altered to fine-grained white mica + calcite or replaced by albite), (ii) high-strain horizons of quartz porphyroclasts immersed in a fine-grained (<20 μm grain size) recrystallized calcite matrix and (iii) calcite antitaxial extensional veins (Fig. 10c-d). Altered plagioclase microlithons are defined by micro-stylolite seams delineating a composite S-C and S-C' foliation (Fig. 10c). Quartz porphyroclasts (i) show undulose extinction, (ii) are locally recrystallized into fine-grained aggregates along grain boundaries and microfractures, and (iii) are surrounded by pressure shadows of fibrous calcite (i.e., strain fringe) (Fig. 10d). Antitaxial veins consist of fibrous calcite, which cut the

plagioclase microlithons and the high-strain horizons. The veins are orthogonal to the micro-stylolite seams and their spatial arrangement is consistent with sinistral strike-slip kinematics (Fig. 10c).

Cataclasites consist of fine-grained matrix of chlorite + epidote + quartz + albite + K-feldspar including angular clasts of altered plagioclase, quartz, and earlier cataclasites (Fig. 10e). Cataclasites are locally foliated and, in the thickest horizons, layered for variable matrix/clasts ratios.

Pseudotachylytes show typical features of quenched melts: chilled margins, flow structures, and presence of microlites and spherulites (e.g., Di Toro et al., 2009; Swanson, 1992). Alteration variably affected the pseudotachylytes. The most pristine pseudotachylytes have a homogeneous cryptocrystalline matrix with a "K-feldspar-rich" composition which contains (i) albite microlites, intergrown with amphibole and titanite (Fig. 10f), locally arranged into spherulitic aggregates and (ii) quartz and plagioclase clasts (Fig. 10f). Altered pseudotachylytes consist of fine-grained (~20-30 μm grain size) albite + chlorite + epidote ± K-feldspar association (Fig. 10g).

5.3. Brittle shallow extensional deformation (T < 150 °C)

In the reddish foliated fault gouges (Fig. 9f), the S-C fabric is marked by fine-grained palygorskite, clays and hematite, which wraps halite and gypsum mantled clasts (Fig. 10h). Halite mantled clasts are up to 1 mm in size and commonly fractured along cleavage planes. Gypsum clasts are up to ~200 μm in size and show undulose extension (Fig. 10h). Veins consist of either (i) blocky-shaped calcite grains or (ii) angular clasts of calcite sealed by microcrystalline calcite and minor opaque minerals. Calcite grains and clasts show thin (< 1 μm) and, locally, tabular thick (i.e., up to 10 μm) twin lamellae, classified as type I and type II twins, respectively, following the scheme of Ferrill et al. (2004).

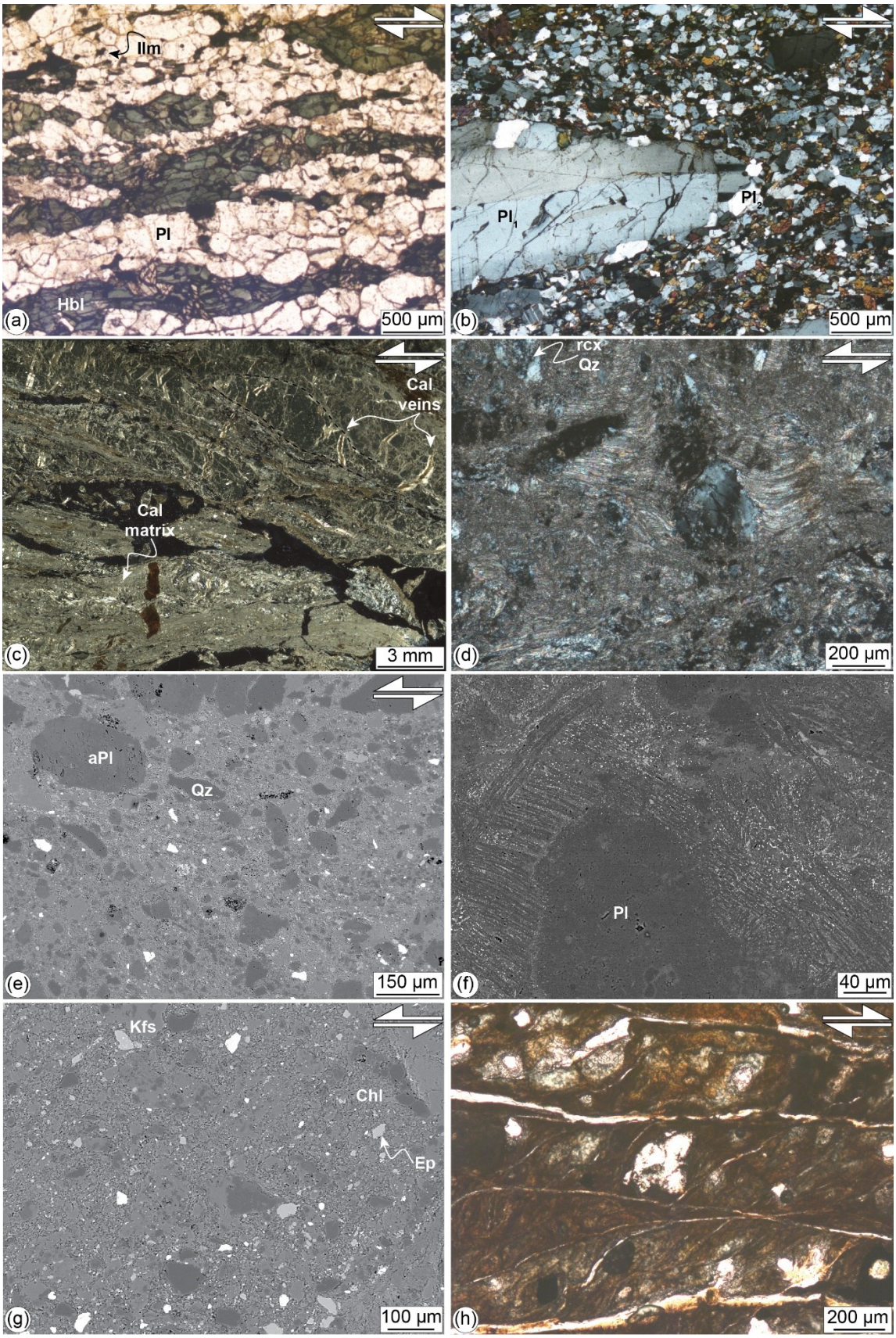

Fig. 10. Caption on next page.

Fig. 10. Microstructures of the fault zone rocks from the Bolfin area. Mineral abbreviations: Pl = plagioclase, aPl= altered plagioclase, Hbl = hornblende, Cal = calcite, Qz = quartz, rcx Qz = recrystallized quartz, Chl = chlorite, Ep = epidote, Ilm = ilmenite. (a) Polygonal aggregates of recrystallized hornblende and plagioclase forming the mafic tectonites of the CCSZ (**deformation stage 1**). Sigmoidal amphibole indicates dextral (top-to-SSW) sense of shear. Parallel-polarized light microphotograph, sample 19-25. WGS84 GPS location: 23.9966700°S, 70.4394900°W. (b) Localized ductile shear zone (**deformation stage 2**). Centimeter in size plagioclase porphyroclast (Pl_1) with undulose extinction shows mantle recrystallized into finer grained grains (Pl_2). The porphyroclast is hosted in fine-grained matrix including equigranular plagioclase and amphibole. Opaque mineral is magnetite present at triple grain junctions. Cross-polarized light microphotograph, sample B09-19. WGS84 GPS location: 23.99998°S, 70.444594°W. (c). Brittle-ductile shear zone with sinistral sense of shear (**deformation stage 4**). Microlithons consist of millimeter in size altered plagioclase (medium grey) delineated by micro-stylolite seams (dashed black lines). The latter define an S-C foliation indicating sinistral kinematics consistently with the orientation of the crack-seal calcite veins (Cal veins). High-strain horizons (light grey) consist of quartz porphyroclasts hosted in fine-grained matrix of calcite. Cross-polarized light thin section scan, sample FB20-676. WGS84 GPS location: 23.942990°S, 70.462819°W. (d). Strain fringes of fibrous calcite around a quartz porphyroclast. The fringe structure indicates sinistral strike-slip kinematics. The quartz porphyroclasts show undulose extension and are recrystallized into fine-grained aggregates along grain boundaries and micro-fractures. Cross-polarized light microphotograph, sample FB20-676. (e) Cataclasite from the BFZ (**deformation stage 4**). Clasts consist mainly of quartz and altered plagioclase. The light-gray matrix includes chlorite, epidote and K-feldspar. BSE-SEM image, sample 19-86. WGS84 GPS location: 24.1753100°S, 70.3901400°W. (f) Microlites of plagioclase (medium grey) and K-feldspar (dark grey), and interstitial acicular biotite and titanite (bright color) in a poorly altered pseudotachylyte fault vein (**deformation stage 4**). The microlites wrap a plagioclase clast with spinifex microstructure. BSE-SEM image, sample SQ09-18. WGS84 GPS location: 23.8830972°S, 70.4880111°W. (g). Altered pseudotachylyte (**deformation stage 4**). The pseudotachylyte fault vein is altered into a fine-grained chlorite, epidote, albite and K-feldspar. BSE image, sample 19-91A. WGS84 GPS location: 24.1747900°S, 70.3899600°W. (h) Fault gouge from the late Cenozoic faults (**deformation stage 5**). The gouge shows an S-C foliation, defined by palygorskite + clay + hematite, wrapping around halite clasts. Parallel-polarized light microphotograph, sample SQ13-18. WGS84 GPS location: 23.8830194°S, 70.4881222°W.

Locality	Rock type	Qz	Pl	Kfs	Amp	Act	Bt/Ms	Chl	Ep	Cal	Spl	Gp	Plg	Hl	Hem/Ant	Others
PE	Altered meta-diorite	15	36	4	28	3		13								
PE	Cataclasite	27	38			16	≤ 1	7	3	3						5(1)
PE	Cataclasite	39	35	2		≤ 1		12	3	4						3(1)
PE	Cataclasite	40	36	5				5	7	3						2(1)
PE	Foliated cataclasite	19	27	7		7		15	25							
PE	Fault gouge	7				≤ 1		≤ 1	11	39		14	20	6		
SQ	Altered meta-diorite	37	20	7		8		10	16							2(1)
SQ	Fault gouge	16	26	5		≤ 1		7	11	6		12	15	≤ 1		
SQ	Fault gouge							2	≤ 1	33		5	42	17		
SQ	Foliated fault gouge							5				≤ 1	75	19		
SQ	Fault gouge	10	49		12			4	6	19			≤ 1			
QC	Meta-diorite		67	4	9		7	7	5		≤ 1					≤ 1(2)
QC	Altered meta-diorite	8	52		19	11		9								≤ 1(2)
QC	Sheared amphibolitic dyke		26		55			14	2							4(3)
QC	Fault gouge	74				5		≤ 1	≤ 1	18						
QC	Fault gouge	46						2		49					3	
QC	Foliated fault gouge	36						16		8		16		3	3	18(4)
QL	Altered granodiorite	27	42	11		3	6	11								
QL	Foliated cataclasite	39	26	4			≤ 1	19	9	4						
QL	Foliated cataclasite	31	38	13			3	13		2						
QM	Mafic tectonites	≤ 1	43		44			8			3					
QM	Sheared amphibolitic dyke	≤ 1	35		52			9			3					

Table 1. Caption on next page.

Table 1. Modal composition of host rocks and fault zone rocks from XRPD-RIR semi-quantitative analysis. PE: Playa Escondida; SQ: Sand Quarry; QC: Quebrada Corta; QL: Quebrada Larga; QM: Quebrada Museo. Mineral abbreviations after (Whitney and Evans (2010). [(1)]: Tnt; [(2)]: Crd; [(3)]: Cpx; [(4):] Ilt.

Locality	**Quebrada Museo**													
Rock type	mafic tectonites						localized ductile shear zones							
Mineral phase	Pl		Amp		Ilm		Pl_1		Pl_2		Amp		Mag	
N° of point analysis	9	s.d.	9	s.d.	2	s.d.	3	s.d.	7	s.d.	13	s.d.	2	s.d.
component (wt%)														
Na_2O	5.27	0.31	1.14	0.24	0.08	0.03	5.93	0.13	7.42	0.17	0.84	0.47	0.03	0.00
MgO	0.09	0.04	13.09	0.49	0.23	0.01	0.06	0.03	0.16	0.21	11.71	1.87	0.20	0.01
Al_2O_3	29.05	0.56	9.03	0.83	0.14	0.05	27.66	0.18	25.44	0.53	5.71	2.43	0.08	0.00
SiO_2	54.23	0.66	45.51	1.12	0.06	0.00	56.01	0.29	59.39	0.34	48.12	3.34	0.08	0.03
K_2O	0.13	0.05	0.67	0.11	0.04	0.00	0.23	0.03	0.15	0.04	0.45	0.26	0.02	0.02
CaO	10.70	0.33	11.87	0.28	0.11	0.00	9.50	0.21	6.61	0.26	11.44	0.42	0.23	0.01
TiO_2	0.02	0.03	1.53	0.26	50.48	0.57	0.04	0.04	0.03	0.03	0.79	0.51	0.00	0.00
Cr_2O_3	0.02	0.03	0.03	0.03	0.08	0.00	0.01	0.02	0.02	0.02	0.03	0.03	0.08	0.01
MnO	0.02	0.02	0.29	0.08	4.00	0.12	0.01	0.01	0.04	0.04	0.53	0.08	0.07	0.04
FeO	0.24	0.07	13.96	0.54	44.53	0.50	0.16	0.07	0.26	0.24	18.02	1.96	92.28	1.21
Total	99.77	0.21	97.11	0.40	99.74	0.13	99.63	0.10	99.52	0.19	97.64	0.42	93.08	0.13
Locality	**Playa Escondida**													
Rock type	cataclasites						Pst with vesicles							
Mineral phase	Chl		Ep		Act		Ab matrix		Kfs matrix		Pl clasts		Amp microlites	
N° of point analysis	16	s.d.	3	s.d.	2	s.d.	3	s.d.	16	s.d.	3	s.d.	5	s.d.
component (wt%)														
Na_2O	0.02	0.03	0.00	0.01	0.18	0.03	7.56	0.38	1.52	0.96	8.32	0.54	1.85	0.39
MgO	15.03	0.53	0.02	0.01	17.37	0.07	0.09	0.10	0.41	0.29	0.08	0.02	8.62	2.73
Al_2O_3	19.56	0.78	21.65	0.23	2.68	1.61	24.39	0.39	17.90	1.01	23.67	0.51	13.55	1.83
SiO_2	26.55	0.79	37.33	0.26	53.16	2.48	60.14	0.31	64.86	1.94	63.10	0.86	47.23	4.86
K_2O	0.05	0.07	0.00	0.00	0.05	0.01	0.55	0.27	12.53	2.50	0.30	0.17	2.95	2.01
CaO	0.09	0.08	23.12	0.23	11.59	1.28	6.01	0.31	1.08	1.04	5.31	0.62	6.48	1.39
TiO_2	0.05	0.02	0.09	0.05	0.05	0.04	0.06	0.03	0.19	0.19	0.05	0.02	1.97	1.01
Cr_2O_3	0.02	0.02	0.02	0.02	0.02	0.00	0.00	0.00	0.01	0.02	0.00	0.00	0.00	0.00
MnO	0.48	0.05	0.13	0.05	0.32	0.04	0.02	0.01	0.03	0.03	0.03	0.03	0.34	0.10
FeO	26.17	0.58	14.27	0.18	12.22	1.23	0.64	0.43	1.34	0.74	0.37	0.07	14.34	3.38
Total	88.02	0.30	96.64	0.10	97.65	0.68	99.45	0.40	99.85	1.01	101.23	0.83	97.33	1.51
Locality	**Sand Quarry**										**Fault Bend**			
Rock type	vein cut by Pst		altered Pst								host rock		Pst	
Mineral phase	Chl		Chl		Ab microlites		Kfs matrix		Tnt		Chl		Ep	
N° of point analysis	7	s.d.	12	s.d.	49	s.d.	16	s.d.	5	s.d.	19	s.d.	6	s.d.
component (wt%)														
Na_2O	0.05	0.03	0.05	0.04	7.82	2.01	0.77	0.77	3.81	4.07	0.16	0.23	0.03	0.02
MgO	17.20	0.42	17.48	0.33	0.65	1.20	0.11	0.04	0.26	0.31	17.45	2.49	0.11	0.03

Al_2O_3	19.85	0.63	20.66	0.33	17.42	2.95	17.63	0.94	15.20	3.70	17.97	1.59	22.84	0.52
SiO_2	27.18	0.82	26.65	0.50	65.35	6.32	66.14	1.99	56.24	6.71	29.94	2.20	37.42	0.12
K_2O	0.02	0.01	0.03	0.02	2.24	1.92	14.97	1.60	6.86	5.04	0.50	0.66	0.02	0.01
CaO	0.15	0.08	0.10	0.04	2.03	1.61	0.18	0.31	7.11	5.70	0.73	1.15	22.92	0.18
TiO_2	0.05	0.03	0.06	0.04	0.62	1.62	0.02	0.03	8.09	7.52	0.88	1.02	0.09	0.07
Cr_2O_3	0.03	0.03	0.02	0.02	0.00	0.00	0.00	0.00	0.00	0.00	0.03	0.02	0.04	0.05
MnO	0.57	0.07	0.58	0.04	0.04	0.05	0.02	0.03	0.04	0.02	0.46	0.09	0.24	0.06
FeO	23.58	1.08	23.05	0.38	3.50	2.19	0.25	0.19	2.00	2.30	21.13	2.82	13.65	0.55
Total	88.68	0.76	88.68	0.58	99.68	1.99	100.10	1.39	99.62	3.54	89.24	1.17	97.34	0.25
Locality	**Fault Bend**		**Quebrada Corta**						**Quebrada Larga**					
Rock type	Pst		host rock		cataclasites		vein cut by Pst		host rock					
Mineral phase	Chl		Pl		Chl		Chl		Amp		Bt		Chl	
N° of point analysis	12	s.d.	2	s.d.	3	s.d.	8	s.d.	3	s.d.	20	s.d.	28	s.d.
component (wt%)														
Na_2O	0.04	0.02	8.65	0.14	0.04	0.03	0.09	0.12	0.47	0.03	0.09	0.05	0.07	0.05
MgO	17.75	1.20	0.13	0.06	18.46	0.15	19.00	1.25	13.08	0.41	11.09	2.21	15.38	2.27
Al_2O_3	20.99	0.68	23.64	0.42	18.59	0.08	17.43	0.92	4.24	0.47	15.63	3.21	17.53	3.10
SiO_2	26.39	0.88	62.89	1.06	28.98	0.29	30.00	1.33	50.13	0.45	35.95	2.25	30.63	3.45
K_2O	0.05	0.04	0.20	0.07	0.06	0.01	0.05	0.03	0.29	0.08	8.18	1.86	2.23	2.43
CaO	0.15	0.05	4.02	0.40	0.38	0.18	0.58	0.48	11.64	0.32	0.24	0.43	0.48	1.06
TiO_2	0.07	0.04	0.01	0.01	0.40	0.24	0.13	0.09	0.27	0.13	3.04	0.90	1.39	1.63
Cr_2O_3	0.02	0.02	0.06	0.03	0.07	0.02	0.03	0.03	0.02	0.01	0.04	0.04	0.03	0.03
MnO	0.46	0.07	0.00	0.00	0.47	0.01	0.50	0.09	0.64	0.01	0.42	0.09	0.50	0.13
FeO	22.42	1.61	0.30	0.07	20.92	0.52	20.67	1.24	15.79	0.31	20.02	3.58	21.17	1.84
Total	88.34	0.86	99.89	0.22	88.37	0.08	88.48	0.63	96.58	0.35	94.70	1.91	89.42	1.56

Locality	**Quebrada Larga**							
Rock type	cataclasites				altered Pst			
Mineral phase	Act		Chl		Kfs matrix		Chl	
N° of point analysis	3	s.d.	13	s.d.	13	s.d.	8	s.d.
component (wt%)								
Na_2O	0.31	0.13	0.07	0.05	0.61	0.39	0.04	0.03
MgO	13.15	0.97	16.15	1.87	0.11	0.07	15.65	0.85
Al_2O_3	3.16	0.64	17.55	2.63	19.06	0.26	22.31	0.80
SiO_2	51.61	1.49	30.05	2.82	63.99	0.31	26.76	1.15
K_2O	0.18	0.07	1.29	1.42	16.22	0.71	0.43	0.65
CaO	12.02	0.49	0.72	1.45	0.06	0.10	0.13	0.03
TiO_2	0.09	0.05	1.08	1.63	0.06	0.03	0.14	0.06
Cr_2O_3	0.03	0.04	0.03	0.03	0.04	0.04	0.04	0.03
MnO	0.72	0.11	0.47	0.11	0.02	0.03	0.63	0.07
FeO	16.00	0.86	20.88	2.03	0.32	0.13	22.54	1.05
Total	97.27	1.47	88.29	0.63	100.47	0.21	88.68	1.02

Table 2. Mineral phase compositions of host rocks and fault zone rocks as obtained from EMPA analysis. Pst: pseudotachylytes. Mineral abbreviation after Whitney and Evans (2010).

6. Discussion

Firstly (section 6.1), we discuss the field and microstructural observations (sections 4-5) that allow us to constrain the P-T deformation conditions and to recognize a sequence of five main deformation stages. This information is required to interpret the formation of the seismogenic Bolfin Fault Zone *sensu strictu* (125-118 Ma). Then (section 6.2), we discuss the role of precursory structures on the evolution of the BFZ s.s. and we propose a more general model of fault growth within a heterogeneous magmatic arc.

6.1. P-T deformation conditions and structural evolution of the Bolfin Fault Zone

The BFZ experienced a polyphase evolution that includes magmatic and solid-state deformation episodes (stages 1-2), followed by the emplacement of multiple generations of dykes (stage 3). This predated the Early Cretaceous brittle seismogenic strike-slip faulting (stage 4) and the late Cenozoic extensional faulting (stage 5). The whole evolution is summarized in the block diagrams of Fig. 11.

Fig. 11. Block diagrams showing the structural evolution of the Bolfin Fault Zone (left column) and features related to each deformation stage (right column). The stress field orientation was inferred from (i) the orientation of dykes and (ii) the kinematics of ductile shear zones and faults. (a) **Deformation stage 1**: emplacement of the Cerro Cristales Pluton at shallow crustal levels (< 10 km depth); formation of the large-scale syn- to post-magmatic Cerro Cristales Shear Zone; emplacement of amphibolitic dykes during late-magmatic stage. (b) **Deformation stage 2**: emplacement of leucocratic dykes and development of high-temperature (>700 °C) localized solid-state ductile shear zones at early stage of pluton cooling. The ductile shear zones are arranged into a conjugate set (E-W dextral strike-slip, and N-S to NW-SE sinistral strike-slip). (c) **Deformation stage 3**: emplacement of steeply-dipping NE- and NW-striking pegmatite and andesite/tonalite dykes. The emplacement of these dykes suggests a mutual switch of the orientation of the maximum (σ_1) and minimum (σ_3) shortening directions. See main text for discussion. (d) **Deformation stage 4:** Bolfin Fault Zone s.s.. The ancient (125-118 Ma) seismic activity of the BFZ is documented by widespread pseudotachylytes. Seismic faulting occurred at ≤ 300 °C and 5-7 km depth in a fluid-rich environment. (e) **Deformation stage 5**: Since the Miocene, the BFZ underwent extensional faulting at shallow crustal levels (< 2-3 km depth).

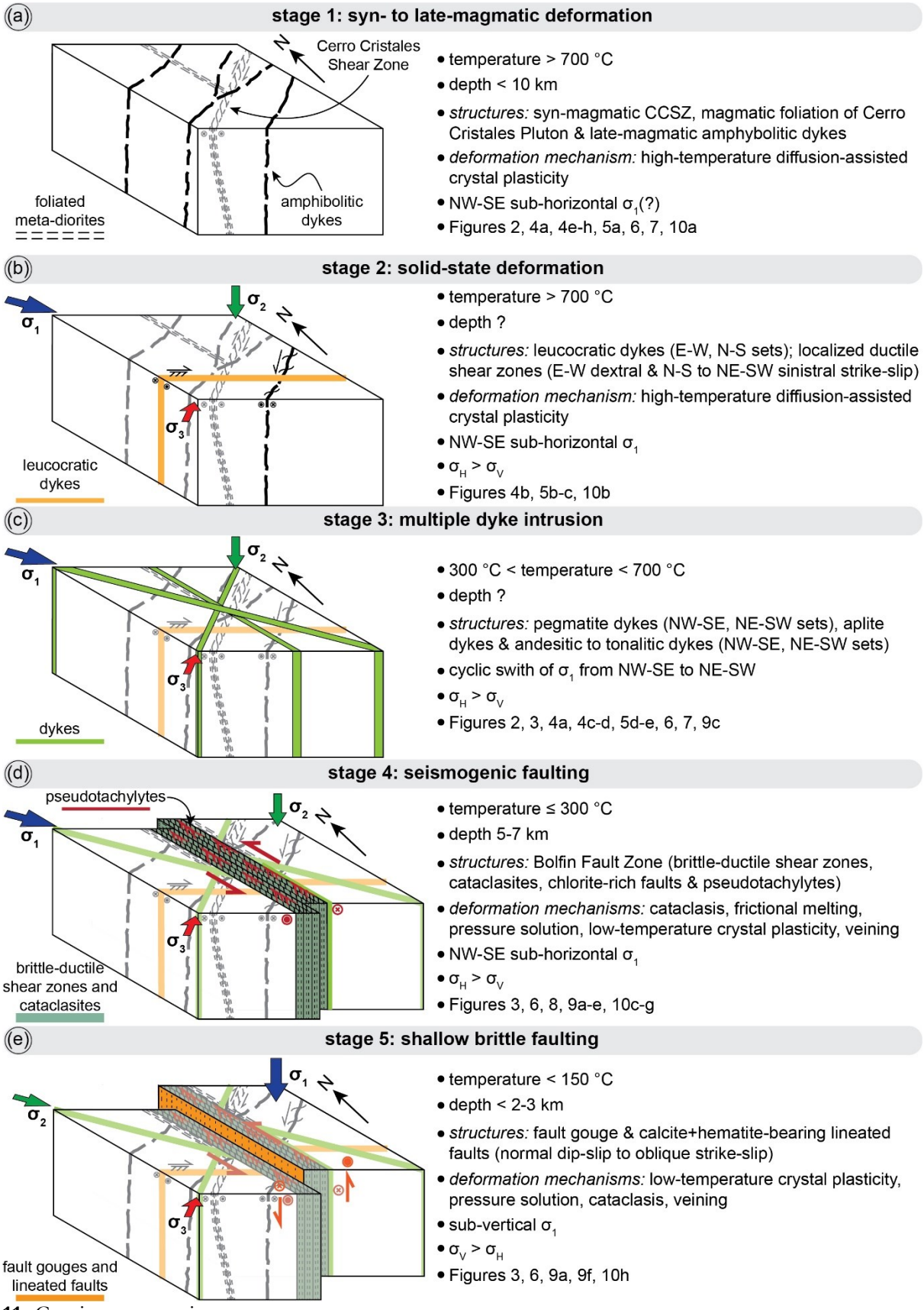

Fig. 11. Caption on previous page.

6.1.1. Stages 1 to 3: Pre-Bolfin Fault Zone s.s. (T > 300 °C)

6.1.1.1. Stages 1 to 2: Syn-magmatic to solid-state deformation (T > 700 °C)

Stage 1 (Syn- to late-magmatic deformation). Along the CCSZ, the orientation of the magmatic and solid-state foliations and of the stretching lineations are similar (Fig. 2). These structural features are characteristic of syn-magmatic thermal aureoles related to pluton emplacement (Clemens, 1998; Miller and Paterson, 1999; Paterson and Vernon, 1995 and references therein). At CCSZ-North locality, dextral strike-slip shearing in the mafic tectonites is spatially associated with melt segregation structures (Fig. 4h) (e.g., Sawyer, 2000; Weinberg, 2006). This indicates that shearing accommodated by the CCSZ initiated during crystallization of the Cerro Cristales Pluton (T > 700 °C) as also supported by the high-temperature conditions (788±50 °C) estimated for the recrystallized matrix of the mafic tectonites.

Based on our observations, we interpret the CCSZ as large-scale syn- to post-magmatic shear zone related to the emplacement of the Cerro Cristales Pluton and the pervasive magmatic foliation of the outer shell of the pluton related to magma inflation/ballooning. Additionally, the dextral slip of the CCSZ may result from the local stress perturbation induced by the pluton emplacement, which possibly perturbed, at least locally, the regional far-stress field associated with the ancient SE-directed oblique subduction (Scheuber and González, 1999). González (1999) estimated an emplacement depth of ~13 km (400 MPa) for the Cerro Cristales Pluton, based on hornblende geobarometry and assuming a geothermal gradient of 30 °C/km. Instead, assuming a geothermal gradient of ~50 °C/km, typical of an active magmatic arc (e.g., the Southern Andes Volcanic Zone: Pearce et al., 2020; Sielfeld et al., 2019) and considering the estimated pressure (185±150 MPa) for recrystallized matrix of the mafic tectonites, the emplacement depth of the pluton results at < 10 km depth, as for plutons of similar age (140-155 Ma) emplaced along the El Salado segment of the AFS (Espinoza et al., 2014; Grocott and Taylor, 2002; Seymour et al., 2020). Moreover, the emplacement of several plutons in a short time span thermally weakens the crust facilitating pluton emplacement at shallow depths (Cao et al., 2016). We conclude that the CCSZ started forming at >700 °C and < 10 km depth during the emplacement of the Cerro Cristales Pluton (Fig. 11a). The Bolfin Complex and the Cerro Cristales Pluton are intruded by the amphibolitic dykes, which cut also the CCSZ. These dykes show mingling structures and evidence of remelting, indicating that they intruded in a still partly molten material during a late-magmatic deformation stage (Figs. 4a, 11a).

Stage 2 (Solid-state deformation). Solid-state deformation is recorded by the meso-scale paired ductile shear zones (*sensu* Pennacchioni and Mancktelow, 2018) flanking leucocratic dykes (Fig. 4b). Discrete ductile shear zones nucleated on compositional and structural precursors are widely reported in several granitoid plutons and meta-granitoids in metamorphic units elsewhere (e.g., Christiansen and Pollard, 1997;

Pennacchioni, 2005; Pennacchioni and Zucchi, 2013; Segall and Simpson, 1986). These localized shear zones have similar microstructural features of the mafic tectonites forming the CCSZ (Fig. 10b) and are inferred to have developed during the earliest cooling stages of the plutons.

The dextral, E-striking ductile shear zones and the sinistral, N-to-NE-striking sheared amphibolitic dykes are arranged to form a conjugate set (Fig. 5c) associated with a sub-horizontal NW-SE compressional direction (i.e., σ_1) (Fig. 11b). This σ_1 is consistent with the SE-directed oblique subduction recorded in the Coastal Cordillera (Scheuber and González, 1999; Veloso et al., 2015).

Scheuber and González (1999) reported localized ductile shear zones formed at greenschist-facies metamorphic conditions, which is not consistent with the high-temperature conditions determined for the localized shear zones described here. The absence (or very scarce occurrence) of greenschist-facies localized ductile shear zones can be explained by the fast eastward migration of the magmatic arc, rapid regional-scale exhumation and the shallow emplacement depth of plutons (< 10 km depth). This likely promoted a sharp transition from high-temperature, ductile deformation to low-temperature, brittle faulting.

6.1.1.2. Stage 3: multiple generation of dykes (300 °C < T < 700 °C)

Several generations of dykes intruded the Coastal Cordillera after most of the plutons crystallization (≤ 147 Ma, U-Pb zircon age from the Cerro Cristales granodiorite; Domagala et al., 2016). Based on orientation and crosscutting relationships of pegmatite and andesitic dykes (Figs. 4-5), σ_1 and σ_3 directions should have cyclically switched their orientation, from NW-SE to NE-SW (stage 3 in Fig. 11c). The σ_1-σ_3 cyclic switching might be related to either (i) several intra-arc sinistral (i.e., NW-SE directed σ_1) and dextral (i.e., NE-SW directed σ_1) deformation stages, as much as the different dyke sets crosscut each other, as proposed by Scheuber and González (1999) or (ii) intermittent transient stress rotations (i.e., switch of principal stress axes) in the upper plate induced by megathrust earthquakes (Acocella et al., 2018; Becker et al., 2018; Hardebeck and Okada, 2018; Lara et al., 2004; Lupi et al., 2020; Lupi and Miller, 2014; Mancktelow and Pennacchioni, 2020; Pérez-Flores et al., 2016). The latter interpretation is also supported by the NNE-striking strike-slip faults exploiting the foliation of the CCSZ and the Cerro Cristales tonalite (Fig. 7). Indeed, these foliations are well-oriented for reactivation as dextral strike-slip faults during the transient tectonic regime with NE-directed σ_1. However, the hypothesis of megathrust earthquakes-related transient stress rotations requires further work to be tested. Lastly, the moderately to shallowly dipping aplite dykes are interpreted as related to exhumation occurring during Late Jurassic and Early Cretaceous.

6.1.2. Stage 4: Bolfin Fault Zone s.s. (T ≤ 300 °C)

The BFZ fault core is spatially associated and kinematically (sinistral sense of shear) consistent with the brittle-ductile shear zones (Figs. 8, 9e, 10c-d). The latter structures accommodated deformation by combined pressure-solution mechanism, incipient low-temperature crystal plasticity and fragmentation of quartz (Fig. 10c-d), suggesting a deformation temperature ≤ 300 °C (Stipp et al., 2002), consistently with their mineral assemblage. The mutual crosscutting relationship between the calcite crack-seal extensional veins and the composite S-C and S-C' fabric indicates cyclic, transient syn-kinematic extensional fracturing, triggered by cyclic increases of pore fluid pressure, during viscous deformation. This combined diffusive to crystal-plastic and cataclastic deformation is typical of the viscous-plastic to elasto-frictional transition in presence of fluids (e.g., Snoke et al., 1998). The spatial association of the brittle-ductile shear zones with the fault core is interpreted as the result of the transition from viscous-plastic to elasto-frictional rheology of the BFZ, as for other fault segments of the AFS (e.g., Grocott and Taylor, 2002; Scheuber et al., 1995; Scheuber and González, 1999; Seymour et al., 2020). The transition may have resulted from (i) different P-T deformation conditions, also during passive exhumation, (ii) variations of strain rate experienced by the BFZ, or (iii) a combination of (i) and (ii). However, the brittle-ductile shear zones are found discontinuously along the BFZ. This could either reflect (i) a change of P-T deformation conditions or strain rate along the fault or (ii) their local obliteration due to pervasive fluid-rock interaction and cataclasis.

Indeed, hydrothermal alteration was pervasive during brittle faulting as recorded by chloritization of amphibole and biotite, and albitization/saussuritization of plagioclase. This greenschist- to sub-greenschist-facies alteration indicates temperatures of 250-350 °C (Gomila et al., 2021) as well as the stable mineral assemblage of the green cataclasites, including chlorite + epidote + albite + quartz (Fig. 10e and Tables 1-2), consistent with the observations from the Caleta Coloso Fault Zone (Arancibia et al., 2014).

The widespread occurrence of pseudotachylytes documents the ancient seismicity of the BFZ as well as of the strike-slip NW-striking faults cutting the CCSZ (Figs. 3, 7, 9b-d, 10f-g). Pseudotachylytes are either pristine or strongly altered and spatially associated with epidote-chlorite-bearing veins (Figs. 9e-h). This indicates that seismic faulting occurred in presence of fluids (Gomila et al., 2021). Brittle faulting along the AFS developed once the magmatism waned (Scheuber and Andriessen, 1990; Scheuber and González, 1999). However, the geothermal gradient remained elevated (~50 °C/km) within the abandoned magmatic arc till ~100 Ma as documented by the cooling evolution of plutons along the El Salado segment (Seymour et al., 2020). Thus, such elevated geothermal gradient rose the brittle-ductile transition at 5-7 km depth (Arancibia et al., 2014; Cembrano et al., 2005; Seymour et al., 2020). As a result, we infer that the ambient conditions for seismogenic faulting were ≤ 300 °C and 5-7 km depth in a fluid-rich environment (Fig. 11d).

6.1.3. Stage 5: Post-Bolfin Fault Zone s.s. (T < 150 °C)

The red-to-purple-colored fault gouges, and the calcite- and hematite-bearing lineated fault surfaces overprint the BFZ s.s. (Figs. 9a, 9f). These late Cenozoic faults accommodated normal dip-slip to oblique strike-slip displacement associated with reactivation of the AFS (Fig. 11e). Fault reactivation was associated with a change of the plate convergence from the SE-directed oblique subduction during Jurassic and Cretaceous to the first NE-directed and the latter ENE-directed oblique subduction during Cenozoic (Pardo-Casas and Molnar, 1987; Scheuber and González, 1999). Moreover, the Coastal Cordillera became part of the forearc of the Central Andes since Cenozoic. Brittle faulting has been related to co- to post-seismic quasi-elastic rebound in the upper plate due to megathrust earthquakes along the Chile-Peru trench (e.g., González et al., 2006, 2003), associated with the ENE-trending subduction of the Nazca oceanic plate (Veloso et al., 2015 and references therein). The fault mineral assemblage, including calcite + palygorskite + halite + gypsum + hematite, indicates temperatures ≤ 150 °C (e.g., Bradbury et al., 2015; Morton et al., 2012). The local occurrence of type II twins in calcite grains and clasts within veins suggests however that the deformation temperatures were locally ≥ 200 °C (Ferrill et al., 2004). Cenozoic faulting occurred at shallow crustal levels (< 2-3 km depth), consistently with the stratigraphic constraints, as indicated by (i) well-developed S-C foliation within fault gouges associated with plastic deformation of gypsum (Fig. 10h) (ii) and low-temperature twinning of calcite within the veins (Ferrill et al., 2004).

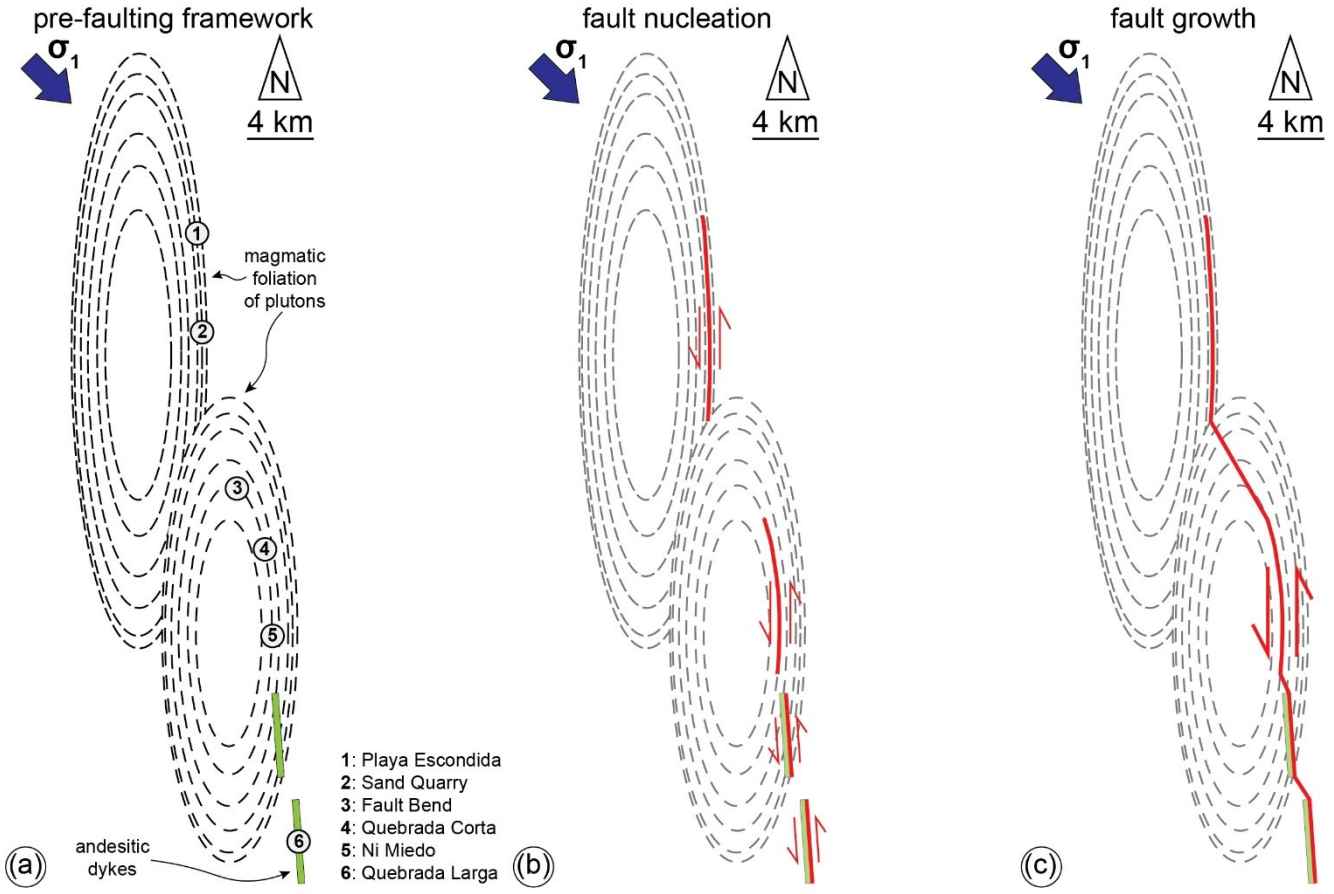

Fig. 12. Conceptual model of the evolution of the Bolfin Fault Zone. (a) Pre-faulting structural framework. (b) Nucleation of the early BFZ segments along structures favorably oriented with respect to the inferred far-stress field associated with the ancient oblique subduction. The precursory geometrical anisotropies exploited by the brittle faults include the magmatic foliation of plutons (northern and central segments) and andesitic dyke swarm (southern segment). This produces overstepping, N-to-NNW-striking, sinistral strike-slip fault segments. (c) Fault growth: NW-striking splay faults developed at the tip of the anisotropy-pinned fault segments. The progressive linkage of the fault segments resulted in the sinuous geometry of the BFZ.

6.2. Role of precursory structures on nucleation of large-scale seismogenic faults

The BFZ has a sinuous fault trace and, although being mostly sub-vertical, the BFZ dip changes from SW to W (northern segment: Playa Escondida and Sand Quarry localities) and NE (southern segment: Quebrada Larga locality) (Fig. 3). This change in dip depends on the control on the BFZ orientation by precursory anisotropies as observed for several meso-scale faults hosted in crystalline basement rocks elsewhere (e.g., d'Alessio and Martel, 2005; Di Toro and Pennacchioni, 2005; Griffith et al., 2008). Indeed, the BFZ exploited the magmatic foliation of the Bolfin Complex and the Cerro Cristales Pluton along its northern (Playa Escondida and Sand Quarry localities) and central segments (Quebrada Corta and Ni Miedo localities) (Fig. 3, 6, 8). The NW-striking subsidiary cataclasites and associated pseudotachylytes within the

damage zone nucleated on NE-dipping andesitic dykes within the isotropic tonalites and granodiorites of the Cerro Cristales Pluton along the southernmost segment (Quebrada Larga locality) (Figs. 3, 9d).

The reactivation of a precursory structure is controlled by its orientation with respect to the local stress field. In the Bolfin area, the brittle faults of the AFS are organized in strike-slip duplexes, which partitioned deformation into hierarchically-arranged faults, and the BFZ is a third-order fault splaying out from the second-order Caleta Coloso Fault Zone (Cembrano et al., 2005). Thus, in the framework of sinistral intra-arc deformation imposed by the ancient subduction of the Aluk (Phoenix) plate, i.e., NW-SE sub-horizontal σ_1 (Fig. 11d) (Brown et al., 1993; Cembrano et al., 2005; Scheuber and González, 1999; Veloso et al., 2015), the optimal direction for third-order splay faults to accommodate sinistral strike-slip shearing should be ~NNW-SSE. As a result, the magmatic foliation of the foliated meta-diorites, tonalites and granodiorites was optimally oriented to be reactivated as a sinistral strike-slip fault in the Early Cretaceous tectonic framework (Fig. 12a). Instead, the NE-dipping andesitic dykes were favorably oriented for NNW-striking sinistral strike-slip fault reactivation related to a NW-SE sub-horizontal σ_1. Several studies however pointed out that faults interaction perturb the regional stress field at fault tip and linkage causing a local stress reorientation (e.g., d'Alessio and Martel, 2004; Kim et al., 2004, 2003; Pachell and Evans, 2002; Segall and Pollard, 1983). Thus, the exploitation of the andesitic dykes may also be partly related to local stress reorientation induced by the interaction between the southernmost proto-segment of the BFZ and the central proto-segment of the Caleta Coloso Fault Zone (Fig. 12b). On the contrary, where misoriented, the precursory structures are cut by the BFZ, which, for instance, displace the CCSZ of 1 km (between Quebrada Museo and CCSZ-North localities).

We propose that the nucleation of the BFZ occurred through the exploitation of favorably oriented precursory geometrical anisotropies (i.e., magmatic foliations and dykes). Thus, the BFZ formed as a series of overstepping anisotropy-pinned fault segments (Fig. 12b). During fault growth, NW-striking splay and horsetail linkage faults developed at the tip of these fault segments (e.g., Fault Bend locality) (Fig. 12c). The progressive growth of the BFZ occurred through hard linkages of anisotropy-pinned fault segments related to the precursory evolution of the magmatic arc and explains the complex and sinuous geometry of the BFZ (Fig. 12).

Based on this model, we propose that magmatic-related structures, such as foliated plutons whose magmatic foliation can extend for several kilometers and dyke swarms, play a pivotal role in controlling the geometry of crustal-scale faults within magmatic arcs, as do cooling joints at the scale of meso-scale faults within a single pluton (e.g., Di Toro and Pennacchioni, 2005; Pennacchioni et al., 2006; Segall and Pollard, 1983; Smith et al., 2013). Indeed, the exploitation of km-long foliated plutons and dyke swarms (fault

nucleation stage) and consequent linkage of anisotropy-controlled segments (fault growth stage) could lead to the formation of non-planar faults with either sinuous trace, as the case of the BFZ, and concave-shaped trace, such as the first-order faults of the AFS. The latter was partially documented along the El Salado segment (Fig. 1a), where the main fault branch exploited the mylonitic foliation of syn-magmatic thermal aureoles bounding several Late Jurassic to Early Cretaceous plutons (Brown et al., 1993; Espinoza et al., 2014; Grocott and Taylor, 2002; Seymour et al., 2020). Fault localization along these anisotropies might be promoted by the syn-kinematic emplacement of both the Late Jurassic-Early Cretaceous plutons, which are ~N-S-elongated, and dyke swarms, controlled by the same far-stress field associated with brittle faulting along the AFS.

7. Conclusions

We described the spatial and temporal distribution of dykes, magmatic and solid-state foliations and brittle faults along the seismogenic Bolfin Fault Zone and the syn- to post-magmatic Cerro Cristales Shear Zone in the Coastal Cordillera in northern Chile (Figs. 1-3). By combining field geological surveys, analysis of satellite and drone images, and microstructural and microanalytical observations, we reconstructed the spatio-temporal evolution of the BFZ, a >40-km-long seismogenic splay fault of the 1000-km-long strike-slip Atacama Fault System. The structural evolution of the Bolfin Fault Zone includes five main deformation stages (Fig. 11):

- *Stage 1:* diachronous magmatic intrusions of the Bolfin Complex and of the Cerro Cristales Pluton, and formation of magmatic foliations and of large-scale syn- to post-magmatic shear zones. The Cerro Cristales Shear Zone formed at T > 700 °C and at < 10 km depth during pluton emplacement (Fig. 11a);
- *Stage 2:* early post-magmatic emplacement of leucocratic dykes. Leucocratic and amphibolitic dykes were exploited as strike-slip ductile shear zones active at >700 °C (Fig. 11b);
- *Stage 3:* emplacement of multiple generations of dykes arranged into two sub-vertical sets striking NW and NE, which mutually cut each other (Fig. 11c);
- *Stage 4:* formation of the Bolfin Fault Zone s.s.. The ancient seismogenic behavior is attested by occurrence of pseudotachylytes. Seismic faulting occurred at ≤ 300 °C and 5-7 km depth in a fluid-rich environment (Fig. 11d);
- *Stage 5:* extensional post-Oligocene fault reactivation of the Bolfin Fault Zone occurred at < 150 °C and shallow crustal levels (< 2-3 km depth) (Fig. 11e).

The crustal-scale Bolfin Fault Zone has a sinuous geometry, which is controlled by precursory geometrical anisotropies represented by magmatic foliation of plutons (northern and central segments) and dyke swarms (southern segments) (Fig. 3). These precursory structures were favorably oriented to be reactivated with respect to the inferred long-term stress field associated with the ancient oblique subduction. We propose a conceptual model of fault growth including (i) the exploitation of these favorably oriented precursory anisotropies during fault nucleation and (ii) hard linkage of these anisotropy-pinned fault segments during fault growth, leading to the formation of the sinuous geometry of the Bolfin Fault Zone (Fig. 12). The fault evolution proposed for the Bolfin Fault Zone may be possibly extended to the formation of the Atacama Fault System and applied to other crustal-scale faults in the crystalline basement associated with widespread magmatism.

Chapter 2

Along-strike architectural variability of an exhumed crustal-scale seismogenic fault (Bolfin Fault Zone, Atacama Fault System, Chile)

This study was performed with the collaboration of Michele Fondriest, Rodrigo Gomila, Erik Jensen, Thomas Mitchell, José Cembrano, Giorgio Pennacchioni and Giulio Di Toro. I was assisted (but not continuously) in the field by Michele Fondriest, Rodrigo Gomila, Erik Jensen, Giorgio Pennacchioni and Giulio Di Toro. I was assisted (but not continuously) during the 3-D modeling reconstruction by Michele Fondriest. I was assisted (but not continuously) during the microstructural analysis by Michele Fondriest, Rodrigo Gomila, Giorgio Pennacchioni and Giulio Di Toro. This chapter was published as the following paper: Masoch, S., Fondriest, M., Gomila, R., Jensen, E., Mitchell, T., Cembrano, J., Pennacchioni, G., Di Toro, G., 2022. Along-strike architectural variability of an exhumed crustal-scale seismogenic fault (Bolfin Fault Zone, Atacama Fault System, Chile). Journal of Structural Geology 165, 104745. https://doi.org/10.1016/j.jsg.2022.104745. All the authors discussed the data and agreed on their interpretation. I wrote the first version of the manuscript and all the co-authors contributed to its final version.

Abstract

Fault zone architecture and its internal structural variability play a pivotal role in earthquake mechanics, by controlling, for instance, the nucleation, propagation and arrest of individual seismic ruptures and the evolution in space and time of foreshock and aftershock seismic sequences. Nevertheless, the along-strike architectural variability of crustal-scale seismogenic sources over regional distances is still poorly investigated. Here, we describe the architectural variability of the >40-km-long exhumed, seismogenic Bolfin Fault Zone (BFZ) of the intra-arc Atacama Fault System (Northern Chile). The BFZ cuts through plutonic rocks of the Mesozoic Coastal Cordillera and was seismically active at 5-7 km depth and ≤ 300 °C in a fluid-rich environment. The BFZ includes multiple altered fault core strands, consisting of chlorite-rich cataclasites-ultracataclasites and pseudotachylytes, surrounded by chlorite-rich protobreccias to protocataclasites over a zone up to 60-m-thick. These fault rocks are embedded within a low-strain damage zone, up to 150-m-thick, which includes strongly altered volumes of dilatational hydrothermal breccias and clusters of epidote-rich fault-vein networks at the linkage of the BFZ with subsidiary faults. The strong hydrothermal alteration of rocks along both the fault core and the damage zone attests an extensive percolation of fluids across all the elements of the structural network during the activity of the entire fault zone. In particular, we interpret the epidote-rich fault-vein networks and associated breccias as an exhumed example of upper-crustal fluid-driven earthquake swarms, similar to the presently active intra-arc Liquiñe-Ofqui Fault System (Southern Andean Volcanic Zone, Chile).

1. Introduction

The three-dimensional architecture of fault zones is described by the spatial distribution of fault rocks, faults, fractures and veins, typically defined by two main structural units, i.e. the fault core and the damage zone (Caine et al., 1996; Faulkner et al., 2003; Mitchell and Faulkner, 2009). The fault core represents the high-strain domain accommodating most of displacement, and commonly includes strongly deformed, low-permeability fault rocks (e.g., fault gouges, cataclasites, fault breccia) (Caine et al., 1996; Chester et al., 1993; Faulkner et al., 2003). The damage zone is a relatively low-strain heterogeneous domain including a network of faults and fractures leading to a relative bulk permeability increase (Billi et al., 2003; Caine et al., 1996; Faulkner et al., 2010; Fondriest et al., 2020a; Gomila et al., 2016; Rempe et al., 2018; Wibberley et al., 2008). A fault zone can contain a single or multiple fault cores (Faulkner et al., 2010) within the enveloping damage zone. This latter can show a structural zoning between the inner and outer portions based on fracture and fault density and intensity (Choi et al., 2016; and references therein). The detailed spatial arrangement of the structural elements within the fault core(s) and damage zone has a strong influence on the fault zone mechanics and fluid-flow paths (Bedford et al., 2022; Caine et al., 1996; Chester et al., 1993; Faulkner et al., 2010, 2008; Wibberley et al., 2008). The fault architecture also strongly affects the mechanical behavior of the fault zone and rupture dynamics (Scholz, 2019), controlling earthquake rupture nucleation, propagation and arrest, spatiotemporal evolution of seismic sequences and ground motion (e.g., Ben-Zion and Sammis, 2003; Boatwright and Cocco, 1996; Chu et al., 2021; Collettini et al., 2022; Dal Zilio et al., 2019; Di Stefano et al., 2011; Howarth et al., 2021; Lockner and Byerlee, 1993; Perrin et al., 2016; Pischiutta et al., 2017; Ross et al., 2020; Sibson, 1986, 1985; Wesnousky, 2006, 1988; Wollherr et al., 2019).

Despite progress in imaging fault zone architecture through geophysical and seismological techniques (double-difference tomography, trapped waves, earthquakes relocation: e.g., Allam and Ben-Zion, 2012; Ben-Zion, 1998; Chiaraluce et al., 2011; Hale, 2013; Lewis and Ben-Zion, 2010; Li et al., 2004; Ross et al., 2020; Unsworth et al., 1997; Valoroso et al., 2014, 2013; Zigone et al., 2015), and in direct local characterization of fault zone rocks at depth from fault-drilling projects over a wide range of geological settings (e.g., Thoku-Oki megathrust, San Andreas Fault, Wenchuan Fault; Chester et al., 2013; Zoback et al., 2011; Li et al., 2013), most information about fault zone architecture comes from field-based studies of exhumed fault zones. The study of exhumed fault zones provides information on the geometry of fault networks, fault kinematics, and fault rock assemblages at high spatial resolution to constrain their mechanical and fluid flow behavior though time (e.g., Bistacchi et al., 2010; Coppola et al., 2021; Demurtas et al., 2016; Di Toro and Pennacchioni, 2005; Fondriest et al., 2020a; Gomila et al., 2016; Grocott, 1981; Jensen et al., 2019; Lucca et al., 2019; Marchesini

et al., 2022; Masoch et al., 2019; Mittempergher et al., 2014; Smith et al., 2013; Snoke et al., 1998; Tesei et al., 2013)

Although field-based studies have significantly contributed to our understanding of fault architecture, only a few contributions have quantitatively recorded the structural architecture of exhumed *crustal-scale* faults in detail over segments of a few kilometers along fault strike (Bistacchi et al., 2010; Delogkos et al., 2020; Faulkner et al., 2008, 2003; Fondriest et al., 2020a; Wedmore et al., 2020). Even more rare in the literature, the cases of fault zones characterized by an excellent preservation of the fault and fracture network over extensive exposures, coupled with the presence of tectonic pseudotachylytes that can attest the ancient fault seismicity (Cowan, 1999; Di Toro and Pennacchioni, 2004; Rowe and Griffith, 2015; Sibson, 1975; Smith et al., 2013; Swanson, 1988).

In this work, we describe the architectural variability of the exhumed Bolfin Fault Zone (BFZ) exposed at the surface over more than 40-km along the fault strike. This fault represents a seismogenic (pseudotachylyte-bearing) splay structure pertaining to the large-scale strike-slip intra-arc Atacama Fault System (AFS), which cuts through the magmatic arc of the Coastal Cordillera (Northern Chile; Fig. 1) (Arabasz, 1971; Cembrano et al., 2005; Masoch et al., 2021; Scheuber and González, 1999). This work integrates and builds on the data presented by Masoch et al. (2021), which addressed the structural evolution of the BFZ. Field surveys were performed in the western and eastern blocks at six localities along the BFZ strike. The BFZ consists of hydrothermally altered inner damage zone (up to 150-m-thick) and fault core. The latter includes multiple strands of foliated cataclasites and pseudotachylytes up to a cumulative thickness of ~60 m. The thickness of the hydrothermal altered damage zone is controlled by splay faults within the damage zone. We propose that the pervasive fluid-rock interaction affecting both the strongly altered fault core and the damage zone is controlled by the large availability of the hydrothermal fluids circulating within the fault zone, which in turn are related to the late cooling stages of the magmatic arc. Moreover, the damage zone is cut by clusters of epidote-rich fault-vein networks localized along linkage faults and fault intersections, and characterized by small-displacement (< 1.5 m) faults decorated by both slickenfibers and polished fault surfaces, and veins showing repeated events of extensional fracturing and sealing. We interpret these fault-vein networks as exhumed sources of upper-crustal fluid-driven swarm sequences, by comparison with the seismicity along the presently active intra-arc Liquiñe-Ofqui Fault System (Southern Andes, Chile).

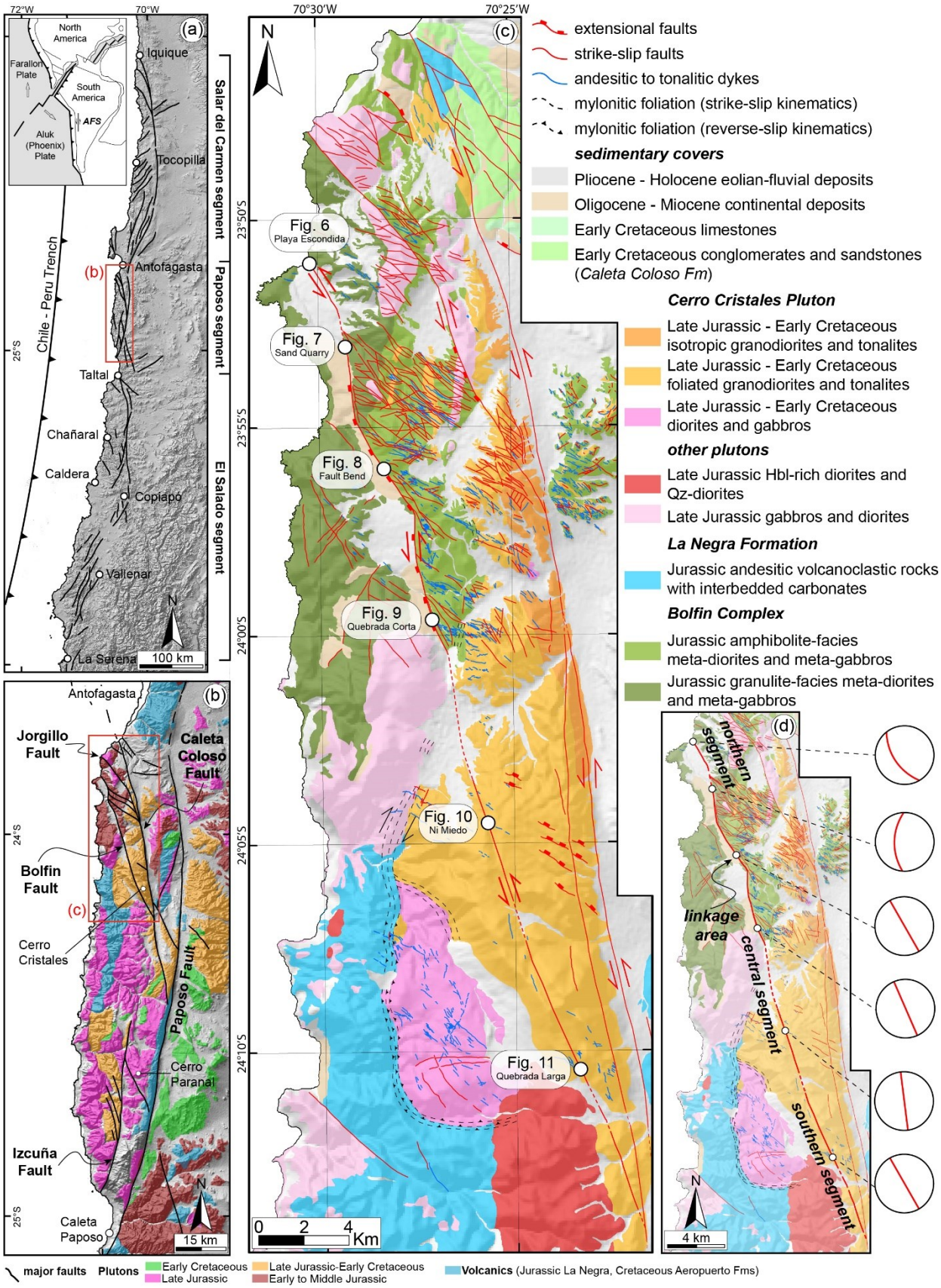

Fig. 1. Caption on next page.

Fig. 1. Geological setting of the Bolfin Fault Zone. (a) Crustal-scale geometry of the AFS comprised of its three concave-shaped segments. Shaded-relief image modified from Cembrano et al. (2005), Masoch et al. (2021) and Veloso et al. (2015). Red box indicates the area shown in (b). The inset map shows the approximate plate configuration coeval with the Mesozoic sinistral strike-slip deformation along the AFS (redrawn from Jaillard et al., 1990). (b) Simplified geological map of the Coastal Cordillera along the Paposo segment. Igneous lithologies are mapped with color coding by age. Unmapped areas represent metamorphic units and sedimentary covers. Data compiled and simplified from Cembrano et al. (2005), Domagala et al. (2016), González and Niemeyer (2005) and SERNAGEOMIN (2003). Red box indicates the area shown in (c). Legend on the bottom. (c) Geological map of the area surrounding the Bolfin Fault Zone. Note that, though based on remote-sensing analysis the lower density of the fault network in the southern area of the BFZ compared to the northern area, this difference could be biased by the limited field work performed in the southern area. Unmapped areas represent post-Miocene sedimentary covers. Modified from Masoch et al. (2021). White circles indicate the locations of the structural maps illustrated in Figs. 6-11. (d) The three fault segments forming the Bolfin Fault Zone. White circles mark the locations of the localities mapped along the BFZ. In the stereonets, the red great circle indicates the mean attitude of the BFZ at each locality.

2. Geological setting

2.1. Atacama Fault System (AFS)

The 1000-km-long AFS is the major crustal-scale, strike-slip fault system of the present-day forearc of the Central Andes (Fig. 1) (Arabasz, 1971; Brown et al., 1993; Cembrano et al., 2005; Scheuber and González, 1999). The crustal-scale geometry of the AFS is highly segmented including several parallel and subsidiary branch faults, and is comprised of three main, curved segments (from north to south): (i) Salar del Carmen, (ii) Paposo and (iii) El Salado (Fig. 1a).

The AFS developed within the Jurassic-Early Cretaceous magmatic arc of Coastal Cordillera, composed of gabbro to granodiorite plutons and basaltic to andesitic volcanic rocks (Parada et al., 2007 and references therein). The AFS accommodated intra-arc sinistral deformation induced by the oblique subduction of the Aluk (Phoenix) oceanic plate beneath the South America plate (inset of Fig. 1a), once the arc magmatism waned and migrated eastwards (Scheuber et al., 1995; Scheuber and González, 1999). Deformation along the AFS is spatially and temporally associated with plutons crystallization and cooling, and brittle faults overprinted mylonites of similar kinematics (Brown et al., 1993; Scheuber et al., 1995; Scheuber and González, 1999; Seymour et al., 2021, 2020). Deformation ages vary along strike and brittle strike-slip faulting is constrained between 130 and 110 Ma (Brown et al., 1993; Espinoza et al., 2014; Olivares et al., 2010; Ruthven et al., 2020; Scheuber et al., 1995; Scheuber and Andriessen, 1990; Scheuber and González, 1999; Seymour et al., 2021, 2020). In detail, brittle strike-slip faulting along the Paposo segment was constrained between 125 and 118 Ma (Olivares et al., 2010; Ruthven et al., 2020; Scheuber and Andriessen, 1990). Since the Miocene, the strike-slip AFS has undergone extensional fault reactivation

interpreted as result from stress redistribution in the upper plate due to large-in-magnitude earthquakes rupturing the subduction zone interface (e.g., González et al., 2006, 2003; Hervé, 1987). The post-Miocene extensional fault reactivation overprinted the Early Cretaceous architecture of the AFS.

2.2. Bolfin Fault Zone (BFZ)

The BFZ is a >40-km-long, exhumed sinistral strike-slip fault zone splaying out from the Caleta Coloso Fault along the Paposo segment (Fig. 1b-c) (Cembrano et al., 2005; Masoch et al., 2021; Scheuber and González, 1999). The BFZ is a third-order fault of the AFS and bounds the western side of the crustal-scale Caleta Coloso Duplex (Fig. 1b) (Cembrano et al., 2005; Jensen et al., 2011; Veloso et al., 2015). The BFZ has a crustal-scale sinuous geometry cutting through meta-diorites of the Jurassic Bolfin Complex and tonalites to granodiorites of the Late Jurassic-Early Cretaceous Cerro Cristales Pluton (Fig. 1b-c). Its sinuous geometry resulted from (i) exploitation of precursory anisotropies favorably oriented with respect to the inferred far-stress field during fault nucleation and (ii) subsequent hard linkage of these anisotropy-pinned fault segments through NW-striking splay and horsetail faults during fault growth (Masoch et al., 2021). The BFZ consists of three fault segments (namely north, central and south segment; Fig. 1d) distinguished on the basis of the exploited precursory anisotropies and changes in fault attitude (Masoch et al., 2021). In detail, the BFZ:

- strikes from NW-SE to N-S and dips towards SW and W, respectively, overprinting the magmatic foliation of meta-diorites (Bolfin Complex) in the northern segment;
- strikes ~N-S, is sub-vertical (>80°) and exploits the magmatic foliation of meta-diorites (Bolfin Complex) and tonalites-granodiorites (Cerro Cristales Pluton) in the central segment;
- exploits NE-dipping andesitic dykes within weakly foliated tonalites (Cerro Cristales Pluton) in the southern segment.

The ancient BFZ seismicity is attested by widespread occurrence of pseudotachylytes (Gomila et al., 2021; Masoch et al., 2021). Seismic faulting occurred at 5-7 km depth and ≤ 300 °C in a fluid-rich environment as documented by extensive propylitic alteration and chlorite-epidote veining (Gomila et al., 2021; Masoch et al., 2021). The Early Cretaceous architecture of the BFZ was overprinted by post-Miocene extensional faulting. This late fault system consists of palygorskite + calcite + halite ± gypsum ± hematite-bearing fault gouges, and hematite- and calcite-bearing fault surfaces associated with calcite-bearing veins (Masoch et al., 2021; Olivares et al., 2010) and active at < 2-3 km depth and < 150 °C (Masoch et al., 2021). The lack of reliable structural markers makes the cumulative displacement accommodated by the BFZ poorly

constrained as well as the polyphase fault activity makes difficult to discriminate from which one is related to. A left-lateral cumulative separation of ~1 km in the central segment is estimated from the offset of the thermal aureole of the Cerro Cristales Pluton (Fig. 1c; Masoch et al., 2021).

3. Methods

Field structural surveys along with remote sensing were performed to characterize the regional-scale fault pattern of the BFZ (analyzed area: 20 km wide, 50 km long). Remote sensing analysis was performed using satellite images (i.e., Sentinel-2, Google Earth® and Bing®) used as reference images coupled with published maps (Cembrano et al., 2005; Domagala et al., 2016; González and Niemeyer, 2005; Masoch et al., 2021; SERNAGEOMIN, 2003). The western and eastern blocks of the BFZ were mapped along and across fault strike in six selected localities (namely from north to south: Playa Escondida, Sand Quarry, Fault Bend, Quebrada Corta, Ni Miedo and Quebrada Larga; Fig. 1). At each locality, we used a DJI® Phantom 4 Pro drone to take nadir-directed aereophotographs. The images were processed in Agisoft Metashape Professional software to produce high-resolution georeferenced orthomosaics (spatial resolution of ~10 cm/pixel) used as base maps for the field structural surveys at 1:300 and 1:500. In this work, we focus on the deformation structures (e.g., structural elements, fault rocks distribution, fault-vein networks distributions) related to the Early Cretaceous seismic faulting (i.e., deformation stage 4; Masoch et al., 2021).

Fault zone structural units were defined on the base of field and microstructural observations, such as:

- preservation of original magmatic features of the host rocks;
- alteration degree of the host rocks;
- spacing of fractures, veins and faults;
- relatively abundance of veins and faults;
- mineral assemblage sealing and decorating veins and faults;
- clast/matrix proportion in the fault rocks.

In particular, six structural units were identified within the BFZ (from the lowest to the highest deformed unit; Figs. 2-5): (i) weakly-fractured unit, (ii) epidote-quartz-prehnite breccia, (iii) epidote-rich veins and faults unit, (iv) chloritized and fractured unit, (v) Cataclastic Unit 1 (CU1), and (vi) Cataclastic Unit 2 (CU2). The CU1 and CU2 represent the fault core, and the other units represent the damage zone. To describe the fault rocks, we make reference to the classification of Sibson (1977) and Woodcock and Mort (2008). Vein and fault abundance was quantified (P_{10} fracture density; Mauldon and Dershowitz, 2000) for

the above defined units (i)-(iv) along scanlines (9-17 m long) traced perpendicular to the main trace of the BFZ. However, to quantify the P_{10} values, we considered only veins and faults sealed and decorated by hydrothermal minerals (chlorite, epidote, quartz, prehnite) associated with Early Cretaceous fault activity (Cembrano et al., 2005; Gomila et al., 2021; Herrera et al., 2005; Masoch et al., 2021; Olivares et al., 2010). In this way, we did not overestimate the fracture density by including structural elements (e.g., fractures, veins, faults) possibly associated with the post-Miocene extensional fault reactivation (see Masoch et al., 2021 for details) and passive exhumation. Thus, our P_{10} estimates are minimum values and were used to quantify and to compare the damaging among the structural units (i)-(iv). The orientation and kinematics of the different structural elements (e.g., magmatic foliations, dykes, faults, fault-veins, veins, fractures) were systematically measured at sites evenly distributed across the outcrops. Structural maps and data were digitalized using ArcGIS© 10.6 and MOVE© software (Figs. 6-11). Five geological cross sections were reconstructed (Fig. 12). Structural measurements (n=4898) were plotted and analyzed using equal area, lower hemisphere projections created in Stereonet 10 (Allmendinger et al., 2011; Cardozo and Allmendinger, 2013) and FaultKin 7 (Allmendinger et al., 2011; Marrett and Allmendinger, 1990).

Oriented samples (n=102) were collected for microanalytical investigations. Microstructural observations were conducted on polished thin sections (n=51) oriented parallel to fault lineation and orthogonal to the fault surface and vein boundary. Transmitted-light optical microscopy (OM) was used to determine microstructural features at thin section scale and to identify areas suitable for microanalytical investigations. Scanning electron microscopy (SEM) was used to acquire high-resolution backscattered electron (BSE) images coupled with semiquantitative energy dispersion spectroscopy (EDS) elemental analysis. SEM investigations were performed with a CamScan MX3000 operating at 25 kV at Department of Geosciences at Università degli Studi di Padova (UniPD). Field-emission SEM investigations were performed with a Tescan Solaris operating at 7-10 kV at the Department of Geosciences (UniPD) and a JOEL JSM-6500F operating at 15 kV at HP-HT laboratories of Istituto Nazionale di Geofisica e Vulcanologia (INGV) in Rome, respectively. Optical microscopy cathodoluminescence (OM-CL) was applied to obtain information on chemical variations within hydrothermal veins and breccia. The OM-CL was employed using a Nikon microscope equipped with a Nikon camera working at 16-18 kV and 180-240 μA in a vacuum of 0.07-0.09 Torr, installed at Department of Geosciences (UniPD). Bulk mineralogy of rock samples was retrieved though X-ray powder diffraction (XRPD), and semiquantitative mineralogical composition were retrieved through Reference Intensity Ratio (XRPD-RIR) method. XRPD analyses were performed with a PANalytical X'Pert Pro diffractometer equipped with a Co radiation source, operating at 40 mA and 40 kV in the angular range of $3° < 2\theta < 85°$, installed at Department of Geosciences (UniPD). Mineral composition

of main mineral phases was obtained by electron wavelength-dispersive microprobe analysis (EMPA). EMPA investigations were performed with a JOEL-JXA8200 microprobe equipped with EDS-WDS (five spectrometers with twelve crystals), installed at INGV-Rome, and a Cameca SX50 microprobe, installed at Department of Geosciences (UniPD). Data were collected using 15 kV as accelerating voltage and 7.5 nA as beam current. A slightly defocused electron beam with a size of 5 μm was used, with a counting time of 5 s on background and 10 s on peak. Albite (Si, Al and Na), forsterite (Mg), pyrite (Fe), rutile (Ti), orthoclase (K) and apatite (Ca and P) were used as standards. Sodium and potassium were analyzed first to prevent alkali migration affects. The precision of the microprobe was measured through the analysis of well-characterized synthetic oxide and mineral secondary standards. Based on counting statistics, analytical uncertainties relative to their reported concentrations indicate that precision was better than 5% for all cations.

4. Structural units and their variability along fault strike

Firstly, we describe macroscopically each structural unit (subsections 4.1 to 4.5). Then, we describe the architectural variability along fault strike (subsection 4.6).

4.1. Weakly-fractured unit

The weakly-fractured unit consists of poorly deformed rock volumes preserving nearly unaltered magmatic protolith (Fig. 2a), crosscut by spaced (1-10 m apart), NW-striking discrete faults and associated veins (stereonet 7 in Fig. 7; stereonet 10 in Fig. 8; stereonet 5 in Fig. 9). Fault surfaces are delineated by chlorite-rich protocataclasites to cataclasites, and locally ornamented by epidote-bearing slickenlines and slickenfibers. The abundant veins are filled with chlorite, epidote, quartz and calcite. Vein abundance (P_{10}) is ~3-5 m^{-1} and the vein thickness ranges between a few mm and 1 cm.

Fig. 2. Weakly-fractured unit, and chloritized and fractured unit. (a) Weakly-fractured unit at Quebrada Corta locality. The nearly fresh protolith shows low vein abundance (P_{10} = 3-5 m^{-1}). Hammer for scale. WGS GPS location: 23.994842°S, 70.448733°W. (b-c) Panoramic view of the chloritized and fractured units at Sand Quarry (b; WGS GPS location: 23.884014°S, 70.486306°W) and Fault Bend (c; WGS GPS location: 23.935952°S, 70.468968°W) localities. Dashed white lines outline the unit. (d) Detail of the chloritized and fractured unit (Sand Quarry locality). Chlorite-rich veins show a black alteration halo and the protolith, altered due to pervasive propylitic alteration, is black to orange in color. 100-pesos coin for scale (diameter: 23.5 mm). WGS GPS location: 23.883298°S, 70.487778°W. (e) Microstructure of the weakly-fractured unit. The nearly fresh tonalite is cut by a chlorite-rich vein. Thin section scan under cross-polarized light. Sample NM20-237-HR. WGS GPS location: 24.073309°S, 70.433348 °W. (f) Microstructure of the chloritized and fractured unit. The altered meta-diorite shows replacement of (i) magmatic amphibole and biotite by chlorite and opaques; and (ii) magmatic plagioclase by sericite + epidote. Thin section scan under plane-polarized light. Sample PA11-19. WGS GPS location: 23.995681°S, 70.449875°W.

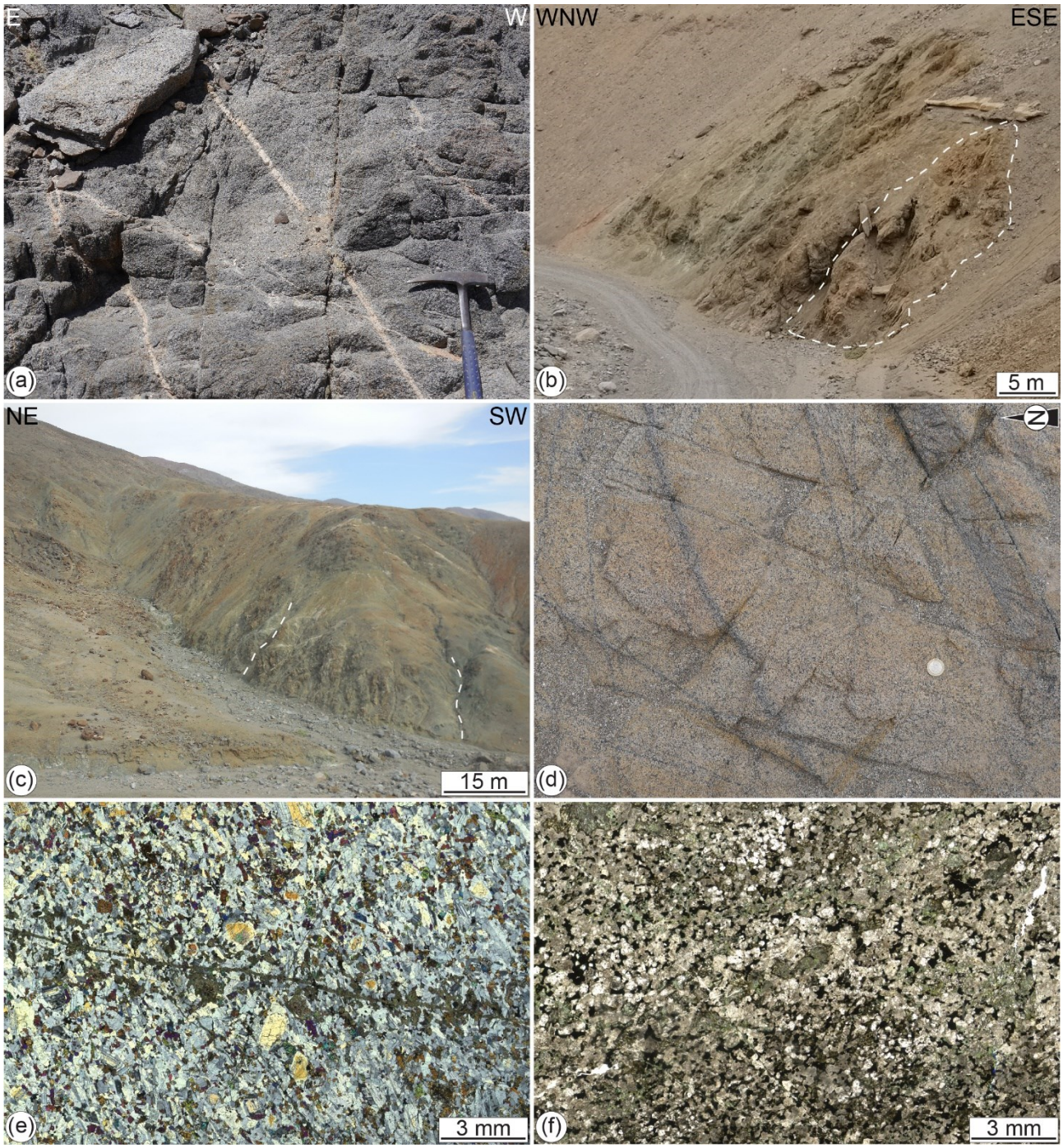

Fig. 2. Caption on previous page.

4.2. Epidote-quartz-prehnite breccia

The epidote-quartz-prehnite breccia consist of green, cohesive mosaic to chaotic breccias (Fig. 3), following the classification proposed by Woodcock and Mort (2008), and crush breccias according to Sibson (1977). The breccias include angular fragments of the host rock and of early breccias and veins (Fig. 3),

cemented by zoned epidote + prehnite + quartz ± chlorite (section 5.2 and Tables 1-2). Pods of the chloritized and fractured unit are present within the breccia unit (Fig. 8). The breccia unit marks bands up to 1-m-wide and mostly shallowly (<40°) dipping towards ENE and the breccia volume increases at the intersection with SW-dipping faults (Fault Bend locality; Fig. 8). The breccia unit is found within a decameter-sized dilational jog, defined by NW-striking splay and NNW-striking faults, in the BFZ damage zone. The transition of the breccia unit to the adjacent structural units is either sharp and fault-bounded (case for the weakly-fractured and the chloritized and fractured units) or transitional, characterized by a progressive intensity decrease of epidote-rich veins mowing towards the breccia unit (case for the epidote-rich veins and faults unit) (Fig. 8). Normal dip-slip to oblique-slip fault surfaces and shear veins inside the breccia unit dip shallowly (<40°) towards SE, SW, NW and NE (stereonets 5-6 in Fig. 8). Some discrete polished fault surfaces show aligned, truncated clasts (Fig. 3g).

4.3. Epidote-rich veins and faults unit

This unit consists of strongly fractured and brecciated rock volumes associated with epidote-rich interlaced fault-vein networks (Fig. 4). The latter are characterized by (i) small-displacement (cumulative <1-1.5 m) normal dip-slip to strike-slip faults decorated by epidote-rich slickenfibers (Fig. 4) and polished fault surfaces (Fig. 4; stereonets 3-6 in Fig. 7), and (ii) veins and breccias sealed by epidote ± quartz ± K-feldspar (section 5.3). Faults and veins are arranged into two sets, striking NW, and N to NE (stereonets 3-6 in Fig. 7). Veins and breccias show multiple episodes of fracturing and sealing as they include angular fragments of early veins and breccias (Fig. 4b, 4e-g). Thicker veins are banded and filled by epidote and minor quartz (Fig. 4g). The epidote-rich fault-vein networks are surrounded by extensive alteration haloes in the damaged host rocks, which are reddish in color in the meta-diorites (Fig. 4a-b, 4f; similar to those described by Faulkner et al., 2011) and whitish in the granodiorites and tonalites (Fig. 4e). The contact with the other structural units is transitional.

Fig. 3. Epidote-quartz-prehnite breccia at Fault Bend locality (Fig. 8). (a) Polished sample of chaotic breccia. The cm-in-size angular fragments consist of early epidote veins (green) and are sealed by a pale green-colored cement of epidote + quartz + prehnite. Sample M2. WGS GPS location: 23.934563°S, 70.465428°W. (b) Chaotic breccia made of angular fragments of altered host rock. Coin for scale. WGS GPS location: 23.934738°S, 70.465626°W. (c) Epidote-bearing veins. Coin for scale. WGS GPS location: 23.934676°S, 70.465544°W. (d) Epidote-quartz-prehnite (pale green) vein including fragment of an early epidote vein (green) cutting the breccia body. Coin for scale. WGS GPS location: 23.934547°S, 70.465406°W. (e) Low-angle extensional shear vein (i.e., extensional + shear fracture) within the breccia unit. Coin for scale. (f) Honeycomb mesh structure at the external border of the breccia body. Cover lens for scale. WGS GPS location: 23.934255°S, 70.465309°W. (g) Polished fault surface with aligned truncated clasts of epidote indicating strike-slip kinematics. WGS GPS location: 23.934419°S, 70.465331°W.

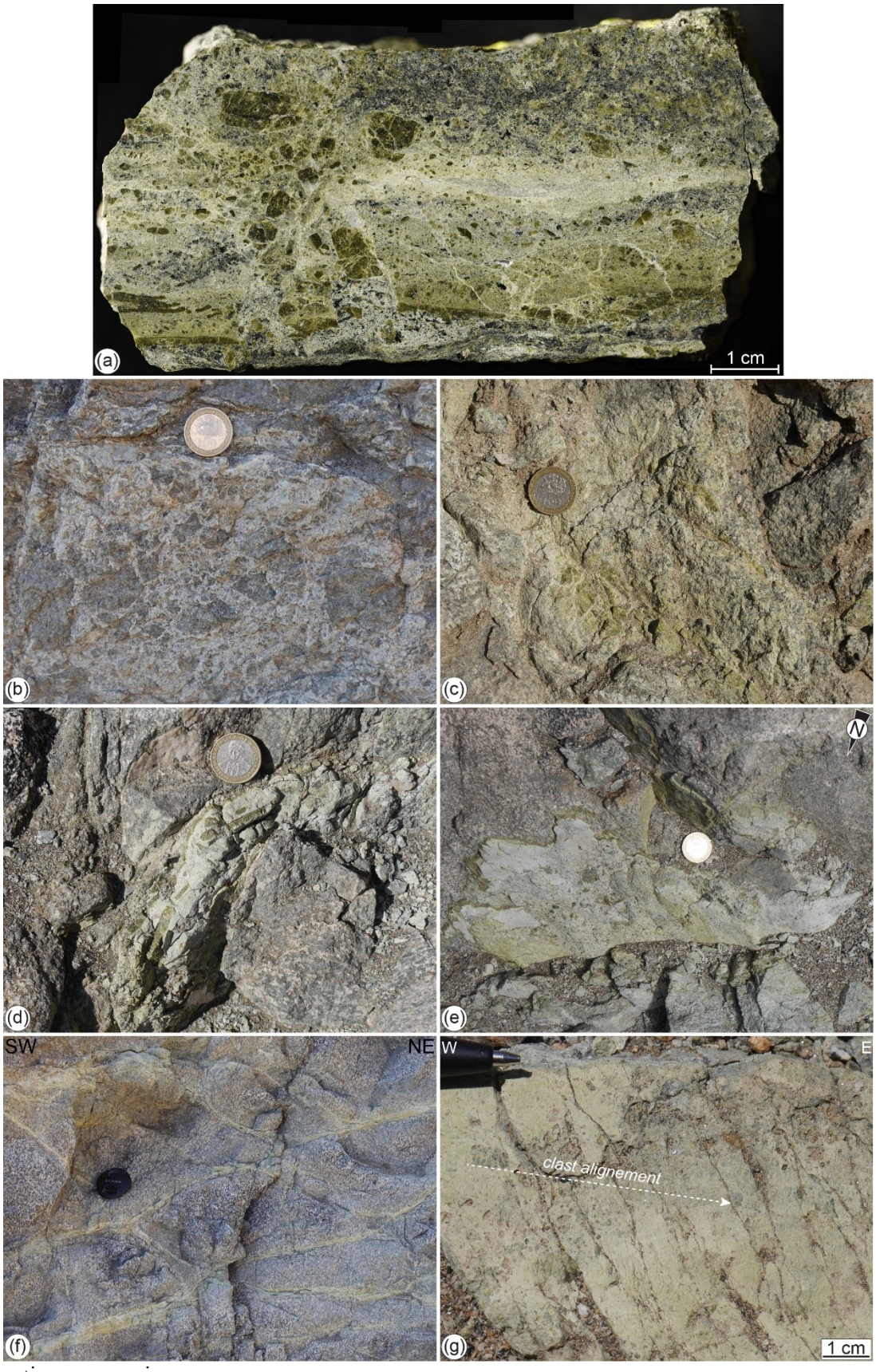

Fig. 3. Caption on previous page.

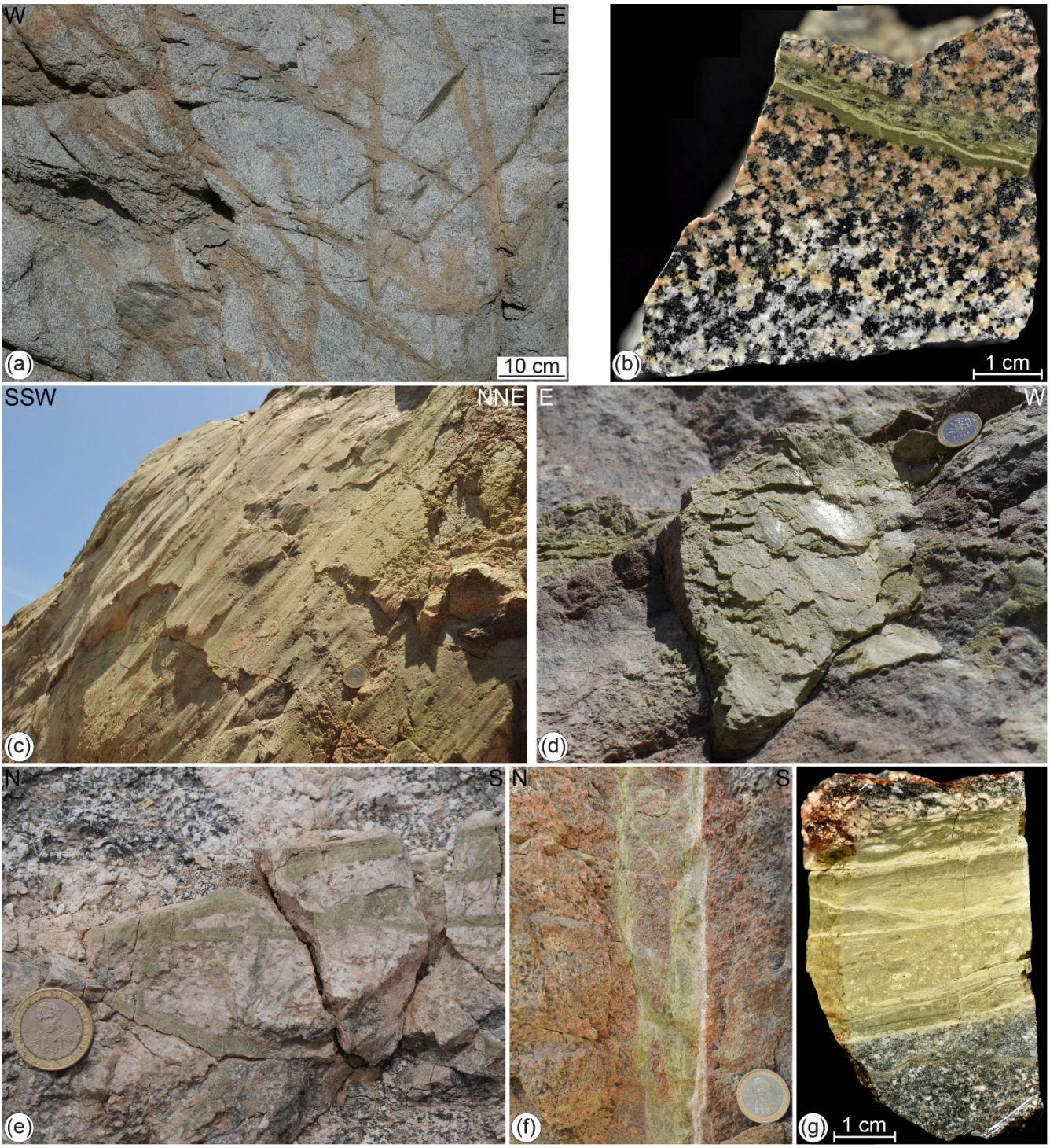

Fig. 4. Caption on next page.

Fig. 4. Epidote-rich veins and faults unit. (a) Epidote-bearing veins are surrounded by a red alteration halo in the damaged host rock (Sand Quarry locality). WGS GPS location: 23.883764°S, 70.487067°W. (b) Polished sample of an epidote vein reworked by a mm-thick cataclasite. The later epidote cataclasite (pale green) includes fragments of early veins (dark green). Sample 19-48 (Sand Quarry locality). WGS GPS location: 23.88442°S, 70.48567°W. (c) Discrete extensional fault surface decorated by epidote-bearing slickenfibers (Sand Quarry locality). Coin for scale. WGS GPS location: 23.883944°S, 70.486689°W. (d) Polished and stepped fault surface decorated by epidote (Sand Quarry locality). Coin for scale. WGS GPS location: 23.883983°S, 70.486614°W. (e) Epidote-rich vein network associated with a whitish alteration halo in the damaged granodiorites (Quebrada Larga locality). Coin for scale. WGS GPS location: 24.17779°S, 70.39066°W. (f) Polyphase epidote-bearing vein includes angular fragments of earlier veins (dark green) and is associated with a pervasive fluid-rock interaction in the surrounding damaged host rock (Sand Quarry locality). The vein is reactivated by a calcite-palygorskite vein during post-Miocene fault reactivation (see Masoch et al., 2021 for details). Coin for scale. WGS GPS location: 23.99803°S, 70.44051°W. (g) Polished sample of a cm-thick polyphase epidote-rich vein. Angular fragments of early epidote-rich veins are sealed by epidote cement. mm-thick quartz vein cut the epidote vein. Sample 19-70 (Quebrada Larga locality). WGS GPS location: 24.17783°S, 70.39077°W.

4.4. Chloritized and fractured unit

The chloritized and fractured unit consists of strongly altered and fractured rock volumes still preserving the pristine fabric, but strongly affected by propylitic alteration (Fig. 2b-d; see section 5.4). The unit bounds the CU 1 and CU2 (see next section, Fig. 12) and, at the outcrop scale, is dark green to black (Fig. 2d). Brittle deformation is accommodated by shear and extensional veins filled with chlorite ± epidote (Fig. 2d). Veins, up to 2-cm-thick, are spaced < 3-4 cm apart (P_{10} ~25-33 m^{-1}) and their spatial density increases towards the fault core.

4.5. Cataclastic Units

At the outcrop scale, two cataclastic units can distinguished as a function on the degree of cataclasis: the low-strain Cataclastic Unit 1 (CU1) and the high-strain Cataclastic Unit 2 (CU2) (Fig. 5). In both units, the cataclastic rocks are cemented by chlorite and minor epidote (section 5.4) and contain pseudotachylyte veins, up to 2-cm-thick (Fig. 5b). The pseudotachylytes are commonly polyphase and dismembered (Fig. 5d, 5e).

4.5.1. Cataclastic Unit 1 (CU1)

CU1 comprises dark green protobreccias to protocataclasites, which locally include lithons of the chloritized and fractured structural unit (Fig. 5a-b). Thin anastomosing bands of cataclasites are commonly observed within the CU1 striking either NW or N. The CU1 also includes a spatially dense (veins spacing < 1 cm) network of chlorite-epidote veins.

4.5.2. Cataclastic Unit 2 (CU2)

CU2 consists of dark green to black cataclasites and ultracataclasites, transitionally or sharply bounding the CU1 (Fig. 5a). The CU2 form anastomosing strands, up to 6-m-thick, and strike subparallel to the CU1 bands. The cataclasites and ultracataclasites are either isotropic or foliated with the S-C-C' foliation consistent with sinistral strike-slip kinematics (Fig. 5c). The few observed slickenlines plunge shallowly towards NNW to N.

4.6. Architectural variability of the BFZ along fault strike

The spatial distribution of the different structural units within the fault zone varies along fault strike. In general, the architecture of the BFZ consists of (i) a fault core formed by CU1 and CU2, and (ii) an inner damage zone including the chloritized and fractured unit. We cannot define the extension of the outer damage zone given the heterogeneous damaging related to the several faults forming the Caleta Coloso Duplex (Cembrano et al., 2005; Mitchell and Faulkner, 2009). The geological maps of the BFZ with the spatial distribution of the different structural units and the orientation of structures at the six studied localities are reported in Figs. 6-11 and cross sections orthogonal to the BFZ strike are shown in Fig. 12.

Fig. 5. Cataclastic units, CU1 and CU2, and pseudotachylytes. (a) Fault core section nearly perpendicular to fault strike (Sand Quarry locality). The fault core (~17-meter-wide) includes multiple strands of the high-strain CU2 and lower-strain CU1. The dashed yellow lines indicate the CU2 strands; while, the black dashed lines mark rock volumes of the chloritized and fractured unit. WGS84 GPS location: 23.8831611°S, 70.4880389°W (b) Pseudotachylyte fault vein (fv) with injection vein (iv) intruding protobreccias and cataclasites of the fault core (CU1; Playa Escondida locality, taken from Gomila et al., 2021). Coin for scale. WGS84 GPS location: 23.8498611°S, 70.5032555°W. (c) Foliated cataclasite forming the high-strain CU2. S-C' foliation indicates sinistral strike-slip kinematics (Playa Escondida locality). WGS84 GPS location: 23.849894°S, 70.503236°W. (d) Low-angle altered pseudotachylytes within the fault core units (Sand Quarry locality). Cover lens for scale. (d) (e) Massive green cataclasites of the CU2 at the fault core of the BFZ. Multiple generations of brown to black, dismembered and altered pseudotachylytes are found in the fault core units (Ni Miedo locality). Hammer for scale. WGS84 GPS location: 24.0796167°S, 70.4270750°W.

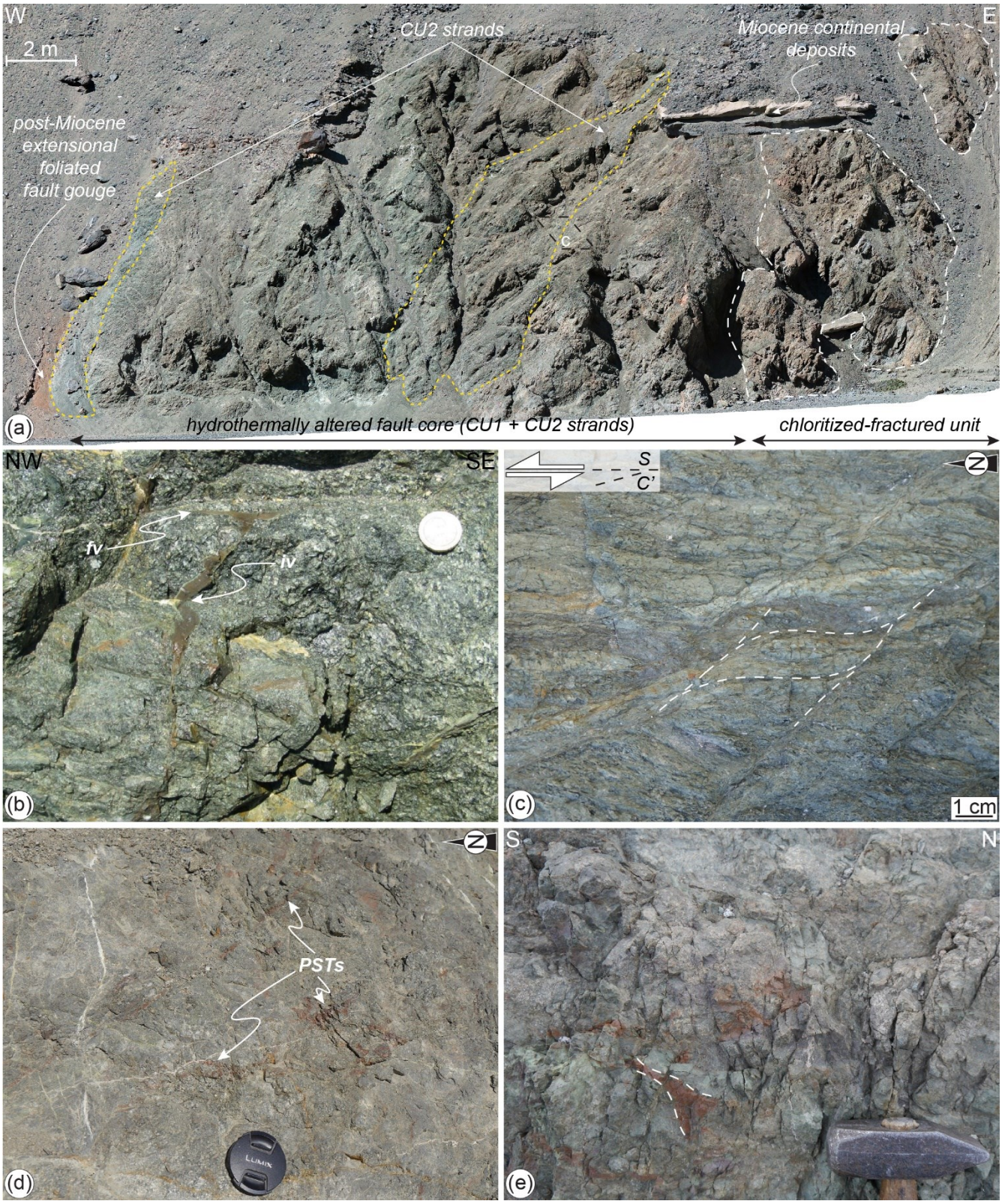

Fig. 5. Caption on previous page.

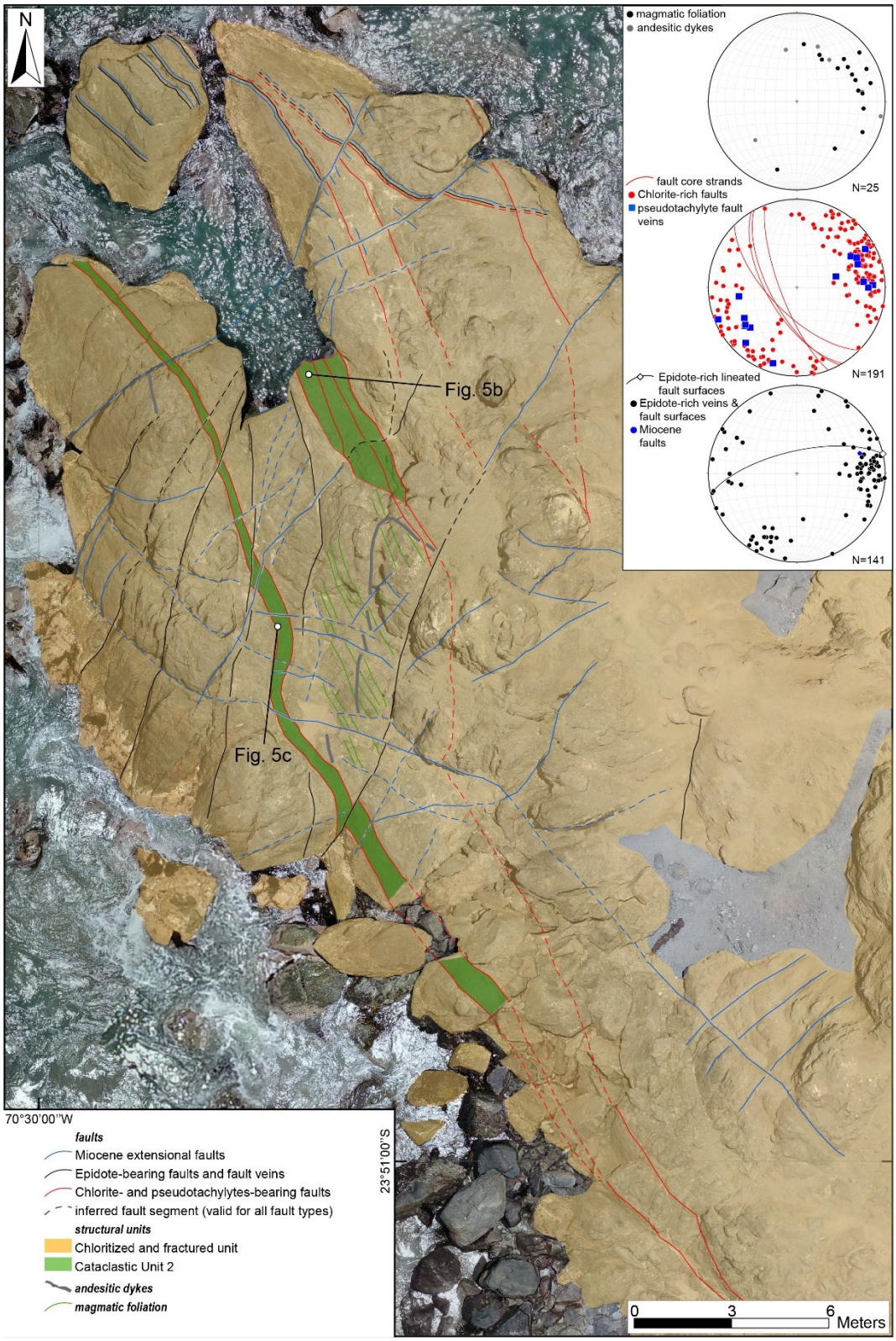

Fig. 6. Structural map of the distribution of the fault zone structural units and structural data at Playa Escondida locality (northern segment, modified from Gomila et al., 2021). The fault core consists of two fault core strands, dipping towards SW, and exploited the magmatic foliation of the meta-diorites (Bolfin Complex). The outcrop covers only the fault core and limited parts of the strongly altered damage zone.

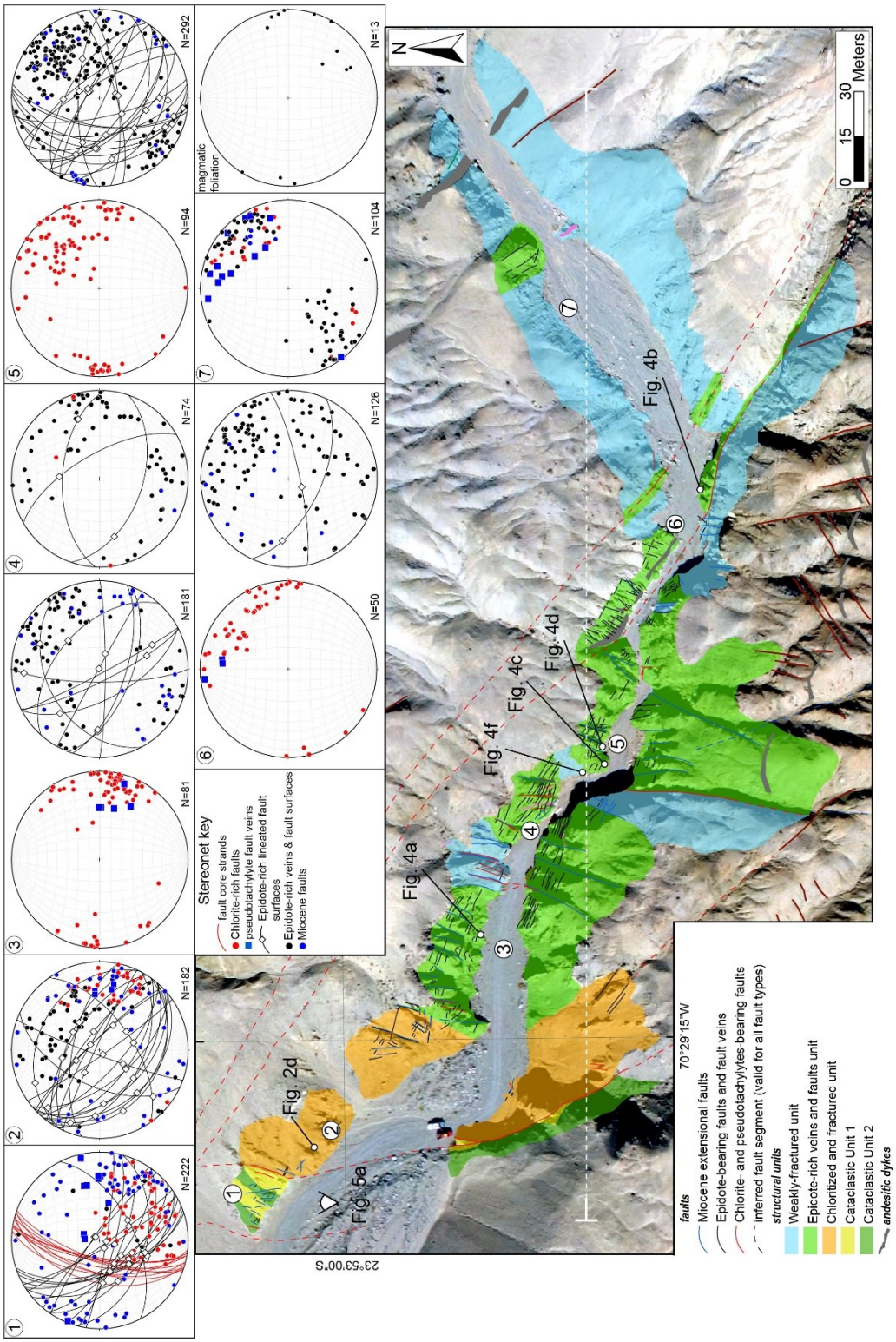

Fig. 7. Structural map of the distribution of the fault zone structural units and structural data at Sand Quarry locality (northern segment). The fault core dips towards W and exploited the magmatic foliation of the meta-diorites (Bolfin Complex). The fault core units are surrounded by the chloritized and fractured unit over a ~50-m-wide zone. In the damage zone, clusters of epidote-rich faults and veins are associated with NW-striking, splay faults of the BFZ (fourth-order faults) and fault intersections with NE-striking faults. Numbers in stereoplots denote the location of structural sites in the map.

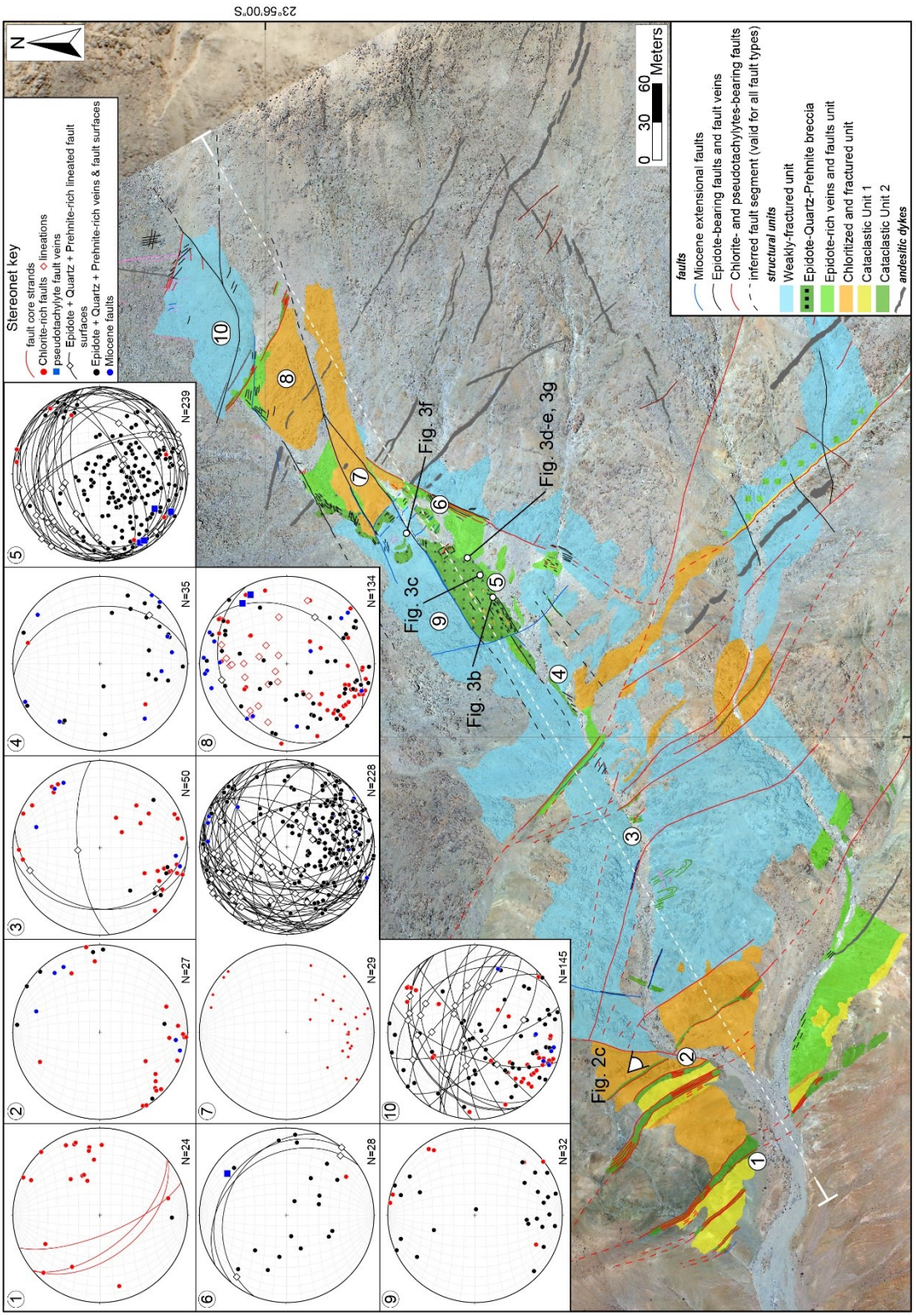

Fig. 8. Structural map of the distribution of the fault zone structural units and structural data at Fault Bend locality (linkage area). The SW- dipping fault core is surrounded by the chloritized and fractured unit over a zone as wide as 75 m. The damage zone is cut by multiple NW-striking splay faults, marking a decameter in size dilational jog, which include the epidote-quartz-prehnite breccia unit. Numbers in stereoplots denote the location of structural sites in the map.

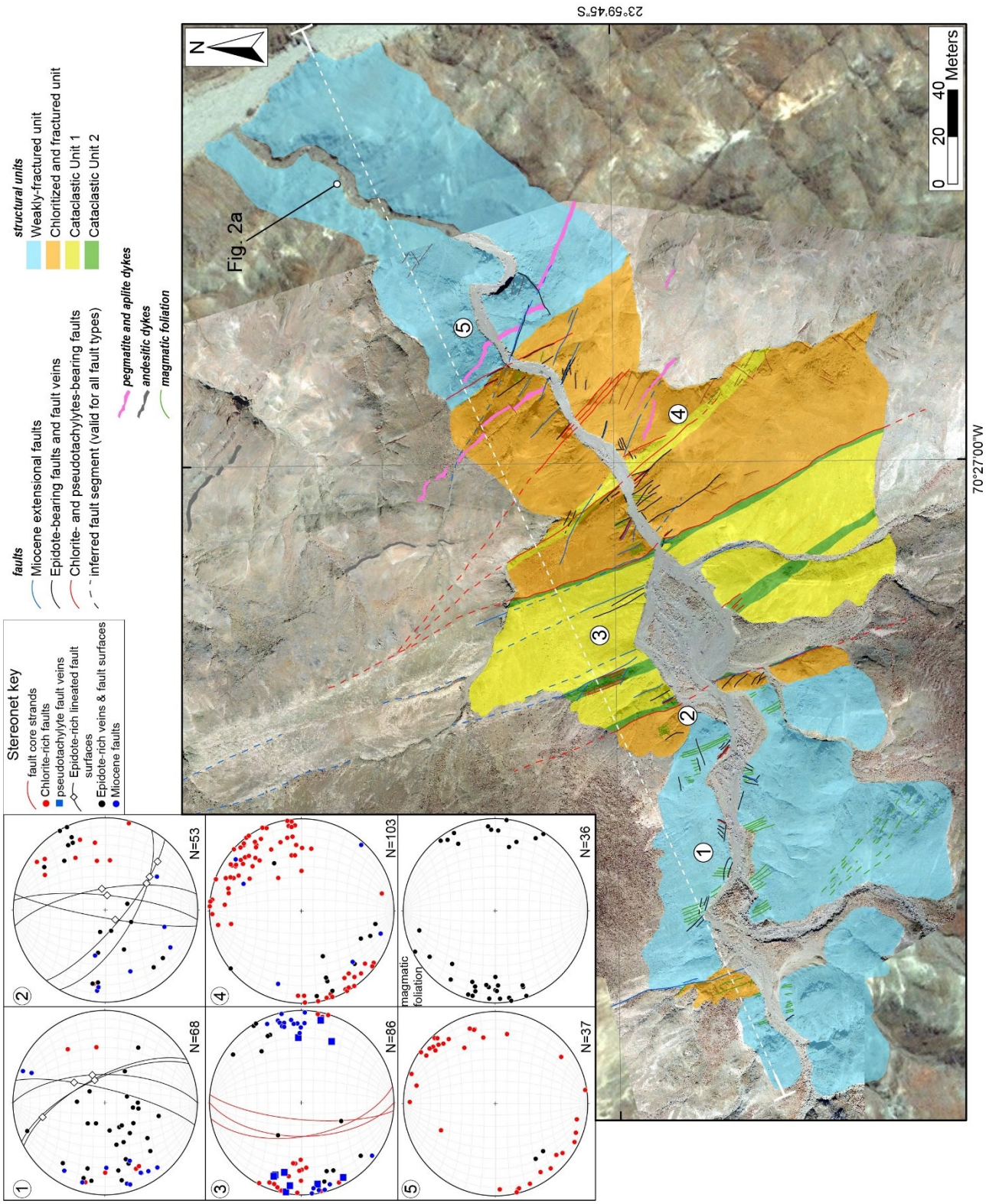

Fig. 9. Structural map of the distribution of the fault zone structural units and structural data at Quebrada Corta locality (central segment). The ~75-m-wide fault core overprints the well-developed sub-vertical magmatic foliation of meta-diorites (Bolfin Complex) and is spatially associated with chloritized and fractured structural units both in the eastern and western blocks. Numbers in stereoplots denote the location of structural sites in the map.

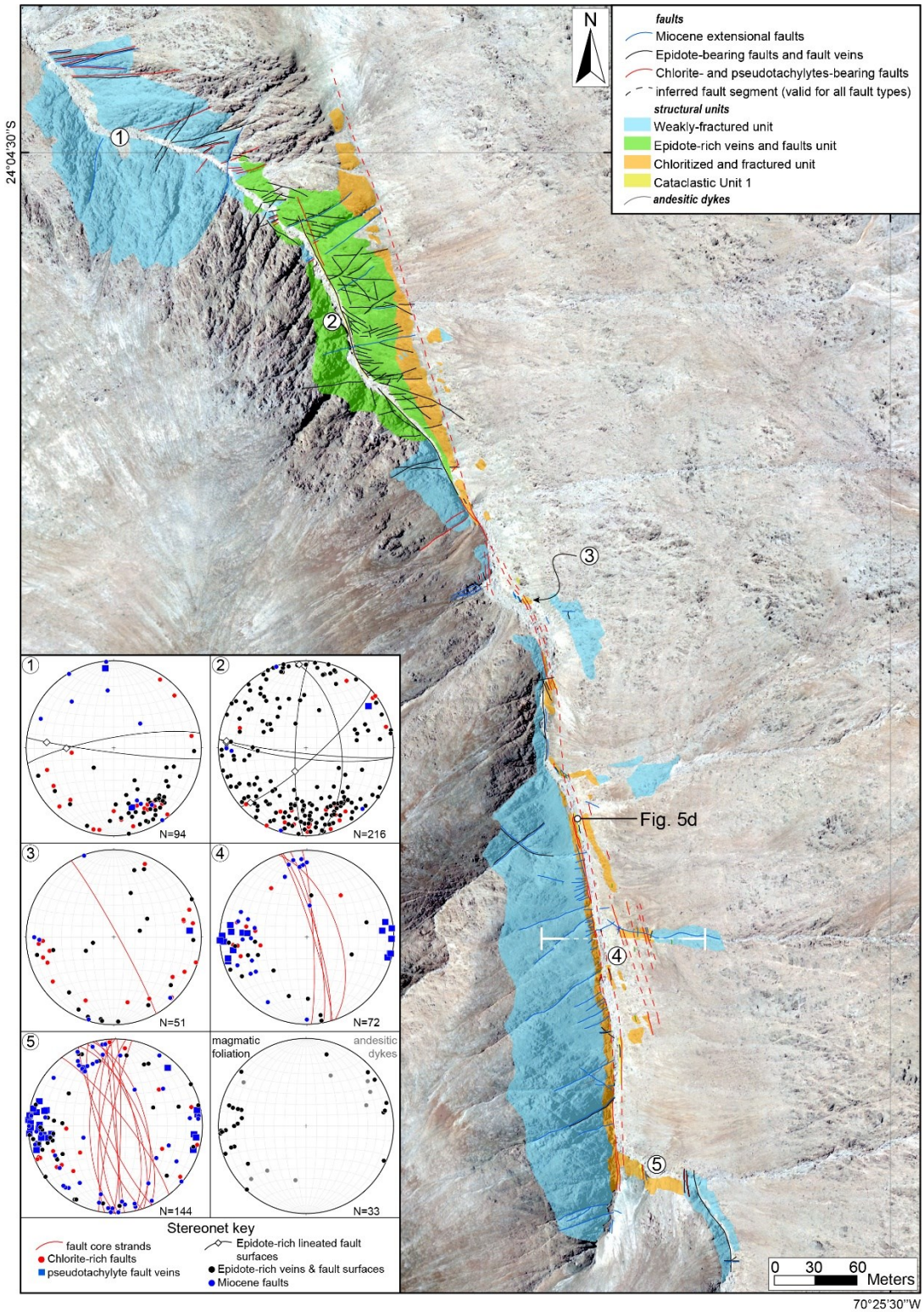

Fig. 10. Structural map of the distribution of the fault zone structural units and structural data at Ni Miedo locality (central segment). The multiple fault core strands overprint the magmatic foliation of the tonalites-granodiorites (Cerro Cristales Pluton) and are associated with the chloritized and fractured structural unit over a zone as wide as 45 m. In the eastern block, clusters of the epidote-rich fault-veins and veins are associated with a NW-striking splay fault. Numbers in stereoplots denote the location of structural sites in the map.

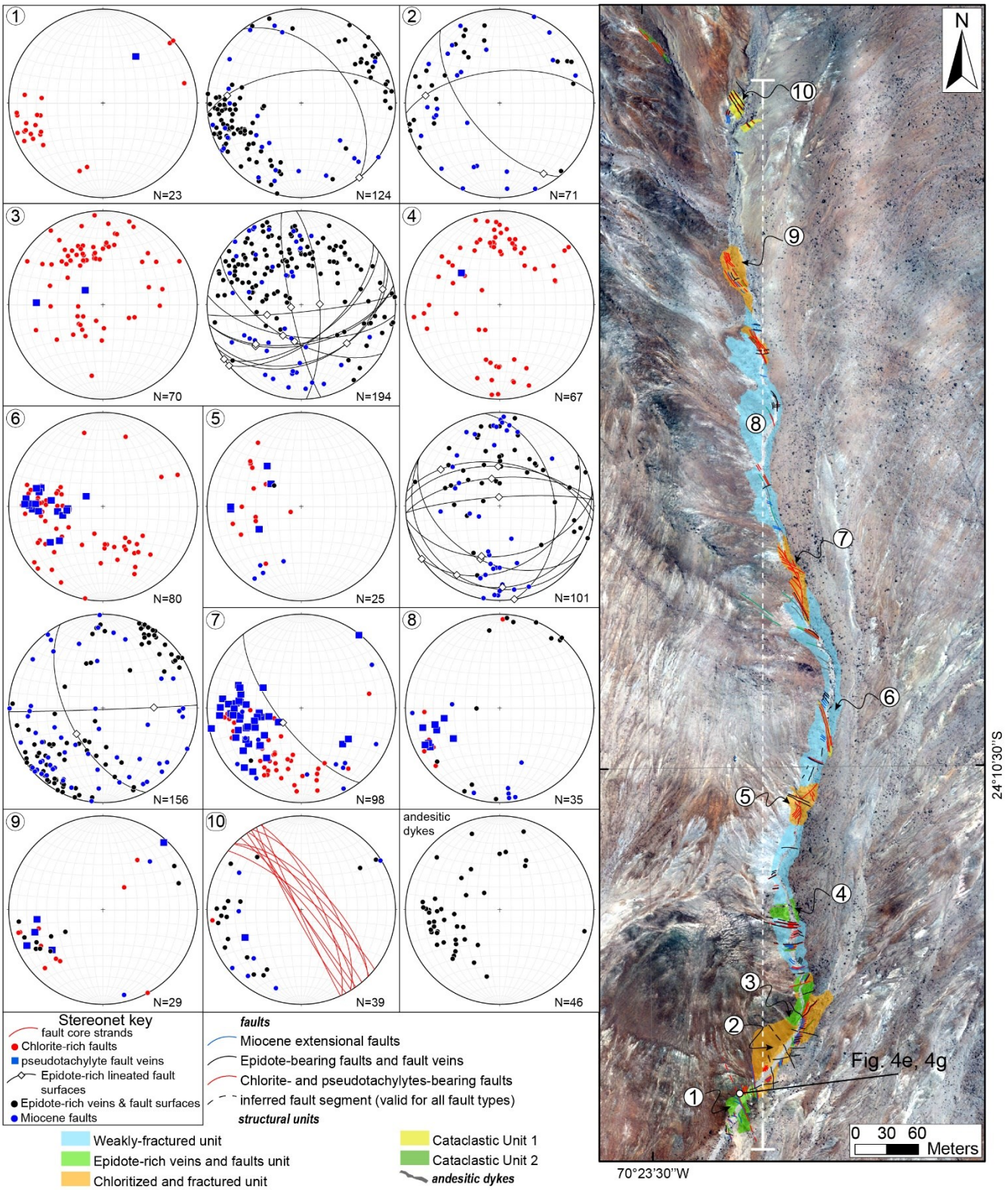

Fig. 11. Structural map of the distribution of the fault zone structural units and structural data at Quebrada Larga locality (southern segment). In the damage zone, pseudotachylyte-bearing faults exploited NE-dipping andesitic dykes and are associated with chloritized and fractured structural unit. Numbers in stereoplots denote the location of structural sites in the map.

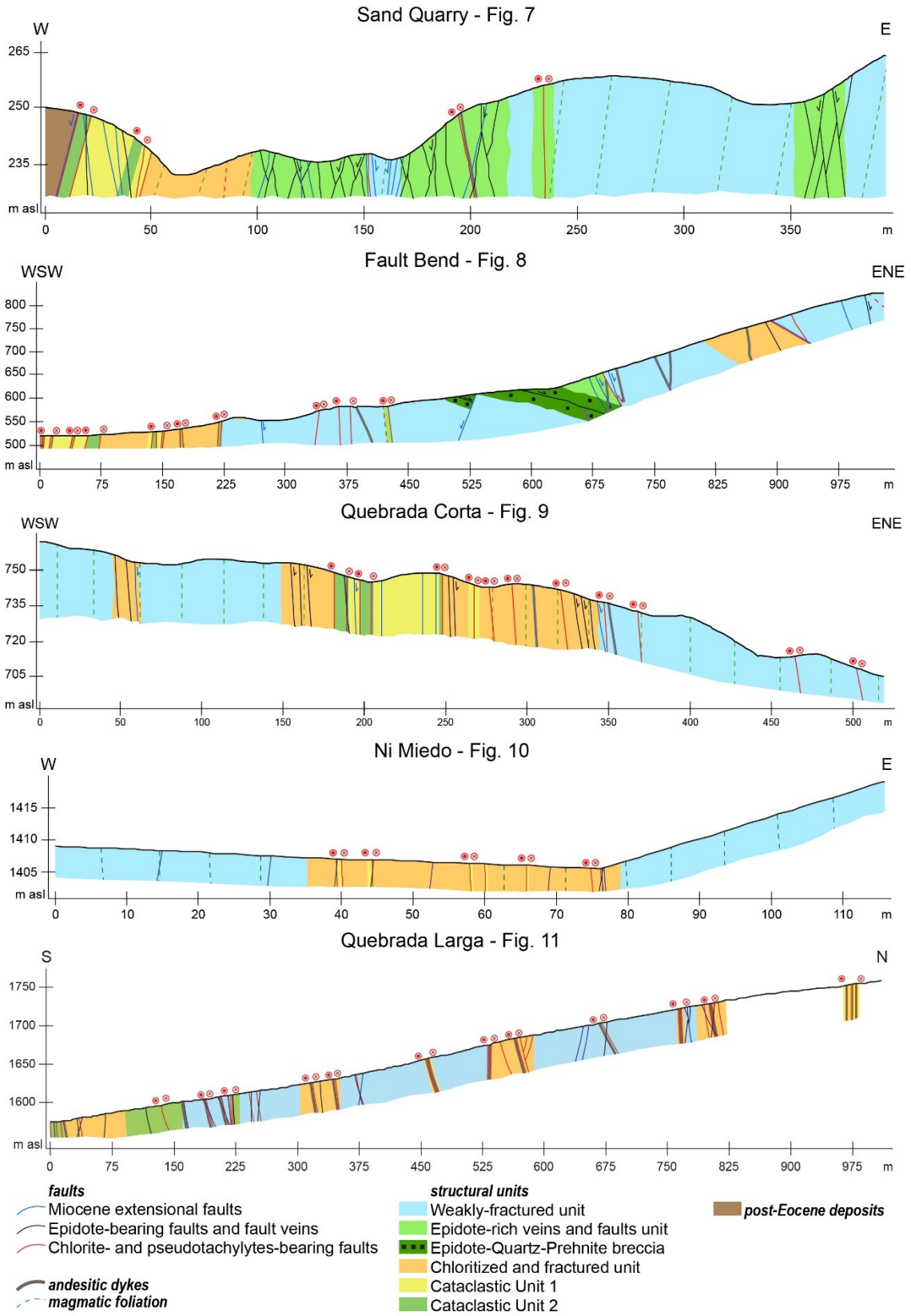

Fig. 12. Cross sections of the structural maps in Figs. 7-11. The cross sections are oriented perpendicular to fault strike, except for one from the Quebrada Larga locality which is at an angle of 45° with respect to the main fault trace. Scale changes from top to bottom for the cross sections.

In particular, the units CU1 + CU2, forming the fault core, increase in width from a minimum width of 25 m in the north, in the Sand Quarry locality, to maximum of 63 m in the central BFZ segment at the Quebrada Corta locality (Figs. 12-13). In this latter locality, the BFZ exploited the well-developed magmatic foliation of the plutons (Bolfin Complex). In the southern segment (Ni Miedo and Quebrada Larga localities; Cerro Cristales Pluton), the width of cataclastic units becomes thinner (Fig. 13b-c) and multiple CU1 strands are distributed among a zone wide up to hundreds of meters (Figs. 12-13).

The chloritized and fractured unit, spatially associated with the fault core units and subsidiary faults in the damage zone (Figs. 6-12), ranges in width between 37 and 58 m in the northern and central segments. The thickness is locally even larger, of as much as 150-200 m (at Fault Bend and Quebrada Larga localities), in association with splay faults in the damage zone. In the southern segment, the larger width is due to large number of pseudotachylyte-bearing faults exploiting andesitic dyke swarms (Figs. 11-12).

The distribution of the epidote-rich veins and faults unit varies strongly along the BFZ. This unit occurs as clusters, up to hundreds of meters wide, of sub-parallel faults associated with (1) NW-striking splay faults (i.e., linkage, forth-order faults of the Caleta Coloso Duplex; see Cembrano et al., 2005) (Figs. 7-8) and, (2) the intersection between NW- and NE-striking epidote-bearing faults (Figs. 7-8). The intersection between these two fault sets and fault/vein abundance strongly controls the across- and along-strike distribution of the clustering distribution of this structural unit. Indeed, where the occurrence of NE-striking epidote-bearing faults decreases, the degree of faulting and veining decreases as well.

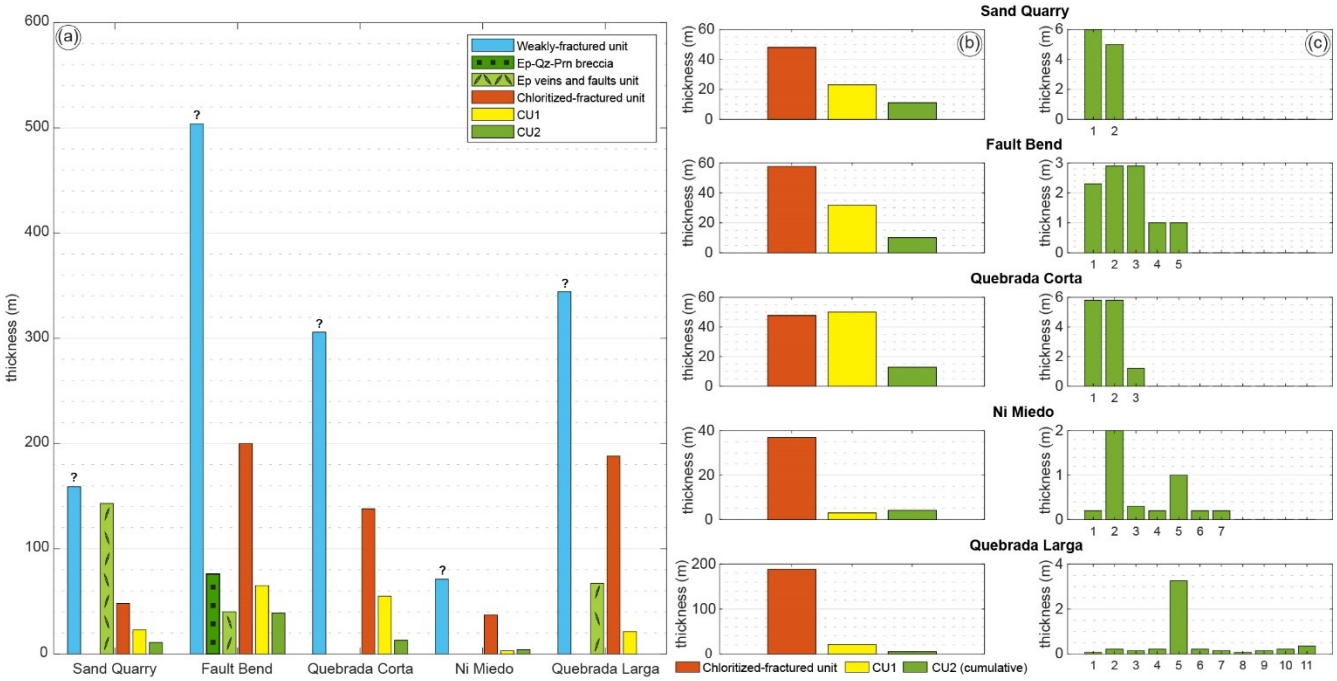

Fig. 13. Thickness of the structural units derived from the cross sections in Fig. 12. The cross sections are oriented perpendicular to fault strike, which is defined by the mean orientation of the CU2 strands at each locality. (a) Apparent thickness of the structural units derived from the cross sections in Fig. 12. The thickness of the weakly-fractured unit is affected by the cross section length, because of along-strike thickness variations in some localities. For Quebrada Larga locality, the thicknesses of structural units were corrected for the 45° orientation of the cross section to the BFZ main trance. (b) True thickness of the fault core units (= CU1 + CU2$^{(*)}$; $^{(*)}$: cumulative thickness of the multiple fault core strands) and the inner damage zone (= chloritized and fractured unit) associated with the fault core of the BFZ (= sensu stricto: no splay faults with their own chloritized domain). (c) True thickness of the multiple fault core strands, i.e. CU2, per each locality (Figs. 7-11).

Locality	Structural unit	Rock type	Qz	Pl	Kfs	Amp	Act	Bt/Ms[(*)]	Chl	Ep	Cal/Dol[(*)]	Prn	Crd	Spl	Ilt	Tnt	Gp
PE	Chloritized and fractured unit	altered protolith	15	36	4	28	3		13								
PE	CU1	cataclasite	39	35	2		1		12	3	4					3	
PE	CU1	cataclasite	40	36	5		0		5	7	3					2	
PE	CU2	foliated cataclasite	19	27	7		7		15	25							
PE	CU2	foliated cataclasite	27	31	5		8	1	15	2	7					3	
SQ	Weakly-fractured unit	protolith	18	34	20	18		7	7		1[(*)]						
SQ	Ep veins and faults unit	hydrothermal breccia	18	45			6		3	28							
SQ	Ep veins and faults unit	alteration halo	37	20	7		8		10	16						2	
SQ	Ep veins and faults unit	fault vein	46	7	7		2		3	31						3	
FB	Weakly-fractured unit	protolith		40		52		3	3						2		
FB	Ep-Qz-Prn breccia	hydrothermal breccia	32				0		18	21	1	26				2	
FB	Ep-Qz-Prn breccia	hydrothermal breccia	11				2		13	57	1	15				1	
QC	Weakly-fractured unit	protolith		67	4	9		7[(*)]	7	5			1	1			
QC	Chloritized and fractured unit	altered protolith	8	52		19	11		9				1				
QC	CU1	fault breccia	41	1	1				30		10				8		10
QC	Chloritized and fractured unit	2-cm-thick vein	44						3	49	4						
NM	Weakly-fractured unit	protolith	18	32	29	11		7	3								
QL	Weakly-fractured unit	protolith	10	50	3	23		6	5		1			2			
QL	Chloritized and fractured unit	altered protolith	27	42	11		3	6	11								
QL	CU1	foliated cataclasite	39	26	4			1	19	9	4						
QL	CU1	foliated cataclasite	31	38	13			3	13		2						
QL	Ep veins and faults unit	Ep vein	26	26					6	35		5				2	
QL	Ep veins and faults unit	Ep breccia	20							78	1					1	

Table 1. Modal composition of protolith and fault zone rocks from XRPD-RIR semi-quantitative analysis. PE: Playa Escondida; SQ: Sand Quarry; QC: Quebrada Corta; NM: Ni Miedo; QM: Quebrada Museo. Mineral abbreviations after Whitney and Evans (2010).

5. Microstructures and mineralogy of fault rocks

We describe the microstructures of the structural units forming the BFZ. The XRPD-RIR and EMPA analysis of the protolith and fault zone rocks and the mineral phases are reported in Tables 1 and 2, respectively.

5.1. Weakly-fractured unit

The weakly-fractured unit consists of meta-diorites (northern and central segments; protolith: Bolfin Complex) and tonalites-granodiorites (central segment; protolith: Cerro Cristales Pluton) with magmatic foliation, and isotropic tonalites-granodiorites (southern segment; protolith: Cerro Cristales Pluton). The meta-diorites consist of plagioclase ($Ab_{60}An_{39}Or_1$ to $Ab_{65}An_{35}Or_0$), quartz, biotite, and minor amphibole, K-feldspar, apatite and opaques (Table 1). The cm-sized idiomorphic plagioclase crystals define the magmatic foliation and the interstitial quartz shows weak undulose extinction. Instead, the magmatic texture is totally annealed at Quedrada Corta locality. The tonalites-granodiorites consist of plagioclase ($Ab_{47}An_{53}Or_0$ to $Ab_{62}An_{38}Or_0$), quartz, K-feldspar, amphibole, biotite, apatite and minor opaques (Fig. 2e; Table 1). The magmatic foliation is marked by cm-sized idiomorphic plagioclase crystals (see also González, 1999). Interstitial quartz crystals show weak undulose extinction (Fig. 2e).

5.2. Epidote-quartz-prehnite breccia

Epidote-quartz-prehnite breccia contain angular fragments of (i) protolith and (ii) earlier veins and breccias (Fig 14a). The latter are the most abundant (>95% in the studied samples) and show multiple generation of veining (Fig. 14a-b). The older vein generation consists of idiomorphic, zoned (i.e., core: Al-rich Ep; outer: Fe-rich Ep) epidote and minor quartz (Fig. 14b); the younger generation consists of quartz + zoned epidote + zoned prehnite ± chlorite (Fig. 14b). The host-rock fragments show pervasive chloritization of amphibole and biotite and albitization of plagioclase and are usually wrapped by concentric rims (up to 200-μm-thick) of prismatic, zoned (i.e., core: Fe-rich; outer: Al-rich) prehnite forming cockade textures (Fig. 14a). The late sealing cement consists of idiomorphic zoned epidote + quartz + zoned prehnite ± chlorite (Fig. 14c-d). Pores are common within the sealing cement and are < 150 μm in size (Fig. 14d).

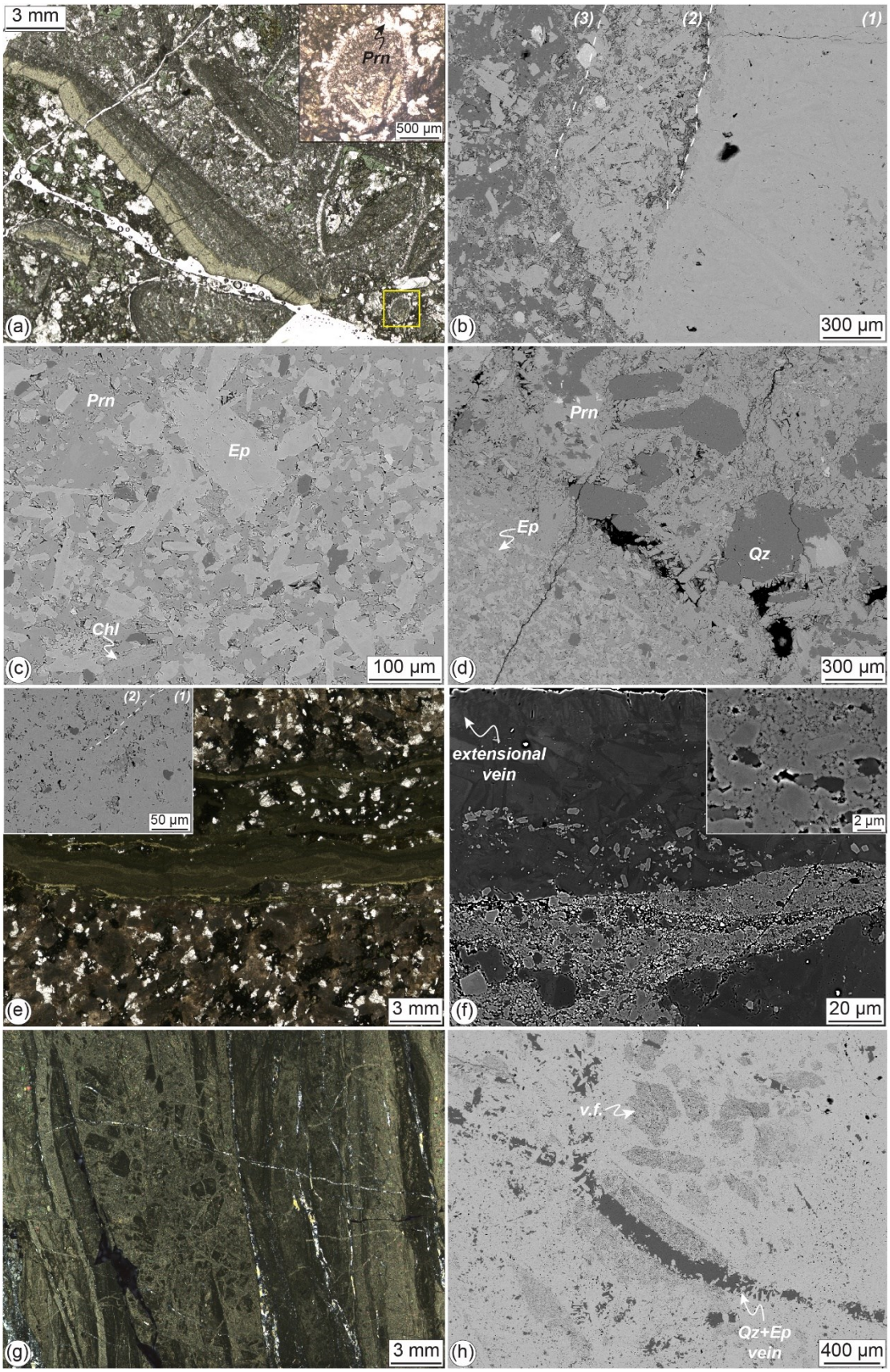

Fig. 14. Caption on next page.

Fig. 14. Microstructures of the epidote-quartz-prehnite breccia (a-d) and of the epidote-rich veins and faults unit (e-h). Mineral abbreviations: Ep = epidote, Prn = prehnite, Qz = quartz, Chl = chlorite. (a) The breccia includes fragments of early veins, which show different textures, and of altered host rock. Fragments are often wrapped by prismatic prehnite-built concentric rims forming cockade textures. The yellow box indicates the zoom of the inset on the top right corner. The inset shows a cockade. Plane-polarized light micrograph, sample 19-177. WGS GPS location: 23.93438°S, 70.46536°W. (b) Different vein textures: (1) cm-sized zoned epidote, (2) epidote + prehnite ± chlorite, (3) sealing cement of epidote, quartz, prehnite and chlorite. BSE image, sample M2. WGS GPS location: 23.934563°S, 70.465428°W. (c) Detail of the sealing cement. BSE image, sample 19-177. (d) Idiomorphic quartz and epidote forming the sealing cement. BSE image, 19-177. (e) Polyphase epidote-bearing vein and cataclasite with the associated alteration halo in the damaged host rock. Plane-polarized light thin section scan, sample 19-48. WGS GPS location: 23.88442°S, 70.48567°W. The top left inset shows the different fabric of the epidote vein (1) and the cataclasite (2). The epidote vein (1) has a grain size of ~20-30 μm (green epidote in hand specimen shown in Fig. 4b); instead, the epidote cataclasite (2) has a finer grain size (<10 μm) and more porous framework (pale green epidote in hand specimen shown in Fig. 4b). The dashed white line marks the boundary between the vein and the cataclasite. BSE image. (f) Microstructure of an epidote-rich shear vein showing multiple events of veining and shearing. The ultracataclasite defining the slip zone of a discrete polished surface includes fragments of zoned epidote (light grey) and prehnite (dark grey). The inset shows that ultracataclasite includes epidote nanoparticles. (g) Epidote-bearing breccia. The angular fragments consist of earlier epidote veins (dark green), sealed by fine-grained epidote cement (lighter green). Cross-polarized light thin section scan, sample 19-70. WGS GPS location: 24.17783°S, 70.39077°W. (h) Highly porous fragments of earlier epidote veins (v.f.) are sealed by epidote cement with similar composition. The breccia is cut by quartz-epidote veins. BSE image, sample 19-70.

5.3. Epidote-rich veins and faults unit

Epidote-rich extensional veins show multiple episodes of veining and include fragments of the host rock and of earlier veins (Fig. 14e, 14g-h). The latter are the most abundant. The epidote veins (dark green epidote in hand specimen) consist of zoned epidote (Al-rich core and Fe-rich rim), with a grain size of ~20-30 μm, and minor interstitial K-feldspar (Fig. 14f). Younger cataclasites (pale green in the hand specimen) reworking the epidote veins have fine-grained (<10 μm) epidote grains and a highly porous framework (pores size up to ~5 μm) (Fig. 14f). Shear veins defining discrete polished fault surfaces (Fig. 4d) show cyclic events of veining and localized shearing (Fig. 14f). Veins consist of zoned epidote and prehnite (Fig. 14f). The slip zones of the polished fault surfaces consist of very fine-grained (<1 μm) ultracataclasites (Fig. 14f). Breccias include fragments of earlier epidote veins, which consist of fine (<5 μm) epidote grains and have a highly porous framework (Fig. 14g-h). The sealing cement consists of fine (<20 μm) epidote grains (Fig. 14h). Fault veins and breccia are locally cut by mm-thick veins filled with quartz and minor epidote (Fig. 14g-h). Epidote-bearing veins, breccias and faults are associated with pervasive fluid-induced alteration in the surrounding damaged host rock. Within the alteration halo, plagioclase is replaced by albite, and biotite and amphibole by chlorite ± opaques (Table 2). Microfractures are filled with epidote + K-feldspar.

5.4. Chloritized and fractured unit

Chloritized and fractured unit contains a pervasive network of microfractures and veins whose spatial density increases towards to the fault core. Veins are filled by chlorite, epidote and chlorite + epidote ± quartz association. Magmatic minerals show intense alteration (Fig. 2f). Plagioclase is either altered to fine-grained sericite + calcite ± epidote or replaced by albite (Table 2). Amphibole is replaced by either (Fe-)actinolite or chlorite and opaques. Biotite is replaced by chlorite and opaques. Quartz shows locally undulose extinction and healed microfractures marked by fluid inclusion trails. K-feldspar is fractured and micro-faulted. Micro-stylolite seams are common in the chloritized and fractured structural unit and are sub-parallel to cataclasites.

5.5. Cataclastic Unit (CU1 and CU2)

Protocataclasites to ultracataclasites consist of fine-grained (<20 μm) chlorite + epidote + quartz + albite + K-feldspar, including angular clasts of albitized plagioclase, quartz, earlier cataclasites (Fig. 15a-b). Quartz clasts show undulose extinction and is locally recrystallized into fine-grained aggregates along grain boundaries and microfractures (see Fig. 10e in Masoch et al., 2021). The thickest cataclasites are layered (Fig. 15a). Cataclasites and ultracataclasites are foliated in the high-strain horizons with the composite S-C-C' foliation defined by either chlorite (Fig. 15a) or epidote + K-feldspar aggregates, enveloping sheared lithons of albitized plagioclase and quartz (Fig. 15c). Lenses of calcite are present in the protocataclasites and cataclasites (Fig. 15a).

5.6. Pseudotachylytes

Pseudotachylytes show flow structures, chilled margins, microlites (Fig. 15d) and spherulites (e.g., Magloughlin and Spray, 1992; Swanson, 1992) and are variously affected by alteration. Less altered pseudotachylytes include (i) albite microlites, intergrown with amphibole and titanite (Fig. 15d; Table 2), (ii) quartz and plagioclase clasts immersed in a homogeneous cryptocrystalline matrix with a "K-feldspar-rich" composition (Table 2). More altered pseudotachylytes consist of a fine-grained (~20-30 μm grain size) matrix of albite + chlorite + epidote (Fig. 15e). Pseudotachylytes cut chlorite + epidote ± calcite-bearing veins and are cut by chlorite-, K-feldspar- and calcite-bearing veins. Some pseudotachylytes include amygdalae or vesicles filled by quartz + calcite + epidote + chlorite (Fig. 15f; see Gomila et al., 2021 for further details).

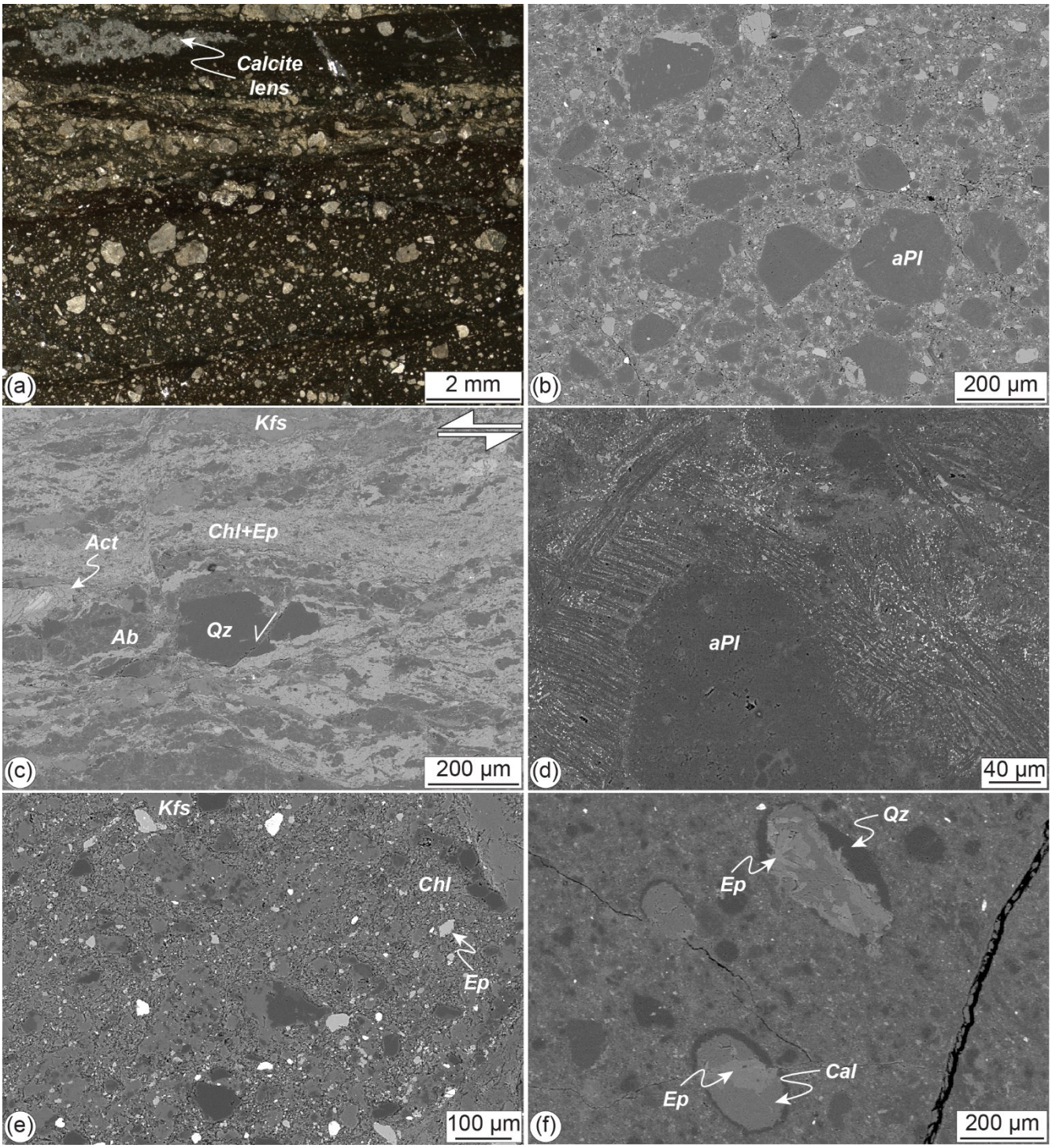

Fig. 15. Caption on next page.

Fig. 15. Microstructures of the cataclastic units, CU1 and CU2, and associated pseudotachylytes. Mineral abbreviation: Qz = quartz, Kfs = K-feldspar, Ab = albite, aPl = altered plagioclase, Act = actinolite, Chl = chlorite, Ep = epidote. (a) Layered cataclasite to ultracataclasite from the CU2. Plane-polarized light microphotograph, sample SQ05-A. WGS GPS location: 23.883067°S, 70.488031°W. (b) Detail of the cataclasite in (a). Clasts consist mainly of quartz and altered plagioclase. Cuspate-lobate quartz clasts have the concavity decorated by chlorite. The light-gray matrix includes chlorite, epidote and K-feldspar. BSE image, sample SQ05-A. (c) Foliated cataclasite from the CU2. Domino structure indicated sinistral sense of shear. Sheared lithons of albitized plagioclase and quartz are immersed in a matrix of chlorite, epidote, K-feldspar and actinolite. The foliation is defined by epidote and K-feldspar. BSE image, sample PE02-18. WGS84 GPS location: 23.849894°S, 70.503236°W. (d) Microlites of plagioclase (medium grey) and K-feldspar (dark grey), and interstitial acicular biotite and titanite (bright color) in a poorly altered pseudotachylyte fault vein. The microlites wrap a plagioclase clast with spinifex microstructure. BSE image, sample SQ09-18. WGS84 GPS location: 23.8830972°S, 70.4880111°W. (e) Altered pseudotachylyte. The pseudotachylyte fault vein is altered into a fine-grained chlorite, epidote, albite and K-feldspar. BSE image, sample 19-91A. WGS84 GPS location: 24.1747900°S, 70.3899600°W. (f) Vesiculated pseudotachylyte. Elliptical amygdalae filled with quartz, calcite, epidote and chlorite. BSE image, sample AT07-2017. WGS84 GPS location: 23.8498611°S, 70.5032555°W.

Locality	Playa Escondida													
Structural unit	CU1													
Rock type	cataclasites						pseudotachylytes with vesicles							
Mineral phase	Chl		Ep		Act		Ab matrix		Kfs matrix		Pl clasts		Amp microlites	
N° of point analysis	16	s.d.	3	s.d.	2	s.d.	3	s.d.	16	s.d.	3	s.d.	5	s.d.
component (wt%)														
Na_2O	0.02	0.03	0.00	0.01	0.18	0.03	7.56	0.38	1.52	0.96	8.32	0.54	1.85	0.39
MgO	15.03	0.53	0.02	0.01	17.37	0.07	0.09	0.10	0.41	0.29	0.08	0.02	8.62	2.73
Al_2O_3	19.56	0.78	21.65	0.23	2.68	1.61	24.39	0.39	17.90	1.01	23.67	0.51	13.55	1.83
SiO_2	26.55	0.79	37.33	0.26	53.16	2.48	60.14	0.31	64.86	1.94	63.10	0.86	47.23	4.86
K_2O	0.05	0.07	0.00	0.00	0.05	0.01	0.55	0.27	12.53	2.50	0.30	0.17	2.95	2.01
CaO	0.09	0.08	23.12	0.23	11.59	1.28	6.01	0.31	1.08	1.04	5.31	0.62	6.48	1.39
TiO_2	0.05	0.02	0.09	0.05	0.05	0.04	0.06	0.03	0.19	0.19	0.05	0.02	1.97	1.01
Cr_2O_3	0.02	0.02	0.02	0.02	0.02	0.00	0.00	0.00	0.01	0.02	0.00	0.00	0.00	0.00
MnO	0.48	0.05	0.13	0.05	0.32	0.04	0.02	0.01	0.03	0.03	0.03	0.03	0.34	0.10
FeO	26.17	0.58	14.27	0.18	12.22	1.23	0.64	0.43	1.34	0.74	0.37	0.07	14.34	3.38
P_2O_5	-	-	-	-	-	-	-	-	-	-	-	-	-	-
Total	88.02	0.30	96.64	0.10	97.65	0.68	99.45	0.40	99.85	1.01	101.23	0.83	97.33	1.51

Locality	Playa Escondida											
Structural unit	CU2											
Rock type	foliated cataclasites											
Mineral phase	Amp fragments		Act - alteration		Chl matrix		Ep matrix		Ab HR lithons		Kfs HR lithons		Wm HR lithons	
N° of point analysis	7	s.d.	1		4	s.d.	3	s.d.	5	s.d.	3	s.d.	3	s.d.
component (wt%)														
Na_2O	0.80	0.10	0.13		0.13	0.06	0.07	0.01	9.44	0.50	0.82	0.10	0.84	0.59
MgO	12.88	0.36	16.43		18.46	0.35	0.20	0.09	0.11	0.04	0.15	0.12	0.61	0.38
Al_2O_3	7.00	0.97	1.04		19.36	0.41	24.52	0.29	22.25	0.78	20.84	1.44	33.97	2.03
SiO_2	48.08	1.37	55.24		28.74	0.69	37.85	0.27	64.65	0.83	62.66	1.59	50.09	1.06
K_2O	0.43	0.22	0.01		0.11	0.05	0.04	0.03	0.32	0.20	14.48	0.12	9.62	1.10
CaO	11.65	0.44	12.85		0.20	0.17	22.80	0.32	2.69	0.68	0.17	0.05	0.28	0.28
TiO_2	0.64	0.48	0.22		0.02	0.02	0.30	0.26	0.04	0.03	0.04	0.04	0.06	0.05
Cr_2O_3	0.06	0.03	0.08		0.06	0.04	0.04	0.04	0.04	0.03	0.05	0.02	0.03	0.02
MnO	0.26	0.05	0.17		0.29	0.03	0.26	0.04	0.02	0.01	0.04	0.03	0.06	0.05
FeO	15.88	0.51	12.86		21.90	0.37	11.76	0.96	0.27	0.09	0.39	0.22	1.56	0.74
P_2O_5	0.04	0.02	0.03		0.03	0.01	0.11	0.10	0.03	0.02	0.04	-	0.06	-
Total	97.68	0.41	99.06		89.29	0.86	97.87	0.23	99.84	0.35	99.64	0.04	97.11	0.32

Locality	Playa Escondida				Sand Quarry									
Structural unit	CU2				Weakly-fract.		Ep unit							
rock type	foliated cataclasites				protolith		alteration halo of Ep slickenfiber							
Mineral phase	Ab fragments		Kfs matrix		Pl		Kfs		Ab		Amp		Chl - Amp alter	
N° of point analysis	3	s.d.	6	s.d.	12	s.d.	8	s.d.	17	s.d.	5	s.d.	11	s.d.
component (wt%)														
Na_2O	8.85	0.48	0.34	0.21	7.10	0.25	0.19	0.04	11.21	0.30	1.37	0.11	0.04	0.02
MgO	0.07	0.02	0.06	0.02	0.13	0.22	0.08	0.03	0.06	0.02	10.94	0.89	15.27	0.40

Al_2O_3	23.42	1.13	18.85	0.12	25.40	0.51	18.98	0.25	20.00	0.35	7.89	1.21	18.40	0.69
SiO_2	63.40	1.31	64.50	0.47	58.38	0.52	64.43	0.17	67.76	0.98	45.32	1.80	27.68	0.36
K_2O	0.14	0.02	16.10	0.33	0.20	0.13	16.44	0.27	0.07	0.02	0.95	0.27	0.05	0.05
CaO	4.01	1.11	0.00	-	7.66	0.32	0.01	-	0.26	0.09	11.43	0.11	0.09	0.05
TiO_2	0.08	0.07	0.06	0.03	0.01	0.01	0.07	0.03	0.05	0.03	1.36	0.25	0.15	0.17
Cr_2O_3	0.03	0.03	0.04	0.03	0.01	0.01	0.03	0.01	0.04	0.03	0.06	0.01	0.09	0.03
MnO	0.02	0.01	0.04	0.01	0.01	0.01	0.04	0.03	0.02	0.01	0.36	0.04	0.28	0.04
FeO	0.22	0.02	0.33	0.09	0.13	0.06	0.14	0.12	0.09	0.06	18.77	1.17	28.26	0.44
P_2O_5	0.02	0.01	0.02	0.01	-	-	0.04	0.01	0.02	0.02	0.05	0.04	0.03	0.02
Total	100.24	0.52	100.30	0.54	99.04	0.53	100.34	0.57	99.50	1.24	98.47	0.47	90.29	0.59

Locality	**Sand Quarry**													
Structural unit	Ep unit													
rock type	Ep slickefiber						alteration halo of Ep polypahse vein							
Mineral phase	Ep subeuhdral		Ep slip zone		Kfs fragments		Kfs		Ab		Ep		Ep - Pl alter	
N° of point analysis	8	s.d.	5	s.d	4	s.d.	7	s.d.	10	s.d.	3	s.d.	2	s.d.
component (wt%)														
Na_2O	0.05	0.02	0.03	0.02	0.18	0.04	0.23	0.16	11.34	0.26	0.04	-	0.02	0.01
MgO	0.19	0.10	0.10	0.04	0.05	0.02	0.08	0.01	0.07	0.02	0.26	0.21	0.12	0.01
Al_2O_3	25.21	0.82	24.98	0.69	19.30	0.15	18.74	0.15	20.14	0.21	25.27	0.49	27.25	0.08
SiO_2	37.61	0.26	37.96	0.26	64.81	0.25	64.44	0.26	68.03	0.55	38.14	0.11	37.43	0.16
K_2O	0.01	0.00	0.02	0.02	16.54	0.27	16.53	0.38	0.06	0.02	0.04	0.02	-	-
CaO	23.23	0.26	22.97	0.21	-	-	0.01	-	0.20	0.07	23.30	0.29	23.46	0.16
TiO_2	0.26	0.36	0.11	0.05	0.06	0.03	0.07	0.05	0.03	0.03	0.22	0.17	0.06	0.04
Cr_2O_3	0.04	0.03	0.03	0.03	0.04	0.03	0.04	0.03	0.03	0.04	0.03	-	0.03	-
MnO	0.10	0.05	0.11	0.02	0.01	-	0.03	0.03	0.03	0.01	0.06	0.04	0.23	0.02
FeO	11.29	0.94	11.35	0.72	0.13	0.06	0.08	0.04	0.05	0.03	11.02	0.09	9.13	0.77
P_2O_5	0.03	0.02	0.02	-	0.03	0.01	0.02	0.02	0.04	0.02	0.02	0.01	0.04	0.05
Total	97.96	0.42	97.63	0.46	101.08	0.59	100.19	0.60	99.95	0.62	98.34	0.47	97.74	1.08

Locality	**Sand Quarry**													
Structural unit	Ep unit								CU1					
rock type	Ep polyphase vein								Altered pseudotachylyte					
Mineral phase	Ep $vein_1$		Chl $vein_1$		Ep $vein_2$ - core		Ep $vein_2$ - rim		Chl		Ab microlites		Kfs matrix	
N° of point analysis	9	s.d.	3	s.d.	8	s.d	6	s.d.	12	s.d.	49	s.d.	16	s.d.
component (wt%)														
Na_2O	0.03	0.02	0.02	0.02	0.03	0.02	0.03	0.02	0.05	0.04	7.82	2.01	0.77	0.77
MgO	0.24	0.41	17.95	0.43	0.11	0.04	0.11	0.04	17.48	0.33	0.65	1.20	0.11	0.04
Al_2O_3	24.70	1.01	18.59	0.28	24.84	1.03	27.45	0.84	20.66	0.33	17.42	2.95	17.63	0.94
SiO_2	37.57	0.44	27.38	0.44	37.65	0.11	38.21	0.42	26.65	0.50	65.35	6.32	66.14	1.99
K_2O	0.03	0.02	0.04	0.01	0.04	0.02	0.03	0.00	0.03	0.02	2.24	1.92	14.97	1.60
CaO	23.35	0.63	0.09	0.02	22.72	0.57	23.32	0.51	0.10	0.04	2.03	1.61	0.18	0.31
TiO_2	0.07	0.05	0.12	0.05	0.05	0.03	0.09	0.04	0.06	0.04	0.62	1.62	0.02	0.03
Cr_2O_3	0.05	0.03	0.03	0.02	0.04	0.02	0.05	0.01	0.02	0.02	0.00	0.00	0.00	0.00
MnO	0.07	0.06	0.25	0.02	0.32	0.25	0.16	0.12	0.58	0.04	0.04	0.05	0.02	0.03
FeO	11.99	1.30	24.02	0.65	11.90	1.16	8.39	1.12	23.05	0.38	3.50	2.19	0.25	0.19

P_2O_5	0.02	0.01	0.03	0.02	0.08	0.03	0.05	0.02	-	-	-	-	-	-
Total	98.06	0.52	88.51	0.32	97.71	0.68	97.82	0.57	88.68	0.58	99.68	1.99	100.10	1.39
Locality	**Sand Quarry**								**Fault Bend**					
Structural unit	CU2								EQP br.					
rock type	ultracataclasites								breccia					
Mineral phase	Ab fragments		Chl		Ep fragments		Tnt		Ep vein$_1$		Ep vein$_2$		Ep vein$_3$	
N° of point analysis	8	s.d.	7	s.d.	8	s.d.	1	s.d.	6	s.d.	4	s.d.	4	s.d.
component (wt%)														
Na_2O	11.12	0.58	0.02	0.02	0.02	0.02	-	-	0.05	0.03	0.04	0.02	0.03	0.01
MgO	0.06	0.03	17.40	0.39	0.11	0.03	0.09	-	0.10	0.02	0.19	0.12	0.68	0.59
Al_2O_3	20.33	0.48	20.69	0.50	25.31	0.74	1.14	-	26.14	1.01	24.75	0.88	25.22	1.07
SiO_2	67.13	1.03	26.35	0.18	37.82	0.23	30.29	-	38.00	0.34	37.94	0.48	38.18	0.83
K_2O	0.09	0.03	0.02	0.02	0.02	0.01	0.05	-	0.01	0.01	0.02	-	0.03	0.00
CaO	0.64	0.58	0.07	0.04	22.99	0.50	27.71	-	22.87	0.62	22.95	0.52	22.56	0.73
TiO_2	0.04	0.02	0.04	0.03	0.06	0.05	37.40	-	0.06	0.05	0.09	0.07	0.06	0.02
Cr_2O_3	0.04	0.02	0.05	0.03	0.04	0.03	0.10	-	0.03	0.03	0.06	0.03	0.03	0.02
MnO	0.02	0.01	0.41	0.02	0.24	0.20	0.06	-	0.46	0.32	0.17	0.14	0.13	0.06
FeO	0.21	0.14	23.81	0.50	11.17	0.55	0.80	-	10.29	1.12	11.94	1.54	10.75	0.46
P_2O_5	0.03	0.02	0.03	0.04	0.07	0.05	0.08	-	0.07	0.05	0.04	0.02	0.05	0.01
Total	99.66	0.89	88.86	0.67	97.80	0.80	97.72	-	98.05	0.22	98.14	0.67	97.65	0.79
Locality	**Fault Bend**										**Ni Miedo**			
Structural unit	EQP br.										Weakly-fractured unit			
rock type	breccia		cockade breccia								protolith			
Mineral phase	Prn - cement		Prn - cockade		Prn - cement		Ep - cement		Chl - cement		Pl		Amp	
N° of point analysis	3	s.d.	4	s.d.	14	s.d.	3	s.d.	7	s.d.	11	s.d.	4	s.d.
component (wt%)														
Na_2O	0.02	0.02	0.03	0.03	0.03	0.03	0.03	0.01	0.05	0.02	6.41	0.49	1.12	0.08
MgO	0.09	0.04	0.10	0.03	0.09	0.03	0.68	0.59	17.36	0.88	0.00	0.01	13.23	0.77
Al_2O_3	23.82	1.26	24.71	0.27	23.42	0.41	25.22	1.07	19.85	0.40	26.71	0.76	7.90	0.31
SiO_2	43.07	0.16	43.54	0.21	43.26	0.34	38.18	0.83	27.99	0.80	56.88	1.15	46.38	0.60
K_2O	0.02	0.01	0.03	0.04	0.02	0.01	0.03	0.00	0.03	0.02	0.09	0.03	0.34	0.06
CaO	26.73	0.41	26.45	0.32	26.63	0.30	22.56	0.73	0.12	0.06	8.89	0.91	11.23	0.30
TiO_2	0.03	0.02	0.05	0.03	0.13	0.08	0.06	0.02	0.10	0.04	0.00	0.01	1.42	0.28
Cr_2O_3	0.09	0.01	0.05	0.02	0.03	0.03	0.03	0.02	0.02	0.02	0.01	0.01	0.02	0.02
MnO	0.06	0.01	0.10	0.03	0.03	0.03	0.13	0.06	0.35	0.06	0.02	0.02	0.83	0.11
FeO	2.09	1.76	0.71	0.08	2.09	0.51	10.75	0.46	23.87	1.01	0.09	0.02	13.95	1.09
P_2O_5	0.08	-	0.03	0.01	0.02	0.01	0.05	0.01	0.03	0.02	-	-	-	-
Total	96.00	0.20	95.74	0.51	95.71	0.46	97.65	0.79	89.70	0.62	99.11	0.37	96.39	0.21
Locality	**Quebrada Larga**													
Structural unit	Ep unit													
rock type	alteration halo						Ep vein				Ep breccia			
Mineral phase	Pl		Kfs		Ep		Ep - cement		Kfs		Ep - cement		Ep - Qz vein	
N° of point analysis	9	s.d.	10	s.d.	2	s.d.	8	s.d.	4	s.d.	10	s.d.	4	s.d.
component (wt%)														

Na_2O	10.96	0.16	0.31	0.05	-	-	0.03	0.03	0.30	0.02	0.08	0.03	0.04	0.00
MgO	0.06	0.02	0.08	0.02	0.13	0.07	0.15	0.05	0.08	0.01	0.10	0.02	0.10	0.02
Al_2O_3	21.09	0.33	19.11	0.18	24.60	0.46	25.75	0.66	19.13	0.08	25.25	0.65	25.54	0.74
SiO_2	66.91	0.37	64.22	0.38	37.78	0.21	37.92	0.24	64.63	0.15	37.94	0.23	37.75	0.34
K_2O	0.11	0.09	16.36	0.22	0.03	0.01	0.04	0.02	16.41	0.15	0.02	0.01	0.02	0.00
CaO	1.00	0.18	0.01	0.01	23.64	0.29	23.28	0.32	0.03	0.03	23.16	0.27	23.29	0.37
TiO_2	0.03	0.02	0.05	0.03	0.21	0.24	0.12	0.09	0.05	0.01	0.10	0.08	0.13	0.09
Cr_2O_3	0.03	0.02	0.05	0.02	0.01	0.01	0.04	0.01	0.03	0.02	0.04	0.01	0.03	0.03
MnO	0.02	0.02	0.04	0.03	0.10	0.00	0.16	0.12	0.04	0.02	0.17	0.11	0.22	0.10
FeO	0.04	0.02	0.05	0.05	11.56	0.04	10.83	0.65	0.16	0.12	11.19	0.97	10.81	0.76
P_2O_5	0.02	0.01	0.03	0.01	-	-	0.09	0.05	0.01	0.00	0.07	0.02	0.08	0.04
Total	100.23	0.56	100.23	0.44	98.05	0.12	98.36	0.32	100.82	0.25	98.02	0.36	97.95	0.74

Table 2. Mineral phase compositions of host rocks and fault zone rocks as obtained from EMPA analysis. EQP br: Epidote-Quartz-Prehnite breccia; alter: alteration. Mineral abbreviation after Whitney and Evans (2010).

6. Discussion

6.1. Architecture of exhumed seismogenic faults in the crystalline basement

Pseudotachylytes are the most reliable indicator of seismic slip in the geological record (Cowan, 1999; Rowe and Griffith, 2015; Sibson, 1975) and occur along the whole length of the BFZ (Masoch et al., 2021; and this work). Pseudotachylytes were likely more widespread in the BFZ than reported, since they can be easily erased by alteration and become difficult to distinguish from chlorite-epidote-K-feldspar-bearing cataclasites (Fondriest et al., 2020b). Ambient conditions of seismic faulting along the BFZ has been constrained at 5-7 km depth, ≤ 300 °C and in presence of fluids (Masoch et al., 2021). These conditions are typical of earthquakes nucleation and propagation in the uppermost continental crust (Scholz, 2019). Given the fault length (>40 km) and the widespread occurrence of pseudotachylytes, the BFZ can be considered an exhumed crustal-scale seismogenic source capable to have generated moderate- to large-in-magnitude (up to M_w 6.5-7.0) earthquakes.

The architecture of the BFZ shares features with other crustal-scale seismogenic fault zones cutting crystalline rocks and exhumed from 5-15 km depth. These fault analogues of the BFZ include the Caleta Coloso Fault Zone of the Atacama Fault System (hosted in foliated granodiorites and tonalites: Arancibia et al., 2014; Cembrano et al., 2005; Faulkner et al., 2008; note that we recently found that also this fault zone has pseudotachylytes: unpublished data) and the Alpine Fault in New Zealand (hosted in granites, gneiss and quartz-feldspathic schist: Sutherland et al., 2012; Toy et al., 2015; Williams et al., 2018, 2017, 2016). These crustal-scale seismogenic faults show hydrothermally altered, multiple, high-strain fault cores (similar to CU2 in this work) and lower-strained cataclastic strands (i.e., CU1 in BFZ). The fault core as wide as tens to

hundreds of meters is surrounded by altered and damaged rock volumes in the inner damage zone (the chloritized and fractured unit in the BFZ) referred to as alteration zone along the Alpine Fault (Sutherland et al., 2012). In the case of the BFZ, pseudotachylytes are distributed across the fault core units as well as across the associated strongly altered and weakly-fractured damage zones (Figs. 5-11). This suggests that deformation and seismicity were spatially distributed among complex, linked strands over a >100-m-wide damaged zone. Comparable with the BFZ, other exhumed seismogenic faults, hosted in crystalline rocks, present a wide damage zone associated with distributed deformation and ancient seismicity (i.e., widespread occurrence of pseudotachylytes across the fault zone) (e.g., the Gole Larghe Fault Zone and Gole Strette Fault Zone in the Adamello batholith: Di Toro and Pennacchioni, 2005; Mittempergher et al., 2021; Pennacchioni et al., 2006; Smith et al., 2013; the Glacier Lakes Fault in the Sierra Nevada batholith: Griffith et al., 2008; Kirkpatrick et al., 2008; the Fort Foster Brittle Zone in Maine: Swanson, 2006b, 1988). Specifically, the Gole Larghe Fault Zone has multiple 2-m-thick cataclastic fault core strands, shows pseudotachylyte-bearing faults over a zone as wide as 600 m (Smith et al., 2013) and accommodated a cumulative displacement of 1-2 km (Di Toro and Pennacchioni, 2005; Mittempergher et al., 2021; Smith et al., 2013). Instead, the Caleta Coloso Fault Zone presents a ~200-300-m-wide fault core with multiple high-strain cataclastic strands and accommodated >5 km of displacement (Arancibia et al., 2014; Faulkner et al., 2008), similar to the BFZ, although the displacement accommodated by the BFZ is not well constrained and could be lower. As a consequence, the Gole Larghe Fault Zone may represent a less evolved continental fault zone than the BFZ and Caleta Coloso Fault Zone of the Atacama Fault System.

In the aforementioned cases, except for the Caleta Coloso Fault Zone, cataclasites and associated pseudotachylytes nucleated along precursory anisotropies (i.e., joints, magmatic foliations of plutons, dykes and metamorphic and mylonitic foliations) at early stages of fault evolution. In turn, seismic ruptures nucleate on precursory anisotropies, especially at the early stages of fault evolution, and then localized cataclastic bands coalescence into well-developed cataclastic fault core strands with progressive slip accumulation. Nevertheless, such exhumed seismogenic faults present (i) a wide damaged zone (fault core + inner damage zone) associated with distributed pseudotachylytes-bearing faults, and (ii) a strongly hydrothermal altered damage zone, whose thickness and distribution varies as a function of the fault length and other parameters discussed below. This fault architecture results from several cycles of (i) co-seismic frictional melting and pervasive damaging of the surrounding host rocks, and (ii) inter- to post-seismic fault healing and sealing due to hydrothermal precipitation of mechanically strong (K-feldspar, epidote), or weak (chlorite) minerals inducing fault strengthening/weakening and fault core widening/localization. The thicknesses of the fault core units and the associated inner damage zone present the following trend: CU2 < CU1 < chloritized and

fractured unit, with the exception of Ni Miedo locality (Fig. 13b). This trend might suggest strain localization within the CU2 strands and fault weakening, induced by progressive chloritization of the protolith (Fig. 2a-d, 2e) and diffusive precipitation of chlorite, especially in the cataclastic rocks (Figs. 5, 15). Nevertheless, the XRPD-RIR analysis does not show any marked increase in mass fraction of chlorite in the CU2 compared to the chloritized and fractured unit and CU1 (Table 1). Indeed, most of the samples share the same mass fraction of chlorite (ranging from 9% to 15%). On the contrary, some CU2 foliated cataclasites show a predominant increase in K-feldspar (up to 13%) and, especially, epidote (up to 25%) (Table 1), which also define the foliation (Fig. 15c). Thus, fault weakening and fault core localization were accompanied by fault strengthening and fault core widening at different stages of fault evolution. In turn, differential hydrothermal precipitation controlled the spatio-temporal evolution of the BFZ architecture, promoting weakening or re-strengthening of each CU2 strand.

This mechanism of fault core widening by fault re-strengthening has been proposed for the Gole Larghe Fault Zone (Di Toro and Pennacchioni, 2005, 2004; Smith et al., 2013) and the Caleta Coloso Fault Zone (Arancibia et al., 2014; Cembrano et al., 2005). In seismogenic faults, solidification of quenched frictional melts (pseudotachylyte) may also result in welding of original slip surfaces and promote migration of new incremental slips and earthquake ruptures to available adjacent un-healed surfaces (Di Toro and Pennacchioni, 2005; Mitchell et al., 2016). However, most pseudotachylyte-bearing faults within the BFZ fault core show fault reactivation. This suggests that the strongly altered fault core and the associated chloritized damage zone (i.e., chloritized and fractured unit) was not so strong as the ones of the Gole Larghe Fault Zone. This might be due to different composition and volume of the hydrothermal fluids circulating within the fault zone (i.e., fluid-rock interaction) during pre-, syn- and post-seismic stages.

The difference between the Gole Larghe Fault Zone and the faults of the Atacama Fault System reflects also the different geodynamic setting. Indeed, the Atacama Fault System developed within the Mesozoic magmatic arc of the Coastal Cordillera, where the elevated geothermal gradient (~50 °C/km) and the devolatilization of magmatic products could have led to an enhanced fluid flow across the fault zones, as attested by the extensive precipitation of chlorite-epidote veins over zones as wide as hundreds of meters and the pervasive fluid-rock interaction within the faults (Fig. 16). Instead, the lower geothermal gradient and the limited amount of fluids during the cooling of the Adamello batholith (Mittempergher et al., 2014, 2009) could have limited the fluid flux through the Gole Larghe Fault Zone during its seismogenic activity.

The architectural variability of the BFZ fault core is controlled by the presence and spatial distribution of precursory anisotropies (i.e., magmatic foliations and dykes). Indeed, where the BFZ exploited foliated meta-diorites (Bolfin Complex; northern and central segments), the fault core strands are thicker (up

to a thickness of 6 m) and fewer in number (between 2 and 5 core strands; Figs. 12-13). Instead, where the BFZ cuts through tonalites-granodiorites (Cerro Cristales Pluton; central and southern segments), the fault core strands are thinner (maximum thickness of 3 m), more numerous (7 to 11 fault core strands) and distributed within a zone up to 700-m-thick (Figs. 12-13). In this latter case, the BFZ exploited favorably-oriented dykes during the early stage of fault evolution (see also Masoch et al., 2021). In summary, the geodynamic setting of the magmatic arc played a pivotal role in controlling the architecture of the BFZ with reference to (i) the spatial arrangement of precursory magmatic anisotropies (magmatic foliations of plutons and dyke swarm) exploited as loci fault nucleation at early stage of fault evolution (Masoch et al., 2021) and (ii) the large availability of fluids and heat during the late cooling stages of the batholiths (Fig. 16).

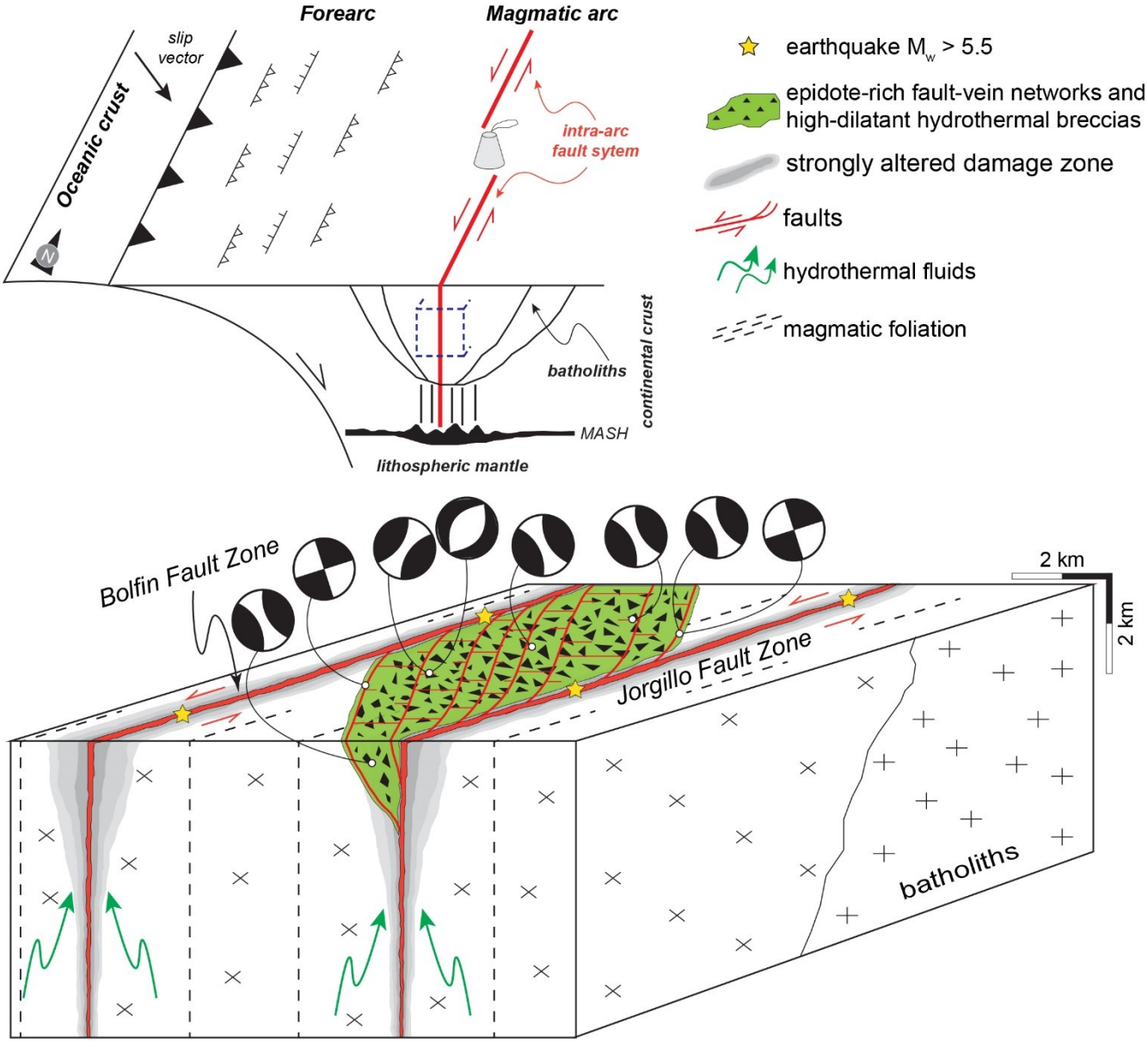

Fig. 16. Cartoon representing the geodynamic setting of the Atacama Fault System during the Early Cretaceous (upper diagram), and the Bolfin Fault Zone which bounds the western side of the Caleta Coloso Duplex (lower diagram). The dashed purple box in the upper diagram indicates the crustal level represented in the lower diagram. The faults of the Caleta Coloso Duplex developed within the Mesozoic magmatic arc of the Coastal Cordillera at 3-7 km depth. The geodynamic setting of the magmatic setting had a primary control on the fault architecture in terms of (i) spatial arrangement of precursory anisotropies exploited as loci of fault nucleation (magmatic foliations of plutons and dyke swarms) and (ii) large availability of hydrothermal fluids and heat. The fault core is associated with a wide hydrothermally altered damage zone. This is due to the circulation of large volume of hydrothermal fluids within the fault zone. In the BFZ damage zone, due to migration of upper-crustal pressurized fluids channelized along linkage faults and fault intersections, low-magnitude distributed seismicity occurs as attested by clusters of fault-vein networks and high-dilatant hydrothermal breccias, which are more widespread in the Caleta Coloso Duplex. The fault-vein networks and high-dilatant hydrothermal breccias are interpreted as fossil analogue of fluid-driven earthquake swarms (see Fig. 17 and text for details).

6.2. Comparison with active seismogenic sources

The architecture of the BFZ and of other exhumed seismogenic faults indicate that their ancient seismicity was distributed across a 100s-meter-wide zone. This is compatible with seismological observations of earthquake sequences distributed between 5 and 15 km depth in the continental crust (e.g., Allam and Ben-Zion, 2012; Viegas et al., 2010; Ye et al., 2012). Indeed, main- and after-shock sequences show that earthquakes occur within broad fault zones as wide as hundreds of meters to few kilometers, most likely containing several sub-parallel fault strands (e.g., Allam and Ben-Zion, 2012; Hauksson, 2010; Ross et al., 2017; Share et al., 2021; Shelly, 2020). In the case of the BFZ, main- and after-shock sequences might be associated with tectonic activity related to the sinistral intra-arc deformation during the Mesozoic.

A relevant characteristic of the BFZ is the occurrence of clusters of epidote-rich fault-vein networks and high-dilation hydrothermal breccias within the fault damage zone. These clusters are spatially associated with NW-striking, linkage splay faults and occur at the intersections with NE-striking faults (Figs. 7-8, 10). The epidote-bearing discrete fault surfaces in the damage zone accommodated small displacement (cumulative <1.5 m) and show variable kinematics (i.e., from normal dip-slip to strike-slip) across the damage zone (see stereonets 2-6 in Fig. 7, stereonet 2 in Fig. 10 and the ancient focal mechanisms retrieved from beach ball stereoplots of the epidote-rich fault-vein networks in Fig. 17a). The same scattering in fault kinematics is also shown by the epidote-quartz-prehnite shear veins within the dilational jog at Fault Bend locality (see stereonets 5-6 in Fig. 8 and the ancient focal mechanisms retrieved from beach ball stereoplots of the epidote-quartz-prehnite shear veins in Fig. 17a). Microstructural observations of epidote-rich shear veins indicate that incremental slip was accommodated and coupled with variable fault slip behavior (Fig. 14f). Indeed, fault slip was accommodated by cyclic events of incremental extensional/hybrid veining and localized cataclasis (Figs. 4b, 14f). The epidote-rich veins and high-dilatant hydrothermal breccias show cyclic events of incremental extensional fracturing and sealing (Figs. 3a-e, 4e-f, 14), typical of hydraulic implosion brecciation (Sibson, 1986). Hydraulic implosion brecciation occurs by sudden wall-rock implosion in cavity space and rapid hydrothermal fluid flow and mineral deposition, especially at dilational fault sites. This brecciation process accommodates incremental dilation, which tends also to develop an extensive extensional vein mesh/stockwork (Sibson, 1986), as observed in the BFZ damage zone (Figs. 3f, 4a). Hydraulic implosion brecciation therefore is the result of rapid transient conditions from high to low fluid pressure (e.g., Berger and Herwegh, 2019; Cox and Munroe, 2016; Dempsey et al., 2014; Masoch et al., 2019; Sibson, 1986; Woodcock et al., 2007). Consistently with this interpretation, the epidote-rich fault-vein networks and high-dilatant hydrothermal breccias, possibly resulting from the ingression of hot and pressurized fluids, show a pervasive fluid-rock interaction with the adjacent damaged host rocks (Figs. 3-4, 14e).

Magmatic-hydrothermal systems are accompanied by sustained earthquake activity with low in magnitude earthquakes, referred as earthquake swarms (Hill, 1977; Mogi, 1963). Earthquake swarms are thought to be primarily driven by transient fluid pressure increases (e.g., Cappa et al., 2009; Shelly et al., 2013a, 2013b) and the associated seismic activity lasts from days to months (e.g., Fischer et al., 2014). Similar sequences are also associated with industrial wastewater injection in boreholes (Ellsworth, 2013; Healy et al., 1968). Natural earthquake swarms have been documented from Yellowstone caldera, Wyoming (Shelly et al., 2013a), Long Valley Caldera, California (Shelly et al., 2016, 2015), Mount Rainer, Washington (Shelly et al., 2013b); Mineral Mountains, Utah (Mesimeri et al., 2021), West-Bohemia/Vogtland, Central and Western Europe (Fischer et al., 2014; Vavryčuk, 2002), Hakone caldera, Japan (Yukutake et al., 2011), and Patagonian batholith, Southern Andes, Chile (Legrand et al., 2011).

Specifically, the latter example from the Southern Andes occurred in a geodynamic setting comparable to that one where the BFZ was active during the Mesozoic. Indeed, the 2007 Aysén Fjord swarm sequence occurred within the Liquiñe-Ofqui Fault System (Southern Andes, Chile), a presently active major, trench-parallel, dextral strike-slip intra-arc fault system of the Patagonian fjord land, associated with the oblique subduction of the oceanic Nazca plate underneath the South America plate (e.g., Cembrano et al., 2002, 1996), similar to the AFS during the Mesozoic (Fig. 17). In detail, the Aysén Fjord swarm was distributed along a second-order (i.e., splay) fault of the main segment of the Liquiñe-Ofqui Fault System, cutting through the Patagonian batholith, and was driven by the ingression of magmatic or hydrothermal fluids (Legrand et al., 2011). Most of the seismic events occurred between 3 and 8 km depth (Fig. 17b) (Legrand et al., 2011), which is the range of inferred formation depth of the epidote-rich fault-vein networks from the Caleta Coloso Duplex (Cembrano et al., 2005; Herrera et al., 2005). Moreover, this swam sequence was associated with a considerable non-double-couple (i.e., isotropic) component for three of the six greatest events. High values of the non-double-couple component were also recently detected in the 2019 Mw 7.1 Ridgecrest sequence (5 to 15% of the total moments for 50 earthquakes; Cheng et al., 2021) and in the 2010 Yellowstone caldera sequence (30% of the total moment for the M_w 3.9 earthquake; Shelly et al., 2013a) A mechanism producing isotropic seismic signal is tensile fracturing, hybrid faulting in a local extensional stress regime possibly augmented by the involvement of pressurized fluids (Sibson, 1994; Stierle et al., 2014; Vavryčuk, 2002),. In turn, the extensive epidote-rich fault-vein networks and high-dilation hydrothermal breccias show features resembling those typical of earthquake swarms, as discussed in the paragraph above. In particular, the fault-vein networks and high-dilatant breccias show evidences of having accommodated dilation vs. slip large enough to have produced seismic events with a considerable non-double-couple component. This hypothesis is supported by the extension (up to 100s of meters) of the interlaced epidote-

rich fault-vein networks (Figs. 7, 10) and the volume of the high-dilatant epidote-quartz-prehnite breccia defining a decameter-sized dilational jog (Fig. 8) and showing cockade texture (Fig. 14a), fault rock typical of high-dilatant faults (e.g., Cox and Munroe, 2016; Frenzel and Woodcock, 2014; Masoch et al., 2019). At larger scale, the Caleta Coloso Duplex formed in a local transtensional regime (Cembrano et al., 2005; Herrera et al., 2005; Veloso et al., 2015), promoting migration of upper-crustal pressurized fluids during brittle deformation (Sibson, 1987, 1981). The epidote-bearing fault-vein networks and high-dilation hydrothermal breccias observed in the damage zone of the BFZ are more widespread within the duplex (see Cembrano et al., 2005; Herrera et al., 2005). For these reasons, we can compare and upscale our findings with the 2007 Aysén Fjord swarm and, in conclusion, we interpret the clusters of epidote-rich fault-vein networks and epidote-quartz-prehnite breccias as exhumed seismic sources of fluid-driven earthquake swarms.

Our interpretation is also supported by the seismological monitoring of earthquakes associated with active hydrothermal systems thanks to the exploitation of dense seismic networks ad of high-resolution double-differences relocation methods (see Ellsworth, 2013). Indeed, complex fault networks are activated during an earthquake swarm sequence: fluids inject along fault zone and diffuse primarily through channels, driving seismicity (Ross et al., 2020, 2017; Shelly et al., 2016, 2015, 2013a). Moreover, the focal mechanisms have remarkable variable kinematics across the active seismogenic volume and geometrical complexities, such as fault linkages and bends, are the location of persistent low-magnitude seismicity (Ross et al., 2020, 2017). These source and spatial features observed in earthquake swarm sequences are compatible with the scattered kinematics (Figs. 7-8, 10 and summery in Fig. 17) and the geometrical characteristics (see points discussed above) of the epidote-rich units of the BFZ. In summary, the epidote-rich fault-vein networks and the epidote-quartz-prehnite breccia observed in the damage zone of the BFZ and, more in general, in the faults of the Caleta Coloso Duplex are interpreted as a fossil example of upper-crustal fluid-driven widespread seismicity associated with a high-fluid flux setting, where little variation of pore fluid pressure can determine small-scale seismic faulting and dilatation at geometrical complexities (Cox, 2020, 2016; Sibson, 1996).

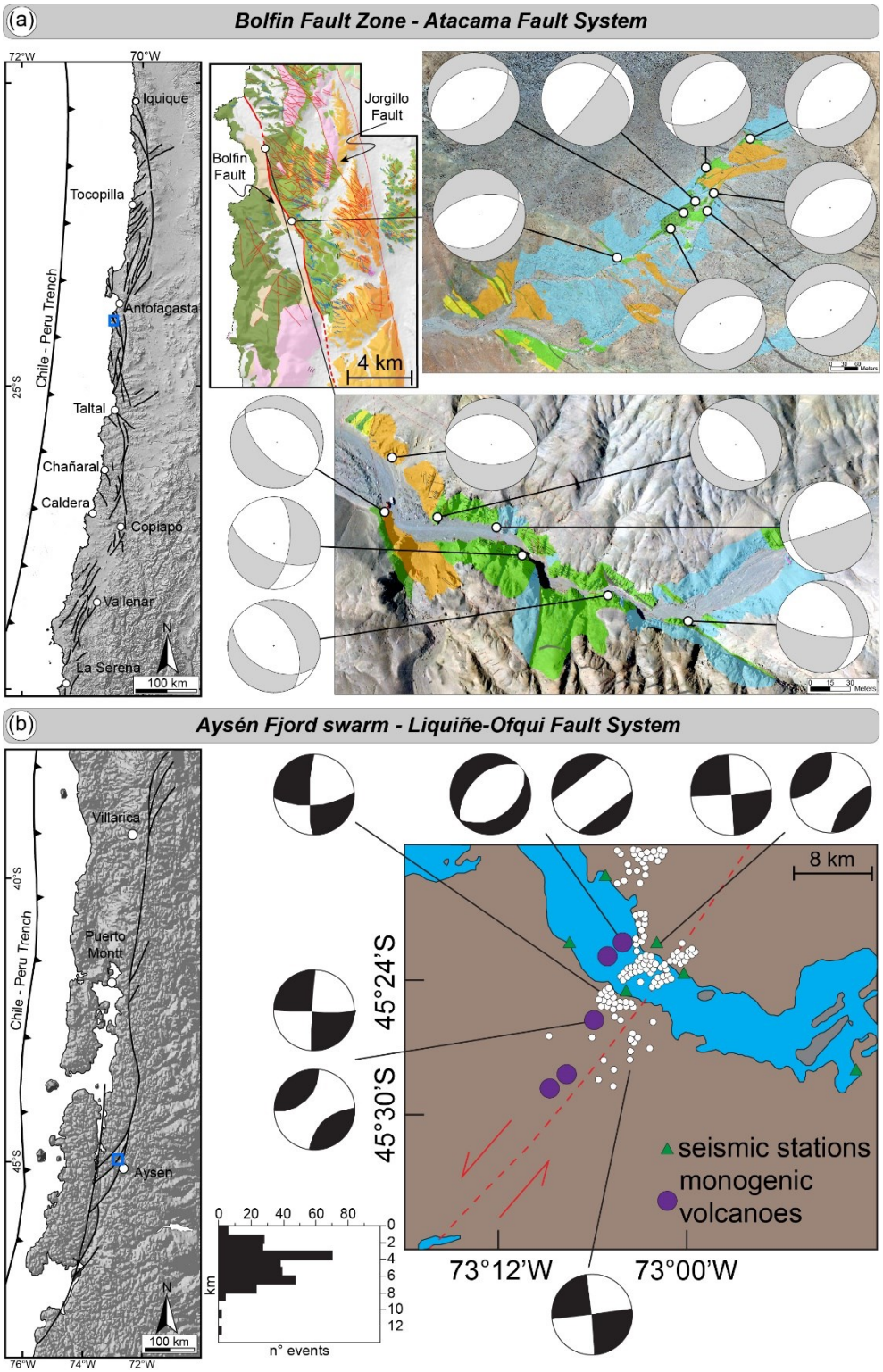

Fig. 17. Comparison between the exhumed clusters of epidote-rich fault-vein networks and high-dilational hydrothermal breccias associated with splay faults in the damage zone of the Bolfin Fault Zone (the blue box indicates the BFZ location along the Atacama Fault System) (a) and the 2007 swarm-type sequence of Aysén Fjord (Southern Chile) within the presently active Liquiñe-Ofqui Fault System (b; modified from Legrand et al., 2011). See the text for details.

7. Conclusions

We described the architecture of the Bolfin Fault Zone, a >40-km exhumed, seismogenic strike-slip fault of the intra-arc Atacama Fault System (Northern Chile). The BFZ is an example of crustal-scale seismogenic source hosted in the continental crust, which could have generated moderate- to large-in-magnitude (up to M_w 6.5-7.0) earthquakes. Ancient seismicity is attested by widespread occurrence of pseudotachylytes within the fault core and the damage zone. The BFZ consists of a hydrothermally altered fault core (thickness ranging from 7 m to ~60 m), including multiple high-strain and lower-strain cataclastic fault strands, and a strongly altered inner damage zone (up to 58-m-thick). The latter is characterized by extensive albitization of plagioclase and chloritization of biotite and amphibole and pervasive chlorite-epidote veining. The intense fluid-rock interaction affecting all the structural elements of the BFZ attests to an extensive circulation of hydrothermal fluids during the ancient activity of the BFZ. In particular, the damage zone of the BFZ presents clusters of epidote-rich fault-vein networks and hydrothermal breccias associated with linkage faults and fault intersections. By comparing the seismicity along the presently active intra-arc Liquiñe-Ofqui Fault System (Southern Andes, Chile), we interpreted these clusters of the epidote-rich fault-vein networks as a fossil record of fluid-driven earthquake swarm sequences.

Chapter 3

Fluid-driven earthquake swarms frozen in an exhumed hydrothermal system (Bolfin Fault Zone, Chile)

This study was conducted with the collaboration of Giorgio Pennacchioni, Michele Fondriest, Rodrigo Gomila, José Cembrano and Giulio Di Toro. I was assisted during the microstructural analysis (but not continuously) by Giorgio Pennacchioni. The material presented here was discussed with Giorgio Pennacchioni, Michele Fondriest, Rodrigo Gomila, José Cembrano and Giulio Di Toro.

Abstract

Fluid-driven earthquake swarms commonly occur in upper-crustal hydrothermal-magmatic systems and activate mesh-like fault-fracture networks. To date, there are few constraints from the geological record on how seismically-active fault-vein networks develop through time in this geodynamic environment. Here, we describe networks of small displacement (< 1.5 m) epidote-rich fault-vein across granitoids, occurring at the intersections of subsidiary faults with the exhumed crustal-scale Bolfin Fault Zone (Atacama Fault System, Chile). High-resolution microstructural analysis conducted on magmatic quartz of the host granitoids located close (≤ 1 cm) to the sheared fault-veins shows the presence of (i) thin (<10 μm) interlaced deformation lamellae and, (ii) a network of quartz veinlets crosscutting the lamellae (healed microfractures). Instead, the epidote-rich sheared veins (i) include clasts of the deformed magmatic quartz, and (ii) record cyclic events of extensional-to-hybrid veining and shearing. We interpret the microstructures preserved in the magmatic quartz as record of transient high stresses associated with dynamic propagation of small seismic ruptures Instead, the overprinting dilation and shearing within the epidote-rich fault-veins attest the development of a mature and hydraulically-connected fault-fracture system cyclically rupturing during swarm-like earthquake sequences, controlled by fluctuations of pore fluid pressure.

1. Introduction

The properties of fault zones and their host rocks affect a wide range of crustal processes, such as earthquake nucleation, propagation and arrest (e.g., Faulkner et al., 2006; Sibson, 1985; Wesnousky, 2006, 1988), crustal rheology (e.g., Behr and Platt, 2014; Handy et al., 2007) and migration of fluids (e.g., hydrothermal, magmatic, oil, gas) in the Earth's crust (e.g., Cembrano and Lara, 2009; Richards, 2013; Tardani et al., 2016). Mechanical and hydraulic proprieties of fault zones vary largely though space and time during the seismic cycle and are intrinsically coupled with each other (Faulkner et al., 2010; Wibberley et al., 2008). Specifically, at seismogenic depths (i.e., 5-15 km depending on the tectonic setting, rock composition, temperature gradient, etc.; Scholz, 2019), permeability in active seismogenic fault zones is expected to change during the seismic cycle, promoting co- to post-seismic episodic fluid flow (i.e., fault-valve behavior; Sibson, 1992a, 1992b, 1989). Indeed, fault rupture events can lead to large, transitory increases of fault permeability (Cox, 2016; Sibson, 1989). Where ruptures breach overpressured fluid reservoirs, high-permeability fault segments provide conduits facilitating fluid redistribution in the Earth's crust. On the other hand, post- to inter-seismic fault healing and sealing due to compaction processes and precipitation of hydrothermal minerals in pores and fractures can reduce the fault permeability, eventually inhibiting fluid flow (Cox, 2016; Sibson, 1992b, 1992a, 1989).

The expression of the coupling among fault activity, fault permeability, fluid flow, fluid pressure and loading conditions in the geological record is documented by hydrothermal (e.g., epidote, quartz, calcite, zeolite) fault-vein networks in exhumed fault zones over several geological settings (e.g., Cox and Munroe, 2016; Dempsey et al., 2014; Lucca et al., 2019; Masoch et al., 2022; Micklethwaite et al., 2010). Mineralized fault-fracture networks present extensive hydrothermal alteration, mutually overprinting extension-to-hybrid vein arrays, and dilational breccias. Hydrothermal fault-vein networks record significant stages of fluid flow and mineralization during fault evolution, possibly associated with ancient seismic activity (e.g., Cox and Munroe, 2016; Dempsey et al., 2014; Masoch et al., 2022). In recently or currently active hydrothermal-magmatic settings, fluid flow is abundant and is commonly accompanied by earthquake swarms (e.g., Fischer et al., 2014; Legrand et al., 2011; Mesimeri et al., 2021; Shelly et al., 2013), i.e., clusters of low-in-magnitude seismic events without a characteristic mainshock (Mogi, 1963). Earthquake swarms have been frequently attributed to pore fluid pressure transients in km-scale mesh-like fault-fracture networks (e.g., Hill, 1977; Shelly et al., 2022; Sibson, 1996) and the associated seismic activity lasts from few days to months (e.g., Fischer et al., 2014). Besides deviating from common mainshock-aftershock sequences, earthquake swarms generate also considerable non-double-couple (i.e., isotropic) seismic signal, as a result of tensile fracturing and hybrid faulting driven by the ingression of pressurized hydrothermal-magmatic fluids in the fault

zone/system (Legrand et al., 2011; Phillips, 1972; Sibson, 1996; Stierle et al., 2014; Vavryčuk, 2002). Similar human-induced seismic sequences may be associated with industrial fluid injection in boreholes (Ellsworth, 2013; Healy et al., 1968).

There has been a great deal of progress in the last years regarding (i) the spatio-temporal imaging of the fault-fracture networks illuminated by earthquake swarms, (ii) the determination of focal mechanisms of very small earthquakes through seismological and geophysical techniques (e.g., Mesimeri et al., 2021; Shelly et al., 2022), and (iii) the relation of injected fluid volumes and rates with seismic energy release through fluid-injection experiments (e.g., Dorbath et al., 2009; Guglielmi et al., 2015). However, to date, little is known from the geological record about how a fault-vein network, large enough to be comparable to currently active cases, develops though time and space in hydrothermal systems. Moreover, evidences of ancient seismic faulting related to fluid-driven seismicity, are rarely documented.

In this work, we examine an extensive epidote-rich fault-vein network resulting from fault linkage and damage zone formation of the Bolfin Fault Zone (BFZ). The fault networks are exceptionally well exposed over tens of square kilometers in the Atacama Desert (Northern Chile). The BFZ is an exhumed, crustal-scale, seismogenic (pseudotachylyte-bearing) fault of the transtensional Caleta Coloso Duplex (Atacama Fault System, Chile, Fig. 1) (Cembrano et al., 2005; Masoch et al., 2022, 2021; Scheuber and González, 1999). Based on the interpretation of field data and high-resolution (FEG-SEM) microstructural analysis of fault zone rocks, we reconstruct different stages during the development of an upper-crustal seismically-active hydrothermal system, from the dynamic nucleation of small seismic ruptures to the formation of mature and hydraulically connected fault-fracture network. We document that the proximal wall-rocks of small-displacement (< 1.5 m) sheared veins initially experienced a high-stress pulse, attested by deformation lamellae developed in the magmatic quartz, and the same deformation features are included in wall-rock fragments within the sheared veins. The latter are associated with epidote mineralization and record overprinting events of both extensional veining and cataclasis. We interpret the combination of these microstructures as evidence of ancient swarm-like seismic activity, from the first stages of dynamic propagation to fluid-driven extensional veining and cataclasis within a mature and hydraulically connected fault-fracture system. This represents a unique record of the evolution in space and time of un upper-crustal swarm-like seismic source, from the early nucleation stages to the later mature architecture.

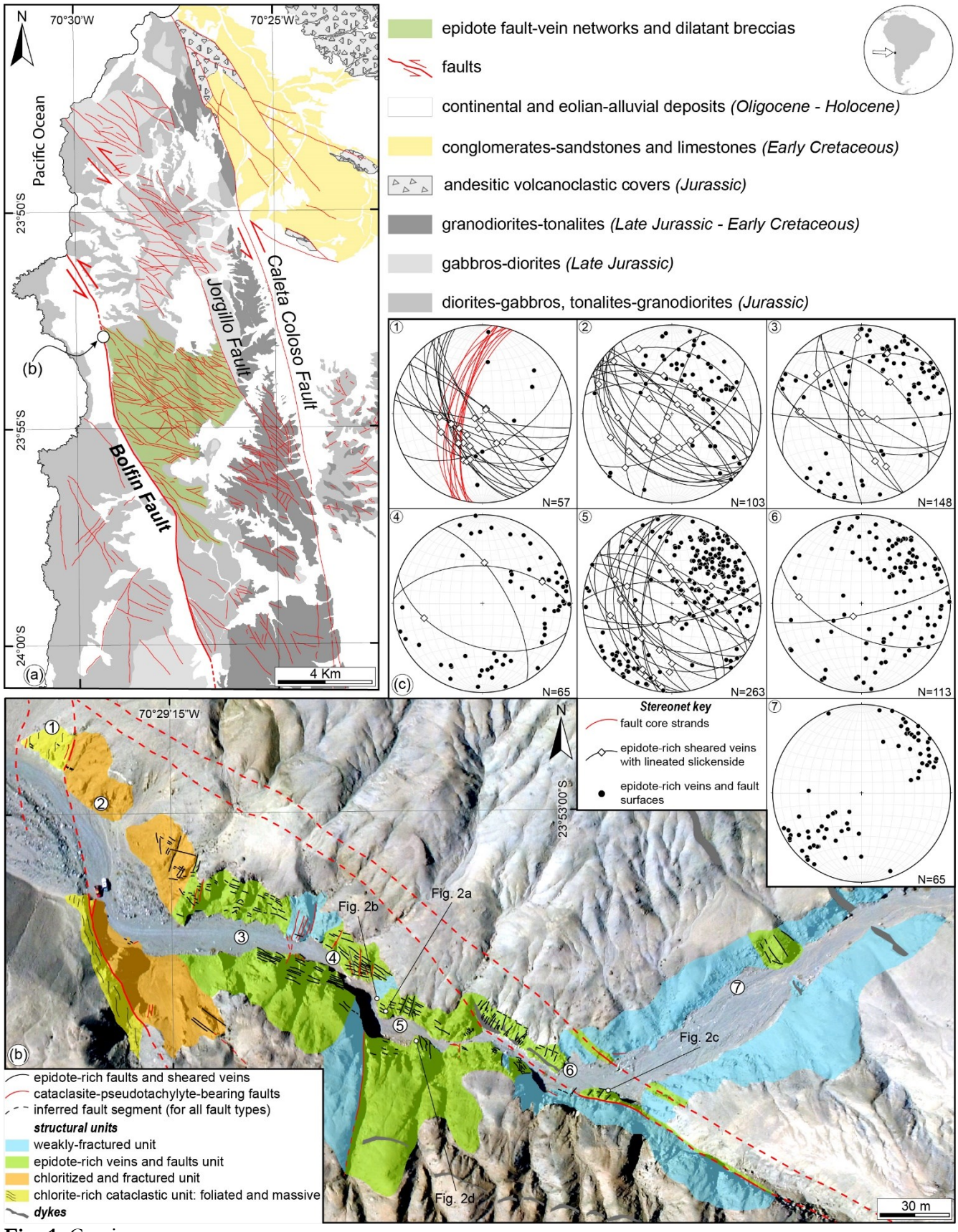

Fig. 1. Caption on next page.

Fig. 1. Geological setting of the Bolfin Fault Zone. (a) Simplified geological map of the Caleta Coloso Duplex. The BFZ bounds the western side of the crustal-scale transtensional duplex. The green layer indicates the distribution of the epidote-rich fault-vein networks and dilatant breccias within the Caleta Coloso Duplex. Modified from Masoch et al. (2021). (b) Structural map of the BFZ architecture at Sand Quarry locality. Clusters of epidote-rich fault-vein networks and breccias are associated with NW-striking, splay faults of the BFZ and NE-striking faults. The faults splaying out from the BFZ represent transtensional faults within the duplex (thick red lines). Modified from Masoch et al. (2022). (c) Structural data of the fault core strands and epidote-rich fault-vein networks. Numbers in stereonets denote the location of structural sites in the map in (b).

2. The epidote-rich fault-vein networks of the Bolfin Fault Zone

The BFZ is a >40-km-long fault pertaining to the 1000-km-long, Early Cretaceous, strike-slip intra-arc Atacama Fault System (Northern Chile; Fig. 1) (Arabasz, 1971; Cembrano et al., 2005; Masoch et al., 2021; Scheuber and González, 1999; Seymour et al., 2021). The BFZ is a sinistral strike-slip fault and bounds the western side of the crustal-scale transtensional Caleta Coloso Duplex (Cembrano et al., 2005; Masoch et al., 2022, 2021) (Fig. 1a). The BFZ has a sinuous crustal-scale geometry cutting through Jurassic-Early Cretaceous diorite-gabbro and tonalite-granodiorite plutons (Fig. 1a). The ancient BFZ seismicity is attested by presence of pseudotachylytes, formed at 5-7 km depth and ≤ 300 °C ambient temperature (Gomila et al., 2021; Masoch et al., 2022, 2021). Seismic faulting occurred in a fluid-rich environment as documented by syn-kinematic chlorite-epidote (-quartz-calcite) veining and extensive propylitic alteration (Gomila et al. 2021).

Overall, the BFZ architecture consists of cataclastic, multiple fault strands, up 6-m-thick, within a 150-m-wide damage zone (see Masoch et al., 2022 for the description of the fault architecture; Fig. 1b). The damage zone consists of variably fractured and brecciated rock volumes characterized by extensive epidote-rich fault-vein networks associated with NW-to-WNW-striking faults splaying from the BFZ (Figs. 1b-c; 2) (Masoch et al., 2022). These subsidiary faults accommodated transtensional slip (Fig. 1c) within the Caleta Coloso Duplex (Cembrano et al., 2005), with an apparent cumulative strike-slip displacement up to 1 km (Cembrano et al., 2005; Jensen et al., 2011; Stanton-Yonge et al., 2020). The epidote-rich fault-vein networks consist of (i) small-displacement (< 1.5 m) sheared veins with lineated slickensides (Fig. 2a-b, 2d-e), and (ii) extensional veins and dilatant breccias sealed by epidote + prehnite ± chlorite ± quartz ± K-feldspar (Fig. 2b-c, 2f; see section 4.2). Sheared and extensional veins are arranged into four sets, dipping towards SW, NE, W and S (Fig. 1c). Epidote lineated slickensides are decorated by either stepped polished surfaces or mirror-like slip surfaces (Fig. 2a, 2d), and present variable kinematics (i.e., normal dip-slip to strike-slip; Fig. 1c). Veins and breccias record multiple episodes of extensional fracturing and sealing, as they include angular fragments of earlier veins and breccias (Fig. 2b-c). The epidote-rich fault-vein networks are surrounded by

extensive reddish alteration haloes in the damaged wall-rock (Fig. 2b-c, 2e-f). The epidote-rich fault-vein networks observed in the BFZ damage zone are spatially distributed within all the duplex (see Cembrano et al., 2005; Herrera et al., 2005) (Fig. 1a).

Fig. 2. The epidote-rich fault-vein network of BFZ. Coin for scale. Mineral abbreviations: *Ab* = albite, *Chl* = chlorite. (a) Discrete extensional fault surface decorated by epidote slickenfibers. WGS84 GPS location: 23.883944°S, 70.486689°W. (b) Epidote-rich hybrid extensional-shear vein including angular fragments of earlier veins (dark green). The vein is reactivated by a whitish calcite-palygorskite vein (boundary on the right side) referable to post-Miocene deformation (see Masoch et al., 2021 for details). Sample 19-33. WGS GPS location: 23.99803°S, 70.44051°W. (c) Polished sample of an epidote sheared vein surrounded by a reddish alteration halo on both sides. The pale green-colored cataclasite includes dark green fragments of early veins. Sample 19-48. WGS84 GPS location: 23.88442°S, 70.48567°W. (d) Sheared vein with lineated and highly reflective (i.e., mirror-like) slickenside. The black line indicates the orientation of the thin section scan shown in (e). Sample 19-38. WGS84 GPS location 23.8842400°S, 70.4864200°W. (e) Plane-polarized light scan of thin section of a lineated sheared vein, showing the spatial distribution of the microstructures observed in the micro-damage zone and in the sheared vein (red lines). (f) Plane-polarized light scan of thin section of a sheared vein with both wall-rock blocks preserved. Sample 19-48.

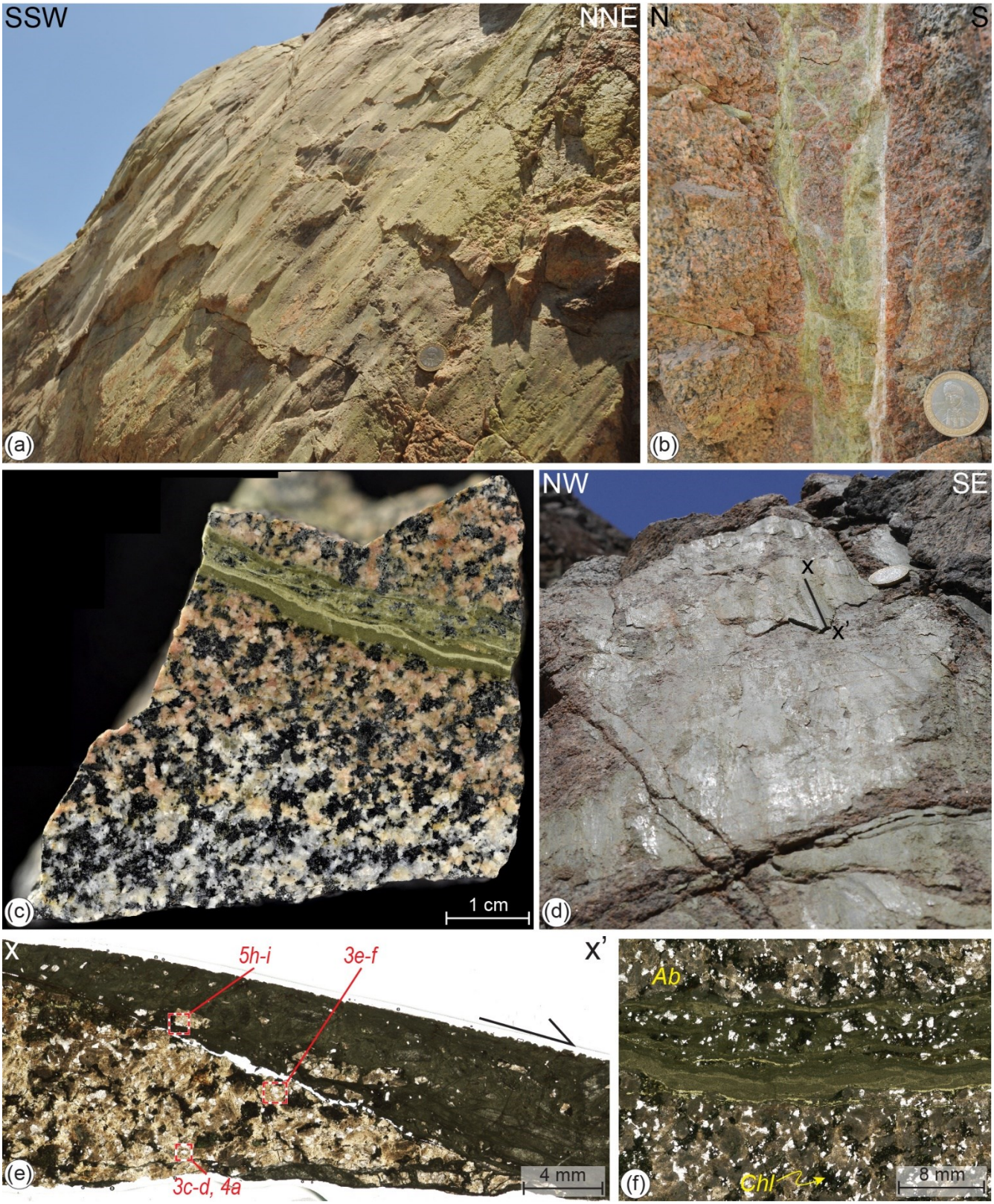

Fig. 2. Caption on previous page.

3. Methods

Microstructural analysis was conducted on syton-polished 100-μm-thick thin sections (n=10) cut parallel to the fault lineation and orthogonal to the fault/vein wall. We used a Tescan Solaris (Field Emission Gun – Scanning Electron Microscope; FEG-SEM) installed at the Department of Geosciences of University of Padova (Italy). The instrument is equipped with backscattered electron (BSE), cathodoluminescence (CL), electron backscattered diffraction (EBSD) and quantitative wavelength-dispersive spectroscopy (WDS) detectors. BSE and CL images were acquired at 7-10 kV and 0.3-3 nA, and 10 kV and 1-3 nA as accelerating voltage and beam current, respectively. The EBSD maps were acquired using the FEG-SEM equipped with a COMOS-Symmetry EBSD detector (AZtec acquisition software, Oxford Instruments), operating at 20 kV as accelerating voltage, 5-10 nA as beam current, 0.15-0.30 μm as step size, 70° sample tilt and high vacuum. EBSD data were elaborated with the MTEX toolbox (https://mtex-toolbox.github.io/).

The composition of main mineral phases was obtained by WDS-FEG analysis. Conditions of data acquisition were: 15 kV (accelerating voltage); 6 nA (beam current); 1 μm (electron beam size); 5 s (counting time for background), 15 s (for Si, Al, Ca, Fe), and 10 s (for Na, K, Mg, Mn, Ti, Cr) on peak. Albite (Si, Al and Na), diopside (Ca), olivine San Carlos (Mg), orthoclase (K), hematite (Fe), and Cr, Ti and Mn oxides were used as standards. Na and K were analyzed first to prevent alkali migration affects.

4. Results

4.1. Weakly-deformed granodiorite and micro-damage zone of the sheared veins

The weakly-deformed granodiorite consists of plagioclase (labradorite to andesine), quartz, K-feldspar with myrmekite, biotite and minor amphibole and opaques (ilmenite and magnetite) (Figs. 2c, a). The magmatic quartz shows weak undulose extinction and has a dominant light grey CL shade locally cut by CL-dark micro-fractures (>10 μm in thickness) sealed by hydrothermal quartz ± K-feldspar (Fig. 3a-b).

The damaged granodiorites associated with the sheared veins is marked by up to 4-cm-thick reddish alteration haloes (Figs. 2b-f) where: (i) magmatic plagioclase is replaced by albite + epidote; and (ii) magmatic biotite and amphibole are replaced by chlorite ± opaques (Fig. 2e-f). A pervasive network of interconnected micro-fractures, sealed by epidote ± chlorite ± prehnite, is present in the alteration halo and becomes spatially denser toward the veins (Fig. 2c, 2e-f). Under CL, magmatic quartz shows heterogeneous, bright to medium grey shade domains, which are cut by interlaced darker-shaded deformation bands up to 10-μm-thick (Fig. 3c-f). K-feldspar is bright in CL whereas albitized plagioclase does not show any CL signal (Fig. 3d, 3f). CL also reveals a network of micro-fractures healed by quartz ± K-feldspar ± albite (hereafter referred as "quartz-filled" veinlets), across quartz and feldspar grains (Fig. 3c-f). These veinlets show a

homogeneous dark CL shade and are oriented at high angle with respect to the vein boundary (Fig. 3d, 3f). These microstructures (i.e., deformation bands and healed microfractures) fade away (≥ 1 cm far; Fig. 3b) from the veins – hereafter we refer to this high-strain damage zone as "micro-damage zone". Deformation bands do not show any texture gradient moving closer to the veins; instead, the density of the quartz-filled veinlets increases moving closer to the veins (Fig. 3d, 3f, 3h). Close to the sharp vein boundary (< 100 μm far from the vein boundary) in the footwall block, the magmatic quartz is strongly brecciated and healed by dark grey-shaded quartz (also surrounded by epitaxial rim of CL-dark quartz; Fig. 3g-h). EBSD maps of the magmatic quartz show that the deformation bands visible in CL are oriented nearly orthogonal to the <c> axis (Fig. 4a-b) and correspond to a minor crystallographic misorientation (< 2-3°; see profiles in Fig. 4c) with respect to the host grain. These features are typical of deformation lamellae (Fairbairn, 1941; Trepmann and Stöckhert, 2003) either referred as short-wavelength undulatory extension (Trepmann and Stöckhert, 2013) or fine extinction bands (Derez et al., 2015). Consequently, hereafter we refer as deformation lamellae to these deformation features. The EBSD maps also show that the quartz-filled veinlets are in epitaxial continuity with the host magmatic quartz (Fig. 4a).

Fig. 3. Quartz microstructures in the weakly-undeformed granodiorite (a-b) and in the micro-damage zone of the veins (c-h). BSE images (left column) and their correspondent CL images (right column) with their distance to the vein boundary. Samples 19-37 and 19-38. Mineral abbreviations: *Ab* = albite, *Kfs* = K-feldspar, *Pl* = plagioclase, *Qz* = quartz. (a) Quartz grains outside the micro-damage zone. (b) Undeformed quartz grains show homogeneous, bright CL signal. (c, e, g) Quartz grains appear almost undeformed in BSE images. (d, f, h) Deformed magmatic quartz shows bright to medium, CL grey-shaded domains, which are pervasively cut by interlaced darker deformation lamellae (DL). These deformation features are cut by CL-dark quartz-filled veinlets. (g-h) Quartz grain close to the vein boundary in the footwall side. In the CL image in (h), the quartz grain appears strongly brecciated (almost pulverized) and is healed by CL-dark quartz.

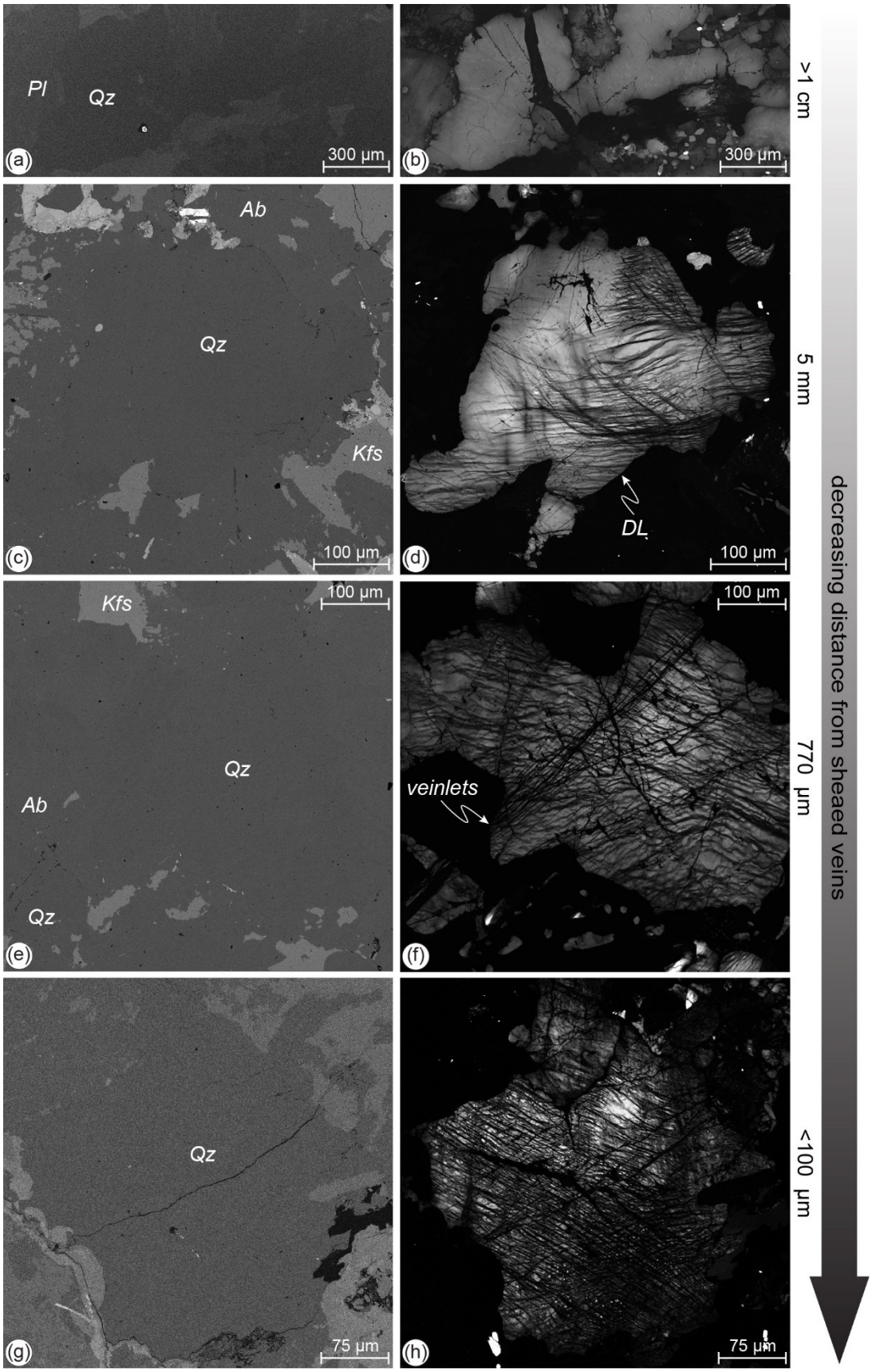

Fig, 3. Caption on previous page.

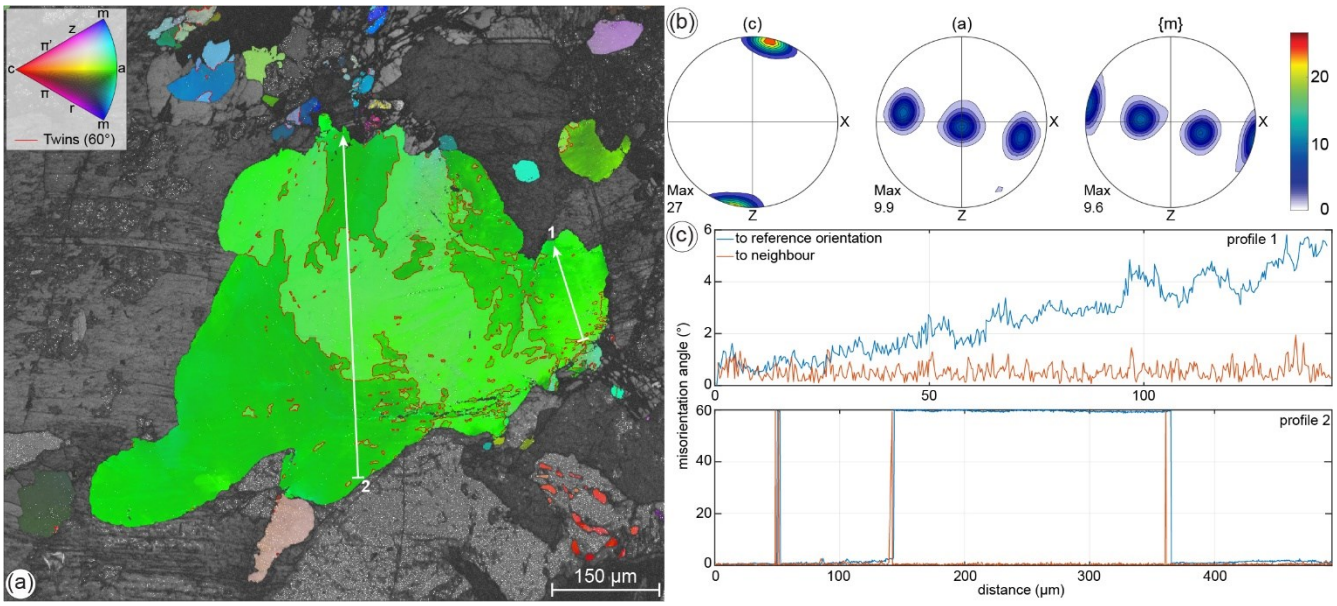

Fig. 4. EBSD analysis of a deformed magmatic quartz in the micro-damage zone. (a) Inverse Pole Figure (IPF) map, color coded according to IPF legend. The analyzed large magmatic quartz grain is the same shown in Fig. 3c-d. The IPF map is overlaid to the orientation contrast image. White lines mark the profiles plotted in (c). (b) Contoured pole figures. (c) Misorientation profiles.

4.2. Epidote-rich sheared veins

The epidote-rich sheared veins have heterogeneous microstructures (Figs. 2e-f, 5-6). In the sample 19-48 where both sides of the wall-rock surrounding the vein are preserved, the sheared veins include both portions of undeformed vein fillings and vein cataclasites (Figs. 2c, 2f, 6a). Undeformed vein portions consist of idiomorphic and zoned epidote (Al-rich; light: Fe-rich; Table 1) ± prehnite (dark: Al-rich; light: Fe-rich; Table 1), with minor interstitial chlorite ± quartz ± K-feldspar, and wall-rock fragments (Fig. 5a). The undeformed vein portions are generally present at the outer part of the vein while the cataclastic vein portion at the core (Figs. 2c, 6a). The core of the vein consists of a porous fine-grained (< 20 µm in size) matrix of epidote including fragments of earlier vein fillings and of the wall-rock.

In the samples 19-37 and 19-38, that include a portion of the vein and of the footwall wall-rock, the sheared veins consist of layered (proto)cataclasites to ultracataclasites with a sharp, knife-like contact with the topping vein (Figs. 2e, 6b). Close to the wall-rock, the (proto)cataclasites consist of a fine-grained (< 20 µm in size) matrix of zoned epidote and minor prehnite with intra-pore chlorite, and includes fragments (up to cm in size) of earlier prehnite-epidote veins and wall-rock (Fig. 5b-c). The ultracataclasites consist of a highly porous, fine-grained (≤ 500 nm in size) matrix of epidote and prehnite, with intra-pore chlorite, and fragments (up to 100 µm in size) of idiomorphic epidote and prehnite grains and wall-rock (Fig. 5d, 5f). Above the lineated slickensides, multiple vein generations are present (Fig. 5d-e). Some veins consist of

zoned prehnite grains elongated orthogonal to the vein boundaries (Fig. 5e). Other veins consist of zoned epidote grains, which present localized (ultra)cataclasite layers at the vein boundaries, marking further lineated slickensides.

Fragments of magmatic quartz within the veins appear brecciated under CL (Fig. 5g). Micro-fractures are sealed by CL-dark quartz, which rims the brecciated magmatic quartz fragment (Fig. 5g). This darker rim shows a faint oscillatory zoning in the external part (Fig. 5g). Magmatic quartz included in large (mm in size) wall-rock fragments shows the same deformation features (i.e., deformation lamellae cut by epitaxial quartz-filled veinlets, Fig. 5h-i) as observed in the micro-damage zone (Fig. 3c-h)

Fig. 5. Microstructures of the epidote-rich sheared veins (samples 19-38 and 19-48). Mineral abbreviations: *Ab* = albite, *Chl* = chlorite, *Ep* = epidote, *Kfs* = K-feldspar, *Prn* = prehnite, *Qz* = quartz. (a) Vein filling consisting of idiomorphic zoned epidote. (b) Angular fragment of an early prehnite-epidote vein (dashed white line) included in epidote-rich vein protocataclasite. (c) Detail of the epidote matrix in a protocataclasite. (d) Ultracataclasite, defining the slip zone of a discrete polished surface, includes angular fragments of zoned epidote (light grey) and prehnite (dark grey). The sheared vein is reactivated by multiple events of extensional veining. (e) Detail of extensional-to-hybrid veins. Vein sealed by elongated prehnite crystals and reactivating a hybrid extensional-shear one. Note the fibrous prehnite crystals above the white dashed line. (f) Matrix of ultracataclasite consisting of epidote nanoparticles (≤ 500 μm in size). Fragmented idiomorphic crystals of epidote and prehnite are included in the matrix. The ultrafine epidote grains have triple junctions and pores (<< 1 μm in size), locally filled with chlorite. (g) Quartz fragments within an epidote cataclasite. The quartz fragments are brecciated and rimmed by CL-darker quartz. (h-i) Quartz grains in wall-rock fragments (the larger is marked by the dashed white line) show the same deformation features observed in the micro-damage zone of the veins, shown in Fig. 3.

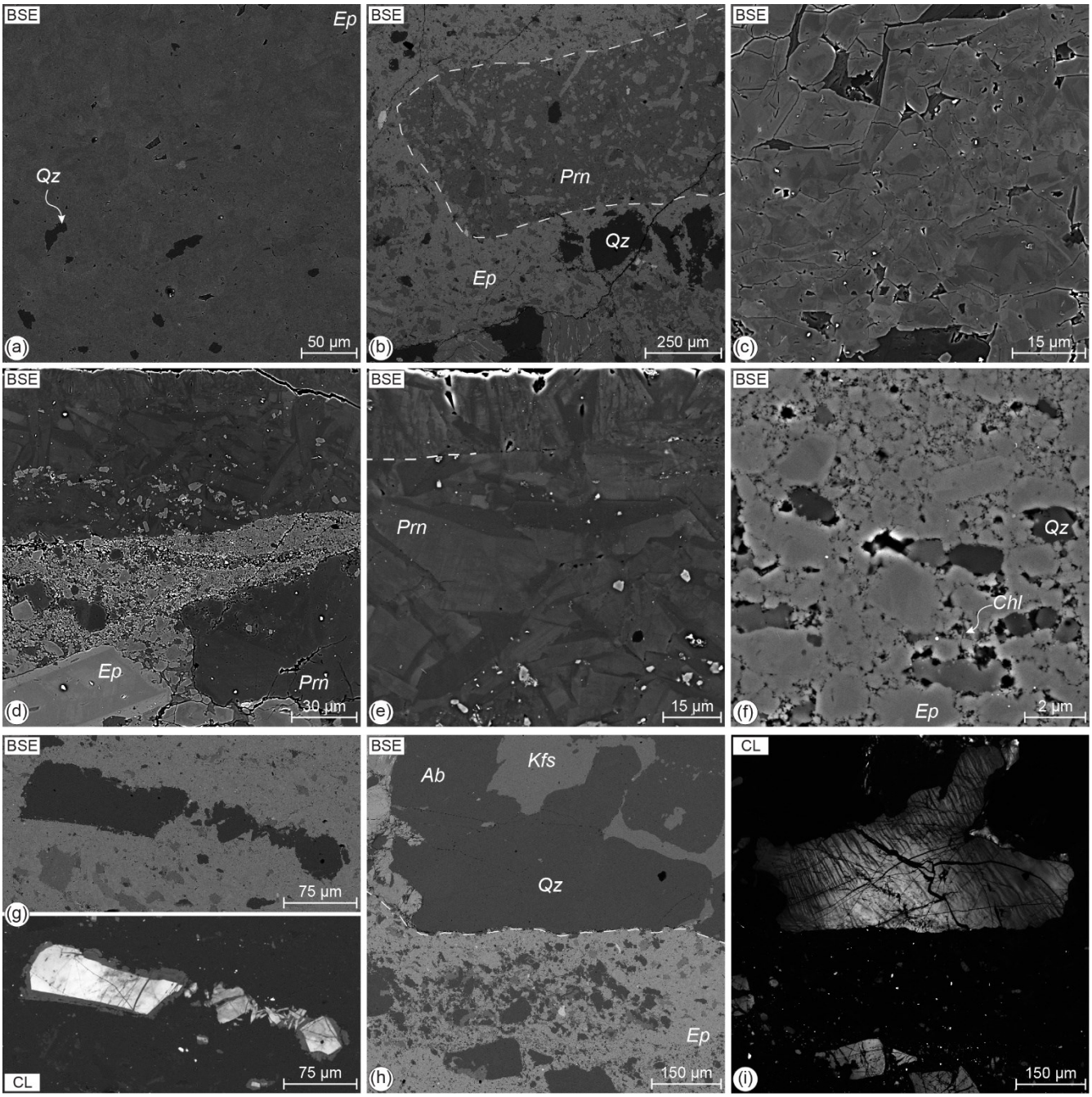

Fig. 5. Caption on previous page.

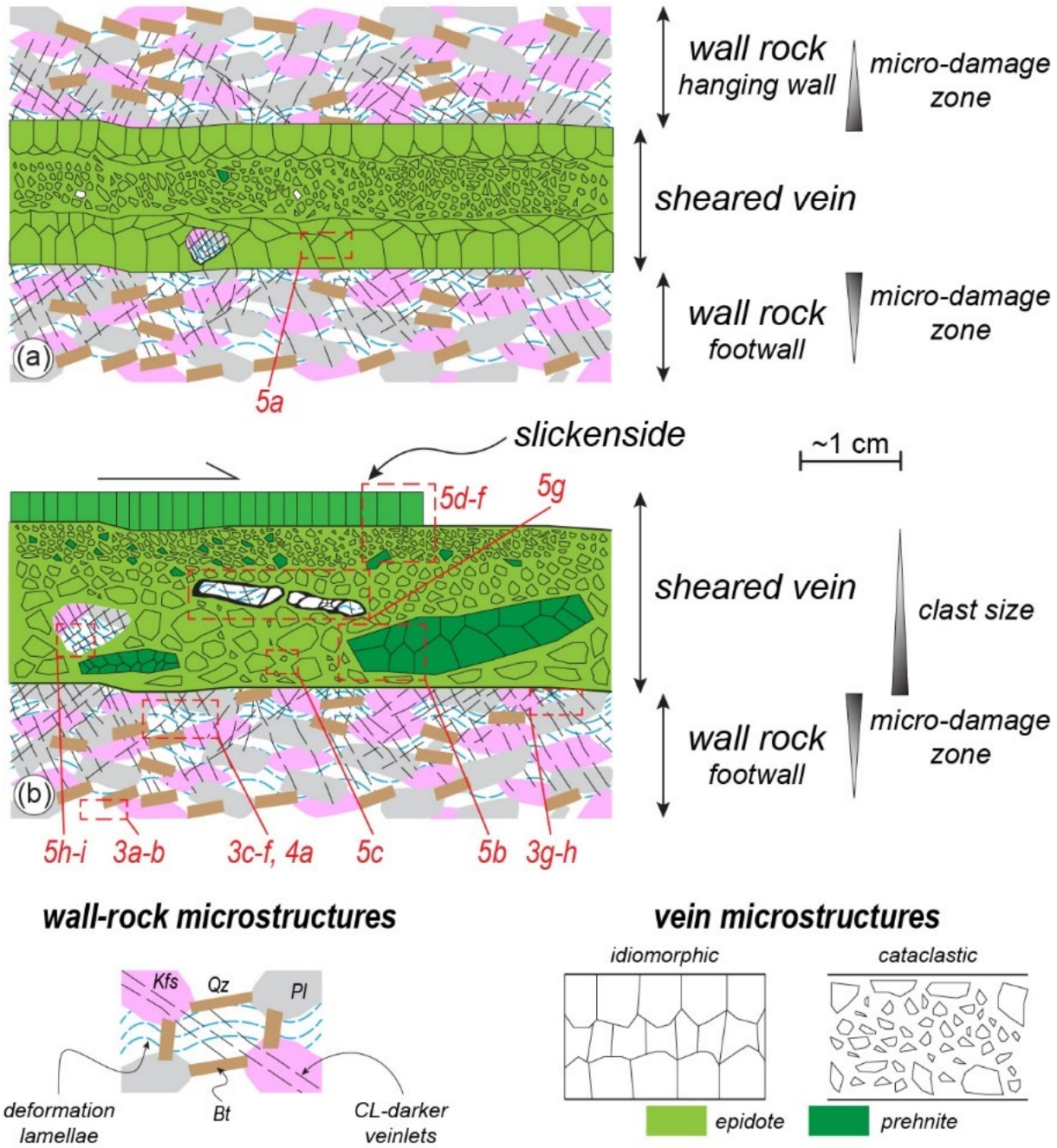

Fig. 6. Schematic illustration summarizing the different microstructures observed in the epidote-rich sheared veins and associated wall-rock. (a) Sheared veins with both footwall and hanging wall blocks preserved. (b) Sheared veins with only the footwall block preserved.

Mineral phase	Ep dark	Ep dark	Ep dark	Ep dark	Ep dark	Ep dark	Ep dark	Ep dark	Ep dark	Ep light	Ep light	Ep light	Ep light	Ep light	Ep light	Ep light	Ep light	Ep light	Ep light	Prn light
Na_2O												0.02	0.03							
MgO										0.20		0.16	0.09	0.16						
Al_2O_3	26.24	26.18	25.12	25.21	24.56	24.94	25.03	25.53	25.04	22.88	24.42	24.94	25.04	23.84	23.68	24.42	24.40	23.36	23.15	21.21
SiO_2	38.57	38.56	38.49	37.18	36.94	37.52	38.19	37.35	37.78	37.51	37.19	36.65	37.03	38.27	37.98	38.21	37.90	37.23	38.31	42.97
K_2O		0.04	0.02							0.02	0.03	0.02					0.03			0.02
CaO	23.09	23.61	23.12	23.08	23.05	23.90	23.93	23.50	23.78	22.05	23.51	23.07	23.04	22.89	23.35	23.15	23.03	23.07	23.66	26.66
TiO	0.11	0.15	0.07		0.04					0.02	0.21	0.09	0.07	0.06	0.10	0.04			0.10	0.17
Cr_2O_3												0.01	0.05			0.03		0.15		
MnO			0.17	0.16	0.20					0.06	0.09	0.08	0.12	0.16			0.11	0.29	0.37	
FeO	9.98	9.24	10.99	10.31	10.47	10.63	9.80	10.12	10.17	13.93	11.41	11.22	11.55	10.72	11.91	12.96	11.99	13.03	11.99	3.76
Total	97.99	97.77	97.98	95.94	95.27	96.99	96.95	96.50	96.77	96.66	96.86	96.26	97.02	96.10	97.02	98.81	97.47	97.13	97.57	94.79

Mineral phase	Prn light	Prn light	Prn light	Prn light	Prn light	Prn light	Prn light	Prn light	Prn light	Prn light	Prn light	Prn light	Prn light	Prn light	Prn dark	Prn dark	Prn dark	Prn dark	Prn dark
Na_2O																			
MgO			0.06												0.10			0.37	
Al_2O_3	22.26	21.79	21.87	22.08	22.20	22.92	22.71	22.27	21.67	22.33	22.77	23.41	21.30	21.86	23.12	23.54	23.78	23.77	24.01
SiO_2	43.84	42.77	43.04	43.26	42.62	43.03	43.93	44.70	43.99	43.94	43.34	43.22	42.44	43.31	42.77	43.55	43.13	43.62	43.98
K_2O	0.02		0.03			0.03	0.01								0.04				
CaO	26.63	26.76	26.35	26.71	26.62	26.61	27.18	27.04	27.04	27.12	27.12	26.94	26.52	27.03	26.53	27.42	27.51	26.88	27.48
TiO	0.21	0.11	0.05	0.07	0.13	0.21	0.09		0.06	0.04					0.15				
Cr_2O_3		0.00				0.18													
MnO		0.12						0.11									0.17	0.16	0.13
FeO	3.31	3.42	4.20	3.12	2.54	2.63	2.95	3.24	3.85	3.40	2.57	2.24	3.47	3.70	1.86	1.11	0.88	1.78	1.17
Total	96.27	94.97	95.60	95.24	94.11	95.63	96.87	97.36	96.61	96.83	95.80	95.82	93.74	95.90	94.57	95.62	95.46	96.57	96.76

Table 1. Compositions of epidote and prehnite from WDS-FEG. Dark and light refer to different grey color in BSE images.

5. Discussion

The SEM images document a complex and polyphase deformation history associated with vein formation which includes at least (i) an initial stage (well-preserved in the rocks surrounding the epidote-rich veins) of high stress with limited and rock-buffered (i.e., low external fluid vs. rock ratio) fluid infiltration along the micro-cracks; and (ii) following pulses of fluid infiltration, with precipitation of epidote ± prehnite, alternating with vein-parallel cataclastic shearing. Below we discuss the microstructural observations and propose a conceptual model for the nucleation (section 5.1) and cyclic development (section 5.2) of a highly connected fault-fracture network in a seismically-active hydrothermal system (Fig. 7).

5.1. Wall-rock damage and fluid redistribution during dynamic crack propagation

Deformation lamellae and quartz-filled veinlets in the magmatic quartz of the wall-rock close (≤ 1 cm far; Figs. 2e, 3, 5h-i) to the epidote-rich sheared veins are interpreted as the precursor stages of the epidote-rich hydrothermal fault-vein system (Fig. 7a).The early-stage evolution of wall-rock quartz deformation is supported by the observation that quartz with identical features (deformation lamellae, and epitaxial quartz-filled veinlets and rims) is included as clasts in the epidote-rich veins (Fig. 5g-i).

Quartz deformation lamellae have been reported in shock-impact rocks (e.g., Carter, 1965) and in exhumed middle-crustal shear zones from the Sesia-Lanzo Zone (Western Alps), associated with other high-stress deformation microstructures (e.g., twinning of jadeite, shattering of garnet), as evidence of upper-

crustal seismic ruptures that propagated in the middle-to-lower crust (Trepmann and Stöckhert, 2003). Deformation lamellae were also produced experimentally in natural quartz deformed at stress under strain rates of 10^{-4} s^{-1}) and relatively low temperatures (i.e., 400 °C) (Trepmann and Stöckhert, 2013). Similarly, these intra-crystalline deformation features are produced in metals deformed at high-strain rates and low temperatures (Drury, 1993).

The epidote-rich fault-vein networks of the BFZ formed at temperatures ≤ 300 °C (Herrera et al., 2005; Masoch et al., 2022). At these temperatures, the dominant deformation mechanisms active in quartz in many geological contexts are fracturing, cataclastic flow and pressure solution (Snoke et al., 1998; Stipp et al., 2002). In the seismogenic crust, high-stress concentrations are produced at the crack tip during crack propagation (Reches and Dewers, 2005). Thus, we propose that the observed deformation lamellae in the wall-rock magmatic quartz bounding the epidote-rich veins record the dynamic high-stress field associated with rupture propagation at seismic speeds (e.g., 0.7-0.9 Rayleigh shear wave velocity, Scholz, 2019) in the process zone of the crack tip (Faulkner et al., 2011; Vermilye and Scholz, 1998) (Fig. 7a). Blenkinsop and Drury (1988) proposed a similar interpretation for formation of this low-temperature intra-crystalline deformation microstructures found in the damage zone of the Bayas Fault hosted in quartzites (Cantabrian Zone, Variscan Orogen, Spain).

Near an earthquake crack tip propagating at speed close to the Rayleigh shear wave velocity, extreme deformation conditions (tensile stresses approaching 5 GPa and volumetric strain rates exceeding 10^{5} s^{-1}: Reches and Dewers, 2005) are achieved. At these extreme deformation conditions, rocks fail and pulverize (Okubo et al., 2019; Reches and Dewers, 2005). Alternatively, micro-cracks may propagate at extremely low rupture velocities (sub-seismic: $10^{-9} \div 10^{-4}$ m/s) compared to typical seismic velocities ($1 \div 4 \times 10^{3}$ m/s), by sub-critical crack growth driven by stress corrosion (Atkinson and Meredith, 1987). This sub-critical crack propagation mechanism is particularly efficient in silicate-built rocks in the presence of pressurized water, which keeps cracks open, and at high fluid temperatures (T ≥ 200°C). These ambient conditions are achieved in the vein network described in this study. However, the extremely low rupture velocities would not allow the achievement of high stress perturbations at the crack tip typical of fractures propagating at km/s (Freund, 1990; Reches and Dewers, 2005) and required for the formation of the deformation lamellae (Trepmann and Stöckhert, 2013) (Figs. 3c-h, 4).

The CL images reveal pervasive quartz-filled veinlets in the microscale damage zone of the epidote-rich veins, sharply cutting the deformation lamellae (Fig. 3d, 3f, 3h). We interpret the epitaxial quartz-filled veinlets as rapid (i.e., co-to-post-seismic) micro-fracture healing at the crack tip during seismic rupture propagation (Fig. 7a), as documented in several exhumed pseudotachylyte-bearing crustal faults hosted in

quartzo-feldspathic rocks (e.g., Bestmann et al., 2012, 2016; Mancktelow et al., 2022). Moreover, at the vein boundary in the footwall blocks, the deformed magmatic quartz appears strongly brecciated (Fig. 3g-h), resembling *in-situ* shattered or pulverized fault rocks found in exhumed upper to mid-lower crustal seismic fault zones (e.g., Doan and Gary, 2009; Fondriest et al., 2017, 2015; Johnson et al., 2021; Mancktelow et al., 2022; Mitchell et al., 2011). This indicates asymmetric fracturing in the damage zone during seismic rupture propagation (Di Toro et al., 2005).

The quartz-filled veinlets show a marked difference in CL signal compared to the deformed magmatic quartz (Fig. 3) consistent with low-temperature deformation of faulting and micro-fracture healing (Bestmann et al., 2016). The veinlet filling is controlled in composition by the crosscut wall-rock-forming minerals (quartz ± K-feldspar ± albite; Figs. 3-4). Thus, rapid (co-to-post-seismic) micro-fracture formation and healing at the earthquake tip occurred in a *rock-buffered* system, where the percolation of external hydrothermal fluids or fluid redistribution was still of a minor extent before the formation of a fully interconnected network of permeable cracks. In conclusion, we interpret the microstructures (i.e., deformation lamellae and epitaxial quartz-filled veinlets) preserved in the deformed magmatic quartz in the proximity of the epidote-rich sheared veins as evidence of dynamic propagation of small seismic ruptures and co- to post-seismic healing of a newly-produced micro-fracture network. Both low-temperature crystal-plasticity (deformation lamellae in quartz) and fracturing accommodated the high-stress conditions around a propagating seismic rupture (Fig. 7a).

Fig. 7. Conceptual model summarizing the development of the seismically-active hydrothermal system recorded in the studied epidote-rich fault-vein networks. (a) Initial stages of dynamic propagation of small seismic ruptures. The fault-fracture network is poorly interconnected and, in turn, fluid circulation is relatively low and at cm-scale (*rock-buffered system*). The blue box marks the zoom at the crack tip and shows the sequences of deformation processes which recorded the initial stages, well preserved in the wall-rocks, of seismic rupture propagation. (b) Late stage of distributed swarm-like seismicity (*fluid-buffered system*). Highly-interconnected fault-fracture networks allow the ingression of overpressured fluids leading to swarm-like earthquake sequences, well recorded in the sheared veins. The cyclic deformation sequence is driven by fluid pressure variation as illustrated in Fig. 8.

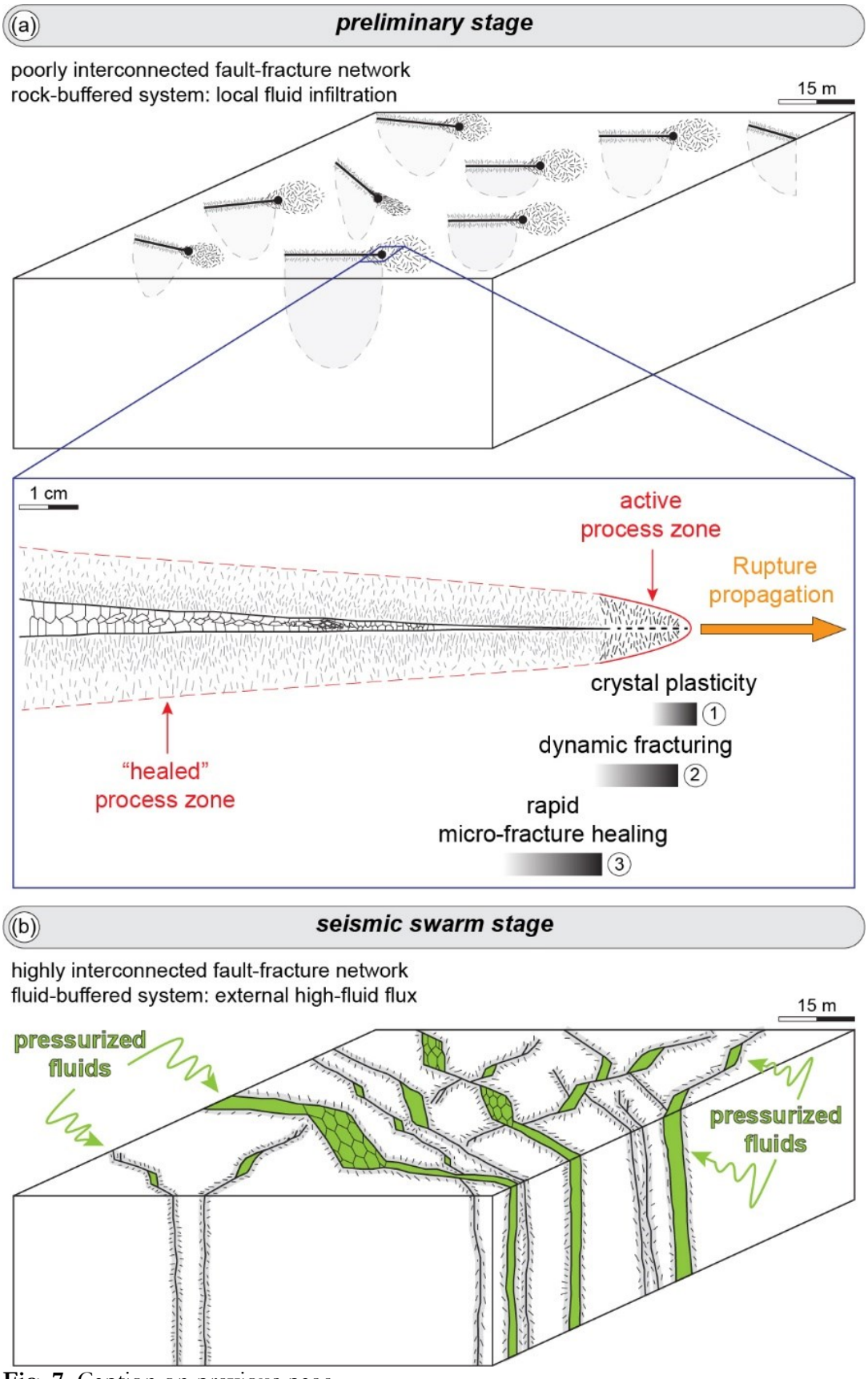

Fig. 7. Caption on previous page.

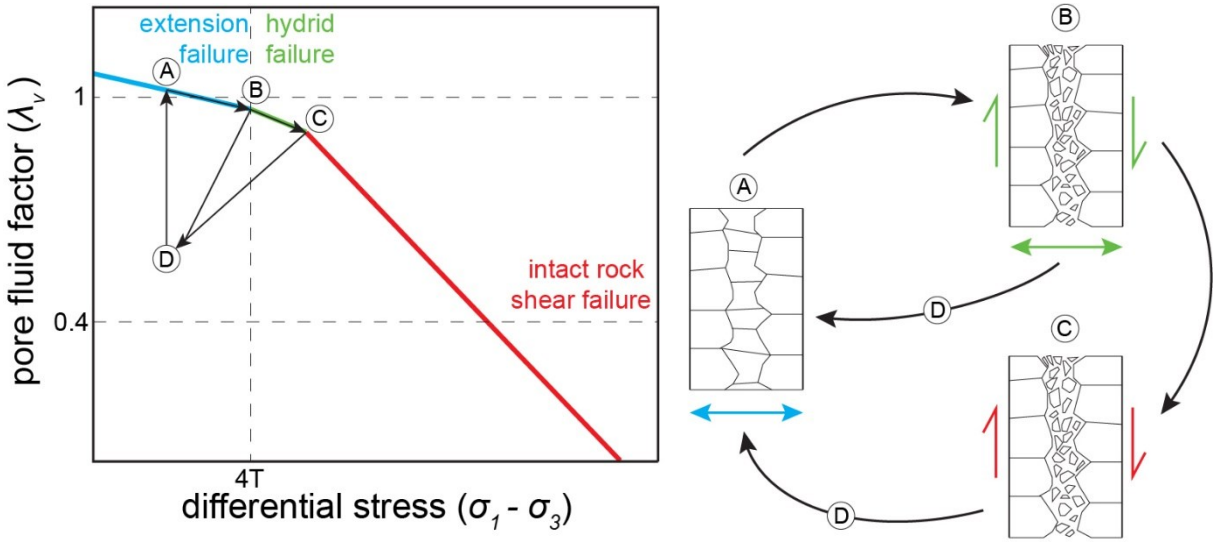

Fig. 8. $\lambda - \angle\sigma$ diagram (left) and cartoon (right) illustrating the deformation cycle governing seismicity during the swarm stage. The schematic $\lambda - \angle\sigma$ diagram illustrates the fluid pressure vs. tectonic stress paths recorded by the sheared veins, which show cyclic fluid-driven extensional-to-hybrid veining and shearing. Evolution of fluid pressure and stress states controls the temporal evolution and deformation path of swarm sequence till fluid depletion.

5.2. Pore pressure oscillations in a highly connected hydrothermal (fluid-buffered) fault-fracture network

The epidote-rich veining and shearing postdate the initial short-term co-seismic deformation recorded in the deformed magmatic quartz, as discussed in the previous section. This initial fracturing and associated wall-rock damage is precursory to development of a more robust fluid ingression within the initially low-permeability crystalline rocks (Fig. 7). This fluid ingression is accompanied by switch from the initially fluid-poor rock-buffered system to a fluid-buffered one (Fig. 7b). In hydrothermal systems, rock failure is governed by fault-valve behavior (Sibson, 1992a, 1992b, 1989), associated with transient fluctuations in pore fluid pressure.

The epidote-rich fault-vein networks show cyclic and mutually overprinting events of extensional veining and shearing (Figs. 2, 5a-f). Cataclasites include fragments of earlier veins (Figs. 2b-c, 2e, 5b-d, 5f), indicating that extensional veining preceded either hybrid extensional-shear fracturing (Figs. 2b, 5f) or shearing (Fig. 2a). This overprinting of structures can be explained considering the $\lambda - \angle\sigma$ failure mode diagram (Cox, 2010), where λ is the pore fluid factor ($\lambda = p/\sigma_v$; where p and σ_v is the pore fluid pressure and the vertical stress, respectively) and $\angle\sigma$ is the differential stress ($\angle\sigma = \sigma_1 - \sigma_3$; where σ_1 and σ_3 are the maximum and minimum principal compressive stresses, respectively). At low differential stresses ($\angle\sigma < 4T$; where T is the tensile strength of the material) and high pore fluid pressure, hydraulic fracturing (and extensional veining) occurs before shear failure (Murrel-Griffith failure criteria, Price and Cosgrove, 1990) (step A in Fig.

8). Then, the increase in tectonic-related differential stress leads to hybrid extensional-shear failure (step B in Fig. 8) to shear failure (step C in Fig. 8), stress drop and fault depressurization (step D in Fig. 8). The build-up of fluid pressure may repeat this cycle of hydraulic fracturing followed by hybrid extensional-shear fracturing till shearing (Cox, 2016; Phillips, 1972).

5.3. Comparison with natural fluid-driven earthquake swarms

Fluid-driven earthquake swarms are caused by transient pore fluid pressure oscillations, triggering distributed small-in-magnitude earthquakes in km-scale mesh-like dilatant fault-fracture networks (e.g., Hill, 1977; Mesimeri et al., 2021; Shelly et al., 2022; Sibson, 1996). High-precision hypocentral localization and the focal mechanisms of earthquakes pertaining to swarm-like sequences show that these earthquakes are associated with both co-seismic dilation and shearing, producing large non-double-couple (i.e., isotropic) and double-couple seismic signals in the same period of time, respectively (e.g., Legrand et al., 2011; Shelly et al., 2013). The microstructures found in the epidote-rich veins and associated micro-damage zones (Figs. 3-5) document that the initial stages of propagation of small seismic ruptures within a low-permeability rock volume produced the pathways for the ingression of external (probably from the Earth's surface; Chapter 4) pressurized fluids within the fault system, leading to swarm-like seismicity (Fig. 7). Swarm-like seismic activity is attested by cyclic extensional veining and cataclasis (i.e., shearing), driven by pore pressure fluctuations (Fig. 8), which resemble non-double-couple (crack opening) and double-couple (shear fracture) seismic signals, currently detected in earthquake swarms (e.g., Legrand et al., 2011; Shelly et al., 2013). At large scale, the epidote-rich fault-vein networks are spatially associated with major transtensional faults of the Caleta Coloso Duplex (i.e., subsidiary faults of the BFZ; Fig. 1a) and occur at structural complexities, i.e., fault intersections and linkage (Masoch et al., 2022) (Fig. 1b). This structural organization is the final expression of the mature architecture of a fault system in a high-fluid flux setting and, thus, the duplex represents a crustal seismic source capable to have generated fluid-driven earthquake swarms in an upper-crustal hydrothermal system.

6. Conclusions

- The extensive epidote-rich fault-vein networks of the damage zone of Bolfin Fault Zone and of the Caleta Coloso Duplex, at larger scale, are exceptionally well-exposed over tens of square kilometers in the Atacama Desert (Northern Chile). The fault-vein networks are spatially distributed around major transtensional faults of the duplex, and consist of sheared veins with lineated slickenside, extensional veins and dilatant breccias with scattered orientations.

- Based on high-resolution microstructural analysis, we document that the wall-rocks in proximity to small-displacement (< 1.5 m) sheared veins initially experienced dynamic high stresses related to the propagation of small seismic ruptures in a poorly connected fault-fracture system with limited fluid infiltration. Instead, the veins recorded cyclic extensional veining and cataclasis driven by fluid pressure fluctuations in a mature and highly interconnected fault-fracture system, resembling fluid-driven swarm-like earthquake sequences.
- The extensive epidote-rich fault-vein networks are a fossil analogue of swarm-like earthquake sequences and represent a unique record of the evolution in space and time of an upper-crustal swarm-like seismic source, from its early nucleation stages to the later mature architecture.

Chapter 4

Transition from mainshock-aftershock to swarm-like seismicity driven by surficial fluid infiltration (Bolfin Fault Zone, Chile)

This study was conducted with the collaboration of Luigi Dallai, Davide Novella, Rodrigo Gomila, Michele Fondriest, Giorgio Pennacchioni, José Cembrano and Giulio Di Toro. I was assisted during the sample preparation (but not continuously) by Davide Novella. I was assisted during the isotope analysis (but not continuously) by Luigi Dallai. The material presented here was discussed with Luigi Dallai, Davide Novella, Rodrigo Gomila, Michele Fondriest, Giorgio Pennacchioni, José Cembrano and Giulio Di Toro.

Abstract

Active hydrothermal systems are characterized by sustained fluid flow and seismic to aseismic activity, including mainshock-aftershock and swarm-like seismicity, slow slip events, etc. However, the origin of fluids controlling the seismicity in these tectonic settings is poorly constrained. By using hydrogen stable geochemistry, we investigate the origin of fluids impregnating the exhumed >40-km-long Bolfin Fault Zone (BFZ). The BFZ is part of the Early Cretaceous Atacama Fault System (Chile), cuts tonalites, granodiorites and diorites, and its ancient seismicity is as attested by the occurrence of pseudotachylytes-cataclasites produced at 5-7 km depth and ≤ 300 °C. The pseudotachylytes are found at the core and in minor faults departing from the BFZ, and are possibly associated with mainshock-aftershock seismic sequences. This fault network is postdated by an extensive hydrothermal fault-vein network, consisting of epidote-rich hydrothermal fault-veins and dilational breccias formed at 3-7 km depth and 200-250 °C. The epidote-rich fault-vein network is located at fault linkages and intersections and is possibly associated with swarm-like seismicity. Pseudotachylytes have hydrogen compositions (-71‰ ≤ δD ≤ -48‰), similar to those of the associated cataclasites (-72‰ ≤ δD ≤ -48‰) and of the wall rocks (-78‰ ≤ δD ≤ -56‰). Instead, the epidote-rich veins and breccias have less negative hydrogen compositions (-31‰ ≤ δD ≤ -9‰). We conclude that seismic faulting recorded by pseudotachylytes associated with mainshock-aftershock sequences occurred in a rock-buffered environment, where the source of hydrous fluids dissolved in the frictional melt were the hydrogen-bearing minerals forming the cataclasites and the wall rocks. Instead, the distributed fluid-driven swarm-like seismicity associated with the hydrothermal fault-vein systems and breccias was controlled by the ingression of surficial (i.e., near-surface-derived) fluids percolating within a more evolved hydraulic system.

1. Introduction

In the Earth's upper crust, seismicity spans from mainshock-aftershock to swarm-like sequences, as described by the Gutenberg-Richter and by the Omori laws (Gutenberg and Richter, 1944; Omori, 1894). In typical mainshock-aftershock sequences, the largest aftershock is about 1.2 in magnitude smaller than the mainshock (Scholz, 2019). In some cases, mainshock-aftershock sequences include "doublets", or one or two aftershocks with magnitude slightly smaller than the one of the mainshock (e.g., Friuli (Italy), 6.5 M_w & 6.0 M_w, 1976; Emilia (Italy), 6.0 M_w & 5.9 M_w, 2012; Amatrice-Norcia (Italy), 6.0 M_w & 6.5 M_w, 2016; Turkey-Syria 7.8 M_w & 7.5 M_w, 2023). Instead, swarm-like sequences are characterized by diffuse seismicity, with several seismic events of similar magnitude driven by fluid migration within fault systems (Cox, 2016; Dempsey et al., 2014; Fischer et al., 2014; Legrand et al., 2011; Masoch et al., 2022; Mesimeri et al., 2021; Mogi, 1963; Shapiro, 2015; Shelly et al., 2022; Sibson, 1996; Sykes, 1978). The mainshock-aftershock sequences can be transitional to swarm-like sequences (e.g., Colfiorito 6.0 M_w sequence, Italy, 1997).

Currently active hydrothermal systems are associated with sustained fluid flow and swarm-like distributed seismicity (e.g., Yellowstone caldera, Wyoming: Shelly et al., 2013a; Long Valley Caldera, California: Shelly et al., 2016, 2015; West-Bohemia/Vogtland, Central and Western Europe: Fischer et al., 2014; Hakone caldera, Japan: Yukutake et al., 2011; Southern Andean Volcanic Zone, Chile: Legrand et al., 2011). Nevertheless, despite progress in imaging the evolution in space and time of seismic sequences through geophysical and seismological techniques (e.g., Legrand et al., 2011; Shelly et al., 2022), the source (e.g., magmatic, meteoric) of the fluids triggering seismicity in these high-fluid flux settings is poorly constrained.

Exhumed mature crustal-scale fault zones record polyphase deformation history which include multiple episodes of faulting (possibly seismic) and fluid infiltration, from the formation of the fault at the base of the seismogenic crust to its exhumation at the surface (Handy et al., 2007). Consequently, microstructural and geochemical investigations of fault zone rocks may constrain the deformation conditions and the geochemical environments where seismic or aseismic fault activity occurred. In particular, stable isotope geochemistry has been extensively used for assessing the source (e.g., magmatic, metamorphic, mantle, meteoric) of fluids which interacted with fault rocks through fault lifetimes (e.g., Hartman et al., 2018; Lucca et al., 2019; Mittempergher et al., 2014; Moecher and Sharp, 2004; O'Hara and Sharp, 2001; Peverelli et al., 2022; Smeraglia et al., 2021; Tardani et al., 2016).

In this study, we investigate the origin of fluids which interacted with fault zone rocks of the >40-km-long well-exposed Bolfin Fault Zone (BFZ), an exhumed, seismogenic crustal-scale fault of the Early Cretaceous intra-arc Atacama Fault System (Atacama Desert; Northern Chile; Fig. 1a). The exceptional

outcrop conditions result from the hyper-arid climate since 25-22 Ma (Dunai et al., 2005) and the slow erosion of the Atacama Desert. The BFZ is a master fault of the crustal-scale transtensional Caleta Coloso Duplex (Fig. 1b) (Masoch et al., 2021). The BFZ was seismically active as attested by occurrence of pseudotachylytes associated with chlorite-rich cataclasites and found in the main fault core strands and in minor faults departing from the BFZ (Masoch et al., 2022). The pseudotachylytes formed at 5-7 km depth and ≤ 300 °C in a fluid-rich environment documented by syn-kinematic chlorite-epidote veining and extensive propylitic alteration (Gomila et al., 2021; Masoch et al., 2022, 2021). This fault architecture, possibly recording mainshock-aftershock sequences, is overprinted by extensive hydrothermal fault-vein networks and dilatant breccias associated with subsidiary faults located at the BFZ linkages and intersections (Masoch et al., 2022). These fault-vein networks formed at 3-7 km depth and ≤ 250 °C and are interpreted as fossil examples of upper-crustal earthquake swarm activity (Masoch et al., 2022; Chapter 3). By using hydrogen isotope geochemistry, a tool sensitive to meteoric waters (e.g., Sharp, 2007), we document that pseudotachylytes production occurred in a rock-buffered system, characterized by limited, local fluid circulation (i.e., fluids with the same hydrogen isotope compositions of those of the magmatic wall rocks) in the fault zone, similar to that found in other upper-crustal pseudotachylytes (Mittempergher et al., 2014; Moecher and Sharp, 2004). Instead, later fluid-driven seismicity attested by the extensive hydrothermal fault-vein networks was controlled by the ingression of surficial (i.e., near-surface-derived) fluids in a more mature, hydraulically-connected, upper-crustal hydrothermal system. We conclude that the transition in type of seismicity, from mainshock-aftershock to the swarm-like sequences, was driven by both fault architectural evolution and ingression of newly-sourced fluids in the fault system.

Fig. 1. Geological setting of the Bolfin Fault Zone. (a) Crustal-scale geometry of the Atacama Fault System comprised of its three concave-shaped segments. Shaded relief image modified from Cembrano et al. (2005), Masoch et al. (2021) and Veloso et al. (2015). Red box indicates the area shown in (b). (b) Geological map of the area surrounding the Bolfin Fault Zone. The green area represents the distribution of the epidote-rich fault-vein networks within the Caleta Coloso Duplex. Modified from Masoch et al. (2021). White circles mark the localities from which the analyzed samples come from.

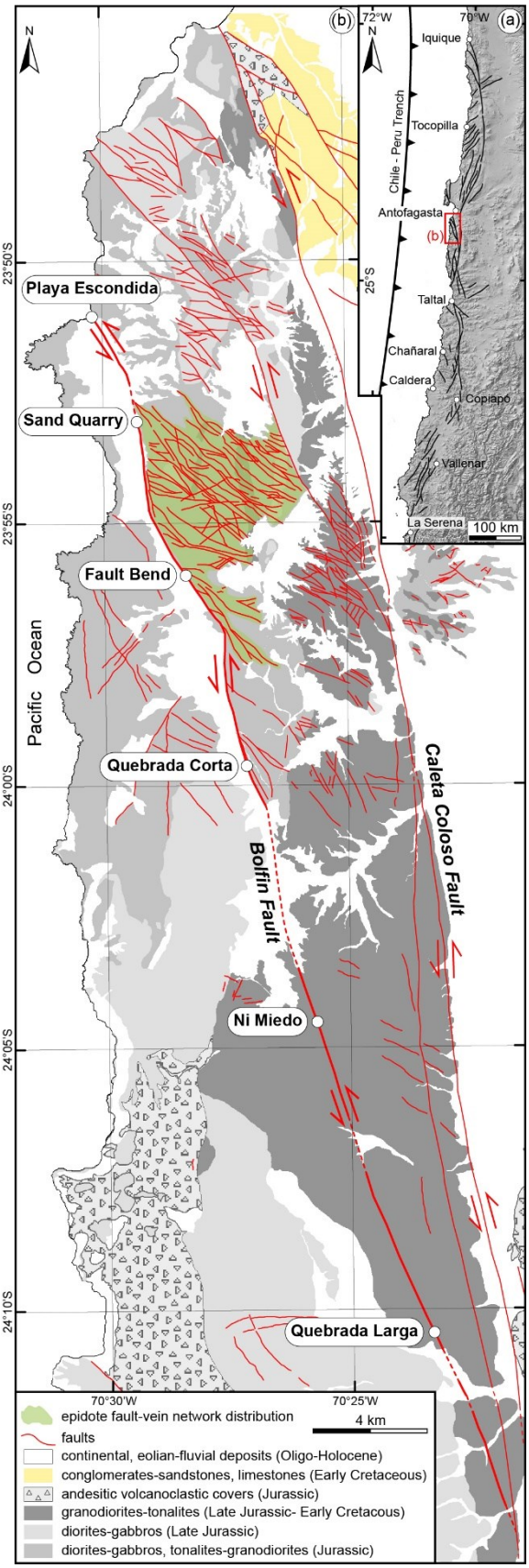

Fig. 1. Caption on previous page.

2. Bolfin Fault Zone

The BFZ is a >40-km-long, exhumed, pseudotachylyte-bearing fault zone of the 1000-km-long, Early Cretaceous, strike-slip intra-arc Atacama Fault System, which cuts through the Jurassic-Early Cretaceous magmatic arc of Coastal Cordillera (Northern Chile; Fig. 1) (Arabasz, 1971; Cembrano et al., 2005; Masoch et al., 2021; Scheuber and González, 1999). The BFZ is a sinistral strike-slip fault cutting through Jurassic diorite-gabbro to tonalite-granodiorite (Bolfin Complex) and Late Jurassic-Early Cretaceous tonalite-granodiorite (Cerro Cristales pluton) plutons (Fig. 1b). The BFZ is a master fault of the crustal-scale transtensional Caleta Coloso Duplex and accommodated an apparent strike-slip displacement of ~1 km (Cembrano et al., 2005; Masoch et al., 2022, 2021). The BFZ has a sinuous (N-to-NNW-striking) crustal-scale geometry (Fig. 1b), resulted from the exploitation of magmatic foliation of plutons and dyke swarms during fault nucleation and subsequent linkage through NW-striking fault segments during fault growth (Masoch et al., 2021).

Overall, the BFZ architecture consists of multiple cataclastic fault strands enveloped within a 150-m-wide damage zone (see Masoch et al., 2022 for a detailed description of the BFZ architecture). Chlorite-rich cataclasites to ultracataclasites host pristine to altered pseudotachylytes (Fig. 2a-b), both in the BFZ core strands and in subsidiary faults in the damage zone (Masoch et al., 2022). The damage zone consists of variably damaged and altered rock volumes (Masoch et al., 2022). The most damaged domains present extensive epidote-rich fault-vein networks associated with NW-to-WNW-striking faults splaying out from the BFZ (i.e., second-order faults of the duplex; Cembrano et al., 2005; Masoch et al., 2022). The extensive epidote-rich networks consist of small-displacement (< 1.5 m) sheared veins with lineated slickensides and extensional veins and dilatant breccias sealed by epidote + prehnite ± chlorite ± quartz ± K-feldspar ± calcite (Fig. 2c-d) (Masoch et al., 2022). The extensive epidote-rich fault-vein networks observed in the BFZ damage zone is more extended in the Caleta Coloso Duplex (see Cembrano et al., 2005; Herrera et al., 2005). At Fault Bend locality, an epidote-quartz-prehnite breccia body is found within a decameter-sized dilational jog in the damage zone (Fig. 2e-f and see Fig. 8 in Masoch et al., 2022).

The extensive epidote-rich fault-vein networks and the epidote-quartz-prehnite breccias crosscut the chlorite-rich cataclasites and associated pseudotachylytes (Gomila et al., 2021; Masoch et al., 2022). Pseudotachylyte-bearing faults formed at 5-7 km depth and ≤ 300 °C (Gomila et al., 2021; Masoch et al., 2022, 2021) in a fluid-rich environment as attested by syn-kinematic chlorite-epidote(-quartz-calcite) veining and extensive propylitic alteration. Instead, epidote-rich veining and faulting occurred at 3-7 km depth and ≤ 250 °C (Herrera et al., 2005; Masoch et al., 2022) and are interpreted as ancient upper-crustal fluid-driven earthquake swarms (Masoch et al., 2022).

Fig. 2. Examples of the different fault zone rocks of the Bolfin Fault Zone. The different domains and minerals separated for the isotopic analysis are indicated according the color code used in the Fig. 3. (a) Fresh pseudotachylyte vein and its associated cataclasite form the fault core. Plane-polarized scan of thin section of sample SQ09-18 (Sand Quarry locality) (b) Microstructure of pseudotachylyte with microlites of plagioclase (medium grey) and K-feldspar (dark grey), and interstitial acicular biotite and titanite (bright color). The microlites wrap an altered plagioclase (aPl) clast with spinifex microstructure. BSE image. WGS84 GPS location: 23.8830972°S, 70.4880111°W. (c) Polished sample of epidote veins surrounded by a reddish alteration halo in the damaged granodiorite. The thickest vein is reworked by by a mm-thick cataclasite (pale green). The dark green epidote vein filling was selected form hydrogen isotope analysis. Sample 19–48 (Sand Quarry locality). WGS GPS location: 23.88442°S, 70.48567°W. (d) Microstructure of the epidote vein filling with idiomorphic zone epidote crystals. BSE image, sample 19-48. (e) Polished sample of a chaotic epidote-quartz-prehnite breccia, including cm-in-size angular fragments of earlier epidote veins (green dots in Fig. 3). The latter are sealed by a pale green cement of epidote + quartz + prehnite (light blue dots in Fig. 3). Sample M2 (Fault Bend locality). WGS GPS location: 23.934563°S, 70.465428°W. (f) Microstructure of the breccia. Vein fragments consist of zoned epidote and are immersed in cement of epidote + quartz + prehnite + chlorite. BSE image, sample M2.

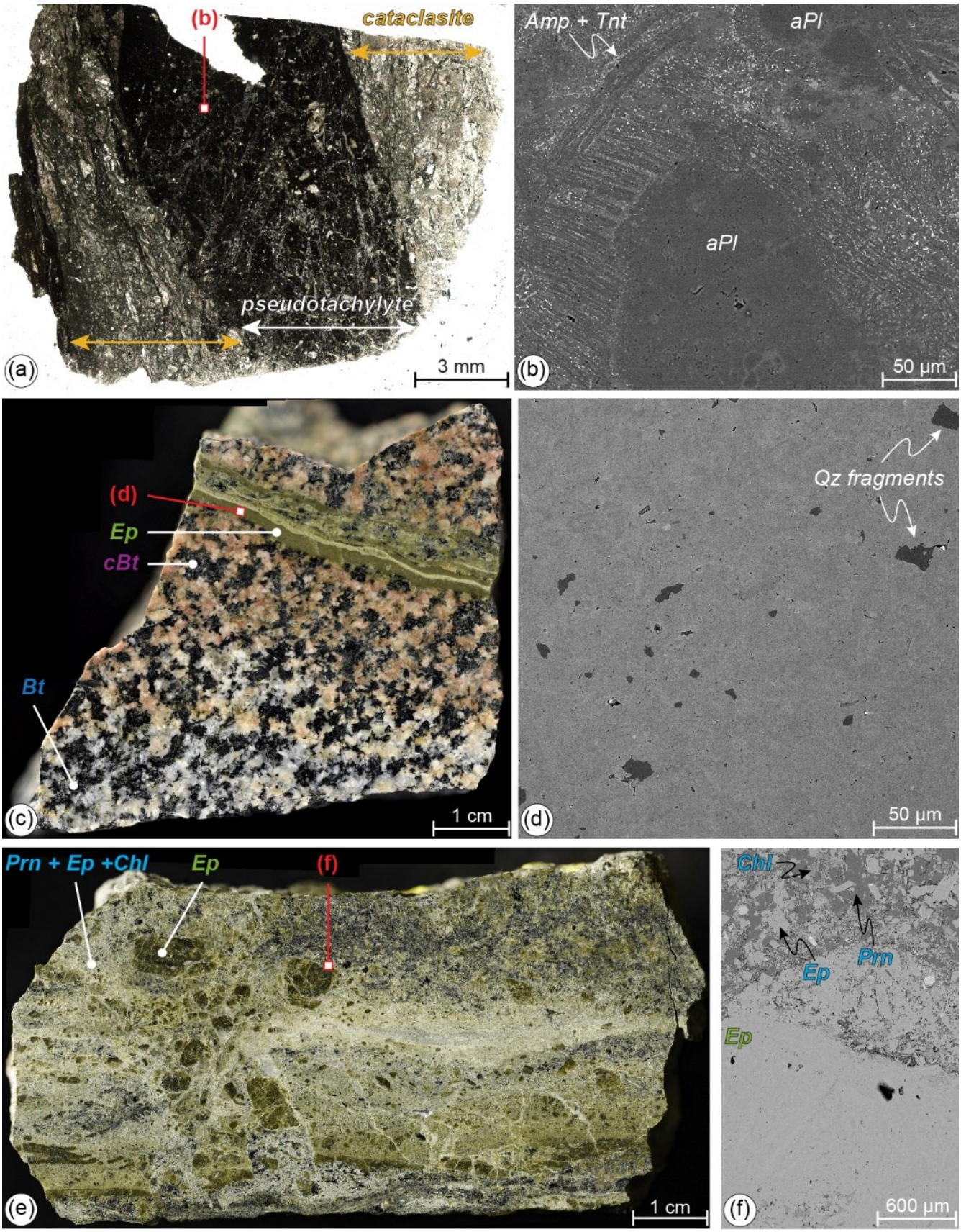

Fig. 2. Caption on previous page.

3. Methods

Microstructural observations were conducted on polished thin sections oriented parallel to fault lineation and orthogonal to fault/vein boundary. Transmitted-light optical microscopy was used to determine microstructural observations at thin section scale and to identify areas suitable for microanalytical investigations. Scanning electron microscopy (SEM) was used to acquire high-resolution backscattered electron (BSE) images coupled with semiquantitative energy dispersion spectroscopy (EDS) elemental analysis. SEM investigations were performed with a CamSCAN MX3000 operating at 25 kV at Department of Geosciences at Università degli Studi di Padova (Uni. Padova). Field-emission SEM investigations were performed with a Tescan Solaris operating at 7-10 kV at the Department of Geosciences (Uni. Padova) and a JOEL JSM-6500F operating at 15 kV at HP-HT laboratories of Istituto di Geofisica e Vulcanologia in Rome, respectively.

Bulk mineralogy of rock samples was retrieved through X-ray powder diffraction (XRPD) and semiquantitative mineralogical composition were retrieved through Reference Intensity Ratio (XRPD-RIR) method. XRPD analyses were performed with a PANalytical X'Pert Pro diffractometer equipped with a Co radiation source, operating at 40 mA and 40 kV in the angular range of $3° < 2\theta < 85°$, installed at Department of Geosciences (Uni. Padova).

Samples representative of the different structural elements pertaining of the BFZ were selected for isotopic analysis from six localities along fault strike (namely from north to south: Playa Escondida, Sand Quarry, Fault Bend, Quebrada Corta, Ni Miedo and Quebrada Larga; Fig. 1). Hydrogen isotope ratios were measured on (i) hydrogen-bearing mineral phases separated from 700-μm-thick double polished thin sections through hand picking under the binocular microscope and (ii) powders of bulk chlorite-rich cataclasites (Cata), bulk pseudotachylytes (Pst), and bulk epidote-quartz-prehnite breccias (Brc). Manually separated hydrogen-bearing mineral phases are biotite from unaltered tonalites-granodiorites (Bt), amphibole from unaltered diorites (Amp), chloritized biotite from alteration halos associated with veins (cBt), epidote from epidote-rich veins and breccias (Ep), epidote from earlier vein fragments within epidote-prehnite-quartz breccias (Ep) and epidote-prehnite-chlorite cement sealing the breccias (FC). The mineralogy of bulk cataclasites, pseudotachylytes and epidote-quartz-prehnite breccias are reported in Table 1. The samples were analyzed using a Flash 2000 Organic Elemental Analyzer in line with a Delta V Advantage IRMS (Dipartimento di Geochimica, Università degli Studi di Roma La Sapienza), following the method described by Sharp et al. (2001). Between 2 and 4 replicates of 1.0-1.5 mg of biotite and powders of cataclasites and pseudotachylytes, and 2.0-2.5 of amphibole, epidote and powders of hydrothermal breccias were analyzed

per each sample, until a reproducibility of ±5‰ was obtained. The results the analyses are presented in the standard *delta* notation:

$$\delta = \left(\frac{R_x - R_{std}}{R_{std}}\right) * 1000$$

where *R* is the ratio of the abundance of the heavy to the light isotope, *x* denotes the sample and *std* the reference standard VSMOW (Vienna Standard Mean Ocean Water). The standards Bonsall biotite, LR151 biotite and LR8 amphibole were analyzed every series of 8-10 analyses, to correct for the apparatus drift, based on standard δD values of -59‰, -115‰ and -178‰, respectively.

Sample	Outcrop	rock	Qtz	Pl	Kfs	Amp	Act	Bt	Chl	Ep	Cal	Prn	Spl	Ilt	Tnt
PE02-2018	Playa Escondida	Cata	19	27	7		7		15	25					0
AT07-2017-HR	Playa Escondida	Cata	27	38			16	1	7	3	3				5
B15-19-HR	Playa Escondida	Cata	39	35	2		1		12	3	4				3
B17-19-HR	Playa Escondida	Cata	40	36	5				5	7	3				2
AT07-2017-PSTV	Playa Escondida	Pst	29	34	17		2		7	5	4				2
B15-19-PST	Playa Escondida	Pst	32	20	20			1	7	5	12				2
B17-19-PSTV	Playa Escondida	Pst	30	31	20		1	1	4	4	8				1
SQ09-18-HR	Sand Quarry	Cata	21	41	7	4		1	15	6	2		1		3
SQ09-18-PST	Sand Quarry	Pst	18	25	34	1		1	15		2		3		4
FB02-HR	Fault Bend	Cata	15	43	6	19		1	10	3			1		2
RGRB02-HR	Fault Bend	Cata	11	47	7	3		3	22	1	2		1		3
FB02-PST	Fault Bend	Pst	18	41	12	3		1	17	2				3	3
RGRB02-PST	Fault Bend	Pst	12	44	9	3		3	24		1		3		4
M2	Fault Bend	Brc	11				2		13	57	1	15			1
19-177	Fault Bend	Brc	32						18	21	1	26			2
FB21-875-BR	Fault Bend	Brc	17	3			4		12	39	1	24			
19-103-HR	Q.da Corta	Cata	11	47	7	3		1	22	1	2		1		3
19-103-PST	Q.da Corta	Pst	12	44	9	3		1	24		1		3		5
NM20-225-HR	Ni Miedo	Cata	19	45		5		1	14		2		2		3
NM20-225-PST	Ni Miedo	Pst	13	13	27			1	18	24			2		3
19-98-C-HR	Q.da Larga	Cata	27	42	11		3	6	11		0				
19-98-C-CATA	Q.da Larga	Cata	31	38	13			3	13		2				
19-98-C-PST	Q.da Larga	Pst	32	31	20			1	8	6	1				2

Table 1. Mineralogy of the bulk samples from XRPD-RIR. Mineral abbreviations from Whitney and Evans (2010).

4. Petrography

4.1. Undeformed wall rocks (diorites, tonalites-granodiorites)

The undeformed wall rocks (i.e., weakly-deformed unit in Masoch et al., 2022) consist of foliated diorites and either foliated or isotropic tonalites-granodiorites. The diorites consist of plagioclase ($Ab_{60}An_{39}Or_1$ to $Ab_{65}An_{35}Or_0$), amphibole (hornblende), quartz, biotite and minor K-feldspar, apatite and opaques (Masoch et al., 2022). The cm-sized idiomorphic plagiocalse crystals define the magmatic foliation and interstitial quartz shows undulose extension. The tonalites-granodiorites consist of plagioclase ($Ab_{47}An_{53}Or_0$ to $Ab_{62}An_{38}Or_0$), quartz, K-feldspar, biotite, amphibole (hornblende), apatite and opaques in variable modal proportions (Masoch et al., 2022). The magmatic foliation is marked by cm-sized idiomorphic plagiocalse crystals and interstitial quartz shows undulose extension. Within the inner damage zone (i.e., chloritized and fractured unit; Masoch et al., 2022), the wall rocks are altered with replacement of magmatic minerals by: biotite by chlorite + opaques, amphibole by (Fe-)actinolite or chlorite + opaques, and plagioclase by albite + epidote.

4.2. Chlorite-rich cataclasites

Chlorite-rich cataclasites contain angular clasts of altered wall rocks and reworked cataclasites in variable proportion, immersed in a fine-grained (< 20 μm) matrix of chlorite + epidote + quartz + albite + K-feldspar + (Fe-)actinolite. The thickest cataclasites are layered. Cataclasites and ultracataclasites are foliated in the high-strain horizons with the composite S-C-C' foliation defined by either chlorite or epidote + K-feldspar aggregates, enveloping sheared lithons of albitized plagioclase and quartz.

4.3. Pseudotachylytes

Pseudotachylytes are associated with chlorite-rich cataclasites (Fig. 2a). Pseudotachylytes show flow structures, chilled margins, microlites and spherulites (e.g., Magloughlin and Spray, 1992) and are variously affected by alteration (Fig. 2a-b). Less altered pseudotachylytes include (i) albite microlites, intergrown with amphibole and titanite (Fig. 2b), (ii) quartz and plagioclase clasts immersed in a homogeneous cryptocrystalline matrix with a "K-feldspar-rich" composition (Gomila et al., 2021; Masoch et al., 2022). More altered pseudotachylytes consist of a fine-grained (~20-30 μm grain size) matrix of albite + chlorite + epidote. Pseudotachylytes cut chlorite-epidote(-calcite) veins and are cut by chlorite-, K-feldspar- and calcite-veins. Some pseudotachylytes include amygdalae or vesicles filled with quartz + calcite + epidote + chlorite (see Gomila et al., 2021 for further details).

4.4. Epidote-rich veins and breccias

Epidote-rich veins show multiple episodes of veining and include fragments of wall rocks and of earlier veins (Fig. 2c-d). The epidote veins (dark green epidote in hand specimen) consist of zoned epidote (Al-rich core and Fe-rich rim), with a grain size of ~20-30 μm, and minor interstitial prehnite + K-feldspar ± calcite (Fig. 2c-d). Cataclasites (pale green in the hand specimen) reworking the epidote veins have fine-grained (<10 μm) epidote grains and a highly porous framework (pores size up to ~5 μm). Dilatant breccias include fragments of earlier epidote veins, which consist of fine (<5 μm) epidote grains and have a highly porous framework. The sealing cement consists of fine (<20 μm) epidote grains. Veins and breccias are associated with pervasive fluid-induced alteration in the surrounding damaged wall rocks (Fig. 2c). Within the alteration halo, plagioclase is replaced by albite, and biotite and amphibole by chlorite ± opaques (Fig. 2c; Masoch et al., 2022). Microfractures are filled with epidote + K-feldspar.

4.5. Epidote-quartz-prehnite breccias

The epidote-quartz-prehnite breccias consist of green, cohesive mosaic to chaotic breccias, including angular fragments of wall rock and earlier breccias and veins (Fig. 2e), cemented by idiomorphic zoned epidote + prehnite + quartz + chlorite (Fig. 2e-f). The vein fragments consist of (i) idiomorphic, zoned (i.e., core: Al-rich Ep; outer: Fe-rich Ep) epidote (sampled for isotopic analysis) and minor quartz, and (ii) quartz + zoned epidote + zoned prehnite ± chlorite vein filling (Fig. 2f).

5. Hydrogen isotope compositions

The hydrogen isotope compositions are reported in Fig. 3. Magmatic biotite and amphibole from the undeformed wall rocks (i.e., diorites, granodiorites and tonalites) have δD between -78‰ and -56‰, and -76‰ and -62‰, respectively. Instead, biotite close (4-5 cm far from the veins) to epidote-rich veins has δD of -39‰, similar to the values of chloritized biotite within the alteration halo of epidote-rich veins (-43‰ ≤ δD ≤ -38‰). The δD values of bulk chlorite-rich cataclasites vary between -72‰ and -58‰, with one sample of foliated cataclasite (rich in epidote; Table 1) from Playa Escondida and one of ultracataclasite from Sand Quarry yielding the highest values (-49‰ and -48‰, respectively). Bulk pseudotachylytes have δD ranging between -71‰ and -53‰ and mostly overlapping with those of the hosting cataclasites. Both cataclasites and pseudotachylytes from Playa Escondida have the lowest δD of the dataset and vesiculated pseudotachylytes have δD of -69‰ and -67‰. Most samples of epidote from veins have -31‰ ≤ δD ≤ -9‰, as for the epidote vein fragments in the epidote-quartz-prehnite breccias from Fault Bend locality, expect for the epidote-calcite vein from Quebrada Corta locality (-47‰) and one sample of vein fragment

from Fault Bend locality (-41‰). The final cement (hydrogen-bearing phases: epidote-prehnite-chlorite) sealing the epidote-quartz-prehnite breccias have δD between -44‰ and -31‰. Instead, the δD of bulk epidote-quartz-prehnite breccias are more scattered with values ranging between -57‰ and -34‰.

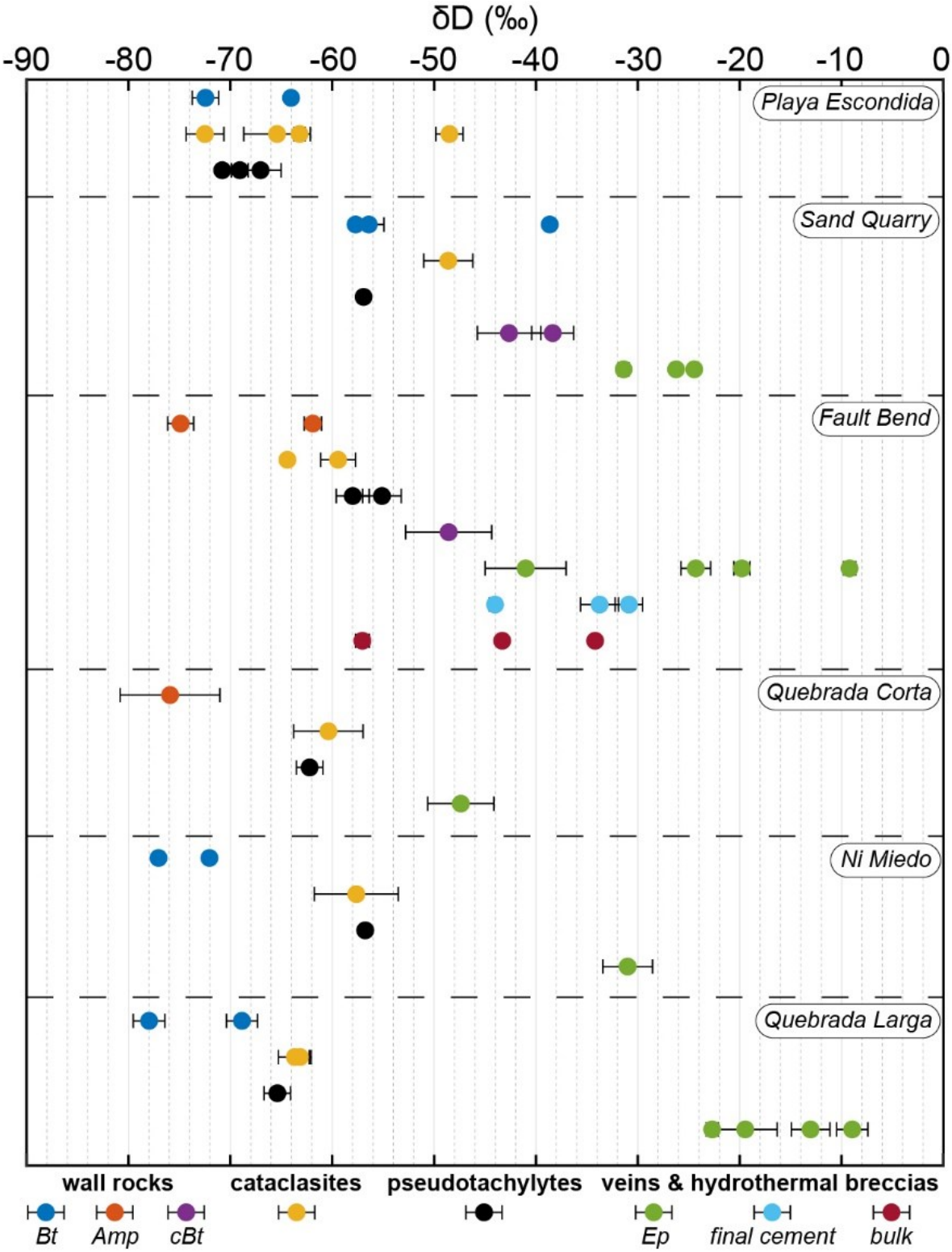

Fig. 3. Hydrogen isotope compositions (as δD‰) of the analyzed samples, grouped by rock type, from the six localities along the Bolfin Fault Zone as shown in Fig. 1b.

6. Discussion

Ancient seismic faulting along the BFZ, as documented by pseudotachylytes, occurred at 5-7 km depth and ≤ 300 °C (Gomila et al., 2021; Masoch et al., 2021). Pseudotachylytes are associated with chlorite-rich cataclasites (Fig. 2a). The hydrogen isotope compositions of bulk pseudotachylytes overlap with those one of the associated cataclasites (Fig. 3), except for the one from the Sand Quarry which however has a similar δD of magmatic biotite from the granodiorites (Fig. 3), which have typical values calc-alkaline series along convergent plate boundaries (Giggenbach, 1992). Our results indicate that the source of hydrous fluids dissolved in the frictional melt were the hydrogen-bearing minerals forming the pseudotachylyte-hosting cataclasites, consistently with that observed in pseudotachylyte-bearing faults from the Gole Larghe Fault Zone (Adamello batholith, Southern Alps; Mittempergher et al., 2014) and the Homestake Shear Zone (Sawatch Range, Colorado; Moecher and Sharp, 2004). However, some cataclasites have δD values slightly higher than the hydrous-bearing minerals from the undeformed and unaltered wall rocks (Fig. 3). The cataclasites show variations in mineral composition compared to undeformed and unaltered wall rocks: (i) breakdown of biotite to chlorite + opaques, amphibole to (Fe-)actinolite or chlorite + opaques, and plagioclase to albite + epidote, (ii) precipitation of K-feldspar, chlorite and epidote in the matrix (Masoch et al., 2021). The same break-down reactions are observed in the altered wall-rock units in the inner damage zone enveloping the cataclastic fault strands (Masoch et al., 2022). This indicates that fluids were circulating within the fault zone during faulting. However, the circulation of external hydrothermal fluids was relatively limited and seismic faulting associated with production of pseudotachylytes occurred in a rock-buffered environment (i.e., relatively high rock/fluid ratio) at seismogenic depths, characterized by limited, local fluid circulation (i.e., fluids with the same isotopic compositions of those of the magmatic wall rocks

The extensive epidote-rich fault-vein networks and the associated dilatant breccias postponed the cataclasite-pseudotachylyte association. These vein-fault networks are related to subsidiary faults in the BFZ damage zone and are more widespread within the fault system forming the duplex (Cembrano et al., 2005; Herrera et al., 2005; Masoch et al., 2022). The epidote-rich veins and breccias have also distinct isotope compositions compared to the undeformed and unaltered wall rocks and the pseudotachylyte-cataclasite association (Fig. 3). Epidote-rich veins have mostly δD ≥ -31‰, with rare and scattered lower values (Fig. 3). Although the epidote-quartz-prehnite breccias from Fault Bend locality show scattered δD compositions for the bulk samples, both the final epidote-prehnite-chlorite cement and the earlier epidote vein fragments have δD values higher than the bulk ones and similar to those of other epidote veins of our dataset. The epidote-rich veining and faulting occurred at ≤ 250 °C (Herrera et al., 2005; Masoch et al., 2022) and considering the coexistence of epidote and prehnite is possible to constrain the minimum precipitation

temperature as 200 °C (Spear, 1993). By using a epidote-water (Chacko et al., 1999) fractionation factor, a fluid in equilibrium with epidote veins and breccias at ~200 °C would have had δD values ranging between -23‰ and -1‰. These δD values indicate that possible sources for this waters (i) are different from the magmatic fluids, (ii) are not meteoric waters sensu-stricto, (iii) are surficial (i.e., near-sruface-derived) waters and (iv) might be marine or evaporated waters (e.g., Gat, 1996; Sheppard, 1986), indicating that the fault network was hydraulically connected with the Earth's surface.

Both structural observations (Masoch et al., 2022) and isotopic data (this work) indicate a clear change in the deformation (rock-buffered to fluid-buffered) environment controlling the spatial evolution of the fault network and associated seismicity (Fig. 4). In all studied localities, the rock-buffered pseudotachylyte-cataclasite fault rock assemblage is found in the core of the BFZ, and in minor faults departing from the main strands of the fault (Fig. 1; Masoch et al, 2022). The pseudotachylytes-bearing slip zones in the fault core cut and are cut by chlorite-epidote-quartz-calcite-rich veins (Gomila et al., 2021). We conclude that seismic faulting occurred in the presence of limited (i.e., the fluid to rock volume ratio was small) amount of fluids (Fig. 2a; Fig. 3) and that this fault rock assemblage and fault network was related to mainshock-aftershock sequences (Allen, 2005; Di Toro et al., 2005; Smith et al., 2013) (Fig. 4).

Instead, the fluid-buffered epidote-rich fault-vein networks present evidences of large fluid infiltration (i.e., the fluid to rock volume ratio was high) associated with ancient seismic faulting driven by fluctuations in pore fluid pressures which triggered distributed seismicity (interpreted as seismic swarms) (this thesis, Chapter 3; Masoch et al., 2022). The fluid driven ancient seismicity was located along up to few km long faults located at BFZ complexities (fault linkage and intersections, Fig. 1; Masoch et al., 2022) in a more mature hydraulic system, open to the infiltration of surficial fluids (Fig. 4). Percolation of these fluids was promoted by the local transtensional regime (i.e., relative low vertical and mean stresses) affecting the strike-slip duplex (Cembrano et al., 2005; Veloso et al., 2015). Multiple seismic events rupturing the BFZ main strands and minor faults in the duplex (as attested by pseudotachylytes) led to transient increase of fault permeability, controlling the fault-controlled pathways for the episodic migration of hydrostatic-pressured surficial fluids at depths. Post-to-inter-seismic compaction and sealing of damaged products leads to fluid reservoir pressurization. Estimates of time-integrated fluxes related to seismic ruptures are up to tens of km^3 on timescales of 10^4-10^5 years (Cox, 2005). As a result, the extensive hydrothermal fault-vein networks represent a fossil analogue of an upper-crustal hydrothermal system where ancient seismicity was controlled by surficial fluids rather than (possibly deep-derived) hydrothermal ones. The BFZ network records the transition from mainshock-aftershock to swarm-like seismicity driven by the fault architectural evolution and

the ingression of surficial fluid infiltration (Fig. 4). These results highlight the relevance of surficial fluids, rather than deep-derived ones, in controlling upper-crustal seismicity in hydrothermal settings.

7. Conclusions

We investigated the origin of fluids associated with the pseudotachylytes and epidote-rich hydrothermal veins and breccias from the Bolfin Fault Zone, an exhumed crustal seismogenic fault (Atacama Fault System, Northern Chile). The pseudotachylytes, found along the main strands of the BFZ and minor faults departing from the BFZ, were produced at 5-7 km depth and ≤ 300 °C in a rock-buffered system. The hydrous fluids dissolved in the frictional melts derived from the melting of the hydrogen-bearing minerals of the wall rocks, as previously documented by other works (Mittempergher et al., 2014; Moecher and Sharp, 2004), and of the epidote-chlorite-quartz-calcite-rich veins (Gomila et al., 2021). Instead, the later epidote-rich fault-vein networks, localized at linkages and intersections of the BFZ, occurred at 3-7 km depth and 200-250 °C. The associated upper-crustal distributed swarm-like seismicity was driven by the ingression of large volumes of surficial fluids, rather than deeper and minor in volume hydrothermal ones, within a more mature, interconnected (also to the Earth's surface) hydraulic system. The transition in type of seismicity, from mainshock-aftershock to swarm-like earthquake sequences, is related to both the structural evolution of the BFZ and the new source of fluids in a seismically-active hydrothermal setting.

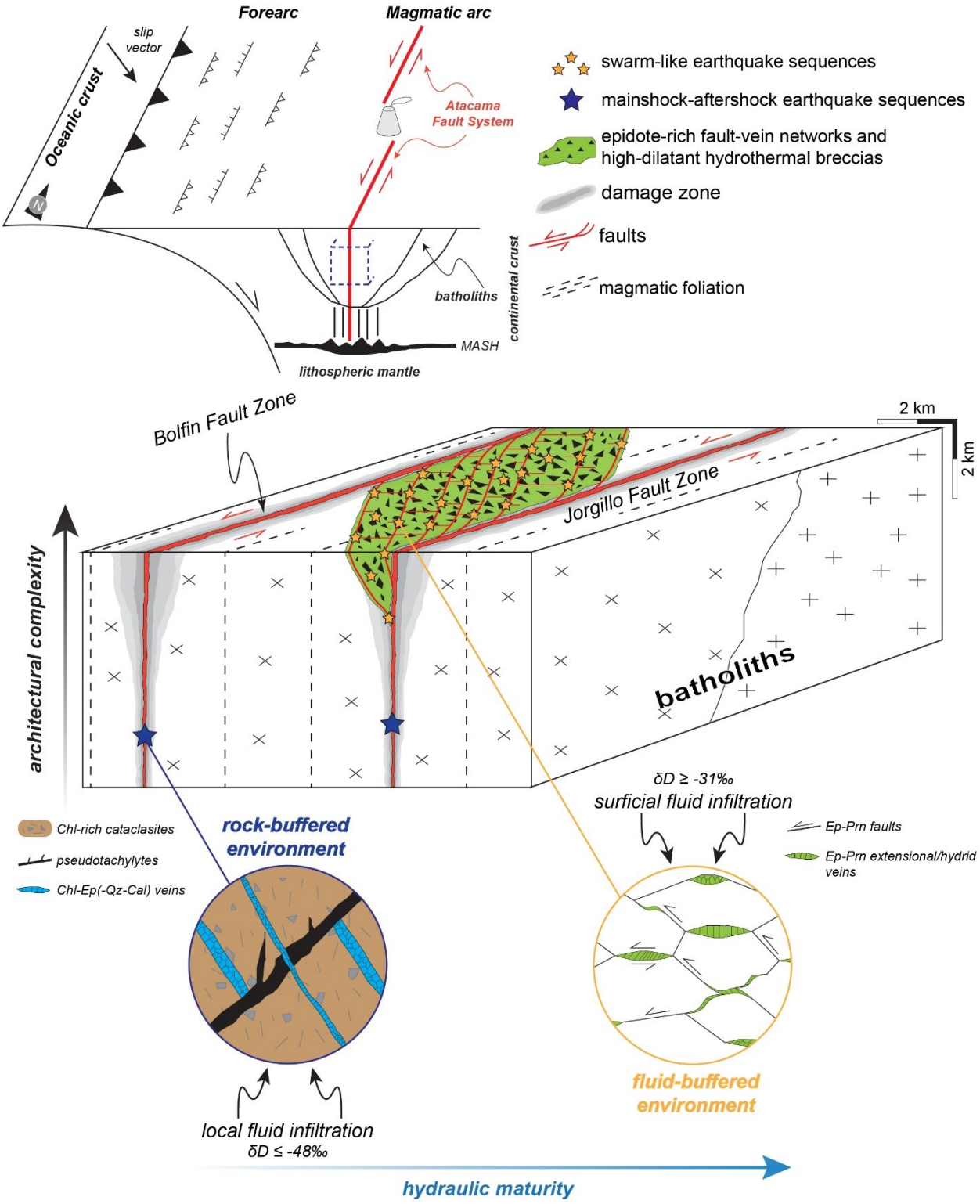

Fig. 4. Cartoon representing the geodynamic setting of the Atacama Fault System during the Early Cretaceous (upper diagram) and summarizing the architectural and environmental evolution (and associated fault zone rocks) of the Bolfin Fault Zone during its activity (lower diagram). The dashed purple box in the upper diagram indicates the crustal level represented in the lower diagram. The dark blue symbols represent features associated with mainshock-aftershock sequences; instead the orange symbols represent features associated with upper-crustal earthquake swarms. See text for details.

Conclusions and future developments

1. Summary of the thesis

In this thesis, I investigated some factors (i.e., fault architecture and evolution, fluid-rock interactions) which affect seismic and aseismic behavior of faults, with the aim of improving our knowledge regarding the spatio-temporal architectural evolution of crustal-scale seismogenic faults hosted in crystalline basement rocks. Specifically, my thesis aimed at (i) characterizing and quantifying the architecture of a crustal-scale seismogenic fault over segments of tens of kilometers (Chapter 2), and (ii) addressing its spatio-temporal evolution, which in turn may affect its architecture (at least during the first stages of fault formation) (Chapter 1). As major crustal faults are usually not well exposed at the Earth's surface, we selected the Bolfin Fault Zone (BFZ) of the Atacama Fault System, which is exceptionally well exposed in the Atacama Desert (Northern Chile). The BFZ was also chosen as case study because of widespread occurrence of pseudotachylytes, attesting the ancient fault seismicity. Further investigations of BFZ architecture motivated the process-oriented research presented in the second section of the thesis (Chapter 3 and 4), aimed at exploring the deformation and geochemical conditions affecting fluid-rock interactions during fault activity at seismogenic depths.

To address the aims of the thesis, I combined high-resolution geological surveys, analysis of satellite and drone images, and construction of digital outcrop models with detailed microstructural, mineralogical and geochemical investigations of wall and fault zone rocks. The main conclusions are summarized below:

1. The sinuous crustal-scale geometry of the BFZ resulted from the (i) exploitation of segments of precursory anisotropies (i.e., magmatic foliation of plutons and dyke swarms) optimally to favorably oriented with respect to the long-term regional stress field, during fault nucleation, and (ii) hard linkage of these anisotropy-pinned fault segments through splay faults during fault growth (Chapter 1). As a result, the spatial arrangement of magmatic-related precursory anisotropies (i.e., magmatic foliation of plutons and dyke swarms) plays a pivotal role in controlling the crustal-scale geometry of crustal-scale faults within a heterogeneous crystalline basement as they can be exploited as loci of fault nucleation and consequently affect fault segmentation.
2. The structural evolution of BFZ highlights a sharp transition from magmatic-related deformation structures and high-temperature, ductile shear zones (T >700 °C) to low-temperature, seismic faulting ($T \leq 300$ °C) (Chapter 1). Such a sharp transition might be explained

by either fast migration of the magmatic arc, rapid regional-scale exhumation and shallow depth emplacement of the plutons. This can have implications on the interplay between magmatism and faulting, and on the temporal window and environmental conditions of the onset of brittle faulting.

3. Seismic faulting attested by pseudotachylytes occurred at ≤ 300 °C and 5-7 km depth in a fluid-rich environment, as documented by extensive propylitic alteration and syn-kinematic epidote-chlorite(-quartz-calcite) veining (Gomila et al., 2021; Chapters 1 and 2). This funding published in Gomila et al. (2021), which I co-authored, documents that frictional melting can occur also in hydrothermal environment, contrary to what commonly thought (Sibson and Toy, 2006). Moreover, we recognized for the first time the occurrence of pseudotachylytes in the Atacama Fault System (and, to our knowledge, in South America).
4. The BFZ architecture consists of multiple fault core strands associated with pseudotachylytes, found also in subsidiary faults in the BFZ damage zone (Chapter 2). The later consists of variable altered and fractured rock volumes, including clusters of epidote-rich fault-vein networks and dilational breccias located at fault intersections and linkages, overprinting the pseudotachylyte-bearing fault networks (Chapter 2). By comparison with other exhumed seismogenic fault zones and active crustal faults zones, we argue that the BFZ represents an exhumed analogue of crustal seismogenic source, which produced both mainshock-aftershock type earthquake sequences (attested by the pseudotachylyte-bearing fault networks) and swarm-type earthquake sequences (attested by extensive hydrothermal fault-vein networks) (Chapters 2 and 3).
5. Selected samples of small-displacement (<1.5 m) epidote-rich sheared veins show microstructures in the veins and the associated wall rock attesting ancient seismic faulting. The microstructures possibly record the development of a seismically-active hydrothermal system, from propagation of small seismic ruptures in a rock-buffered system to cyclic veining and cataclasis in a fluid-buffered environment (Chapter 3).
6. Hydrogen isotope geochemistry (Chapter 4) indicates that pseudotachylytes formed in a rock-buffered environment, characterized by limited and local fluid circulation. Instead, the later fluid-driven seismicity attested by the hydrothermal fault-vein network was controlled by the ingression of surficial fluids in a more mature, hydraulically connected, upper-crustal hydrothermal system. In conclusion, the transition in seismic activity from mainshock-aftershock to swarm-like seismic sequences was controlled by the fault architecture evolution and the geochemical environment (Chapters 2 to 4).

2. Future developments

The Atacama Fault System has a complex, concave-shaped fault pattern. Although the BFZ represents only a small segment of the 1000-km-long Atacama Fault System, this thesis highlighted how the spatial arrangement of magmatic-related precursory anisotropies influence fault geometry and segmentation. It will be of interest to test whether the conceptual model of fault growth proposed in Chapter 1 could be extended to the entire or part of fault system or not. Observations from the main segments of the El Salado segment, located 150-200 km to the south of the BFZ, might suggest that magmatic structures had a key a role in forming the segmented pattern of the Atacama Fault System. This future work will also take into account the investigation of the temporal relation between the emplacement of plutons and dyke swarms and faulting activity, which might be affected by active magmatism within the arc, and the variability along strike. Besides the implication at regional scale and how fault structures evolve in space and time, this would help to determine the fault roughness at crustal scale. This study could contribute to better understanding of seismic hazard.

The studies presented in the thesis show that all the structural elements of the fault zones were affected by fluid-rock interaction in different geochemical environments and associated deformation conditions. Ad-hoc experiments and investigations might be performed to constrain the physico-chemical processes (e.g., pressurization, isotopic fraction) occurring during fluid-rock interactions in an hydrothermal system. Moreover, the evolution of the mechanical properties of many hydrothermal minerals at "true" hydrothermal conditions in presence of hot and pressurized fluids ($T > 200$ °C; pore fluid pressure > 30 MPa) are poorly known. Experimental work could be conducted to explore the mechanical response of these minerals at hydrothermal conditions. These studies could find application also to the safe exploitation of geothermal reservoirs and systems.

References

Abercrombie, R.E., Mori, J., 1994. Local observations of the onset of a large earthquake: 28 June 1992 Landers, California. Bull. Seismol. Soc. Am. 84, 725.

Acocella, V., Bellier, O., Sandri, L., Sébrier, M., Pramumijoyo, S., 2018. Weak Tectono-Magmatic Relationships along an Obliquely Convergent Plate Boundary: Sumatra, Indonesia. Front. Earth Sci. 6. https://doi.org/10.3389/feart.2018.00003

Allam, A.A., Ben-Zion, Y., 2012. Seismic velocity structures in the southern California plate-boundary environment from double-difference tomography. Geophys. J. Int. 190, 1181–1196. https://doi.org/10.1111/j.1365-246X.2012.05544.x

Allen, J.L., 2005. A multi-kilometer pseudotachylyte system as an exhumed record of earthquake rupture geometry at hypocentral depths (Colorado, USA). Tectonophysics 402, 37–54. https://doi.org/https://doi.org/10.1016/j.tecto.2004.10.017

Allmendinger, R.W., Cardozo, N., Fisher, D.M., 2011. Structural Geology Algorithms: Vectors & Tensors. Cambridge University Press, Cambridge, England.

Anderson, E.M., 1951. Dynamics of Faulting and Dyke Formations with Application to Britain, Oliver & Boy, Edinburgh.

Arabasz, W.J.J., 1971. Geological and geophysical studies of the Atacama fault zone in northern Chile. PhD thesis, California Institute of Technology, Pasadena.

Arancibia, G., Fujita, K., Hoshino, K., Mitchell, T.M., Cembrano, J., Gomila, R., Morata, D., Faulkner, D.R., Rempe, M., 2014. Hydrothermal alteration in an exhumed crustal fault zone: Testing geochemical mobility in the Caleta Coloso Fault, Atacama Fault System, Northern Chile. Tectonophysics 623, 147–168. https://doi.org/10.1016/j.tecto.2014.03.024

Atkinson, B.K., Meredith, P.G., 1987. The theory of subcritical crack growth with application to mineral and rocks, in: Fracture Mechanics of Rocks. Academic Press, pp. 111–166.

Aydin, A., 2000. Fractures, faults, and hydrocarbon entrapment, migration and flow. Mar. Pet. Geol. 17, 797–814. https://doi.org/10.1016/S0264-8172(00)00020-9

Bailey, G.N., Reynolds, S.C., King, G.C.P., 2011. Landscapes of human evolution: models and methods of tectonic geomorphology and the reconstruction of hominin landscapes. J. Hum. Evol. 60, 257–280. https://doi.org/10.1016/j.jhevol.2010.01.004

Balázs, A., Matenco, L., Vogt, K., Cloetingh, S., Gerya, T., 2018. Extensional Polarity Change in Continental Rifts: Inferences From 3-D Numerical Modeling and Observations. J. Geophys. Res. Solid Earth 123, 8073–8094. https://doi.org/10.1029/2018JB015643

Becker, T.W., Hashima, A., Freed, A.M., Sato, H., 2018. Stress change before and after the 2011 M9 Tohoku-oki earthquake. Earth Planet. Sci. Lett. 504, 174–184. https://doi.org/https://doi.org/10.1016/j.epsl.2018.09.035

Bedford, J.D., Faulkner, D.R., Lapusta, N., 2022. Fault rock heterogeneity can produce fault weakness and reduce fault stability. Nat. Commun. 13, 326. https://doi.org/10.1038/s41467-022-27998-2

Behr, W.M., Platt, J.P., 2014. Brittle faults are weak, yet the ductile middle crust is strong: Implications for lithospheric mechanics. Geophys. Res. Lett. 41, 8067–8075. https://doi.org/10.1002/2014GL061349

Bellahsen, N., Daniel, J.M., 2005. Fault reactivation control on normal fault growth: an experimental study. J. Struct. Geol. 27, 769–780. https://doi.org/10.1016/j.jsg.2004.12.003

Ben-Zion, Y., 1998. Properties of seismic fault zone waves and their utility for imaging low-velocity structures. J. Geophys. Res. Solid Earth 103, 12567–12585. https://doi.org/10.1029/98JB00768

Ben-Zion, Y., Sammis, C.G., 2003. Characterization of Fault Zones. Pure Appl. Geophys. 160, 677–715. https://doi.org/10.1007/PL00012554

Berger, A., Herwegh, M., 2019. Cockade structures as a paleo-earthquake proxy in upper crustal hydrothermal systems. Sci. Rep. 9, 1–9. https://doi.org/10.1038/s41598-019-45488-2

Berger, B.R., Henley, R.W., 2011. Magmatic-vapor expansion and the formation of high-sulfidation gold deposits: Structural controls on hydrothermal alteration and ore mineralization. Ore Geol. Rev. 39, 75–90. https://doi.org/10.1016/j.oregeorev.2010.11.004

Bestmann, M., Pennacchioni, G., Mostefaoui, S., Göken, M., de Wall, H., 2016. Instantaneous healing of micro-fractures during coseismic slip: Evidence from microstructure and Ti in quartz geochemistry within an exhumed pseudotachylyte-bearing fault in tonalite. Lithos 254–255, 84–93. https://doi.org/10.1016/j.lithos.2016.03.011

Bestmann, M., Pennacchioni, G., Nielsen, S., Göken, M., de Wall, H., 2012. Deformation and ultrafine dynamic recrystallization of quartz in pseudotachylyte-bearing brittle faults: A matter of a few seconds. J. Struct. Geol. 38, 21–38. https://doi.org/10.1016/j.jsg.2011.10.001

Billi, A., Salvini, F., Storti, F., 2003. The damage zone-fault core transition in carbonate rocks: implications for fault growth, structure and permeability. J. Struct. Geol. 25, 1779–1794. https://doi.org/10.1016/S0191-8141(03)00037-3

Bistacchi, A., Massironi, M., Menegon, L., 2010. Three-dimensional characterization of a crustal-scale fault zone: The Pusteria and Sprechenstein fault system (Eastern Alps). J. Struct. Geol. 32, 2022–2041. https://doi.org/10.1016/j.jsg.2010.06.003

Bistacchi, A., Massironi, M., Menegon, L., Bolognesi, F., Donghi, V., 2012. On the nucleation of non-Andersonian faults along phyllosilicate-rich mylonite belts. Geol. Soc. London, Spec. Publ. 367, 185–199. https://doi.org/10.1144/SP367.13

Blenkinsop, T.., Drury, M.., 1988. Stress estimates and fault history from quartz microstructures. J. Struct. Geol. 10, 673–684. https://doi.org/10.1016/0191-8141(88)90075-2

Boatwright, J., Cocco, M., 1996. Frictional constraints on crustal faulting. J. Geophys. Res. Solid Earth 101, 13895–13909. https://doi.org/10.1029/96JB00405

Boullier, A.-M., Yeh, E.-C., Boutareaud, S., Song, S.-R., Tsai, C.-H., 2009. Microscale anatomy of the 1999 Chi-Chi earthquake fault zone. Geochemistry, Geophys. Geosystems 10, n/a-n/a. https://doi.org/10.1029/2008GC002252

Bradbury, K.K., Davis, C.R., Shervais, J.W., Janecke, S.U., Evans, J.P., 2015. Composition, Alteration, and Texture of Fault-Related Rocks from Safod Core and Surface Outcrop Analogs: Evidence for Deformation Processes and Fluid-Rock Interactions. Pure Appl. Geophys. 172, 1053–1078. https://doi.org/10.1007/s00024-014-0896-6

Brown, M., Diàz, F., Grocott, J., 1993. Displacement history of the Atacama fault system 25°00'S-27°00'S, northern Chile. Geol. Soc. Am. Bull. 102, 1165–1174.

Butler, R.W.H., Bond, C.E., Shipton, Z.K., Jones, R.R., Casey, M., 2008. Fabric anisotropy controls faulting in the continental crust. J. Geol. Soc. London. 165, 449–452. https://doi.org/10.1144/0016-76492007-129

Caine, J.S., Evans, J.P., Forster, C.B., 1996. Fault zone architecture and permeability structure. Geology 24, 1025–1028. https://doi.org/10.1130/0091-7613(1996)024<1025:FZAAPS>2.3.CO;2

Cao, W., Kaus, B.J.P., Paterson, S., 2016. Intrusion of granitic magma into the continental crust facilitated by magma pulsing and dike-diapir interactions: Numerical simulations. Tectonics 35, 1575–1594. https://doi.org/10.1002/2015TC004076

Cappa, F., Rutqvist, J., Yamamoto, K., 2009. Modeling crustal deformation and rupture processes related to upwelling of deep CO 2 -rich fluids during the 1965–1967 Matsushiro earthquake swarm in Japan. J. Geophys. Res. 114, B10304. https://doi.org/10.1029/2009JB006398

Cardozo, N., Allmendinger, R.W., 2013. Spherical Projections with OSXStereonet. Comput. Geosci. 51, 193–205. https://doi.org/10.1016/j.cageo.2012.07.021

Carter, N., 1965. Basal quartz deformation lamellae - A criterion for recognition of impactites. Am. J. Sci. 263.

Cembrano, J., González, G., Arancibia, G., Ahumada, I., Olivares, V., Herrera, V., 2005. Fault zone development and strain partitioning in an extensional strike-slip duplex: A case study from the Mesozoic Atacama fault system, Northern Chile. Tectonophysics 400, 105–125. https://doi.org/10.1016/j.tecto.2005.02.012

Cembrano, J., Hervé, F., Lavenu, A., 1996. The Liquiñe Ofqui fault zone: a long-lived intra-arc fault system in southern Chile. Tectonophysics 259, 55–66. https://doi.org/10.1016/0040-1951(95)00066-6

Cembrano, J., Lara, L., 2009. The link between volcanism and tectonics in the southern volcanic zone of the Chilean Andes: A review. Tectonophysics 471, 96–113. https://doi.org/10.1016/j.tecto.2009.02.038

Cembrano, J., Lavenu, A., Reynolds, P., Arancibia, G., López, G., Sanhueza, A., 2002. Late Cenozoic transpressional ductile deformation north of the Nazca-South America-Antarctica triple junction. Tectonophysics 354, 289–314. https://doi.org/10.1016/S0040-1951(02)00388-8

Chacko, T., Riciputi, R., Cole, R., Horita, J., 1999. A new technique for determining equilibrium hydrogen isotope fractionation factors using the ion microprobe: application to the epidote-water system.

Geochim. Cosmochim. Acta 63, 1–10. https://doi.org/https://doi.org/10.1016/S0016-7037(99)00007-1

Chemenda, A.I., Cavalié, O., Vergnolle, M., Bouissou, S., Delouis, B., 2016. Numerical model of formation of a 3-D strike-slip fault system. Comptes Rendus Geosci. 348, 61–69. https://doi.org/10.1016/j.crte.2015.09.008

Cheng, Y., Wang, X., Zhan, Z., Ben-Zion, Y., 2021. Isotropic Source Components of Events in the 2019 Ridgecrest, California, Earthquake Sequence. Geophys. Res. Lett. 48. https://doi.org/10.1029/2021GL094515

Chester, F.M., Evans, J.P., Biegel, R.L., 1993. Internal structure and weakening mechanisms of the San Andreas Fault. J. Geophys. Res. Solid Earth 98, 771–786. https://doi.org/10.1029/92JB01866

Chester, F.M., Logan, J.M., 1986. Implications for mechanical properties of brittle faults from observations of the Punchbowl fault zone, California. Pure Appl. Geophys. PAGEOPH 124, 79–106. https://doi.org/10.1007/BF00875720

Chester, F.M., Rowe, C., Ujiie, K., Kirkpatrick, J., Regalla, C., Remitti, F., Moore, J.C., Toy, V., Wolfson-Schwehr, M., Bose, S., Kameda, J., Mori, J.J., Brodsky, E.E., Eguchi, N., Toczko, S., 2013. Structure and Composition of the Plate-Boundary Slip Zone for the 2011 Tohoku-Oki Earthquake. Science (80-.). 342, 1208–1211. https://doi.org/10.1126/science.1243719

Chiaraluce, L., Valoroso, L., Piccinini, D., Di Stefano, R., De Gori, P., 2011. The anatomy of the 2009 L'Aquila normal fault system (central Italy) imaged by high resolution foreshock and aftershock locations. J. Geophys. Res. Solid Earth 116, 1–25. https://doi.org/10.1029/2011JB008352

Choi, J.-H., Edwards, P., Ko, K., Kim, Y.-S., 2016. Definition and classification of fault damage zones: A review and a new methodological approach. Earth-Science Rev. 152, 70–87. https://doi.org/https://doi.org/10.1016/j.earscirev.2015.11.006

Christiansen, P.P., Pollard, D.D., 1997. Nucleation, growth and structural development of mylonitic shear zones in granitic rock. J. Struct. Geol. 19, 1159–1172. https://doi.org/10.1016/S0191-8141(97)00025-4

Chu, S.X., Tsai, V.C., Trugman, D.T., Hirth, G., 2021. Fault Interactions Enhance High-Frequency Earthquake Radiation. Geophys. Res. Lett. 48. https://doi.org/10.1029/2021GL095271

Cirella, A., Piatanesi, A., Tinti, E., Chini, M., Cocco, M., 2012. Complexity of the rupture process during the 2009 L'Aquila, Italy, earthquake. Geophys. J. Int. 190, 607–621. https://doi.org/10.1111/j.1365-246X.2012.05505.x

Clemens, J.D., 1998. Observations on the origins and ascent mechanisms of granitic magmas. J. Geol. Soc. 155, 843–851.

Cocco, M., Aretusini, S., Cornelio, C., Nielsen, S.B., Spagnuolo, E., Tinti, E., Di Toro, G., 2023. Fracture Energy and Breakdown Work During Earthquakes. Annu. Rev. Earth Planet. Sci. https://doi.org/10.1146/annurev-earth-071822-100304

Cocco, M., Rice, J.R., 2002. Pore pressure and poroelasticity effects in Coulomb stress analysis of earthquake interactions. J. Geophys. Res. 107, 2030. https://doi.org/10.1029/2000JB000138

Collanega, L., Siuda, K., A.-L. Jackson, C., Bell, R.E., Coleman, A.J., Lenhart, A., Magee, C., Breda, A., 2019. Normal fault growth influenced by basement fabrics: The importance of preferential nucleation from pre-existing structures. Basin Res. 31, 659–687. https://doi.org/10.1111/bre.12327

Collettini, C., Barchi, M.R., De Paola, N., Trippetta, F., Tinti, E., 2022. Rock and fault rheology explain differences between on fault and distributed seismicity. Nat. Commun. 13, 5627. https://doi.org/10.1038/s41467-022-33373-y

Coppola, M., Correale, A., Barberio, M.D., Billi, A., Cavallo, A., Fondriest, M., Nazzari, M., Paonita, A., Romano, C., Stagno, V., Viti, C., Vona, A., 2021. Meso- to nano-scale evidence of fluid-assisted co-seismic slip along the normal Mt. Morrone Fault, Italy: Implications for earthquake hydrogeochemical precursors. Earth Planet. Sci. Lett. 568, 117010. https://doi.org/10.1016/j.epsl.2021.117010

Cowan, D.S., 1999. Do faults preserve a record of seismic slip? A field geologist's opinion. J. Struct. Geol. 21, 995–1001. https://doi.org/10.1016/S0191-8141(99)00046-2

Cox, S.F., 2010. The application of failure mode diagrams for exploring the roles of fluid pressure and stress states in controlling styles of fracture-controlled permeability enhancement in faults and shear zones. Geofluids. https://doi.org/10.1111/j.1468-8123.2010.00281.x

Cox, S.F., 2016. Injection-Driven Swarm Seismicity and Permeability Enhancement: Implications for the Dynamics of Hydrothermal Ore Systems in High Fluid-Flux, Overpressured Faulting Regimes—An Invited Paper. Econ. Geol. 111, 559–587. https://doi.org/10.2113/econgeo.111.3.559

Cox, S.F., 2020. Chapter 2: The Dynamics of Permeability Enhancement and Fluid Flow in Overpressured, Fracture-Controlled Hydrothermal Systems, in: Applied Structural Geology of Ore-Forming Hydrothermal Systems. Society of Economic Geologists, pp. 25–82. https://doi.org/10.5382/rev.21.02

Cox, S.F., 2005. Coupling between Deformation, Fluid Pressures, and Fluid Flow in Ore-Producing Hydrothermal Systems at Depth in the Crust, in: One Hundredth Anniversary Volume. Society of Economic Geologists. https://doi.org/10.5382/AV100.04

Cox, S.F., Munroe, S.M., 2016. Breccia formation by particle fluidization in fault zones: Implications for transitory, rupture-controlled fluid flow regimes in hydrothermal systems. Am. J. Sci. 316, 241–278. https://doi.org/10.2475/03.2016.02

Crider, J.G., 2015. The initiation of brittle faults in crystalline rock. J. Struct. Geol. 77, 159–174. https://doi.org/10.1016/j.jsg.2015.05.001

Crider, J.G., Peacock, D.C.P., 2004. Initiation of brittle faults in the upper crust: a review of field observations. J. Struct. Geol. 26, 691–707. https://doi.org/10.1016/j.jsg.2003.07.007

d'Alessio, M., Martel, S.J., 2005. Development of strike-slip faults from dikes, Sequoia National Park, California. J. Struct. Geol. 27, 35–49. https://doi.org/10.1016/j.jsg.2004.06.013

d'Alessio, M.A., Martel, S.J., 2004. Fault terminations and barriers to fault growth. J. Struct. Geol. 26, 1885–1896. https://doi.org/10.1016/j.jsg.2004.01.010

Dal Zilio, L., Jolivet, R., van Dinther, Y., 2020. Segmentation of the Main Himalayan Thrust Illuminated by Bayesian Inference of Interseismic Coupling. Geophys. Res. Lett. 47. https://doi.org/10.1029/2019GL086424

Dal Zilio, L., van Dinther, Y., Gerya, T., Avouac, J.-P., 2019. Bimodal seismicity in the Himalaya controlled by fault friction and geometry. Nat. Commun. 10, 48. https://doi.org/10.1038/s41467-018-07874-8

Davatzes, N.C., Aydin, A., 2003. The formation of conjugate normal fault systems in folded sandstone by sequential jointing and shearing, Waterpocket monocline, Utah. J. Geophys. Res. Solid Earth 108. https://doi.org/10.1029/2002JB002289

Deichmann, N., Kraft, T., Evans, K.F., 2014. Identification of faults activated during the stimulation of the Basel geothermal project from cluster analysis and focal mechanisms of the larger magnitude events. Geothermics 52, 84–97. https://doi.org/10.1016/j.geothermics.2014.04.001

Delogkos, E., Manzocchi, T., Childs, C., Camanni, G., Roche, V., 2020. The 3D structure of a normal fault from multiple outcrop observations. J. Struct. Geol. 136, 104009. https://doi.org/10.1016/j.jsg.2020.104009

Dempsey, E.D., Holdsworth, R.E., Imber, J., Bistacchi, A., Di Toro, G., 2014. A geological explanation for intraplate earthquake clustering complexity: The zeolite-bearing fault/fracture networks in the Adamello Massif (Southern Italian Alps). J. Struct. Geol. 66, 58–74. https://doi.org/10.1016/j.jsg.2014.04.009

Demurtas, M., Fondriest, M., Balsamo, F., Clemenzi, L., Storti, F., Bistacchi, A., Di Toro, G., 2016. Structure of a normal seismogenic fault zone in carbonates: The Vado di Corno Fault, Campo Imperatore, Central Apennines (Italy). J. Struct. Geol. 90, 185–206. https://doi.org/10.1016/j.jsg.2016.08.004

Derez, T., Pennock, G., Drury, M., Sintubin, M., 2015. Low-temperature intracrystalline deformation microstructures in quartz. J. Struct. Geol. 71, 3–23. https://doi.org/10.1016/j.jsg.2014.07.015

Di Stefano, R., Chiarabba, C., Chiaraluce, L., Cocco, M., De Gori, P., Piccinini, D., Valoroso, L., 2011. Fault zone properties affecting the rupture evolution of the 2009 (M w 6.1) L'Aquila earthquake (central Italy): Insights from seismic tomography. Geophys. Res. Lett. 38, n/a-n/a. https://doi.org/10.1029/2011GL047365

Di Toro, G., Nielsen, S., Pennacchioni, G., 2005. Earthquake rupture dynamics frozen in exhumed ancient faults. Nature 436, 1009–1012. https://doi.org/10.1038/nature03910

Di Toro, G., Pennacchioni, G., 2004. Superheated friction-induced melts in zoned pseudotachylytes within the Adamello tonalites (Italian Southern Alps). J. Struct. Geol. 26, 1783–1801. https://doi.org/10.1016/j.jsg.2004.03.001

Di Toro, G., Pennacchioni, G., 2005. Fault plane processes and mesoscopic structure of a strong-type seismogenic fault in tonalites (Adamello batholith, Southern Alps). Tectonophysics 402, 55–80. https://doi.org/10.1016/j.tecto.2004.12.036

Di Toro, G., Pennacchioni, G., Nielsen, S., 2009. Pseudotachylytes and Earthquake Source Mechanics, in: Fault-Zone Properties and Earthquake Rupture Dynamics. pp. 87–133. https://doi.org/10.1016/S0074-6142(08)00005-3

Doan, M.-L., Gary, G., 2009. Rock pulverization at high strain rate near the San Andreas fault. Nat. Geosci. 2, 709–712. https://doi.org/10.1038/ngeo640

Domagala, J.P., Escribano, J., De La Cruz, R., Saldias, J., Joquera, R., 2016. Cartas Blanco Encalada y Pampa Remiendos, Region de Antofagasta. Servicio Nacional de Geología y Minería, Carta Geológica de Chile, Serie Geología Básica 187-188 mapa escala 1:100.000. Santiago.

Dorbath, L., Cuenot, N., Genter, A., Frogneux, M., 2009. Seismic response of the fractured and faulted granite of Soultz-sous-Forêts (France) to 5 km deep massive water injections. Geophys. J. Int. 177, 653–675. https://doi.org/10.1111/j.1365-246X.2009.04030.x

Drury, M.R., 1993. Deformation lamellae in metals and minerals, in: Boland, J.N., Fitzgerald, J.D. (Eds.), Defects and Processes in the Solid State: Geoscience Applications. The McLaren Volume, pp. 195–212.

Dunai, T.J., González López, G.A., Juez-Larré, J., 2005. Oligocene–Miocene age of aridity in the Atacama Desert revealed by exposure dating of erosion-sensitive landforms. Geology 33, 321. https://doi.org/10.1130/G21184.1

Duncan, R.J., Hitzman, M.W., Nelson, E.P., Togtokhbayar, O., 2014. Structural and Lithological Controls on Iron Oxide Copper-Gold Deposits of the Southern Selwyn-Mount Dore Corridor, Eastern Fold Belt, Queensland, Australia. Econ. Geol. 109, 419–456. https://doi.org/10.2113/econgeo.109.2.419

Ellsworth, W.L., 2013. Injection-Induced Earthquakes. Science (80-.). 341. https://doi.org/10.1126/science.1225942

Espinoza, M., Contreras, J.P., Jorquera, R., De La Cruz, R., Kraus, S., Ramirez, C., Naranjo, J., 2014. Carta Cerro del Pingo, Regiones de Antofagasta y Atacama. Servicio Nacional de Geología y Minería, Carta Geológica de Chile, Serie Geología Básica 169, 1 mapa escala 1:100.000. Santiago.

Fairbairn, H., 1941. Deformation lamellae in quartz from the Ajibik Formation, Michigan. Geol. Soc. Am. Bull. 52, 1265–1278.

Faulkner, D.R., Jackson, C.A.L., Lunn, R.J., Schlische, R.W., Shipton, Z.K., Wibberley, C.A.J., Withjack, M.O., 2010. A review of recent developments concerning the structure, mechanics and fluid flow properties of fault zones. J. Struct. Geol. 32, 1557–1575. https://doi.org/10.1016/j.jsg.2010.06.009

Faulkner, D.R., Lewis, A.C., Rutter, E.H., 2003. On the internal structure and mechanics of large strike-slip fault zones: Field observations of the Carboneras fault in southeastern Spain. Tectonophysics 367, 235–251. https://doi.org/10.1016/S0040-1951(03)00134-3

Faulkner, D.R., Mitchell, T.M., Healy, D., Heap, M.J., 2006. Slip on "weak" faults by the rotation of regional stress in the fracture damage zone. Nature 444, 922–925. https://doi.org/10.1038/nature05353

Faulkner, D.R., Mitchell, T.M., Jensen, E., Cembrano, J., 2011. Scaling of fault damage zones with displacement and the implications for fault growth processes. J. Geophys. Res. Solid Earth 116, 1–11. https://doi.org/10.1029/2010JB007788

Faulkner, D.R., Mitchell, T.M., Rutter, E.H., Cembrano, J., 2008. On the structure and mechanical properties of large strike-slip faults. Geol. Soc. Spec. Publ. 299, 139–150. https://doi.org/10.1144/SP299.9

Ferrill, D.A., Morris, A.P., Evans, M.A., Burkhard, M., Groshong, R.H., Onasch, C.M., 2004. Calcite twin morphology: A low-temperature deformation geothermometer. J. Struct. Geol. 26, 1521–1529. https://doi.org/10.1016/j.jsg.2003.11.028

Fischer, T., Horálek, J., Hrubcová, P., Vavryčuk, V., Bräuer, K., Kämpf, H., 2014. Intra-continental earthquake swarms in West-Bohemia and Vogtland: A review. Tectonophysics 611, 1–27. https://doi.org/10.1016/j.tecto.2013.11.001

Fondriest, M., Aretusini, S., Di Toro, G., Smith, S.A.F., 2015. Fracturing and rock pulverization along an exhumed seismogenic fault zone in dolostones: The Foiana Fault Zone (Southern Alps, Italy). Tectonophysics 654, 56–74. https://doi.org/10.1016/j.tecto.2015.04.015

Fondriest, M., Balsamo, F., Bistacchi, A., Clemenzi, L., Demurtas, M., Storti, F., Di Toro, G., 2020a. Structural Complexity and Mechanics of a Shallow Crustal Seismogenic Source (Vado di Corno Fault Zone, Italy). J. Geophys. Res. Solid Earth 125. https://doi.org/10.1029/2019JB018926

Fondriest, M., Doan, M.-L., Aben, F., Fusseis, F., Mitchell, T.M., Voorn, M., Secco, M., Di Toro, G., 2017. Static versus dynamic fracturing in shallow carbonate fault zones. Earth Planet. Sci. Lett. 461, 8–19. https://doi.org/10.1016/j.epsl.2016.12.024

Fondriest, M., Mecklenburgh, J., Passelegue, F.X., Artioli, G., Nestola, F., Spagnuolo, E., Rempe, M., Di Toro, G., 2020b. Pseudotachylyte Alteration and the Rapid Fade of Earthquake Scars From the Geological Record. Geophys. Res. Lett. 47. https://doi.org/10.1029/2020GL090020

Fondriest, M., Smith, S.A.F., Di Toro, G., Zampieri, D., Mittempergher, S., 2012. Fault zone structure and seismic slip localization in dolostones, an example from the Southern Alps, Italy. J. Struct. Geol. 45, 52–67. https://doi.org/10.1016/j.jsg.2012.06.014

Frenzel, M., Woodcock, N.H., 2014. Cockade breccia: Product of mineralisation along dilational faults. J. Struct. Geol. 68, 194–206. https://doi.org/10.1016/j.jsg.2014.09.001

Freund, L.B., 1990. Dynamic Fracture Mechanics. Cambridge University Press.

Gat, J.R., 1996. Oxygen and hydrogen isotopes in the hydrologic cycle. Annu. Rev. Earth Planet. Sci. 24, 225–262. https://doi.org/10.1146/annurev.earth.24.1.225

Giggenbach, W.F., 1992. Isotopic shifts in waters from geothermal and volcanic systems along convergent plate boundaries and their origin. Earth Planet. Sci. Lett. 113, 495–510. https://doi.org/10.1016/0012-821X(92)90127-H

Goldfarb, R.J., Baker, T., Dubé, B., Groves, D.I., Hart, C.J.R., Gosselin, P., 2005. Distribution, Character, and Genesis of Gold Deposits in Metamorphic Terran, in: One Hundredth Anniversary Volume. Society of Economic Geologists. https://doi.org/10.5382/AV100.14

Gomila, R., Arancibia, G., Mitchell, T.M., Cembrano, J.M., Faulkner, D.R., 2016. Palaeopermeability structure within fault-damage zones: A snap-shot from microfracture analyses in a strike-slip system. J. Struct. Geol. 83, 103–120. https://doi.org/10.1016/j.jsg.2015.12.002

Gomila, R., Fondriest, M., Jensen, E., Spagnuolo, E., Masoch, S., Mitchell, T.M., Magnarini, G., Bistacchi, A., Mittempergher, S., Faulkner, D., Cembrano, J., Di Toro, G., 2021. Frictional Melting in Hydrothermal Fluid-Rich Faults: Field and Experimental Evidence From the Bolfín Fault Zone (Chile). Geochemistry, Geophys. Geosystems 22. https://doi.org/10.1029/2021GC009743

González, G., 1999. Mecanismo y profundidad de emplazamiento del Pluton de Cerro Cristales, Cordillera de la Costa, Antofagasta, Chile. Rev. Geol. Chile 26, 43–66.

González, G., Cembrano, J., Carrizo, D., Macci, A., Schneider, H., 2003. The link between forearc tectonics and Pliocene-Quaternary deformation of the Coastal Cordillera, northern Chile. J. South Am. Earth Sci. 16, 321–342. https://doi.org/10.1016/S0895-9811(03)00100-7

González, G., Dunai, T., Carrizo, D., Allmendinger, R., 2006. Young displacements on the Atacama Fault System, northern Chile from field observations and cosmogenic 21Ne concentrations. Tectonics 25, 1–15. https://doi.org/10.1029/2005TC001846

González, G., Niemeyer, H., 2005. Cartas Antofagasta y Punta Tetas, Region de Antofagasta. Servicio Nacional de Geología y Minería, Carta Geológica de Chile, Serie Geología Básica 89 mapa escala 1:100.000. Santiago.

Grauls, D., Pascaud, F., Rives, T., 2002. Quantitative fault seal assessment in hydrocarbon-compartmentalised structures using fluid pressure data, in: Koestler, A.G., Hunsdale, R. (Eds.), Hydrocarbon Seal Quantification. pp. 141–156. https://doi.org/10.1016/S0928-8937(02)80012-1

Griffith, W.A., Di Toro, G., Pennacchioni, G., Pollard, D.D., 2008. Thin pseudotachylytes in faults of the Mt. Abbot quadrangle, Sierra Nevada: Physical constraints for small seismic slip events. J. Struct. Geol. 30, 1086–1094. https://doi.org/10.1016/j.jsg.2008.05.003

Grocott, J., 1981. Fracture geometry of pseudotachylyte generation zones: a study of shear fractures formed during seismic events. J. Struct. Geol. 3, 169–178. https://doi.org/10.1016/0191-8141(81)90012-2

Grocott, J., Brown, M., Dallmeyer, R.D., Taylor, G.K., Treloar, P.J., 1994. Mechanisms of continental growth in extensional arcs: An example from the Andean plate-boundary zone. Geology 22, 391–394.

Grocott, J., Taylor, G.K., 2002. Magmatic arc fault systems, deformation partitioning and emplacement of granitic complexes in the Coastal Cordillera, north Chilean Andes (25°30'S to 27°00'S). J. Geol. Soc. London. 159, 425–442. https://doi.org/10.1144/0016-764901-124

Guglielmi, Y., Cappa, F., Avouac, J.-P., Henry, P., Elsworth, D., 2015. Seismicity triggered by fluid injection–induced aseismic slip. Science (80-.). 348, 1224–1226. https://doi.org/10.1126/science.aab0476

Gutenberg, B., Richter, C.F., 1944. Frequency of Earthquakes in California. Bull. Seismol. Soc. Am. 34, 185–188.

Hale, D., 2013. Methods to compute fault images, extract fault surfaces, and estimate fault throws from 3D seismic images. Geophysics 78, O33–O43. https://doi.org/10.1190/geo2012-0331.1

Handy, M.R., Hirt, G., Hovius, N., 2007. Tectonic Faults. Agents of Change on a Dynamic Earth. The MIT Press, Cambdrige, Massachusetts. London, Uk.

Hardebeck, J.L., Okada, T., 2018. Temporal Stress Changes Caused by Earthquakes: A Review. J. Geophys. Res. Solid Earth 123, 1350–1365. https://doi.org/10.1002/2017JB014617

Hartman, S.M., Paterson, S.R., Holk, G.J., Kirkpatrick, J.D., 2018. Structural and hydrothermal evolution of a strike-slip shear zone during a ductile-brittle transition, Sierra Nevada, CA. J. Struct. Geol. 113, 134–154. https://doi.org/10.1016/j.jsg.2018.05.010

Hauksson, E., 2010. Spatial Separation of Large Earthquakes, Aftershocks, and Background Seismicity: Analysis of Interseismic and Coseismic Seismicity Patterns in Southern California. Pure Appl. Geophys. 167, 979–997. https://doi.org/10.1007/s00024-010-0083-3

Healy, J.H., Rubey, W.W., Griggs, D.T., Raleigh, C.B., 1968. The Denver Earthquakes. Science (80-.). 161, 1301–1310. https://doi.org/10.1126/science.161.3848.1301

Herrera, V., Cembrano, J., Olivares, V., Kojima, S., Arancibia, G., 2005. Precipitación por despresurización y ebullición en vetas hospedadas en un dúplex de rumbo extensional: Evidencias microestructurales y microtermométricas. Rev. Geol. Chile 32, 207–227.

Hervé, F., 1987. Movimiento normal de la falla Paposo, zona de Falla Atacama, en el Mioceno, Chile. Rev. Geol. Chile 31–36.

Hervé, F., Faundez, V., Calderón, M., Massonne, H.-J., Willner, A.P., 2007. Metamorphic and plutonic basement complexes, in: Moreno, T., Gibbons, W. (Eds.), The Geology of Chile. The Geological Society of London, pp. 5–19. https://doi.org/10.1144/GOCH.2

Hill, D.P., 1977. A model for earthquake swarms. J. Geophys. Res. 82, 1347–1352. https://doi.org/10.1029/JB082i008p01347

Hodge, M., Fagereng, Å., Biggs, J., Mdala, H., 2018. Controls on Early-Rift Geometry: New Perspectives From the Bilila-Mtakataka Fault, Malawi. Geophys. Res. Lett. 45, 3896–3905. https://doi.org/10.1029/2018GL077343

Holdsworth, R.E., van Diggelen, E.W.E., Spiers, C.J., de Bresser, J.H.P., Walker, R.J., Bowen, L., 2011. Fault rocks from the SAFOD core samples: Implications for weakening at shallow depths along the San Andreas Fault, California. J. Struct. Geol. 33, 132–144. https://doi.org/https://doi.org/10.1016/j.jsg.2010.11.010

Holland, T., Blundy, J., 1994. Non-ideal interactions in calcic amphiboles and their bearing on amphibole-plagioclase thermometry. Contrib. to Mineral. Petrol. 116, 433–447. https://doi.org/10.1007/BF00310910

Howarth, J.D., Barth, N.C., Fitzsimons, S.J., Richards-Dinger, K., Clark, K.J., Biasi, G.P., Cochran, U.A., Langridge, R.M., Berryman, K.R., Sutherland, R., 2021. Spatiotemporal clustering of great earthquakes on a transform fault controlled by geometry. Nat. Geosci. https://doi.org/10.1038/s41561-021-00721-4

Jaeger, J.C., Cook, N.G.W., Zimmerman, R., 2009. Fundamentals of Rock Mechanics, 4th ed. Wiley-Blackwell.

Jaillard, E., Soler, P., Carlier, G., Mourier, T., 1990. Geodynamic evolution of the northern and central Andes during early to middle Mesozoic times: a Tethyan model. J. Geol. Soc. London. 147, 1009–1022. https://doi.org/10.1144/gsjgs.147.6.1009

Jensen, E., Cembrano, J., Faulkner, D., Veloso, E., Arancibia, G., 2011. Development of a self-similar strike-slip duplex system in the Atacama Fault system, Chile. J. Struct. Geol. 33, 1611–1626. https://doi.org/10.1016/j.jsg.2011.09.002

Jensen, E., González, G., Faulkner, D.R., Cembrano, J., Mitchell, T.M., 2019. Fault-fluid interaction in porphyry copper hydrothermal systems: Faulted veins in radomiro Tomic, northern Chile. J. Struct. Geol. 126, 301–317. https://doi.org/10.1016/j.jsg.2019.06.013

Johnson, S.E., Song, W.J., Vel, S.S., Song, B.R., Gerbi, C.C., 2021. Energy Partitioning, Dynamic Fragmentation, and Off-Fault Damage in the Earthquake Source Volume. J. Geophys. Res. Solid Earth 126. https://doi.org/10.1029/2021JB022616

Kaven, J.O., Pollard, D.D., 2013. Geometry of crustal faults: Identification from seismicity and implications for slip and stress transfer models. J. Geophys. Res. Solid Earth 118. https://doi.org/https://doi.org/10.1002/jgrb.50356

Keegan-Treloar, R., Irvine, D.J., Solórzano-Rivas, S.C., Werner, A.D., Banks, E.W., Currell, M.J., 2022. Fault-controlled springs: A review. Earth-Science Rev. 230, 104058. https://doi.org/10.1016/j.earscirev.2022.104058

Kim, Y.S., Peacock, D.C.P., Sanderson, D.J., 2003. Mesoscale strike-slip faults and damage zones at Marsalforn, Gozo Island, Malta. J. Struct. Geol. 25, 793–812. https://doi.org/10.1016/S0191-8141(02)00200-6

Kim, Y.S., Peacock, D.C.P., Sanderson, D.J., 2004. Fault damage zones. J. Struct. Geol. 26, 503–517. https://doi.org/10.1016/j.jsg.2003.08.002

King, G., Bailey, G., 2006. Tectonics and human evolution. Antiquity 80, 265–286. https://doi.org/10.1017/S0003598X00093613

Kirkpatrick, J.D., Bezerra, F.H.R., Shipton, Z.K., Do Nascimento, A.F., Pytharouli, S.I., Lunn, R.J., Soden, A.M., 2013. Scale-dependent influence of pre-existing basement shear zones on rift faulting: a case study from NE Brazil. J. Geol. Soc. London. 170, 237–247. https://doi.org/10.1144/jgs2012-043

Kirkpatrick, J.D., Shipton, Z.K., 2009. Geologic evidence for multiple slip weakening mechanisms during seismic slip in crystalline rock. J. Geophys. Res. Solid Earth 114. https://doi.org/10.1029/2008JB006037

Kirkpatrick, J.D., Shipton, Z.K., Evans, J.P., Micklethwaite, S., Lim, S.J., McKillop, P., 2008. Strike-slip fault terminations at seismogenic depths: The structure and kinematics of the Glacier Lakes fault, Sierra Nevada United States. J. Geophys. Res. Solid Earth 113, 1–15. https://doi.org/10.1029/2007JB005311

Lara, L.E., Naranjo, J.A., Moreno, H., 2004. Rhyodacitic fissure eruption in Southern Andes (Cordón Caulle; 40.5°S) after the 1960 (Mw:9.5) Chilean earthquake: a structural interpretation. J. Volcanol. Geotherm. Res. 138, 127–138. https://doi.org/10.1016/j.jvolgeores.2004.06.009

Legrand, D., Barrientos, S., Bataille, K., Cembrano, J., Pavez, A., 2011. The fluid-driven tectonic swarm of Aysen Fjord, Chile (2007) associated with two earthquakes (Mw=6.1 and Mw=6.2) within the Liquiñe-Ofqui Fault Zone. Cont. Shelf Res. 31, 154–161. https://doi.org/10.1016/j.csr.2010.05.008

Lewis, M.A., Ben-Zion, Y., 2010. Diversity of fault zone damage and trapping structures in the Parkfield section of the San Andreas Fault from comprehensive analysis of near fault seismograms. Geophys. J. Int. 183, 1579–1595. https://doi.org/10.1111/j.1365-246X.2010.04816.x

Li, H., Wang, H., Xu, Z., Si, J., Pei, J., Li, T., Huang, Y., Song, S.-R., Kuo, L.-W., Sun, Z., Chevalier, M.-L., Liu, D., 2013. Characteristics of the fault-related rocks, fault zones and the principal slip zone in the Wenchuan Earthquake Fault Scientific Drilling Project Hole-1 (WFSD-1). Tectonophysics 584, 23–42. https://doi.org/10.1016/j.tecto.2012.08.021

Li, Y.G., Vidale, J.E., Cochran, E.S., 2004. Low-velocity damaged structure of the San Andreas Fault at Parkfield from fault zone trapped waves. Geophys. Res. Lett. 31. https://doi.org/10.1029/2003GL019044

Liu, Y.-K., Ross, Z.E., Cochran, E.S., Lapusta, N., 2022. A unified perspective of seismicity and fault coupling along the San Andreas Fault. Sci. Adv. 8. https://doi.org/10.1126/sciadv.abk1167

Lockner, D.A., Byerlee, J.D., 1993. How geometrical constraints contribute to the weakness of mature faults. Nature 363, 250–252. https://doi.org/10.1038/363250a0

Lucassen, F., Franz, G., 1994. Arc related Jurassic igneous and meta-igneous rocks in the Coastal Cordillera of northern Chile/Region Antofagasta. Lithos 32, 273–298. https://doi.org/10.1016/0024-4937(94)90044-2

Lucassen, F., Thirlwall, M.F., 1998. Sm – Nd ages of mafic rocks from the Coastal Cordillera at 24°S , northern Chile. Geol. Rundschau 86, 767–774.

Lucca, A., Storti, F., Balsamo, F., Clemenzi, L., Fondriest, M., Burgess, R., Di Toro, G., 2019. From Submarine to Subaerial Out-of-Sequence Thrusting and Gravity-Driven Extensional Faulting: Gran Sasso Massif, Central Apennines, Italy. Tectonics 38, 4155–4184. https://doi.org/10.1029/2019TC005783

Lupi, M., Miller, S.A., 2014. Short-lived tectonic switch mechanism for long-term pulses of volcanic activity after mega-thrust earthquakes. Solid Earth 5, 13–24. https://doi.org/10.5194/se-5-13-2014

Lupi, M., Trippanera, D., Gonzalez, D., D'amico, S., Acocella, V., Cabello, C., Stef, M.M., Tassara, A., 2020. Transient tectonic regimes imposed by megathrust earthquakes and the growth of NW-trending volcanic systems in the Southern Andes. Tectonophysics 774, 228204. https://doi.org/10.1016/j.tecto.2019.228204

Magloughlin, J.F., Spray, J.G., 1992. Frictional melting processes and products in geological materials: introduction and discussion. Tectonophysics 204, 197–204. https://doi.org/10.1016/0040-1951(92)90307-R

Mancktelow, N., Pennacchioni, G., 2020. Intermittent fracturing in the middle continental crust as evidence for transient switching of principal stress axes associated with the subduction zone earthquake cycle. Geology 48. https://doi.org/10.1130/G47625.1

Mancktelow, N.S., Camacho, A., Pennacchioni, G., 2022. Time-Lapse Record of an Earthquake in the Dry Felsic Lower Continental Crust Preserved in a Pseudotachylyte-Bearing Fault. J. Geophys. Res. Solid Earth 127. https://doi.org/10.1029/2021JB022878

Mandl, G., 1988. Mechanics of Tectonic Faulting: Models and Basic Concepts. Elsevier.

Marchesini, B., Carminati, E., Aldega, L., Mirabella, F., Petrelli, M., Caracausi, A., Barchi, M.R., 2022. Chemical interaction driven by deep fluids in the damage zone of a seismogenic carbonate fault. J. Struct. Geol. 161, 104668. https://doi.org/10.1016/j.jsg.2022.104668

Marrett, R., Allmendinger, R.W., 1990. Kinematic analysis of fault-slip data. J. Struct. Geol. 12, 973–986. https://doi.org/10.1016/0191-8141(90)90093-E

Martel, S.J., 1990. Formation of compound strike-slip fault zones, Mount Abbot quadrangle, California. J. Struct. Geol. 12, 869–882. https://doi.org/10.1016/0191-8141(90)90060-C

Masoch, S., Fondriest, M., Gomila, R., Jensen, E., Mitchell, T.M., Cembrano, J., Pennacchioni, G., Di Toro, G., 2022. Along-strike architectural variability of an exhumed crustal-scale seismogenic fault (Bolfin Fault Zone, Atacama Fault System, Chile). J. Struct. Geol. 165, 104745. https://doi.org/10.1016/j.jsg.2022.104745

Masoch, S., Fondriest, M., Preto, N., Secco, M., Di Toro, G., 2019. Seismic cycle recorded in cockade-bearing faults (Col de Teghime, Alpine Corsica). J. Struct. Geol. 129, 103889. https://doi.org/10.1016/j.jsg.2019.103889

Masoch, S., Gomila, R., Fondriest, M., Jensen, E., Mitchell, T., Pennacchioni, G., Cembrano, J., Di Toro, G., 2021. Structural Evolution of a Crustal-Scale Seismogenic Fault in a Magmatic Arc: The Bolfin Fault Zone (Atacama Fault System). Tectonics 40. https://doi.org/10.1029/2021TC006818

Massironi, M., Bistacchi, A., Menegon, L., 2011. Misoriented faults in exhumed metamorphic complexes: Rule or exception? Earth Planet. Sci. Lett. 307, 233–239. https://doi.org/10.1016/j.epsl.2011.04.041

Mauldon, M., Dershowitz, W., 2000. A multi-dimensional system of fracture abundance measures. Geol. Soc. Am. Abstr. with Programs 32, A474.

Melosh, B.L., Rowe, C.D., Smit, L., Groenewald, C., Lambert, C.W., Macey, P., 2014. Snap, crackle, Pop: Dilational fault breccias record seismic slip below the brittle-plastic transition. Earth Planet. Sci. Lett. 403, 432–445. https://doi.org/10.1016/j.epsl.2014.07.002

Mesimeri, M., Pankow, K.L., Baker, B., Hale, J.M., 2021. Episodic Earthquake Swarms in the Mineral Mountains, Utah Driven by the Roosevelt Hydrothermal System. J. Geophys. Res. Solid Earth 126. https://doi.org/10.1029/2021JB021659

Micklethwaite, S., Sheldon, H.A., Baker, T., 2010. Active fault and shear processes and their implications for mineral deposit formation and discovery. J. Struct. Geol. 32, 151–165. https://doi.org/10.1016/j.jsg.2009.10.009

Miller, R.B., Paterson, S.R., 1999. In defense of magmatic diapirs. J. Struct. Geol. 21, 1161–1173. https://doi.org/10.1016/S0191-8141(99)00033-4

Miller, S.A., Collettini, C., Chiaraluce, L., Cocco, M., Barchi, M., Kaus, B.J.P., 2004. Aftershocks driven by a high-pressure CO2 source at depth. Nature 427, 724–727. https://doi.org/10.1038/nature02251

Mitchell, T.M., Ben-Zion, Y., Shimamoto, T., 2011. Pulverized fault rocks and damage asymmetry along the Arima-Takatsuki Tectonic Line, Japan. Earth Planet. Sci. Lett. 308, 284–297. https://doi.org/10.1016/j.epsl.2011.04.023

Mitchell, T.M., Faulkner, D.R., 2009. The nature and origin of off-fault damage surrounding strike-slip fault zones with a wide range of displacements: A field study from the Atacama fault system, northern Chile. J. Struct. Geol. 31, 802–816. https://doi.org/10.1016/j.jsg.2009.05.002

Mitchell, T.M., Toy, V., Di Toro, G., Renner, J., Sibson, R.H., 2016. Fault welding by pseudotachylyte formation. Geology 44, 1059–1062. https://doi.org/10.1130/G38373.1

Mittempergher, S., Dallai, L., Pennacchioni, G., Renard, F., Di Toro, G., 2014. Origin of hydrous fluids at seismogenic depth: Constraints from natural and experimental fault rocks. Earth Planet. Sci. Lett. 385, 97–109. https://doi.org/10.1016/j.epsl.2013.10.027

Mittempergher, S., Pennacchioni, G., Di Toro, G., 2009. The effects of fault orientation and fluid infiltration on fault rock assemblages at seismogenic depths. J. Struct. Geol. 31, 1511–1524. https://doi.org/10.1016/j.jsg.2009.09.003

Mittempergher, S., Zanchi, A., Zanchetta, S., Fumagalli, M., Gukov, K., Bistacchi, A., 2021. Fault reactivation and propagation in the northern Adamello pluton: The structure and kinematics of a kilometre-scale seismogenic source. Tectonophysics 228790. https://doi.org/10.1016/j.tecto.2021.228790

Moecher, D.P., Sharp, Z.D., 2004. Stable isotope and chemical systematics of pseudotachylyte and wall rock, Homestake shear zone, Colorado, USA: Meteoric fluid or rock-buffered conditions during coseismic fusion? J. Geophys. Res. 109, B12206. https://doi.org/10.1029/2004JB003045

Mogi, K., 1963. Some Discusions on Aftershocks, Foreshocks and Earthquake Swarms: The Fracture of a Semi-Infinite Body Caused by Inner Stress Origin and Its Relation to the Earthquake Phenomena (3rd Paper). Bull. Earthq. Res. Inst. 41, 615–658.

Molina, J.F., Moreno, J.A., Castro, A., Rodríguez, C., Fershtater, G.B., 2015. Calcic amphibole thermobarometry in metamorphic and igneous rocks: New calibrations based on plagioclase/amphibole Al-Si partitioning and amphibole/liquid Mg partitioning. Lithos 232, 286–305. https://doi.org/https://doi.org/10.1016/j.lithos.2015.06.027

Moretti, I., 1998. The role of faults in hydrocarbon migration. Pet. Geosci. 4, 81–94. https://doi.org/10.1144/petgeo.4.1.81

Morton, N., Girty, G.H., Rockwell, T.K., 2012. Fault zone architecture of the San Jacinto fault zone in Horse Canyon, southern California: A model for focused post-seismic fluid flow and heat transfer in the shallow crust. Earth Planet. Sci. Lett. 329–330, 71–83. https://doi.org/10.1016/j.epsl.2012.02.013

Naliboff, J.B., Glerum, A., Brune, S., Péron-Pinvidic, G., Wrona, T., 2020. Development of 3-D Rift Heterogeneity Through Fault Network Evolution. Geophys. Res. Lett. 47, e2019GL086611. https://doi.org/10.1029/2019GL086611

Nasseri, M.H., Rao, K.S., Ramamurthy, T., 1997. Failure mechanism in schistose rocks. Int. J. Rock Mech. Min. Sci. 34, 219.e1-219.e15. https://doi.org/10.1016/S1365-1609(97)00099-3

Nasseri, M.H.., Rao, K.S., Ramamurthy, T., 2003. Anisotropic strength and deformational behavior of Himalayan schists. Int. J. Rock Mech. Min. Sci. 40, 3–23. https://doi.org/10.1016/S1365-1609(02)00103-X

Naylor, M.., Mandl, G., Supesteijn, C.H.., 1986. Fault geometries in basement-induced wrench faulting under different initial stress states. J. Struct. Geol. 8, 737–752. https://doi.org/10.1016/0191-8141(86)90022-2

O'Hara, K.., Sharp, Z.., 2001. Chemical and oxygen isotope composition of natural and artificial pseudotachylyte: role of water during frictional fusion. Earth Planet. Sci. Lett. 184, 393–406. https://doi.org/10.1016/S0012-821X(00)00331-9

Okubo, K., Bhat, H.S., Rougier, E., Marty, S., Schubnel, A., Lei, Z., Knight, E.E., Klinger, Y., 2019. Dynamics, Radiation, and Overall Energy Budget of Earthquake Rupture With Coseismic Off-Fault Damage. J. Geophys. Res. Solid Earth 124, 11771–11801. https://doi.org/10.1029/2019JB017304

Olivares, V., Herrera, V., Cembrano, J., Arancibia, G., Reyes, N., Faulkner, D., 2010. Tectonic significance and hydrothermal fluid migration within a strike-slip duplex fault-vein network: An example from the Atacama Fault System. Andean Geol.

Omori, F., 1894. On the Aftershocks of Earthquakes. J. Coll. Sci. Imp. Univ. Tokyo 7, 111–120.

Pachell, M.A., Evans, J.P., 2002. Growth, linkage, and termination processes of a 10-km-long strike-slip fault in jointed granite: the Gemini fault zone, Sierra Nevada, California. J. Struct. Geol. 24, 1903–1924. https://doi.org/10.1016/S0191-8141(02)00027-5

Parada, M.A., López-Escobar, L., Oliveros, V., Fuentes, F., Morata, D., Calderón, M., Aguirre, L., Féraud, G., Espinoza, F., Moreno, H., Figueroa, O., Muñoz, J., Rosa, B., Vásquez, T., Stern, C.R., 2007. Andean magmatism, in: Moreno, T., Gibbons, W. (Eds.), The Geology of Chile. The Geological Society of London, pp. 115–146. https://doi.org/10.1144/GOCH.4

Pardo-Casas, F., Molnar, P., 1987. Relative motion of the Nazca (Farallon) and South American Plates since Late Cretaceous time. Tectonics 6, 233–248. https://doi.org/10.1029/TC006i003p00233

Peacock, D.C.P., Sanderson, D.J., 1995. Strike-slip relay ramps. J. Struct. Geol. 17, 1351–1360. https://doi.org/10.1016/0191-8141(95)97303-W

Pearce, R.K., Sánchez de la Muela, A., Moorkamp, M., Hammond, J.O.S., Mitchell, T.M., Cembrano, J., Araya Vargas, J., Meredith, P.G., Iturrieta, P., Pérez Estay, N., Marshall, N.R., Smith, J., Yañez, G., Griffith, W.A., Marquardt-Román, C., Stanton-Yonge, A., Núñez, R., 2020. Reactivation of fault systems by compartmentalized hydrothermal fluids in the Southern Andes revealed by magnetotelluric and seismic data. Tectonics. https://doi.org/10.1029/2019TC005997

Pennacchioni, G., 2005. Control of the geometry of precursor brittle structures on the type of ductile shear zone in the Adamello tonalites, Southern Alps (Italy). J. Struct. Geol. 27, 627–644. https://doi.org/10.1016/j.jsg.2004.11.008

Pennacchioni, G., Di Toro, G., Brack, P., Menegon, L., Villa, I.M., 2006. Brittle-ductile-brittle deformation during cooling of tonalite (Adamello, Southern Italian Alps). Tectonophysics 427, 171–197. https://doi.org/10.1016/j.tecto.2006.05.019

Pennacchioni, G., Mancktelow, N.S., 2013. Initiation and growth of strike-slip faults within intact metagranitoid (Neves area, eastern Alps, Italy). Bull. Geol. Soc. Am. 125, 1468–1483. https://doi.org/10.1130/B30832.1

Pennacchioni, G., Mancktelow, N.S., 2018. Small-scale ductile shear zones: Neither extending, nor thickening, nor narrowing. Earth-Science Rev. https://doi.org/10.1016/j.earscirev.2018.06.004

Pennacchioni, G., Zucchi, E., 2013. High temperature fracturing and ductile deformation during cooling of a pluton: The Lake Edison granodiorite (Sierra Nevada batholith, California). J. Struct. Geol. 50, 54–81. https://doi.org/10.1016/J.JSG.2012.06.001

Pérez-Flores, P., Cembrano, J., Sánchez-Alfaro, P., Veloso, E., Arancibia, G., Roquer, T., 2016. Tectonics, magmatism and paleo-fluid distribution in a strike-slip setting: Insights from the northern termination of the Liquiñe–Ofqui fault System, Chile. Tectonophysics 680, 192–210. https://doi.org/10.1016/j.tecto.2016.05.016

Perrin, J., Luetscher, M., 2008. Inference of the structure of karst conduits using quantitative tracer tests and geological information: example of the Swiss Jura. Hydrogeol. J. 16, 951–967. https://doi.org/10.1007/s10040-008-0281-6

Peverelli, V., Berger, A., Mulch, A., Pettke, T., Piccoli, F., Herwegh, M., 2022. Epidote U-Pb geochronology and H isotope geochemistry trace pre-orogenic hydration of midcrustal granitoids. Geology 50, 1073–1077. https://doi.org/10.1130/G50028.1

Phillips, T.B., Fazlikhani, H., Gawthorpe, R.L., Fossen, H., Jackson, C.A.-L., Bell, R.E., Faleide, J.I., Rotevatn, A., 2019. The Influence of Structural Inheritance and Multiphase Extension on Rift Development, the Northern North Sea. Tectonics 38, 4099–4126. https://doi.org/10.1029/2019TC005756

Phillips, W.J., 1972. Hydraulic fracturing and mineralization. J. Geol. Soc. London. 128, 337–359. https://doi.org/10.1144/gsjgs.128.4.0337

Piquer, J., Sanchez-Alfaro, P., Pérez-Flores, P., 2021. A new model for the optimal structural context for giant porphyry copper deposit formation. Geology. https://doi.org/10.1130/G48287.1

Pischiutta, M., Fondriest, M., Demurtas, M., Magnoni, F., Di Toro, G., Rovelli, A., 2017. Structural control on the directional amplification of seismic noise (Campo Imperatore, central Italy). Earth Planet. Sci. Lett. 471, 10–18. https://doi.org/10.1016/j.epsl.2017.04.017

Price, N.J., Cosgrove, J.W., 1990. Analysis of Geological Structures. Cambridge University Press.

Reches, Z., Dewers, T., 2005. Gouge formation by dynamic pulverization during earthquake rupture. Earth Planet. Sci. Lett. 235, 361–374. https://doi.org/10.1016/j.epsl.2005.04.009

Rempe, M., Mitchell, T.M., Renner, J., Smith, S.A.F., Bistacchi, A., Di Toro, G., 2018. The Relationship Between Microfracture Damage and the Physical Properties of Fault-Related Rocks: The Gole

Larghe Fault Zone, Italian Southern Alps. J. Geophys. Res. Solid Earth 123, 7661–7687. https://doi.org/10.1029/2018JB015900

Richards, J.P., 2013. Giant ore deposits formed by optimal alignments and combinations of geological processes. Nat. Geosci. 6, 911–916. https://doi.org/10.1038/ngeo1920

Rizza, M., Bollinger, L., Sapkota, S.N., Tapponnier, P., Klinger, Y., Karakaş, Ç., Kali, E., Etchebes, M., Tiwari, D.R., Siwakoti, I., Bitri, A., Bes de Berc, S., 2019. Post Earthquake Aggradation Processes to Hide Surface Ruptures in Thrust Systems: The M8.3, 1934, Bihar-Nepal Earthquake Ruptures at Charnath Khola (Eastern Nepal). J. Geophys. Res. Solid Earth 124, 9182–9207. https://doi.org/10.1029/2018JB016376

Robert, F., Poulsen, K.., 2001. Vein Formation and Deformation in Greenstone Gold Deposits, in: Structural Controls on Ore Genesis. Society of Economic Geologists, pp. 111–155. https://doi.org/10.5382/Rev.14.05

Rosenberg, C.L., 2004. Shear zones and magma ascent: A model based on a review of the Tertiary magmatism in the Alps. Tectonics 23, n/a-n/a. https://doi.org/10.1029/2003TC001526

Ross, Z.E., Ben-Zion, Y., Zaliapin, I., 2022. Geometrical properties of seismicity in California. Geophys. J. Int. 231, 493–504. https://doi.org/10.1093/gji/ggac189

Ross, Z.E., Cochran, E.S., Trugman, D.T., Smith, J.D., 2020. 3D fault architecture controls the dynamism of earthquake swarms. Science (80-.). 368, 1357–1361. https://doi.org/10.1126/science.abb0779

Ross, Z.E., Hauksson, E., Ben-Zion, Y., 2017. Abundant off-fault seismicity and orthogonal structures in the San Jacinto fault zone. Sci. Adv. 3, e1601946. https://doi.org/10.1126/sciadv.1601946

Ross, Z.E., Trugman, D.T., Hauksson, E., Shearer, P.M., 2019. Searching for hidden earthquakes in Southern California. Science (80-.). 364, 767–771. https://doi.org/10.1126/science.aaw6888

Rowe, C.D., Griffith, W.A., 2015. Do faults preserve a record of seismic slip: A second opinion. J. Struct. Geol. https://doi.org/10.1016/j.jsg.2015.06.006

Rowe, C.D., Moore, J.C., Meneghini, F., McKeirnan, A.W., 2005. Large-scale pseudotachylytes and fluidized cataclasites from an ancient subduction thrust fault. Geology 33, 937. https://doi.org/10.1130/G21856.1

Ruthven, R., Singleton, J., Seymour, N., Gomila, R., Arancibia, G., Stockli, D.F., Ridley, J., Magloughlin, J., 2020. The geometry, kinematics, and timing of deformation along the southern segment of the Paposo fault zone, Atacama fault system, northern Chile. J. South Am. Earth Sci. 97, 102355. https://doi.org/10.1016/j.jsames.2019.102355

Sanchez-Alfaro, P., Reich, M., Driesner, T., Cembrano, J., Arancibia, G., Pérez-Flores, P., Heinrich, C.A., Rowland, J., Tardani, D., Lange, D., Campos, E., 2016. The optimal windows for seismically-enhanced gold precipitation in the epithermal environment. Ore Geol. Rev. 79, 463–473. https://doi.org/10.1016/j.oregeorev.2016.06.005

Sánchez-Reyes, H., Essing, D., Beaucé, E., Poli, P., 2021. The Imbricated Foreshock and Aftershock Activities of the Balsorano (Italy) Mw 4.4 Normal Fault Earthquake and Implications for Earthquake Initiation. Seismol. Res. Lett. 92, 1926–1936. https://doi.org/10.1785/0220200253

Sawyer, E.W., 2000. Grain-scale and outcrop-scale distribution and movement of melt in a crystallising granite. Earth Environ. Sci. Trans. R. Soc. Edinburgh 91, 73–85. https://doi.org/10.1017/S0263593300007306

Scheuber, E., Andriessen, P.A.M., 1990. The kinematic and geodynamic significance of the Atacama fault zone, northern Chile. J. Struct. Geol. 12, 243–257. https://doi.org/10.1016/0191-8141(90)90008-M

Scheuber, E., González, G., 1999. Tectonics of the Jurassic-Early Cretaceous magmatic arc of the north Chilean Coastal Cordillera (22°-26°S): A story of crustal deformation along a convergent plate boundary. Tectonics 18, 895–910. https://doi.org/10.1029/1999TC900024

Scheuber, E., Hammerschmidt, K., Friedrichsen, H., 1995. 40Ar/39Ar and Rb-Sr analyses from ductile shear zones from the Atacama Fault Zone, northern Chile: the age of deformation. Tectonophysics 250, 61–87. https://doi.org/10.1016/0040-1951(95)00044-8

Scholz, C.H., 2019. The Mechanics of Earthquakes and Faulting, The Mechanics of Earthquakes and Faulting. Cambridge University Press. https://doi.org/10.1017/9781316681473

Segall, P., Pollard, D.P., 1983. Nucleation and growth of strike slip faults in granite. J. Geophys. Res. 88, 555–568. https://doi.org/10.1029/JB088iB01p00555

Segall, P., Simpson, C., 1986. Nucleation of ductile shear zones on dilatant fractures. Geology 14, 56. https://doi.org/10.1130/0091-7613(1986)14<56:NODSZO>2.0.CO;2

SERNAGEOMIN, 2003. Mapa Geológico de Chile: versión digital. Base geológica escala 1:1.000.000.

Seymour, N.M., Singleton, J.S., Gomila, R., Mavor, S.P., Heuser, G., Arancibia, G., Williams, S., Stockli, D.F., 2021. Magnitude, timing, and rate of slip along the Atacama fault system, northern Chile: implications for Early Cretaceous slip partitioning and plate convergence. J. Geol. Soc. London. jgs2020-142. https://doi.org/10.1144/jgs2020-142

Seymour, N.M., Singleton, J.S., Mavor, S.P., Gomila, R., Stockli, D.F., Heuser, G., Arancibia, G., 2020. The Relationship Between Magmatism and Deformation Along the Intra-arc Strike-Slip Atacama Fault System, Northern Chile. Tectonics 39, e2019TC005702. https://doi.org/10.1029/2019TC005702

Shapiro, S.A., 2015. Fluid-induced Seismicity. Cambridge University Press, Cambridge, England. https://doi.org/https://doi.org/10.1017/CBO9781139051132

Share, P.-E., Castro, R.R., Vidal-Villegas, J.A., Mendoza, L., Ben-Zion, Y., 2021. High-resolution seismic imaging of the plate boundary in northern Baja California and southern California using double-pair double-difference tomography. Earth Planet. Sci. Lett. 568, 117004. https://doi.org/10.1016/j.epsl.2021.117004

Sharp, Z.D., 2007. Principles of Stable Isotope Geochemistry, 2 edition. ed. Pearson/Prentice Hall, Upper Saddle River. https://doi.org/https://doi.org/10.25844/h9q1-0p82

Sharp, Z.D., Atudorei, V., Durakiewicz, T., 2001. A rapid method for determination of hydrogen and oxygen isotope ratios from water and hydrous minerals. Chem. Geol. 178, 197–210. https://doi.org/10.1016/S0009-2541(01)00262-5

Shelly, D.R., 2020. A High-Resolution Seismic Catalog for the Initial 2019 Ridgecrest Earthquake Sequence: Foreshocks, Aftershocks, and Faulting Complexity. Seismol. Res. Lett. 91, 1971–1978. https://doi.org/10.1785/0220190309

Shelly, D.R., Ellsworth, W.L., Hill, D.P., 2016. Fluid-faulting evolution in high definition: Connecting fault structure and frequency-magnitude variations during the 2014 Long Valley Caldera, California, earthquake swarm. J. Geophys. Res. Solid Earth 121, 1776–1795. https://doi.org/10.1002/2015JB012719

Shelly, D.R., Hill, D.P., Massin, F., Farrell, J., Smith, R.B., Taira, T., 2013a. A fluid-driven earthquake swarm on the margin of the Yellowstone caldera. J. Geophys. Res. Solid Earth 118, 4872–4886. https://doi.org/10.1002/jgrb.50362

Shelly, D.R., Moran, S.C., Thelen, W.A., 2013b. Evidence for fluid-triggered slip in the 2009 Mount Rainier, Washington earthquake swarm. Geophys. Res. Lett. 40, 1506–1512. https://doi.org/10.1002/grl.50354

Shelly, D.R., Skoumal, R.J., Hardebeck, J.L., 2022. Fracture-mesh faulting in the swarm-like 2020 Maacama sequence revealed by high-precision earthquake detection, location, and focal mechanisms. Geophys. Res. Lett. https://doi.org/10.1029/2022GL101233

Shelly, D.R., Taira, T., Prejean, S.G., Hill, D.P., Dreger, D.S., 2015. Fluid-faulting interactions: Fracture-mesh and fault-valve behavior in the February 2014 Mammoth Mountain, California, earthquake swarm. Geophys. Res. Lett. 42, 5803–5812. https://doi.org/10.1002/2015GL064325

Sheppard, S.M.F., 1986. Characterization and isotopic variations in natural waters, in: Valley, J.W., Taylor Jr., H.P., O'Neil, J.R. (Eds.), Stable Isotopes in High Temperature Geological Processes. Mineralogical Society of America, Washington, DC, pp. 165–183.

Shigematsu, N., Kametaka, M., Inada, N., Miyawaki, M., Miyakawa, A., Kameda, J., Togo, T., Fujimoto, K., 2017. Evolution of the Median Tectonic Line fault zone, SW Japan, during exhumation. Tectonophysics 696–697, 52–69. https://doi.org/10.1016/j.tecto.2016.12.017

Shipton, Z.K., Cowie, P.A., 2001. Damage zone and slip-surface evolution over mm to km scales in high-porosity Navajo sandstone, Utah. J. Struct. Geol. 23, 1825–1844.

Sibson, R H, 1986. Earthquakes and Rock Deformation in Crustal Fault Zones. Annu. Rev. Earth Planet. Sci. 14, 149–175. https://doi.org/10.1146/annurev.ea.14.050186.001053

Sibson, R.H., 1975. Generation of Pseudotachylyte by Ancient Seismic Faulting. Geophys. J. R. Astron. Soc. 43, 775–794. https://doi.org/10.1111/j.1365-246X.1975.tb06195.x

Sibson, R.H., 1977. Fault rocks and fault mechanisms. J. Geol. Soc. London. 133, 191 LP – 213. https://doi.org/10.1144/gsjgs.133.3.0191

Sibson, R.H., 1981. Fluid Flow Accompanying Faulting: Field Evidence and Models, in: Simpson, D.W., Richards, P.G. (Eds.), Earthquake Prediction: An International Review, Volume 4. pp. 593–603. https://doi.org/10.1029/ME004p0593

Sibson, R.H., 1985. Stopping of earthquake ruptures at dilational fault jogs. Nature 316, 248–251. https://doi.org/10.1038/316248a0

Sibson, R.H., 1986. Brecciation processes in fault zones: Inferences from earthquake rupturing. Pure Appl. Geophys. PAGEOPH 124, 159–175. https://doi.org/10.1007/BF00875724

Sibson, R.H., 1987. Earthquake rupturing as a mineralizing agent in hydrothermal systems. Geology 15, 701. https://doi.org/10.1130/0091-7613(1987)15<701:ERAAMA>2.0.CO;2

Sibson, R.H., 1989. Earthquake faulting as a structural process. J. Struct. Geol. 11, 1–14. https://doi.org/10.1016/0191-8141(89)90032-1

Sibson, R.H., 1990. Faulting and fluid flow, in: Nesbitt, B.E. (Ed.), Fluids in Tectonically Active Regimes of the Continental Crust. Mineralogical Association of Canada, Short Course on Crustal Fluids, Handbook 18, pp. 93–132.

Sibson, R.H., 1992a. Fault-valve behavior and the hydrostatic-lithostatic fluid pressure interface. Earth Sci. Rev. 32, 141–144. https://doi.org/10.1016/0012-8252(92)90019-P

Sibson, R.H., 1992b. Implication of fault-valve behaviour for rupture nucleation and recurrence. Tectonophysics 211, 283–293.

Sibson, R.H., 1994. Crustal stress, faulting and fluid flow. Geol. Soc. London, Spec. Publ. 78, 69–84. https://doi.org/10.1144/GSL.SP.1994.078.01.07

Sibson, R.H., Scott, J., 1998. Stress/fault controls on the containment and release of overpressured fluids: examples from gold-quartz vein systems in Juneau, Alaska; Victoria, Australia and Otago, New Zealand. Ore Geol. Rev. 13, 293–306. https://doi.org/10.1016/S0169-1368(97)00023-1

Sielfeld, G., Lange, D., Cembrano, J., 2019. Intra-Arc Crustal Seismicity: Seismotectonic Implications for the Southern Andes Volcanic Zone, Chile. Tectonics 38, 552–578. https://doi.org/10.1029/2018TC004985

Sillitoe, R.H., 2010. Porphyry Copper Systems. Econ. Geol. 105, 3–41. https://doi.org/10.2113/gsecongeo.105.1.3

Simmons, S.F., White, N.C., John, D.A., 2005. Geological Characteristics of Epithermal Precious and Base Metal Deposits, in: One Hundredth Anniversary Volume. Society of Economic Geologists. https://doi.org/10.5382/AV100.16

Smeraglia, L., Giuffrida, A., Grimaldi, S., Pullen, A., La Bruna, V., Billi, A., Agosta, F., 2021. Fault-controlled upwelling of low-T hydrothermal fluids tracked by travertines in a fold-and-thrust belt, Monte Alpi, southern apennines, Italy. J. Struct. Geol. 144, 104276. https://doi.org/10.1016/j.jsg.2020.104276

Smith, S.A.F., Bistacchi, A., Mitchell, T.M., Mittempergher, S., Di Toro, G., 2013. The structure of an exhumed intraplate seismogenic fault in crystalline basement. Tectonophysics 599, 29–44. https://doi.org/10.1016/j.tecto.2013.03.031

Snoke, A.W., Tullis, J., Todd, V.R., 1998. Fault-Related Rocks: A Photographic Atlas. Princeton University Press. https://doi.org/10.2307/j.ctt7zvg0k

Spear, F.S., 1993. Metamorphic phase equilibria and pressure-temperature-time paths. Mineralogical Society of America Monograph Series I.

Stanton-Yonge, A., Cembrano, J., Griffith, W.A., Jensen, E., Mitchell, T.M., 2020. Self-similar length-displacement scaling achieved by scale-dependent growth processes: Evidence from the Atacama Fault System. J. Struct. Geol. 133, 103993. https://doi.org/10.1016/j.jsg.2020.103993

Stewart, M., Holdsworth, R.E., Strachan, R.A., 2000. Deformation processes and weakening mechanisms within the frictional–viscous transition zone of major crustal-scale faults: insights from the Great Glen Fault Zone, Scotland. J. Struct. Geol. 22, 543–560. https://doi.org/https://doi.org/10.1016/S0191-8141(99)00164-9

Stierle, E., Bohnhoff, M., Vavryčuk, V., 2014. Resolution of non-double-couple components in the seismic moment tensor using regional networks—II: application to aftershocks of the 1999 Mw 7.4 Izmit earthquake. Geophys. J. Int. 196, 1878–1888. https://doi.org/10.1093/gji/ggt503

Stipp, M., Stünitz, H., Heilbronner, R., Schmid, S.M., 2002. The eastern Tonale fault zone: a 'natural laboratory' for crystal plastic deformation of quartz over a temperature range from 250 to 700°C. J. Struct. Geol. 24, 1861–1884. https://doi.org/10.1016/S0191-8141(02)00035-4

Storti, F., Holdsworth, R.E., Salvini, F., 2003. Intraplate strike-slip deformation belts, in: Storti, F., Holdsworth, R.E., Salvini, F. (Eds.), Intraplate Strike-Slip Deformation Belts. Geological Society of London, Special Publications, London, pp. 1–14. https://doi.org/10.1144/GSL.SP.2003.210.01.01

Sutherland, R., Toy, V.G., Townend, J., Cox, S.C., Eccles, J.D., Faulkner, D.R., Prior, D.J., Norris, R.J., Mariani, E., Boulton, C., Carpenter, B.M., Menzies, C.D., Little, T.A., Hasting, M., De Pascale, G.P., Langridge, R.M., Scott, H.R., Lindroos, Z.R., Fleming, B., Kopf, A.J., 2012. Drilling reveals fluid control on architecture and rupture of the Alpine fault, New Zealand. Geology 40, 1143–1146. https://doi.org/10.1130/G33614.1

Swanson, M.T., 1988. Pseudotachylyte-bearing strike-slip duplex structures in the Fort Foster Brittle Zone, S. Maine. J. Struct. Geol. 10, 813–828. https://doi.org/10.1016/0191-8141(88)90097-1

Swanson, M.T., 1992. Fault structure, wear mechanisms and rupture processes in pseudotachylyte generation. Tectonophysics 204, 223–242. https://doi.org/10.1016/0040-1951(92)90309-T

Swanson, M.T., 1999a. Dextral transpression at the Casco Bay restraining bend, Norumbega fault zone, coastal Maine, in: Norumbega Fault System of the Northern Appalachians. Geological Society of America. https://doi.org/10.1130/0-8137-2331-0.85

Swanson, M.T., 1999b. Kinematic indicators for regional dextral shear along the Norumbega fault system in the Casco Bay area, coastal Maine, in: Norumbega Fault System of the Northern Appalachians. Geological Society of America, pp. 1–24. https://doi.org/10.1130/0-8137-2331-0.1

Swanson, M.T., 2006a. Late Paleozoic strike-slip faults and related vein arrays of Cape Elizabeth, Maine. J. Struct. Geol. 28, 456–473. https://doi.org/10.1016/j.jsg.2005.12.009

Swanson, M.T., 2006b. Pseudotachylyte-bearing strike-slip faults in mylonitic host rocks, Fort Foster Brittle Zone, Kittery, Maine, in: Abercrombie, R., McGarr, A., Di Toro, G., Kanamori, H. (Eds.), Earthquakes: Radiated Energy and the Physics of Faulting. American Geophysical Union (AGU), pp. 167–179. https://doi.org/10.1029/170GM17

Sykes, L.R., 1978. Intraplate seismicity, reactivation of preexisting zones of weakness, alkaline magmatism, and other tectonism postdating continental fragmentation. Rev. Geophys. 16, 621–688. https://doi.org/https://doi.org/10.1029/RG016i004p00621

Sylvester, A.G., 1988. Strike-slip faults. Geol. Soc. Am. Bull. 100, 1666–1703. https://doi.org/10.1130/0016-7606(1988)100<1666:SSF>2.3.CO;2

Tardani, D., Reich, M., Roulleau, E., Takahata, N., Sano, Y., Pérez-Flores, P., Sánchez-Alfaro, P., Cembrano, J., Arancibia, G., 2016. Exploring the structural controls on helium, nitrogen and carbon isotope signatures in hydrothermal fluids along an intra-arc fault system. Geochim. Cosmochim. Acta 184, 193–211. https://doi.org/10.1016/j.gca.2016.04.031

Tesei, T., Collettini, C., Viti, C., Barchi, M.R., 2013. Fault architecture and deformation mechanisms in exhumed analogues of seismogenic carbonate-bearing thrusts. J. Struct. Geol. 55, 167–181. https://doi.org/10.1016/j.jsg.2013.07.007

Toy, V.G., Boulton, C.J., Sutherland, R., Townend, J., Norris, R.J., Little, T.A., Prior, D.J., Mariani, E., Faulkner, D., Menzies, C.D., Scott, H., Carpenter, B.M., 2015. Fault rock lithologies and architecture of the central Alpine fault, New Zealand, revealed by DFDP-1 drilling. Lithosphere 7, 155–173. https://doi.org/10.1130/L395.1

Trepmann, C.A., Stöckhert, B., 2003. Quartz microstructures developed during non-steady state plastic flow at rapidly decaying stress and strain rate. J. Struct. Geol. 25, 2035–2051. https://doi.org/10.1016/S0191-8141(03)00073-7

Trepmann, C.A., Stöckhert, B., 2013. Short-wavelength undulatory extinction in quartz recording coseismic deformation in the middle crust – an experimental study. Solid Earth 4, 263–276. https://doi.org/10.5194/se-4-263-2013

Unsworth, M.J., Malin, P.E., Egbert, G.D., Booker, J.R., 1997. Internal structure of the San Andreas fault at Parkfield, California. Geology 25, 359–362. https://doi.org/10.1130/0091-7613(1997)025<0359:ISOTSA>2.3.CO;2

US Geological Survey, 2016. Global death toll due to earthquakes from 2000 to 2015 [WWW Document]. Statistica. URL https://www.statista.com/statistics/263108/global-death-toll-due-to-earthquakes-since-2000/?locale=en (accessed 3.22.23).

Valoroso, L., Chiaraluce, L., Collettini, C., 2014. Earthquakes and fault zone structure. Geology 42, 343–346. https://doi.org/10.1130/G35071.1

Valoroso, L., Chiaraluce, L., Piccinini, D., Di Stefano, R., Schaff, D., Waldhauser, F., 2013. Radiography of a normal fault system by 64,000 high-precision earthquake locations: The 2009 L'Aquila (central Italy) case study. J. Geophys. Res. Solid Earth 118, 1156–1176. https://doi.org/10.1002/jgrb.50130

Vavryčuk, V., 2002. Non-double-couple earthquakes of 1997 January in West Bohemia, Czech Republic: evidence of tensile faulting. Geophys. J. Int. 149, 364–373. https://doi.org/10.1046/j.1365-246X.2002.01654.x

Veloso, E.E., Gomila, R., Cembrano, J., González, R., Jensen, E., Arancibia, G., 2015. Stress fields recorded on large-scale strike-slip fault systems: Effects on the tectonic evolution of crustal slivers during oblique subduction. Tectonophysics 664, 244–255. https://doi.org/10.1016/j.tecto.2015.09.022

Vermilye, J.M., Scholz, C.H., 1998. The process zone: a microstructural view of fault growth. J. Geophys. Res. Solid Earth 103.

Viegas, G., Abercrombie, R.E., Kim, W.-Y., 2010. The 2002 M5 Au Sable Forks, NY, earthquake sequence: Source scaling relationships and energy budget. J. Geophys. Res. 115, B07310. https://doi.org/10.1029/2009JB006799

Wedmore, L.N.J., Williams, J.N., Biggs, J., Fagereng, Å., Mphepo, F., Dulanya, Z., Willoughby, J., Mdala, H., Adams, B.A., 2020. Structural inheritance and border fault reactivation during active early-stage rifting along the Thyolo fault, Malawi. J. Struct. Geol. 139, 104097. https://doi.org/10.1016/j.jsg.2020.104097

Weinberg, R.F., 2006. Melt segregation structures in granitic plutons. Geology 34, 305. https://doi.org/10.1130/G22406.1

Wesnousky, S.G., 1988. Seismological and structural evolution of strike-slip faults. Nature 335, 340–343. https://doi.org/10.1038/335340a0

Wesnousky, S.G., 2006. Predicting the endpoints of earthquake ruptures. Nature 444, 358–360. https://doi.org/10.1038/nature05275

Whipp, P.S., Jackson, C.A.-L., Gawthorpe, R.L., Dreyer, T., Quinn, D., 2014. Normal fault array evolution above a reactivated rift fabric; a subsurface example from the northern Horda Platform, Norwegian North Sea. Basin Res. 26, 523–549. https://doi.org/10.1111/bre.12050

Whitney, D.L., Evans, B.W., 2010. Abbreviations for names of rock-forming minerals. Am. Mineral. 95, 185–187.

Wibberley, C.A.., Shimamoto, T., 2003. Internal structure and permeability of major strike-slip fault zones: the Median Tectonic Line in Mie Prefecture, Southwest Japan. J. Struct. Geol. 25, 59–78. https://doi.org/10.1016/S0191-8141(02)00014-7

Wibberley, C.A.J., Yielding, G., Di Toro, G., 2008. Recent advances in the understanding of fault zone internal structure: A review. Geol. Soc. Spec. Publ. 299, 5–33. https://doi.org/10.1144/SP299.2

Wikipedia, n.d. 2023 Turkey–Syria earthquake [WWW Document]. Wikipedia, Free Encycl. URL https://en.wikipedia.org/w/index.php?title=2023_Turkey–Syria_earthquake&oldid=1146763502 (accessed 3.27.23).

Williams, J.N., Toy, V.G., Massiot, C., McNamara, D.D., Smith, S.A.F., Mills, S., 2018. Controls on fault zone structure and brittle fracturing in the foliated hanging wall of the Alpine Fault. Solid Earth 9, 469–489. https://doi.org/10.5194/se-9-469-2018

Williams, J.N., Toy, V.G., Massiot, C., McNamara, D.D., Wang, T., 2016. Damaged beyond repair? Characterising the damage zone of a fault late in its interseismic cycle, the Alpine Fault, New Zealand. J. Struct. Geol. 90, 76–94. https://doi.org/10.1016/j.jsg.2016.07.006

Williams, J.N., Toy, V.G., Smith, S.A.F., Boulton, C., 2017. Fracturing, fluid-rock interaction and mineralisation during the seismic cycle along the Alpine Fault. J. Struct. Geol. 103, 151–166. https://doi.org/10.1016/j.jsg.2017.09.011

Williams, P.J., Barton, M.D., Johnson, D.A., Fontboté, L., Haller, A. de, Mark, G., Oliver, N.H.S., Marschik, R., 2005. Iron Oxide Copper-Gold Deposits<subtitle>Geology, Space-Time Distribution, and Possible Modes of Origin</subtitle>, in: One Hundredth Anniversary Volume. Society of Economic Geologists. https://doi.org/10.5382/AV100.13

Wollherr, S., Gabriel, A., Mai, P.M., 2019. Landers 1992 "Reloaded": Integrative Dynamic Earthquake Rupture Modeling. J. Geophys. Res. Solid Earth 124, 6666–6702. https://doi.org/10.1029/2018JB016355

Woodcock, N.H., 1986. The role of strike-slip fault systems at plate boundaries. Philos. Trans. R. Soc. London. Ser. A, Math. Phys. Sci. 317, 13–29. https://doi.org/10.1098/rsta.1986.0021

Woodcock, N.H., Dickson, J.A.D., Tarasewics, J.P.T., 2007. Transient permeability and reseal hardening in fault zones: Evidence from dilation breccia textures. Geol. Soc. Spec. Publ. 270, 43–53. https://doi.org/10.1144/GSL.SP.2007.270.01.03

Woodcock, N.H., Mort, K., 2008. Classification of fault breccias and related fault rocks. Geol. Mag. 145, 435–440. https://doi.org/10.1017/S0016756808004883

Ye, L., Lay, T., Kanamori, H., 2012. Intraplate and interplate faulting interactions during the August 31, 2012, Philippine Trench earthquake (M w 7.6) sequence. Geophys. Res. Lett. 39, 2012GL054164. https://doi.org/10.1029/2012GL054164

Yukutake, Y., Ito, H., Honda, R., Harada, M., Tanada, T., Yoshida, A., 2011. Fluid-induced swarm earthquake sequence revealed by precisely determined hypocenters and focal mechanisms in the 2009 activity at Hakone volcano, Japan. J. Geophys. Res. 116, B04308. https://doi.org/10.1029/2010JB008036

Zigone, D., Ben-Zion, Y., Campillo, M., Roux, P., 2015. Seismic Tomography of the Southern California Plate Boundary Region from Noise-Based Rayleigh and Love Waves. Pure Appl. Geophys. 172, 1007–1032. https://doi.org/10.1007/s00024-014-0872-1

Zoback, M., Hickman, S., Ellsworth, W., 2011. Scientific Drilling Into the San Andreas Fault Zone - An Overview of SAFOD's First Five Years. Sci. Drill. https://doi.org/10.2204/iodp.sd.11.02.2011